

---


Electronic Theses and Dissertations, 2004-2019

---

2018

## A Framework for Miniaturized Mechanical Characterization of Tensile, Creep, and Fatigue Properties of SLM Alloys

Jonathan Torres-Caceres  
*University of Central Florida*

 Part of the [Mechanical Engineering Commons](#)  
Find similar works at: <https://stars.library.ucf.edu/etd>  
University of Central Florida Libraries <http://library.ucf.edu>

This Doctoral Dissertation (Open Access) is brought to you for free and open access by STARS. It has been accepted for inclusion in Electronic Theses and Dissertations, 2004-2019 by an authorized administrator of STARS. For more information, please contact [STARS@ucf.edu](mailto:STARS@ucf.edu).

---

### STARS Citation

Torres-Caceres, Jonathan, "A Framework for Miniaturized Mechanical Characterization of Tensile, Creep, and Fatigue Properties of SLM Alloys" (2018). *Electronic Theses and Dissertations, 2004-2019*. 5833.  
<https://stars.library.ucf.edu/etd/5833>

A FRAMEWORK FOR MINIATURIZED MECHANICAL CHARACTERIZATION OF  
TENSILE, CREEP, AND FATIGUE PROPERTIES OF SLM ALLOYS

by

JONATHAN DAVID TORRES

B.S. University of Central Florida, 2011

M.S. University of Central Florida, 2013

A dissertation submitted in partial fulfillment of the requirements  
for the degree of Doctor of Philosophy  
in the Department of Mechanical & Aerospace Engineering  
in the College of Engineering & Computer Science  
at the University of Central Florida  
Orlando, Florida

Spring Term  
2018

Major Professor: Ali P. Gordon

© 2018 Jonathan D. Torres

## **ABSTRACT**

With the heightened complexity of component design that may be achieved through additive manufacturing (AM) comes an equally complex set of distinct material characteristics characteristic of the manufacturing method. To properly characterize new materials for use with AM technologies like selective laser melting (SLM), extensive material testing and analysis is necessary. Traditional testing techniques, however, can be prohibitive due to the time and cost incurred. Miniaturized testing then becomes an attractive option for assessing the material properties of SLM materials. The small punch test (SPT) has been developed for such purposes, where material is scarce or costly. Although lacking standardization, SPT has been successfully employed with various materials to assess material properties such as the yield and ultimate strengths and verified by traditional testing results. With the accompaniment of numerical simulations for use in the inverse method and determining correlation factors, several methods exist for equating SPT results with traditional stress-strain results. There are, however, some areas of weakness with SPT which still require development, such as fracture and fatigue, although inferences garnered through tensile testing can draw out reasonably accurate first approximations for either of these modes of mechanical damage, and the solution of the inverse method can be demanding of time and resources. Additionally, the combination of SPT and SLM is relatively unexplored in literature, though studies have shown that SPT is sensitive to the types of structures and unique material characteristics present in SLM components. The present research therefore focuses on developing a framework for characterizing SLM materials via the small punch test. Several types of SLM materials in various orientations and processing states are small punch tested to test the sensitivity of SPT to track the effects of these as they cause the

materials to evolve. A novel cyclic test method is proposed to fill the gap in SPT fatigue testing with an adaptable design for fully-reversed loading and evaluated using several different materials and testing conditions. Results from these tests are evaluated via numerical modelling using the inverse method solved with a least squares regression optimization to determine material properties. New correlation factors were proposed as determined by comparing pertinent SPT inflection points and the respective equivalent material properties as determined via conventional tensile testing. The validity of these solutions was determined via comparison to conventional testing results. Samples were also evaluated using digital microscopy to connect fracture morphology to processing parameter variations. A framework is thus presented with which SPT may be utilized to more economically and expeditiously characterize SLM materials.

*For Dani, who supported me through countless setbacks  
For my parents, who made it possible  
For Bash, who lit the fire*

## ACKNOWLEDGMENTS

The work presented here would not have been possible without the support and contributions of a number of individuals in both personal and professional capacities. For their varied contributions, I would like to convey my gratitude.

Primarily, I would like to thank my dissertation advisor, Dr. Ali Gordon, without whose guidance and support this effort would not have been possible. Dr. Gordon has provided me with instruction and advice for a long time, encouraging my work since my time as an undergraduate, and guiding me in my efforts to pursue academic achievement through a number of projects. His example as both an instructor and researcher served as encouragement during a sometimes very arduous process. For all of his support, I will always be grateful.

I would like to thank my dissertation committee for their contributions to my work. The comments of Dr. Jayanta Kapat, Dr. Seetha Raghavan, and Dr. Martin Richardson helped to craft and refine the focus of this work. Their contributions have helped to improve this work.

The years I have spent working in the Mechanics of Materials Research Group have introduced and indebted me to a number of my peers, more than I could possibly name here, especially those who served as co-authors in journal articles. However, in the context of this work, I must especially extend my gratitude towards Jose Cotelo, Daniela Ojeda, Aaron Santomauro, Nicholas Stoll, Alex Strebeck, and Ryan Reedy, without whose direct contributions this work would not have been possible. Collaborative efforts with fellow graduate student Sanna Siddiqui provided for additional testing materials, and prior investigations of group alumni Justin Karl and Scott Keller proved invaluable to validation efforts in this work.

For their material and professional support, I would like to thank Ed Kawecki and the SLM R&D group at Power Systems Mfg., LLC. Their guidance and collaboration with SLM systems and materials provided me with a strong foundation and familiarity with the technology, providing invaluable experience and the use of experimental data acquired during my time there provided a base by which to evaluate my work with the SPT. For financial and academic support I would like to thank the Florida Education Fund and their awarding of the McKnight Doctoral Fellowship and additional support towards experimental costs, as well as Mrs. Judith M. Langston for awarding me the Gerald R. Langston Endowed Scholarship.

Finally, and most importantly, I must express my gratitude for the endless support given to me by my family and friends. I owe more to my parents than I can ever repay, and I credit my abilities in finishing this work to them, my resolve is borne of their examples of success and determination. My brother, sister-in-law, and nephew always served as welcome company, giving words of support or providing for necessary respite, and always knowing which was needed. Yet no one has supported me more through times of doubt and trepidation than my wife, Danielle, and nothing served as greater inspiration than the birth of my son, Sebastian. I have gained and experienced a lot through this endeavor, but nothing is greater than their love and support, without which I would not have been able to accomplish what I have.



## TABLE OF CONTENTS

LIST OF FIGURES .....	xii
LIST OF TABLES .....	xix
CHAPTER 1: INTRODUCTION .....	1
1.1 Background and Motivation .....	1
1.2 Objectives .....	7
CHAPTER 2: LITERATURE REVIEW .....	11
2.1 Nickel Superalloys .....	11
2.2 Selective Laser Melting .....	23
2.2.1 Background and History of SLM.....	23
2.2.2 Overview of Methods .....	25
2.2.3 Variations Due to Process Parameters .....	31
2.2.4 Post-processing Effects .....	48
2.3 Small Punch Testing .....	62
2.3.1 Introduction to Small Punch Testing .....	63
2.3.2 Basics of Small Punch Testing.....	67
2.3.3 Direct Correlation with Tensile Properties .....	70
2.3.4 Creep Testing .....	78
2.3.5 Fracture Properties .....	82

2.3.6 Shear Properties .....	91
2.3.7 FEA of SPT .....	96
2.3.8 Fatigue.....	101
2.4 Summary .....	105
2.4.1 Knowledge Gaps .....	106
2.4.2 Applicability of SPT to SLM.....	107
CHAPTER 3: EXPERIMENTAL PROCEDURE.....	109
3.1 Overview.....	109
3.2 Post-processing .....	112
3.2.1 Recrystallization Cycle .....	112
3.2.2 Heat Treatment.....	120
3.3 SPT Sample Preparation .....	121
3.4 Planned Experimental Matrices .....	122
3.5 Reliability and Error .....	129
3.6 SPT Assembly.....	133
3.7 Microscopy .....	142
3.8 Data Post-processing.....	143
3.9 Data Management .....	144
CHAPTER 4: NUMERICAL APPROACH.....	146

4.1 FEA Model .....	147
4.2 Cyclic Modeling .....	154
4.3 Parametric Study.....	156
4.4 Intended Use: Inverse Solution Method .....	164
<b>CHAPTER 5: EXPERIMENTAL RESULTS .....</b>	<b>169</b>
5.1 Small Punch Test Results .....	169
5.1.1 Effects of Post-Processing Routines .....	169
5.1.2 Effects of Testing Temperature.....	179
5.1.3 Effects of SLM Sample Donor Geometry.....	185
5.1.4 Effects of Manufacturing Orientation .....	190
5.1.5 Other AM Materials .....	193
5.1.6 Effects of Clamping Pressure.....	196
5.2 Cyclic Small Punch Test Results .....	199
5.2.1 Differences from Load Level.....	200
5.2.2 Effects of Testing Temperature.....	201
5.2.3 Differences from Loading Type.....	207
5.2.4 Differences from Reversible Control Modes .....	209
5.2.5 Effects of Hold Time.....	212
5.2.6 SLM Materials and the Effects of Heat Treatment and Orientation .....	215

5.2.7 Summary of Cyclic SPT Results and Conditions .....	222
5.3 FEA Correlations .....	224
5.3.1 Simulations of 304 Stainless Steel.....	225
5.4 Observations from Microscopy .....	227
CHAPTER 6: CORRELATION OF SMALL PUNCH AND CONVENTIONAL TEST RESULTS .....	251
6.1 Comparison of SPT and Conventional Test Result Trends .....	251
6.1.1 Conventional 304SS.....	251
6.1.2 SLM IN939V .....	256
6.1.3 DMLS GP1 .....	260
6.1.4 DMLS IN625 and IN718 .....	261
6.2 Correlation of Material Properties .....	262
6.3 Summary.....	275
CHAPTER 7: CONCLUSIONS .....	277
CHAPTER 8: RECOMMENDATIONS.....	282
APPENDIX A: ANSYS WORKBENCH MODEL.....	286
APPENDIX B: REPRODUCTION PERMISSIONS .....	290
REFERENCES .....	292

## LIST OF FIGURES

Figure 1.1 - Fuel nozzle for the GE LEAP jet engine manufactured via SLM [7].	2
Figure 2.1 - Weldability of high-strength, high-temperature alloys as relating to content of strengthening $\gamma'$ precipitate-forming constituents, Al and Ti [31, 62].	19
Figure 2.2 - Typical schematic of selective laser melting and selective laser sintering systems [80].	26
Figure 2.3 - Cross-sectioned SLM sample displaying typical macrostructural features [81].	27
Figure 2.4 - Residual stress distribution per SLM build height [83].	28
Figure 2.5 - Columnar microstructure characteristic to SLM components caused by the heat gradients present during construction extending from the build surface to the build plate [90].	30
Figure 2.6 - Detrimental effects of increasing scan speed and layer thickness, emphasize by the combination of such [119].	35
Figure 2.7 - SLM component fracture surface showing the effects of process parameter variations causing inclusions of unmelted particles and pore defects [114].	36
Figure 2.8 - The interaction of power and scan speed can have high a high impact on the surface finish and adhesion of layers with an iron-based SLM powder [126].	37
Figure 2.9 - Surface morphology of SLM IN718 with varying energy densities increasing from (a) 180 J/m, (b) 275 J/m, (c) 300 J/m, to (d) 330 J/m [131].	39
Figure 2.10 - The effects of the (a) scan speed, (b) hatch spacing, (c) laser power, and (d) focus distance on the resultant energy density and the effect of its variance on porosity [139].	42
Figure 2.11 - Increased variation in (b) scanning strategies has shown a positive correlation with (a) higher relative density [119].	46
Figure 2.12 - The substitution or mixing of the typical Argon or Nitrogen environments with other protective gas environments has been shown to have detrimental consequences on component density [149].	47
Figure 2.13 - The effects of post-processing are evident as the (a) as-manufactured microstructure responds to (b) stress-relief heat treatment with some reorientation and (b) solution heat treatment hot isostatic pressing with grain growth and pore elimination [161].	51

Figure 2.14 - Fracture behavior of as-built specimens is dependent on the build direction, but is independent of it once a suitable HIP cycle is employed [161].	52
Figure 2.15 - Tensile properties after heat treat depend on the temperature used for the anneal [106].	57
Figure 2.16 - Aging of SLM IN939 shows grain growth between (a) 0° and (b) 90° manufactured samples, though anisotropy between the two persists, and grain are still significantly smaller than (c) as-cast material [103].	59
Figure 2.17 - Schematic of typical SPT setup.	64
Figure 2.18 - Typical SPT load-displacement curve with important inflection and correlation points denoted.	65
Figure 2.19 - Compliance effects in load-displacement curve from measurement of displacement via crosshead as compared to direct contact deflection transducer.	69
Figure 2.20 - Load-displacement response of a brittle vs. a ductile material [202]	70
Figure 2.21 - Various methods for determining the yield load, $P_y$ , of the load-displacement curve of SPT, created using AW6016 T4 $P$ - $\delta$ data from [206].	72
Figure 2.22 - Comparison of SPT response and fracture of powdered metal as compared to structural steel [30].	77
Figure 2.23 - Examples of specimen geometries utilized in SPT fracture studies including (a) standard round, (b) standard square, (c) central notched [248], (d) single edge notched [250], (e) circumferentially notched, and (f) lateral cracked.	85
Figure 2.24 - Energy difference method for calculation of $J$ integral.	88
Figure 2.25 - Typical cyclic small punch test loading profile found in literature.	103
Figure 3.1 - Build orientation terminology diagram.	111
Figure 3.2 - Hexagonal transverse and round longitudinal bars produced for full-sized tension samples and blocks produced for fracture tests, all of which were utilized for SPT samples.	112
Figure 3.3 - Recrystallization study tensile test results, with a detailed view of the elastic sections.	116
Figure 3.4 - Comparison of material properties from tensile tests between different treatments.	118

Figure 3.5 - Reversed cyclic loading as imparted by dual-punch SPT configuration. ....	128
Figure 3.6 - Load-unload cyclic history of IN939V sample. ....	130
Figure 3.7 - Normal distribution and histogram of $k/t$ values for collective results of L-UL cyclic tests. ....	131
Figure 3.8 - Example of MTS Criterion Model 42 [291], to which the small punch test jig attached to load frame in single punch configuration used for monotonic style tests. ...	134
Figure 3.9 - Detailed views of the dual punch configuration and sample dies with a 10x10mm sample in place.....	137
Figure 3.10 - Industrial Heater Corp. B74772 furnace mounted to a custom 80/20 frame, shown (a) as designed to fit SPT rig, and (b) fitted with insulation, heat shield, and directed air cooling used during operation.....	139
Figure 3.11 - Reversed loading of 1040 steel with a displacement range of $\pm 1.0$ mm measured with both the load frame crossbar and LVDT. ....	141
Figure 3.12 - Optical and digital microscopy station for sample inspection. ....	143
Figure 4.1 - Axis-symmetric small punch test modeled in ANSYS. ....	148
Figure 4.2 - Strain distribution within the SPT sample at a displacement of 0.1mm, as compared to [277].....	149
Figure 4.3 - Stress-strain response from single element in free area of sample between punch and dies as compared to actual tensile results [292]. ....	150
Figure 4.4 - Fracture morphology based on directional grain growth orientation [233]. ....	151
Figure 4.5 - Simulation compared to published experimental results of AL 6061-T4 [206, 292]. ....	152
Figure 4.6 - SPT responses of comparatively tough and soft materials, AISI S7 and AL 6061-T6 [292, 294, 295]. ....	153
Figure 4.7 - Dual punch configuration for reversed-loading cyclic testing. ....	155
Figure 4.8 - Cyclic test data acquired with an LVDT using 1040 carbon steel with reversed loading as compared to FEA simulation output.....	156
Figure 4.9 - Percent contribution of main factors to the various sections of the SPT force-displacement curve.....	159

Figure 4.10 - Select curves from the parametric study, and the linear portions of such [292]...	162
Figure 4.11 - Graphical representation of the piecewise manner in which the inverse solution method is used to match the simulated response to the experimental response [276]....	167
Figure 5.1 - Small punch tech test response of samples sourced from tensile tests conducted during the recrystallization study outlined in section 3.2.1. ....	171
Figure 5.2 - Monotonic SPT responses of SLM IN939V samples tested at room temperature in as-manufactured and heat-treated conditions for transverse and longitudinal orientations. ....	177
Figure 5.3 - Monotonic SPT responses of 304SS samples tested at room temperature and 300°C, with initial loading of 200°C fatigue test shown for additional comparison. ....	181
Figure 5.4 - Monotonic response of SLM IN939V varies by orientation when subjected to elevated temperature. ....	183
Figure 5.5 - Comparison plots of transverse and longitudinal manufactured samples sourced from both CT blocks and tension test bars. ....	189
Figure 5.6 - Monotonic room temperature test responses of transverse GP1 samples built with the long axis rotated with respect to the build plate axes. ....	192
Figure 5.7 - SPT responses of as-manufactured IN625 and IN718. ....	194
Figure 5.8 - Warping of sample edges resulting from unconstrained bending of samples due to excessive lower die pocket depth.....	197
Figure 5.9 - The effects of clamping pressure on otherwise identically tested 304SS samples can be readily observed. ....	198
Figure 5.10 - Variation in response of 304SS tests F1 and F2, cycled at R=0 with loads of 1kN and 1.5kN, respectively.....	201
Figure 5.11 - Cyclic response of 304SS tests F1 and F5, tested with R=0 to 1kN at room temperature and 200°C, respectively. ....	203
Figure 5.12 - Cyclic response of 304SS with R=-1 load controlled at -0.5kN to 0.5kN at room temperature and 200°C .....	204
Figure 5.13 - Cyclic response of 304SS with R=-1 displacement controlled at -0.5mm to 0.5mm at room temperature and 200°C .....	207
Figure 5.14 - Hysteretic responses of 304SS cycled at RT with (a) R=0 to 1kN and (b) R=-1 with a range of $\pm 0.5$ kN. ....	208



Figure 5.15 - Comparison of results for displacement and load controlled tests of 304SS when tested with R=-1.....	210
Figure 5.16 - Comparison of cyclic behavior of 304SS at RT and 200°C for samples tested with R=-1 utilizing both load and displacement controls. ....	212
Figure 5.17 - Load-displacement response of 304SS cycled at R=-1 with load control and a 15s hold time at 0.5kN.....	213
Figure 5.18 - Displacement vs cycle response of 304SS at 200°C cycled at R=-1 with ±0.5kN, with (CF1) and without (F6) a hold time. ....	214
Figure 5.19 - Displacement-life responses for IN939V samples tested with various conditional variations at 427°C with R=0.....	216
Figure 5.20 - Single hysteresis loops for IN939V samples tested with R=0 and various conditional variations at 427°C.....	219
Figure 5.21 - Fully reversed, load controlled cycling of GP1 DMLS samples at room temperature after monotonic testing. ....	220
Figure 5.22 - Maximum displacement with respect to cycles of GP1 samples produced transversely along the x and y axes.....	221
Figure 5.23 - Optimized FEA inverse solutions as compared to experimental results.....	226
Figure 5.24 - Fracture surface of samples produced from SLM IN718 (left) and SLM IN625 (right) showing crack growth characteristic to layered AM materials. ....	229
Figure 5.25 - Monotonic loading fracture behavior depends on orientation: (a) T10 is longitudinal and as-manufactured, (b) T11 is transverse and as-manufactured. ....	230
Figure 5.26 - Microstructures of as-manufactured IN939V sample loading surfaces for longitudinal (left) and transverse (right) samples. ....	231
Figure 5.27 - Cross-sectioned fractures of longitudinal (left) and transverse (right) as-manufactured IN939V samples.....	233
Figure 5.28 - Fracture surfaces of as-manufactured IN939V (a) vertical and (b) horizontal samples tested in cyclic conditions in the as-manufactured condition with R=0 at 427°C. ....	234
Figure 5.29 - Cross-sectioned as-manufactured longitudinal (left) and transverse (right) IN939V samples tested under cyclic loading with R=0 to 0.5kN and 427°C.....	235

Figure 5.30 - Samples of fully heat treated IN939V tested with R=0 to 0.4kN at 427°C in (a) longitudinal and (b) transverse orientations.....	236
Figure 5.31 - Fracture surfaces of fully heat treated monotonic tests at room temperature (a) longitudinal (T2) and (b) transverse (T3) orientations and at 427°C for (c) longitudinal (T13) and (d) transverse (T14) orientations.....	238
Figure 5.32 - Cross-sectioned views of fracture morphologies of fully heat-treated IN939V samples in the longitudinal (left) and transverse (right) directions. ....	239
Figure 5.33 - Cross-sectioned fully heat-treated longitudinal (left) and transverse (right) IN939V samples tested under cyclic loading with R=0 to 0.4kN and 427°C.....	240
Figure 5.34 - Fracture surfaces of samples sourced from RX study samples for tests (a) T7 (RX1), (b) T6 (RX2), (c) T5 (RX3), (d) T4 (RX4), (e) T9 (RX7), and (f) T8 (RX8). ...	242
Figure 5.35 - Fracture surfaces of monotonically loaded 304SS at (a) RT and (b) 300°C.....	244
Figure 5.36 - Fracture morphology of 304SS tested at room temperature with cyclic loading of R=0 to (a) 1kN and (b) 1.5kN.....	245
Figure 5.37 - Samples of fully heat treated IN939V tested with R=0 to 0.5kN at 427°C in (a) longitudinal (F10) and (b) transverse (F11) orientations.....	246
Figure 5.38 - Fracture morphology for cyclically loaded 304SS room temperature samples with control modes of (a) R=0 load control (F2), (b) R=-1 load control (F3), and (c) R=-1 displacement control (F4). ....	248
Figure 5.39 - Fracture of cyclically loaded 304SS samples at 200°C with control modes of (a) R=-1 load control, (b) R=-1 displacement control, and (c) R=-1 load control with 15s hold time. ....	249
Figure 6.1 - Comparison of (a) conventional fatigue tests [302] with (b) dual-punch reverse-loading SPT cyclic tests (F6 and F7) of 304SS at 200°C. ....	255
Figure 6.2 - Normalized correlation plots of material properties from tension tests with corresponding SPT inflection points.....	264
Figure 6.3 - Normalized correlation plot of $\sigma_{uts}$ for IN939V data with outliers omitted. ....	266
Figure 6.4 - Normalized correlation plots for assimilated data of all AM materials tested.....	268
Figure 6.5 - Correlation of tensile and SPT yield data, compiled from experimental data and [12, 19, 24, 30, 207, 213, 215, 219, 220, 276, 277, 283, 302-304, 307-310].....	271

Figure 6.6 - Correlation of tensile and SPT tensile strength data, compiled from experimental data and [12, 19, 24, 30, 207, 213, 215, 219, 220, 276, 277, 283, 302-304, 307-311]... 272

## LIST OF TABLES

Table 2.1 - Common alloying elements of nickel-based superalloys and their effects. ....	16
Table 2.2 - Chemical composition of IN939 [55, 56].....	18
Table 2.3 - Phase composition of SLM IN718 during different states of processing [168]. ....	55
Table 2.4 - Mechanical properties of AM IN718 through several stages of post-processing. ....	58
Table 3.1 - Test matrix for recrystallization study.....	114
Table 3.2 - Tensile test equivalent SPT matrix.....	125
Table 3.3 - Fatigue test equivalent SPT matrix.....	126
Table 4.1 – Factor levels for full factorial parametric design study. ....	158
Table 4.2 - Factor levels of select runs for comparison of effects.....	161
Table 5.1 – Relevant inflection points and normalized values corresponding to material properties for small punch tests of recrystallization study test samples. ....	175
Table 5.2 – SPT material property value results of SLM IN939V samples tested at room temperature in as-manufactured and heat-treated conditions for both orientations.....	179
Table 5.3 – Property values of 304 stainless steel samples tested at various temperatures.....	182
Table 5.4 – Comparison of directional variation of monotonic responses of SLM IN939V at room temperature and 427°C.....	185
Table 5.5 - Maximum load and displacement at maximum load for fully post-processed samples in longitudinal and transverse directions sourced from RX study tension bars and CT block.....	187
Table 5.6 – Property variation of transverse GP1 samples with dependency on in-plane rotation. ....	193
Table 5.7 – SPT material properties of AM IN625 and IN718. ....	195
Table 6.1 – Material properties of 304 stainless steel at various temperatures [302, 303].....	252
Table 6.2 – Material property values from tensile test results of the recrystallization study outlined in section 3.2.1.....	257

Table 6.3 – Directional differences of tensile tested SLM IN939V at room temperature and 427°C, using transverse values as a basis for calculation.....	258
Table 6.4 – Material properties of DMLS GP-1 [304]. .....	261
Table 6.5 – Material properties of AM IN625 and IN718 as reported by Stratasys and EOS, respectively [305, 306].....	262
Table 6.6 – Error calculation for strength properties predicted using experimental results and correlation relationships established in this study. ....	274

## **CHAPTER 1: INTRODUCTION**

Additive manufacturing (AM) methods have gained rapid traction within various industries as not just technologies useful for rapid prototyping, but as advanced methods for designing and manufacturing production-quality components. The nature of additive manufacturing techniques allows for the inclusion of added complexity and features in components that are not practical with conventional manufacturing techniques. With the continued maturation of these techniques, various industries are turning to AM as a means to advance component design while simplifying production. As such, AM methods now require a level of characterization that is pursuant with the inherent complexities of the macro- and microstructures of materials produced with AM technologies. It is necessary to characterize the processing-structure-property trends of such materials used with these methods, as they will in turn determine the viability of not just the components produced with them, but of the methods being refined and becoming the new standard in industrial manufacturing.

### **1.1 Background and Motivation**

Various industries have been integrating advanced additive manufacturing techniques into their production lines, producing not just one-off components or prototypes, but marketable, highly functional components with previously unachievable levels of complexity in design. In many industries, such as in automotive and energy production, AM processes have been utilized to produce higher performance tooling, integrating high efficiency cooling channels in cast molds into the design which are not possible with traditional tooling [1, 2]. The energy industry has taken a similar approach, integrating the design of high efficiency cooling holes into vanes

and blades for turbines into the production design rather than being limited by conventional tooling and manufacturing methods [3, 4]. Medical applications include the use of various AM technologies and materials for tissue engineering, prosthetics, and implants for bone scaffolding and dental fixtures [5]. The aerospace industry has also begun to invest heavily in technologies like selective laser melting (SLM), with companies such as General Electric (GE) developing advanced components for turbofan engines. GE manufactured numerous components as a single unit using Direct Metal Laser Melting (DMLM) for each of the 19 fuel nozzles in each GE LEAP jet engine, shown in Figure 1.1, rather than welding each of the individually produced components together as had been traditionally done, strengthening the parts and shedding significant weight in the process [1, 6, 7]. These production pieces represent a vast advancement in both technology and manufacturing, as they lay the groundwork for the acceptance of these methods into mainstream manufacturing and drive the development of AM technologies onwards. In fact, as of 2014, end-use functional components now make up the major portion of applications for AM-produced products at 29% [1].



Figure 1.1 - Fuel nozzle for the GE LEAP jet engine manufactured via SLM [7].

Access to SLM and other AM technologies is limited, however, as production-quality machines are very expensive, as is the source material used to manufacture components. As such, traditional material characterization techniques encounter the difficulty of not just dealing with new technologies with various interacting variables that affect component properties, but also the high cost associated with conducting the necessary experiments. Implementation of full factorial test arrays utilizing full-sized conventional test specimens to thoroughly characterize material behavior then become prohibitive, especially given the directionally-dependent properties which often characterize AM materials. This presents a barrier to the accessibility and acceptance of the technology, as components must be shown to meet or exceed the performance of conventionally produced counterparts in order to gain widespread acceptance and use. This is exacerbated by the added costs associated with producing AM products. Including the repeated builds necessary for producing the numerous samples with varying process parameters, long build times, errors and failures, and other factors can quickly add to the costs of characterizing AM-produced components which are not typically present when testing conventional materials. A report by the Air Force Research Lab (AFRL) cited the cost of evaluating a new alloy for use with an additive manufacturing technique to be around \$2M, including material production and consumption, sample manufacturing, and the execution and analysis of a comprehensive testing array [8]. It becomes necessary then to establish a methodology for characterizing not just the materials used to produce components, but also the technologies themselves, in the most efficient way possible.

The small punch test (SPT), in which a spherical punch is driven through a small, thin plate, has been developed for such purposes, where material is scarce or costly. Although lacking



widespread formal standardization, SPT has been successfully employed with various materials to assess several material properties which have been verified by traditional testing results. With the accompaniment of numerical simulations for use in the inverse method and determining correlation factors, several methods exist for equating SPT results with traditional stress-strain results. Small punch test samples are thus designed to be sourced from existing structures with minimal impact to the integrity of the mechanism and with much less material than traditional testing procedures allow, giving a clear picture as to the remaining lifetime of components [9, 10]. As such, the SPT is useful where source material is expensive and large quantities are hard to acquire as in the testing of precious metals, such as gold alloys [11]. Relationships exist for equating SPT results with conventional stress-strain results, such as the yield strength, ultimate tensile strength, Young's modulus, and elongation [12, 13]. Additional research exists in the areas of fracture and creep equivalent testing, with some small contributions in the area of fatigue testing [14-19]. The combination of SPT and SLM, however, is relatively unexplored in literature, though studies have shown that SPT is sensitive to the types of structures present in SLM components.

Literature on the topic is sparse when the subject matter is combined with additive manufacturing techniques such as SLM, due to the recent emergence of both topics. Most recently, direct laser deposited (DLD) C263 Ni-superalloy with varying heat treatments was tested at room and high temperature in SPT, and compared to cast material and tensile tests [20]. While the DLD material showed anisotropy and dependencies on heat treat and testing temperature, the significance of such was not as pronounced as in tensile tests, skewing correlations when compared to literature. In one study, SPT was utilized with stainless steel

components manufactured via SLM, though to a very limited extent, exploring only the effects of layout and gas flow on the parts, and using SPT as a way to evaluate bond strength between particles [21]. Even then, however, the estimated mechanical properties calculated by the investigators show good correlation to values published elsewhere. Hurst et al. conducted a series of small punch tests on samples made from layer additive manufactured IN718 typically employed in aerospace structure repair and on electron beam deposition of Ti6Al4V [22, 23]. These experiments showed the SPT was responsive to the anisotropy typically present in AM layered materials, and results showed sensitivity to grain size, distribution, and orientation, and also differences between AM and conventional materials in terms of both material properties and fracture behavior. Similarly, a 12% Cr oxide dispersion strengthened steel, which displays highly directional properties due to the elongated grain structure, showed delamination fracture behavior similar to layered materials such as those produced via AM techniques when tested in SPT, and confirmed directional dependencies of material properties [24]. Additionally, IN718 samples taken from a direct laser deposition manufactured airfoil at several different heights of the build and tested with SPT showed responses varied based on location, highlighting changes in microstructure which caused differences in strength and ductility; this study, however, did not quantify material properties, but tracked changes in strength relative to each other and to a sample of equivalent wrought material [23]. Small punch testing has also been used to explore the variation in shear strength along laser and electron beam welds, processes which are arguably similar in theory to SLM, and in other studies to find the evolution of yield strength ultimate strength, elongation, fracture energy, and toughness along the different regions of the heat affected zone of a weld [25-28]. Given the process of adding layers to welds to create them, and

that the SPT method was used successfully to track variations in the materials was validated in [27] by giving correlating hardness tests with matching trends, it stands to reason that a layered process with anisotropic properties such as SLM would benefit from the sensitivity of SPT. Small punch tests have also been used with pressed powder materials, which present complexities in their behavior similar to those of layer-wise construction methods, and achieved acceptable correlation with traditionally determined material property values such as yield and ultimate strength [29, 30]. Beyond those examples, the combined use of SPT and SLM or other additively manufactured materials is extremely limited or nonexistent. The current study will serve to summarize and distill the various techniques used in literature in order to determine mechanical properties from small punch test results, with the aim of assembling a reliable set of procedures for full material characterization via SPT, as this method has yet to be standardized, so as to apply them to samples manufactured via SLM.

In the present study, the suitability of using small punch testing to evaluate selective laser melted materials is evaluated. It is envisioned that the research presented here establishes a novel methodology for characterizing and subsequently optimizing new materials to be used with additive manufacturing methods, along with the characterization of the behaviors of a particular class of materials used with one of these technologies, selective laser melting. The resultant data and framework will show that additive manufactured parts can be made with material properties which meet or exceed those of more conventional manufacturing methods, but with the added advantage of complexity which was previously unattainable, and that new materials can be adapted to these methods in a structured way so as to prevent excess cost. The results of this

study will be used to make a case as to how well SPT can track the changes in SLM materials when manufactured with varying processing parameters or post-processing routines.

## **1.2 Objectives**

Expanding on the existing body of knowledge of the small punch test, a novel SPT mechanism will be utilized to evaluate several different materials. The variety of materials will serve to validate the function and methods of SPT using the design discussed herein, creating continuity between established methodologies and those proposed here by using well-established materials to verify the functionality of the novel design. The primary focus, however, will be on extending the use of SPT to evaluating and optimizing SLM materials, comparing SPT results of SLM materials produced with varied processing conditions to conventional testing results utilizing the same materials as a benchmark for evaluation. In order to design a framework by which future evaluation of AM materials may be conducted more quickly and economically via utilization of the small punch test, the following research objectives serve to direct the research in a manner that is conducive to achieving said goals:

- **Develop a framework for evaluating transversely isotropic materials with SPT.**

Traditional testing techniques require a significant amount of time and material in order to fully characterize a material, especially a transversely isotropic material with directionally dependent properties. With samples which consume significantly less material than those utilized for conventional tests, the small punch test poses a viable alternative to determining the material properties of a material with previously unknown characteristics. As such, small punch tests are to be compared to results determined from

traditional testing techniques, including tensile, creep, and fatigue. The SPT matrix will therefore need to be adapted to meet the conditions of the test matrix which uses full-size samples. Comparison of these two test matrices will gauge the sensitivity and accuracy of SPT results in detecting microstructurally-driven material property changes due to variations in processing parameters, post-processing routines, and testing conditions.

- **Develop a mixed mechanical characterization framework needed to design the models necessary for SLM material life prediction.** Due to the unique microstructures produced by SLM, and the limited research done on material evaluations, the combination of SLM and SPT is relatively unproven. This requires the design of a methodology for evaluating SLM material with SPT using both experiments and simulations so as to design the framework for future material evaluation. The inverse method will be utilized to optimize curve fitting simulations to derive mechanical properties from test results. The test results from the SP tests equivalent to tensile tests will then be used to further help determine material constants. It is of high interest to determine if test results from one type of SP test can be used to interpret the results of another. That is, for example, determining if the material properties from a monotonic small punch test, such as the Young's modulus and yield strength, can be used for accurately interpreting results from creep and fatigue tests. If so, then it could be said that SPT can be used as the sole method for evaluating the properties of new materials produced with SLM.
- **Design and verification of a novel SPT device capable of reversible fatigue loading.** Due to the limited space in the design of an SPT setup, fatigue tests cannot currently be

conducted in a fully-reversed mode. Thus, it is of interest to determine if the capabilities of an SPT setup can meet those of a traditional test, thus expanding the current capabilities of SPT. Due to the aforementioned space limitations, a novel design for conducting cyclic SP tests will be developed and tested for validity, so as to enhance and verify the fatigue capabilities of SPT beyond the limited data found in literature. Fatigue results from conventional tests will be compared to cyclic SPT results using both single, zero-to-load, and dual, reversed-loading, punch configurations, to determine the validity of the approach.

- **Develop a direct framework for directly translating force-displacement results into tensile properties, in lieu of use of the inverse method.** It is necessary to determine if small punch tests can be used to directly determine material constants of SLM materials. Though research utilizing both SLM and SPT is very limited, SPT has been shown to be capable of assessing mechanical properties utilizing concurrent FEM simulations to establish correlation factors or calculated via the inverse method. These correlation factors, while having been shown valid for a number of materials, have not been determined to be universal or suitable for materials with inherent anisotropy. This study presents the opportunity to verify correlation factors presented in literature as being applicable to a wide variety of materials with a different class of materials with a unique microstructure inherent from the manufacturing process. Alternatively, new correlation factors may be proposed if necessary which apply to a broad range of conventional and AM-produced materials. This will further efforts of expanding SPT utilization, acceptance, and standardization, especially as a method for evaluating AM materials.

The chapters following the motivation, introduction, and objectives detailed here will give necessary background information on the topics of interest, outline a detailed experimental plan, and give and discuss results from such. Chapter 2 consists of a literature review giving necessary background and details for both SPT and SLM. The experimental plan, design of the SPT mechanism, and analysis techniques will be outlined in Chapter 3. The numerical approach used to convert SPT results into stress-strain data is given in Chapter 4, including a detailed description of the model design, validation, sensitivity study, and a description of the approach utilized for obtaining a solution via the inverse method. Chapters 5 and 6 of the document will detail results from the experiments, drawing comparisons to traditional data to comment on accuracy, and noting validity of correlation values. Finally, conclusions of the study will be made in Chapter 7 and used to give recommendations in Chapter 8 for directing future studies and for the overall suitability of utilizing SPT to evaluate SLM materials.

## **CHAPTER 2: LITERATURE REVIEW**

This chapter will impart the necessary background knowledge for achieving the objectives outlined in Chapter 1, outlining relevant research in the areas of interest. Information is provided on nickel superalloys, its alloy constituents, and post-processing as it pertains to the primary material of study. Then, this information will be tied into a discussion on selective laser melting, the effects of varying process parameters, and implementation of various post-processing techniques on the microstructure and resultant material properties. Finally, the history, development, and implementation of the small punch test and the relationships with conventional testing techniques are discussed, with particular attention paid to highlighting studies which strengthen the case for utilizing SPT to characterize SLM materials. Although comparisons are made with conventional testing techniques such as tension, fracture, creep, and fatigue, these will not be reviewed here, as they are generally well understood and standardized. Instead, this review focuses on information pertinent to the advancement of SLM and SPT, ending with a summary review of the areas of need for developing small punch testing capabilities and utilizing it as a tool to optimize the SLM manufacturing process.

### **2.1 Nickel Superalloys**

Nickel-based superalloys were developed in response to a need for alloys for use in high-temperature applications exceeding 540°C, the limiting temperature for most stainless steel alloys [31]. These alloys are useful in applications for much higher temperature applications, with operating limits dependent on the alloy composition and resultant microstructure. Applications for these include selective hot-side components for automotive applications such as



turbochargers and exhaust valves, in the medical field for dentistry and prosthetics, and most especially in the production of components for energy and aerospace components, including blades, vanes, combustors, and more [32]. The proliferation of superalloy use can be exemplified by the increase of use of superalloys in aircraft gas turbine engines from 10% to 50% from 1950 to 1985 [32]. This is due to the ability of superalloys to withstand high levels of mechanical and thermal stress from long durations of operation at high temperature with little change microstructurally [33]. Growth of use for superalloys can be mainly attributed to the increasing demand for energy production with concurrent demands for increases in capability, efficiency, and component life, thus driving the development of alloys which can operate at higher temperatures for longer periods of time [34]. Nomenclature for superalloys is typically dependent and indicative of the developers, with some of the earliest and still highly utilized alloys, the Inconel (IN) series, having been developed by the International Nickel Company in the 1940's and 1950's, with further development in the field being generated by various entrepreneurs and large producers such as GE (René alloys) and subsequent efforts by these and other companies such as Pratt and Whitney (PWA alloys) and Cannon-Muskegon (CMSX series) focused on processing to create directionally solidified and single crystal materials for engine component use to promote creep properties [35].

At room temperature superalloys have relatively high strengths, often featuring yield strengths of 900-1300 MPa and tensile strengths of 1200-1600MPa, which are typically preserved up to high temperatures [36]. Nickel-based superalloys consist of at least 50% nickel, which makes up the strength matrix of the alloys, and is combined with other elements to impart certain characteristics, the major of these typically being Cr, Co, Ti, and Al, along with other

elements in small quantities. In alloys with high content of other solid solution formers, such as Co, Cr, and Fe, nickel makes up the largest component of the alloy, so as to still form the base matrix of the microstructure. The high temperature performance and weldability depends on the quantity and control of content trace elements, and especially impurities for optimization alloys [37]. The same blend of elements which lends the material its strength and corrosion resistance, however, makes these alloys difficult to machine due to factors such as work hardening of the austenitic matrix, formation of hardening precipitate phases, and presence of abrasive carbides forming within the microstructure. Additionally, the friction of the tool on the abrasive and hard phases causes high tool wear and heat generation, which can lead to welding of the tool and alloy [38].

Nickel-based superalloys consist of a face-centered cubic (fcc) structured matrix hardened by solutes and precipitates, depending on the alloy the primary of these taking the form of  $\text{Ni}_3(\text{Al, Ti, Ta, Nb}) \gamma'$  precipitates or  $\gamma''$  precipitates for alloys with high Fe and Nb content, and feature other elements in different quantities for different alloys which serve other purposes [39]. Precipitate  $\gamma'$  and  $\gamma''$  phases for strengthening and hardening take the form of ordered  $L1_2$  (fcc) and  $D0_{22}$  body-centered tetragonal (bct) crystal structures, respectively [40, 41]. Strengthening via  $\gamma'$  precipitates is caused by their similar, but slightly mismatched crystal structure in terms of shape and size allowing for a highly coherent structure, as the small mismatch prevents slippage, especially at higher temperatures [40]. The  $\gamma''$  bct phase can be otherwise interpreted as two  $L1_2$  fcc crystals stacked upon one another in terms of lattice parameters and atomic arrangement, thus facilitating a low mismatch despite the overall different structure and strengthening the matrix, but alloys strengthened in this manner are also

particularly vulnerable to quick formation of orthorhombic  $\beta$  and  $\delta$  phases which can degrade material properties due to incoherency with the  $\gamma$  matrix [41, 42]. The balance of elements within this group is of particular importance, as  $\gamma'$  precipitates are essential to strengthening, but even small additions of Nb can quickly increase formation of Laves phase, which is often seen as detrimental to ductility, tensile strength, and impact and fracture toughness due to its brittle nature, though additions of Ti can cause increases in both  $\gamma'$  and  $\gamma''$  while decreasing Laves phase and carbides, thus presenting a need for balance [43, 44]. Solid solution hardening can be achieved by additions of solutes such as iron, chromium, and cobalt, the latter being especially relevant for strength at higher temperatures [39, 45]. Large quantities of Fe can form a Ni-Fe matrix in certain alloys, the most common of which is IN718, and high quantities of which promote Laves phase formation, with high concentration presenting detrimental effects [36, 46]. The addition of Cr in large quantities provides oxidation and corrosion behavior at high temperature, but an excess of the body centered cubic (bcc) crystal structure elements within the fcc nickel matrix can cause destabilization of the microstructure, and as such Cr content is typically limited to around 20% [36, 39]. The presence of excess Cr and other metals can also form carbides as they bond with carbon, and while the presence of carbides can increase hardness and creep resistance, they can also serve as sites for crack initiation during fatigue [36]. In certain applications, such as in IN740 for use in coal-fired energy equipment, the high content of Cr (~25%) also provides protection against carburization and sulphuring, while the high nickel and low iron content provide resistance of halides at high temperatures [47].

Control of alloying elements is highly important, as excess quantities of constituents and impurities from residual gasses, trace metallic, and non-metallics from manufacturing can be

detrimental to alloy properties. Even minor increases of 0.5% or less of C, Nb, Al, and Ti to IN718 were shown to alter the peaks in the differential thermal analysis, which indicates a change in enthalpy and possible changes in crystallization and phase formation behavior [43]. The presence of O and N can cause formation of oxides and micropores, respectively, which can become fatigue crack initiation sites, and the non-metallics S and P have been shown to reduce ductility through embrittlement of grain boundaries, as well as causing a reduction in oxidation resistance and the ability of protective coatings to adhere to the surface of components [37]. Susceptibility to sulfur and sulfide formation at grain boundaries can cause an increase in hot corrosion leading to a loss in tensile, fatigue, and impact strength loss [48]. However, alloying elements can be added as trace elements for deliberate beneficial consequences; Ca and Mg can combine with and reduce the presence of detrimental elements in the molten bath while the excess of these is typically vaporized in the melt, and rare earth elements such as Ce, La, and Y combine with the non-metallics to improve alloy properties and oxidation resistance, and as rare earth oxides are reactive to sulfur, they also improve hot corrosion [37, 39]. Specifically, addition of Mg is often utilized as a deoxidizing agent, along with air purging manufacturing practices such as the use of a vacuum melting environment [37, 47]. The elements C, B, Zr, and Hf are added in very low levels for property improvement through grain boundary strengthening and ductility, but can have negative effects at high levels, such as the formation of carbides to act as fatigue initiation sites with even small increases of carbon content, boron causing incipient melting, and zirconium causing grain boundary cracking [37, 39, 43]. The roles of many of the alloying elements found in nickel-based superalloys are summarized in Table 2.1. Depending on

the quantity and overall alloying contents, each element can serve various purposes and its overall effect on the final microstructure will vary.

Table 2.1 - Common alloying elements of nickel-based superalloys and their effects.

<b>Purpose</b>	<b>Element</b>
Solid solution strengthening	Cr, Co, Mo, W, Nb, Re, Fe
Precipitate strengthening	Al, Ti, Ta, Nb
Primary MC carbide formers	C, Hf, Zr, Ta, Ti, Nb, W, Mo, V, Cr
Oxidation/Corrosion	Cr, Y, La, Co, Al, Cs, Ce, Th
Grain boundary strengthening	B, C, Hf, Zr
Control of S and other impurities	Mg, Cr, Ca

Processing factors and heat treatment routines can also have a profound effect on superalloy properties. Grain boundary engineering to alter the size, shape, and composition of grain boundaries has also been shown to reduce susceptibility to oxidation and increase creep, fatigue, and weldability by 50% or more [48]. Differences in cooling rates during solution heat treats showed that slow cooling rates induced a slight overaging of IN718, which reduced monotonic material properties such as tensile and creep strength, but also caused a slight increase in ductility [49]. Additionally, cast versions of both IN740 and IN600 have been shown to possess lower strength than their wrought counterparts, though the difference decreases with increasing temperatures [47]. Properly structured post-processing routines have also been shown to be highly effective in manipulating resultant microstructures and subsequent material properties. The combination of homogenization heat treatment with a hot isostatic press (HIP) cycle has been shown to be effective for eliminating Laves in IN718 [44].

The most dominantly produced nickel-based superalloy is Inconel 718, as it has excellent weldability due to relatively low levels of Al and Ti when compared with other similar  $\gamma'$

hardening alloys, though several different alloys exist by the variation of constituents or quantities thereof [38, 50]. The improved weldability from the low Al and Ti content makes it easier to repair, a factor which can limit the use of other alloys, as blades are susceptible to premature failure due to hot corrosion and fatigue cracking causing airfoil tip loss [51]. Although 718 is the most popular alloy, it is limited in use for applications which will experience temperatures over 650°C, as it can cause coarsening of  $\gamma''$  precipitates which affects the structural stability at those temperatures, causing a transformation to  $\delta$  phase equilibrium, which is detrimental to yield strength and creep performance [50, 52-54]. As such, higher temperature applications require alternate alloys. The alloy 939 was developed with these objectives in mind, and features superior strength, fatigue performance, and corrosion and oxidation resistance at operating temperatures of up to 850°C due to its high content of Cr and Co relative to other alloys, the nominal composition of IN939 is given in Table 2.2 [33]. Despite being formulated to promote high temperature performance and stability, however, degradation still occurs in IN939 as the microstructure evolves when exposed to service conditions for long durations. Degradation has been shown to occur due to coarsening and morphological changes of  $\gamma'$  particles due to extended times at high temperature due to increased lattice mismatch, embrittlement of the material due to formation of carbides continuously along grain boundaries, and formation of oxidation at and below the material surface, including an external scale and a depletion of  $\gamma'$ , along with other microstructural changes, when exposed to high temperature oxy-combustion environments for long durations [55-59].

Table 2.2 - Chemical composition of IN939 [55, 56].

<b>Chemical Composition (Wt%)</b>			
<b>C</b>	0.15	<b>Nb</b>	1
<b>Cr</b>	22.4	<b>Ta</b>	1.4
<b>Ni</b>	Bal	<b>Ti</b>	3.7
<b>Co</b>	19	<b>Al</b>	1.9
<b>W</b>	1.6	<b>B</b>	0.01
<b>Zr</b>	0.1		
<b>Material Properties at Room Temperature</b>			
<b>Density</b>	8.17 g/cm <sup>3</sup>	<b>Tensile strength</b>	954.3-1236.3 MPa
<b>Melting range</b>	1235-1338°C	<b>Elongation</b>	4.7-9.3%
<b>Yield strength</b>	805.3-830.2 MPa	<b>Reduction in Area</b>	7.2-10.4%

Although IN939 is primarily and increasingly featured for use in the fabrication of gas turbine components, as high purity IN939 features an acceptable balance of strength and weldability, it is not as readily weldable for repair from service or casting damage as some other alloys, such as IN718 [50]. This is due to the fact that IN939 is primarily heat treat hardenable through the precipitation of  $\gamma'$  particles of the  $\text{Ni}_3(\text{Al}, \text{Ti})$  into the solid solution  $\gamma$  matrix, which help preserve strength at higher temperatures than  $\gamma''$  hardenable alloys, but which also makes the alloy susceptible to microfissuring and cracking during welding repairs, especially within the heat-affected zone (HAZ) [57, 60]. In addition to this, these alloys have been shown to be very sensitive to the welding process employed and the processing parameters used therein [61]. The plot in Figure 2.1 shows the weldability of several superalloys, and how the content of Al and Ti within the alloy directly affects it. Increasing content of either Al or Ti makes an alloy more difficult to weld, with a total quantity exceeding about 4% being grounds for designating an alloy as very difficult to weld [31, 62].

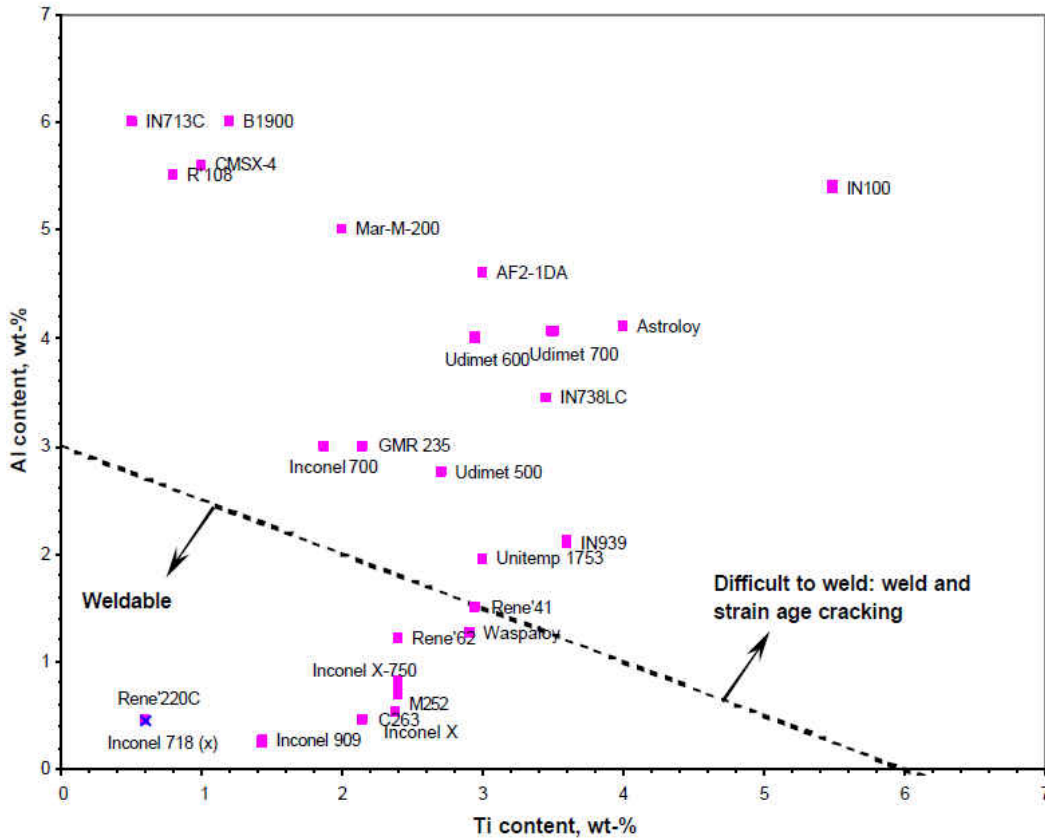


Figure 2.1 - Weldability of high-strength, high-temperature alloys as relating to content of strengthening  $\gamma'$  precipitate-forming constituents, Al and Ti [31, 62].

The difference in melting temperatures, among other factors such as grain size and grain boundary segregation of precipitates, causes the formation of unstable phases and stresses which cause cracking upon both liquidation of said phases and solidification of the HAZ [61, 62]. Cracking is primarily caused along grain boundaries due to the high concentration of precipitates being liquidated, initiating cracks and is propagated by the morphology of said grain boundaries [60]. Microfissuring in the HAZ is further promoted by the re-precipitation of dissolved precipitates during the cooling stage, and it is suggested that an increase of these could reduce the minimum heating rate necessary for liquidating them, causing further detriment to the HAZ



and during subsequent post-weld heat treatments [63]. As such, improvements in the weldability of high  $\gamma'$  hardenable alloys, especially 939, are of high interest, and can be accomplished through methods targeting the content and morphology of these phases. One such method is through the control and alteration of alloying constituent quantities, as was done by Canon-Muskegon to create CM 939 Weldable alloy, which has significantly reduced levels of Al, Ti, Ta, and Cb to reduce the occurrence of weld-restricting  $\gamma'$  phases, along with optimization of minor alloying additives for enhanced control of harmful impurities [64]. Additionally, heat treatment processes have been shown capable of altering the microstructure to improve weldability, through the dissolution and redistribution of strengthening phases [60]. The heat treated microstructure can minimize or eliminate the misfit between the  $\gamma$  matrix and  $\gamma'$  precipitates, leading to a more uniform microstructure which is better able to accommodate the stresses generated during welding [51]. Overaging of the original material structure, while typically harmful to mechanical properties, can dissolve and redistribute  $\gamma'$  precipitates in order to soften the base material, making it more receptive to welding while also increasing ductility, though a concurrent loss of yield strength will occur [50, 65].

The dendritic microstructure resulting from casting will vary based on the size and shape of the cast, due to differences in cooling, and as such microstructure throughout a component will vary, reinforcing the need for heat treatment [33, 55]. Additionally, addition of a HIP cycle has been shown effective in healing a majority of the production defects, such as pores and cracks which can result from casting, while conserving microstructure, and so HIP is sometimes employed before heat treatment to result in more favorable final microstructure [66]. Left uncorrected, pores formed during casting have been shown to be highly influential in limiting the

high cycle fatigue life of IN939 at high temperatures [67]. Design of heat treatments for superalloys presents various difficulties, including variation of phase transformation temperatures due to changes in alloying quantities and heating or cooling rates, along with the possibility of localized melting occurring before complete dissolution of precipitates [68]. Traditional heat treatment for IN939 consists of a four-stage process, and though temperatures and times can vary, the general aim is to dissolve precipitate phases such as  $\gamma'$  and  $\eta$  into the matrix, and later precipitate the desired phases homogeneously [42]. The original, standardized heat treatment was then established as producing the best balance of properties with the four stages defined as 4h/1600°C + 6h/1000°C + 24h/900°C + 16h/700°C, though omission of certain aging stages and variations in cooling rates have shown differences in material properties while still being suitable for certain applications [65]. As discussed, strengthening of IN939 is mainly achieved through uniform precipitation of the  $\gamma'$  phase, which is achieved through a secondary precipitation heat treatment, and the third stage causes growth and coarsening. The first stage of heat treatment, however, is typically the solution anneal aimed at dispersing this and other phases into the matrix, and the selection of temperature can affect properties related to creep and fatigue resistance due to the segregation of alloying elements or causing partial melting of the alloy, both of which can cause inhomogeneity within the final microstructure and material properties throughout [33]. A two-step annealing process combining a high temperature anneal to dissolve  $\gamma'$  precipitates with a low temperature anneal of higher duration allows for the dissolution of the  $\eta$  phases which persists during normal heat treatments while avoiding localized melting, thus improving the resultant microstructure and the hot workability of the material, which is greatly impacted by the presence of  $\eta$  phases [33]. However, adequate properties and an increase in

fatigue performance have also been achieved by implementing a much shorter duration solution and age heat treat [50]. Slow cooling rates during the aging cycle have been shown to be beneficial in producing serrated grain boundaries, which reduce oxidation and creep crack growth in  $\gamma'$  and  $\gamma''$  hardened superalloys, and should benefit subsequent material weldability by the same mechanism of interrupting propagation of cracks produced during such an operation [50, 55]. Evolution of precipitates during long-term exposure to service conditions (or extended aging at high temperatures) has been shown to be dependent on the initial heat treatment routine employed, though the manufacturing process, when casting or hot forming were employed, had an insignificant effect [56].

The material of interest in this study can be considered a derivative of IN939. It is a proprietary nickel superalloy developed for use in high temperature turbine component casting. To protect its proprietary nature, this alloy shall heretofore be referred to as IN939V. Similar to the aforementioned CM939, IN939V has been optimized for improved weldability over traditional IN939 while conserving its high temperature performance. Its primary use is in cast turbine vane applications, though it is also of high interest for the production of high-complexity turbine components via SLM. As such, since the properties and microstructures present within IN939V produced via SLM have been seen to differ greatly from those of cast applications, the post-processing routines need to be optimized and the material properties need to be evaluated and shown to be equal or better than those of cast applications.

## **2.2 Selective Laser Melting**

Due to their high-strength properties in elevated temperature conditions, nickel superalloys are of high interest for use with additive manufacturing techniques. Technologies such as these offer the ability to design and manufacture components with unmatched complexity. Pursuant to that is an equally complex microstructure with unique material properties, which is affected by processing conditions during and after component manufacture.

### **2.2.1 Background and History of SLM**

The additive manufacturing landscape is becoming increasingly complex and advanced, as are the capabilities now available due to layer-wise AM technologies. The first of the AM systems was introduced by 3D Systems in 1987, using a UV light cured polymer, and each subsequent year more materials and technologies have been introduced. The 1990s saw the proliferation of various systems using different technologies, including plastic extrusion based technologies such as fused deposition modeling (FDM), laminated object bonding which bonds layers of a structure into a solid from sheets cut with a laser, and powder bed techniques such as selective laser sintering (SLS) which uses a laser to sinter together powder particulates [1, 69]. In the mid-90s Dieter Schwarze and Matthias Fockele with the Fraunhofer Institute for Laser Technology developed and introduced selective laser melting (SLM), a layer-wise laser based manufacturing technology which has, like other AM systems, progressed beyond the use of prototyping to full-scale manufacturing of production-quality components to be used in various applications with the ability to integrate complex geometries within the structure that are not achievable with traditional manufacturing techniques [1, 70]. Numerous other systems and

variations of such have come to be developed since then, utilizing a variety of materials and binding mechanisms, as AM systems become more commonplace for research, education, hobbies, and industry [71].

As additive manufacturing systems become more complex, accessible, and reliable, the presence of AM parts in industrial applications becomes increasingly commonplace. Rapid prototyping and AM systems have been of interest for the design of custom tooling since their inception, such as the design and production of investment casts and molds, and with the quick turnaround several prototype iterations of a mold can be produced and tested before the final design production while still economizing cost and time from traditional machining [2, 72, 73]. One such application of this has been shown in the production of structural components for fuel cells, the production of which can quickly drive up fuel cell stack costs, severely limiting their return on investment. Bipolar plates act as both structural and functional components in fuel cell stacks, and research into their production using AM methods has been done with both direct manufacture using direct metal laser sintering or production of a cast through binder jetting for use with thermal spray deposition [74, 75]. Additionally, fuel inlet manifolds for use in microtubular solid oxide fuel cell stack assemblies have been produced using fused deposition modeling of ABS plastic with promising results [76]. Selective laser melting has been shown to be useful in the production of porous media and small structural components such as microtrusses [77]. As the titanium alloy Ti-6Al-4V is a common material for SLM processing and concurrently highly biocompatible, biomedical applications are of high interest using AM systems and reliable, and cost effective production of implants and porous support structures has been shown with both electron beam melting and SLM [78]. Similarly, both titanium and cobalt-

chromium alloys have been investigated for use with SLM in conjunction with digital imaging to produce patient-specific dental implants [79]. The energy and aerospace industries have also taken advantage of the advanced design complexity available through additive manufacturing, producing fuel nozzles and hot-side engine components with integrated cooling technology [3, 4, 6].

### **2.2.2 Overview of Methods**

Components manufactured in SLM begin as 3D CAD models which are sliced into layers parallel to the build plate, which are then translated into building instructions for the machine with the input of specified processing parameters such as layer height, laser scan speed, and laser power. The build plate lowers a depth corresponding to the desired layer height and a layer of powder, typically metallic alloys in the case of SLM, is deposited and leveled on the build plate in a sealed environment filled with an inert gas such as Argon or Nitrogen. The laser scans the shape of each layer, moving according to programmed instructions, the build plate is lowered the depth of another build layer, and the process is repeated in a successive, layer-wise manner to produce the solid, as is diagramed in Figure 2.2 [80]. Once the build is finished, the build plate is removed from the machine, shedding the excess powder back into the system, and the component is removed from the build plate by cutting, often with the use of wire-EDM.

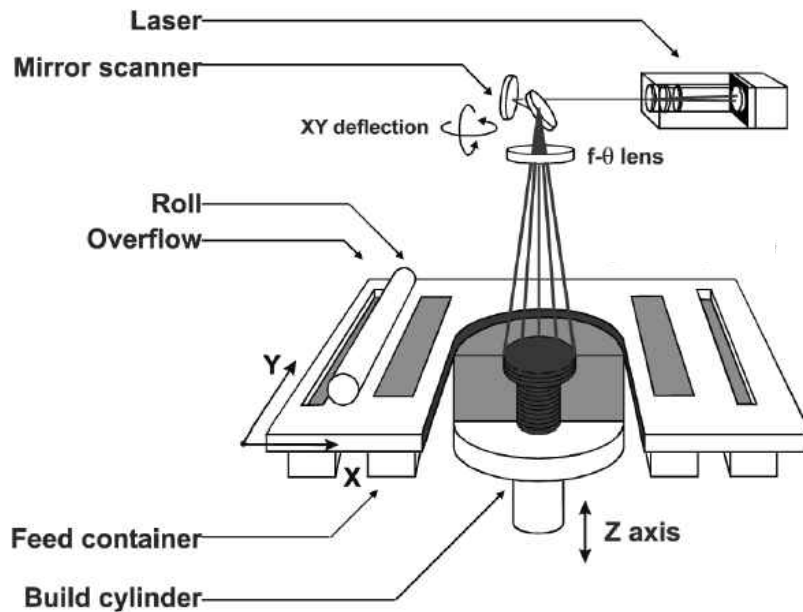


Figure 2.2 - Typical schematic of selective laser melting and selective laser sintering systems [80].

The process of layer-wise manufacturing via laser scanning introduces a characteristic microstructure to SLM components. On the macroscale, the appearance of as-built components feature small ridges the thickness of the specified powder layer height in the SLM machine. These layers are characterized by long, thin scan tracks following the laser scanning direction, or scan path, as seen in Figure 2.3 [81]. The top view shows a cross-section of the sectioned layer, in which the scanning direction follows the x-axis. The front and side views show the build direction follows the z-axis, as is evident from the multiple layers. The appearance of some long tracks in these views shows that the scan strategy employed here is one where the direction alternates between being parallel to the x and y axes. The arched lines which are the cross sections of the scan tracks indicate the shape and size of the melt pool, with the overlap of scan

tracks showing the order of scans, and the depth of some of these crossing several layers enhancing the bond between layers as the melt pool penetrates and re-melts previous layers.



Figure 2.3 - Cross-sectioned SLM sample displaying typical macrostructural features [81].

The rapid, repetitive heating and cooling causes a high thermal gradient from the surface of the component towards the build plate. The stresses induced by the thermal gradients are formed by the rapid heating of the newest layer and slow conduction of heat into the already cooled and solidified previous layer, which restricts the expansion of the new layer to the point of causing plastic compressive deformation within it, and a resultant tensile stress on the layer below [82]. Once the top layer cools and shrinkage sets in, the plastically deformed compressive zone shrinks less than the rest, causing the layer to be in tension and compression in the previous



layer. The repetition causes the resultant stress profile of the part to be that of tensile stress at the top and bottom of the component, while the center features high compressive stresses, as shown in Figure 2.4 [83]. The resultant residual stress levels are affected by the geometry and stiffness of both the build plate and the component; the higher the yield strength of the material and the larger the number of layers, the higher the residual stress will be [83, 84]. Residual stresses, if not thermally removed, are relaxed through the shrinkage and bending deformation of the part upon removal from the build plate [81].

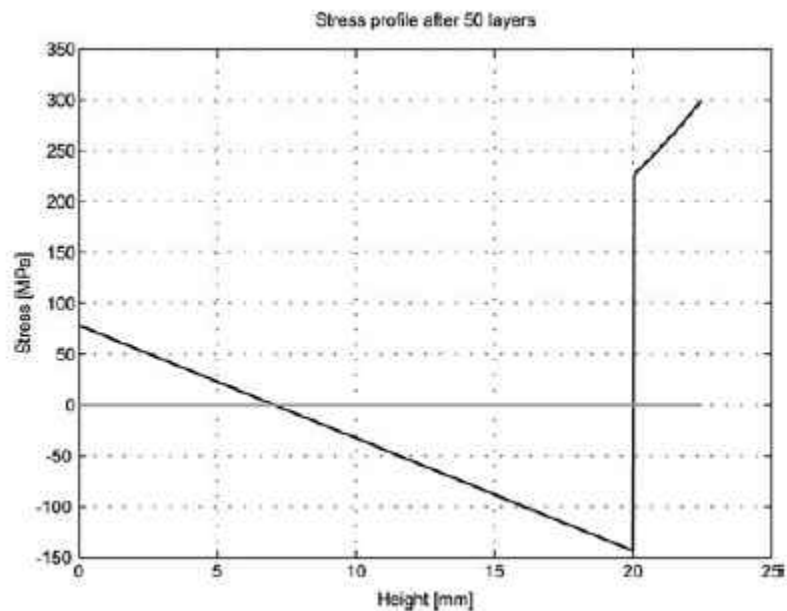


Figure 2.4 - Residual stress distribution per SLM build height [83].

The repetitive rapid heating and cooling of the material and resultant heat gradient causes the microstructure to feature a fine, needle-like dendritic structure which is highly anisotropic, along with the microsegregation of constituents, such as Nb and Mo, which form Laves phase in

Inconel alloys [85]. The columnar microstructure has been shown to be present in components produced by several different layer-based AM technologies, such as SLM and electron beam melting, and with a variety of different materials [86]. The scale of the columnar grains can vary in single components depending on the scanning strategy employed, in IN718 this ranges from less than 100microns to larger than 500microns depending on whether regions are exposed on one or more passes [82]. The strength of the texture is affected by the scanning strategy and laser power which determines the mode of solidification which is dependent on the thermal gradient and the growth rate, with the strongest texture being produced by scanning in the same direction for every layer [87]. Figure 2.5 shows an electron backscatter diffraction of SLM AlSi10Mg from the front and top views displaying the columnar nature of the microstructure, where the dendrite growth is oriented towards the center of the melt pool, each of which is denoted by the dashed lines, and the top view shows different passes and the variation in grain size, with the finer grain regions denoting the overlapping sections of the two adjacent scan tracks [87]. For nickel-based superalloys such as the Inconel family, the as-manufactured microstructure of layer-based AM produced components such as SLM and EBM consists of monoliths generally parallel to the build direction mainly composed of a  $\gamma$  phase Ni-Cr matrix with an fcc structure, with coincident thin  $\gamma''$   $\text{Ni}_3\text{Nb}$  bct precipitates, along with a minority of  $\gamma'$  phase precipitate and carbides, though the majority of these precipitates dissolve in the matrix and do not have a chance to form strengthening precipitates due to the high cooling rate [86, 88]. Additionally, element segregation within the dendrites of phases rich in Nb, Mo, and Ti causes formation of Laves phase to be rather prominent due to their high melting points [88, 89]. Increasing the laser power (or the energy input in general) reveals the presence of delta phase and causes a

concurrent increase in the size and presence of Laves phase which is taken to be detrimental to ductility and fatigue performance, though proper post-processing techniques can dissolve Laves phase back into the matrix and form strengthening precipitate phases for an overall more uniformly distributed microstructure [89, 90]. The small grains from which the microstructure is composed of lend SLM components very high strengths, typically exceeding those of traditionally manufactured components, following the Hall-Petch relationship, which inversely relates yield strength to average grain size, or the volumetric average grain size [81, 91-93].

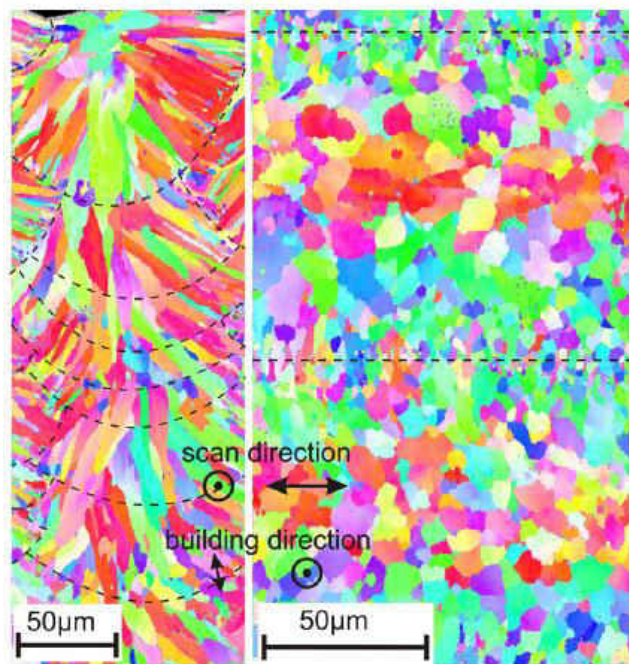


Figure 2.5 - Columnar microstructure characteristic to SLM components caused by the heat gradients present during construction extending from the build surface to the build plate [90].

### **2.2.3 Variations Due to Process Parameters**

With the complexity of modern additive manufacturing (AM) machines comes a range of options and processing parameters that can be controlled by the user depending on the alloy and application in question. The importance of processing parameters in selective laser melting (SLM) machines as linked to material properties has been very well documented. Among these, some of the more popularly manipulated parameters include the layer thickness, scan speed, laser focus diameter, and laser power. Other factors to consider are part orientation during builds and the various effects they can have on the finished product, the effects of the flow characteristics of the inert gas environment within the build space, and the laser scanning pattern.

Part orientation in additive manufacturing systems has been thoroughly documented to alter strength in finished components. In [94-96], the material properties of components made of polylactic acid (PLA) via fused deposition modeling (FDM), the popular filament extrusion 3D printing method, were tested in tension, torsion, and fracture. Various processing parameters were tested for their effects on material properties, with orientation having a high effect on component strength in all three test types. Similarly, Starr et al. [97] showed the effects of various processing parameters and their interactions on material properties of laser-sintered nylon, finding that orientation can disproportionately affect properties such as yield strength and ductility, especially when considering the interaction with laser power. Orientation has also been tested for metal AM systems, including laser cladding and SLM [98-100]. An increase in tensile properties has been seen for coupons manufactured in the xy direction, while those manufactured in the z direction were characterized by slightly higher hardness values [98, 101]. The inequalities in strength due to orientation were confirmed by Rickenbacker et al. [99], while also

noting that those components with increased strength properties (xy direction) suffered from reduced creep and expected fatigue performance as compared to those manufactured in the z direction. Additionally, notably higher scatter has been seen in both the yield and tensile strengths of both Ti-6Al-4V and 15-5PH stainless steel tension samples manufactured vertically [101]. Samples manufactured from a material equivalent to Hastelloy X in SLM and loaded in the z direction were found to have a low cycle fatigue performance analogous to hot rolled materials, with LCF performance decreasing as the build angle decreased [102]. Samples built from IN 939 were shown to have finer grains when built in the z direction than in the xy direction, about half the size on average, which was attributed to higher residual thermal stresses in as-built samples manufactured in the z direction [103]. In addition, samples built in the z direction were characterized by nearly double the elongation of those built in the xy direction. An aging cycle reduced the elongation of both directions to a significantly lower level. Anisotropy between build directions is further pronounced when testing at elevated temperatures, as elongation suffers with increasing temperature, more so for parts not built in the z direction, which still meet or exceed those of forged or cast equivalents [104]. In contrast, Vilaro et al. determined that for parts containing defects, the xy samples displayed higher ductility due to the loading causing the defects to close, in contrast to the z samples in which defects stretched and became more pronounced, quickly causing failure [105]. The effect of orientation is also material and production parameter dependent, however, as SLM samples produced at varying angles between xy and z sample directions out of Al-12Si showed a negligible effect of resultant microstructural texture on yield strengths, with a range of difference of only 5-10MPa [106].

Layer thickness can severely affect material properties in SLM parts, along with part quality and overall build time, as thinner layers means more total powder recoater passes and laser scans, quickly increasing time. In general, thinner layers means higher material bonding due to increased melt and re-melt, as the melt pool created by the laser can penetrate deeper. As layer thickness increases, the porosity and number of internal microcracks also increases, which inherently decreases component density and strength [107, 108]. Additionally, it could be said that the thicker layers of powder act as a cooling agent, as was seen in laser cladding experiments, so that with thicker layers not only does the melt pool not reach as deeply into the previously built structure, but that structure is cooled somewhat by the freshly laid powder, causing there to be less residual heat for bonding of the subsequent layer [109]. As such, with thinner layers an increase in the yield strength, ultimate tensile strength, elongation and hardness were witnessed in [110], regardless of scan speed.

Scan speed is, however, also of high influence to material properties for SLM materials. Beyond a certain scan speed, sintering of powder is incomplete or does not occur, resulting in increased porosity [107, 111]. Surface roughness has also been found to increase with increasing scan speeds, likely due to the onset of balling and partial melt of surrounding powder particles attaching to the surface and the higher prominence of the layered structure, a finishing quality parameter which can be of concern when components are to be used in fluid flow and heat transfer sensitive application where surface roughness can affect flow characteristics [112-114]. Surface roughness features may also act as fracture initiation sites due to the inherent ability to act as stress concentrations, and roughness has been shown to strongly influence fatigue strength limits, though lifetimes were largely unaffected [101, 115, 116]. While finishing processes for

improving surface quality have been studied, often the results can be somewhat unpredictable or inconsistent based on factors such part geometry and material type, with final component geometry differing from that which was intended if too much material is removed, thus introducing geometric error [112, 117]. A literature review and study of SLM 17-4PH by Stoffregen et al. is illustrative of the influence of surface roughness and finish, as the fatigue strength of as-fabricated samples was found to be significantly lower than that of much smoother machined samples [118]. The influence of surface finish on performance can be a detriment to the advantages presented by SLM manufacturing, as small scale structures become adversely affected by the variations in the component microstructures, cross-sections, and surfaces due to differences in cooling and the partial melt of particles to the surface of the part, with internal surfaces that cannot be modified by post-process surfacing techniques becoming fracture initiation sites [77].

The effects of scan speed become more pronounced as layer thickness increases. The dependence of material density on scan speed with various fixed layer thicknesses is illustrated in Figure 2.6 [119]. Intuitively, then, a lower scan speed should work best at ensuring adequate melt between powder particles. As such, it has been shown that at lower scanning speeds, the increased laser exposure time increases melting and diffusion, resulting in lower porosity and subsequently higher strength values [110]. It has, however, also been shown that too slow of a scan speed can be detrimental to resultant material density, due to an instability in the melt pool from irregularities in the scan tracks, suggesting a limitation to both the lower and upper scan speeds which can be utilized on a certain material [120-122].

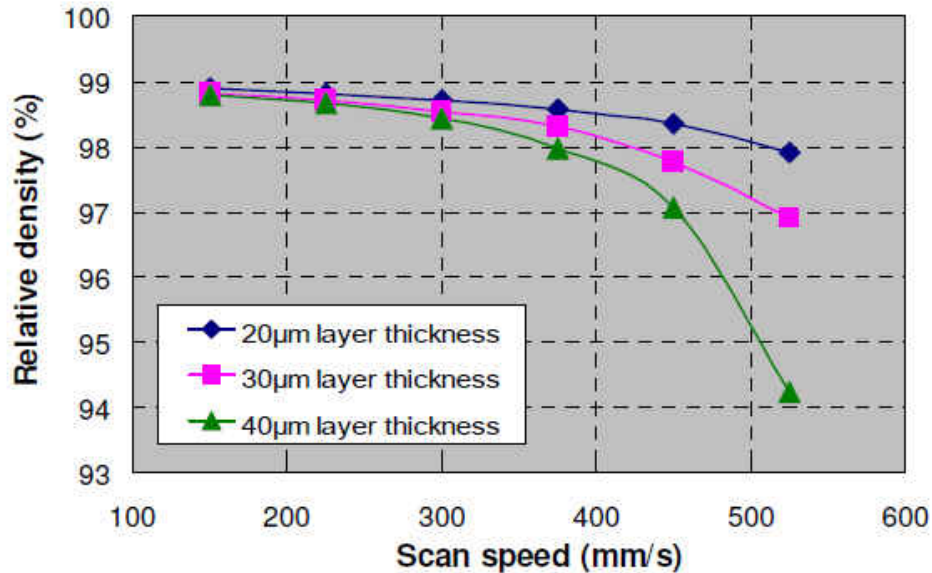


Figure 2.6 - Detrimental effects of increasing scan speed and layer thickness, emphasize by the combination of such [119].

In fact, the limited melting which can occur at higher scan speeds can leave powder particles within the component to act as inclusions or voids, which can lead to premature rupture by acting as crack initiation sites, inherently lowering component strength, life, and increasing scatter in material properties. As scan speed increases, the size of the melt pool will decrease, which in turn decreases the adhesion of powder particles to those around them [109]. Figure 2.7 shows the fracture surface of a sample exemplifying the effects of such unmelted powder particles acting as inclusions or pores [114]. Excessive scan speeds have been shown to correlate with increases in porosity due to a lack of scan track overlap and partially non-melted powder particles, which inevitably lead to lower tensile and fatigue strengths and corresponding decrease in microhardness [113, 123]. In one study by Brenne et al., components were manufactured using both a high-power 1kW laser and a 400W laser and heat treated and aged at varying



temperatures, whereas most other studies reviewed here utilized a laser of 200-500W, leading to deviations in resultant microstructures [90]. Microstructures of parts processed with the higher power laser presented a much higher aspect ratio than those processed with the lower power, producing longer columnar structures in the  $\langle 001 \rangle$  direction due to the increased power producing higher heat flux from the build surface to the build plate. Consequently, this strong texture lowered the Young's Modulus to almost half of that achieved with the 400W laser, and the high-power laser also exaggerated the effects of laser path and velocity [90, 124].

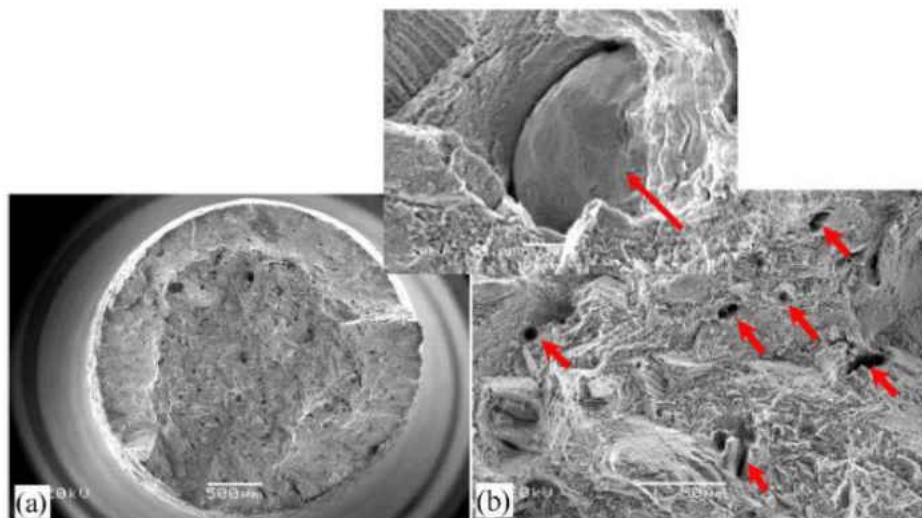


Figure 2.7 - SLM component fracture surface showing the effects of process parameter variations causing inclusions of unmelted particles and pore defects [114].

These effects are due to the fact that several parameters can be linked together in their importance to affecting material properties, as the accumulation of these parameters affects how much energy is absorbed by the powder. As noted previously, it has generally been seen that slower scan speeds, thinner layers, and higher power result in higher strength components due to increased energy absorption by any given amount of powder volume [124, 125]. This can be

referred to as the energy density. This is a measure of how much energy is absorbed per unit powder, and takes into account the scan speed, layer thickness, and power. The relationship between these must be balanced to achieve optimal results, as Figure 2.8 shows the impacts of speed and power directly affecting adhesion and surface quality [126]. A balance must exist between the two, as an excess or deficit in either will cause detrimental effects such as balling or lack of binding. It can also be said that beam diameter and scan or track spacing can affect this, as these parameters also affect the size of the melt pool and the amount of overlap between subsequent laser passes, thus affecting the re-melt of previous tracks and their bond to new ones. In fact, a study using analysis of variance by Singh and Prakash shows the high importance of both power and scan spacing on the density of layer-wise laser formed components using the similar technology of SLS [127].

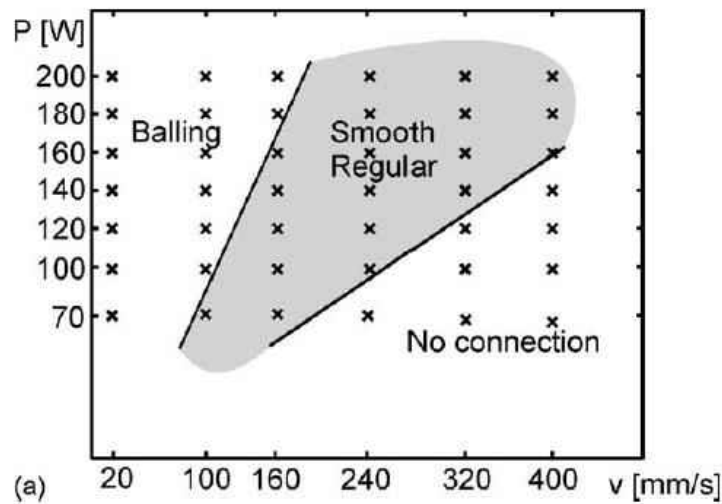


Figure 2.8 - The interaction of power and scan speed can have high a high impact on the surface finish and adhesion of layers with an iron-based SLM powder [126].

Gu and Shen defined this phenomenon via a parameter labeled as the “linear energy density (LED)” in multiple works, which is presented simply as the ratio of laser power to scan speed, and as such featured units of kJ/m [128, 129]. They characterized the resultant melted surface under four categories; 1) slight but incomplete melting, 2) continuous melting, where the outcome was ideal, 3) melting with balling, where excess laser power and high speed caused formation of metallic spheres due to surface tension, and 4) melting with breakage, where the combination of high power and low scan speeds significantly increased the local energy density so that excess heat input can cause partial gasification of the powder and excessive shrinkage during cooling which causes cracking in the material [108, 113, 128, 130]. Figure 2.9 shows the evolution of the surface morphology of IN718 with increasing energy density showing partial melting, balling phenomena, and an ideal, fully sintered surface [131]. The different surfaces are generated by varying the linear laser energy density by way of manipulation of laser power and scan speed. The levels of linear energy density tested corresponded to distinct levels of porosity: 25% for 180J/m, around 15% for 275J/m, less than 10% at 300J/m, and only 1 or 2% at 330J/m. Thus, the level of porosity and surface quality have been shown to be intrinsically linked by the linear energy density, which affects both.

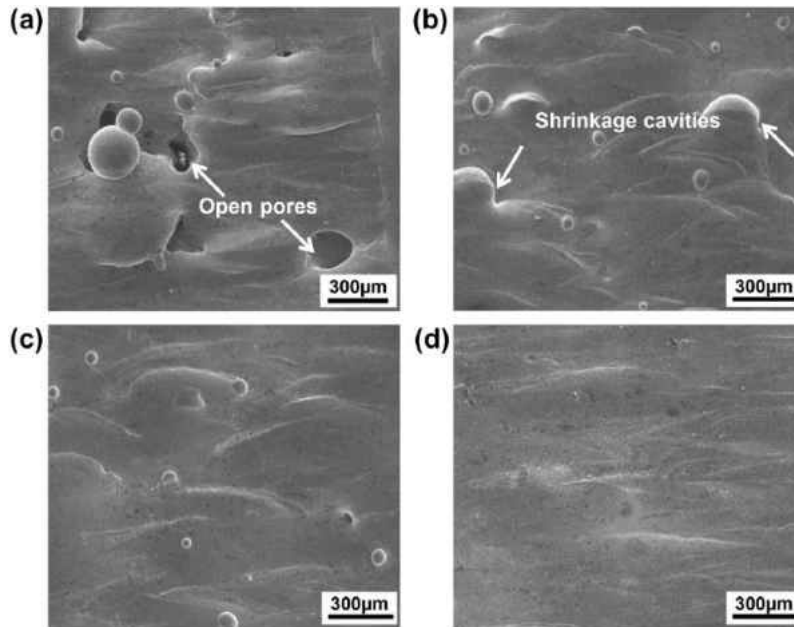


Figure 2.9 - Surface morphology of SLM IN718 with varying energy densities increasing from (a) 180 J/m, (b) 275 J/m, (c) 300 J/m, to (d) 330 J/m [131].

Ultimately, production of samples outside of the second category defined by Gu and Shen produced parts characterized by pores and microcracks, due to either insufficient or excess localized heat input, as has been corroborated by other studies [126]. Contrastingly, by defining the combinations for which each type of melt occurs, the same parameters can be optimized to deliberately produce porous metallic structures as well [129]. A similar parameter, denoted as the “nominal laser power density”, has been defined as the ratio of laser power over the combination of the scan speed and scan spacing and is intrinsically tied to the laser spot size, with units of  $J/mm^2$  [111, 114, 132]. A threshold value of energy density exists at which voids are eliminated, and further manipulation of the resulting texture and quality of the microstructure can be achieved by altering the parameters of interest to mitigate the detrimental effects of each, such as residual stress and cracking, while maintaining the necessary threshold energy density value

[132, 133]. One particular study using iron powder in SLM, found that at a constant laser power of 100W, above the threshold energy density, increasing scan speed produced higher strength parts and concurrently decreasing grain size [134]. Similar values for the threshold energy density can be observed for similar materials to eliminate voids, such as Ni superalloys including IN625, IN718, CMSX486, CM247LC, and Hastelloy X [114, 133]. Finding the lower threshold of power density for Hastelloy X, for example, led to parts with density better than 99.5%, though higher values of power density only yielded slightly higher density and fewer cracks, full density was never reached [114].

Taking into account the layer thickness and hatch (scan/track) spacing combined with the scan speed and laser power a “volumetric energy density (VED)”,  $\varepsilon$ , was defined by Gu and Shen [128], which is the ratio of the power,  $P$ , to the combination of the scan speed,  $v$ , hatch/scan spacing,  $h$ , and layer thickness,  $t$ , as shown in Equation 1 ( $\text{J}/\text{mm}^3$ ).

$$\varepsilon = \frac{P}{vht} \quad (1)$$

The optimization of this parameter leads to part production with the highest densities, regardless of the material [128, 135]. Increased homogeneity of the microstructures due to the application of a higher energy density and uniform melting was also found to improve oxidation behavior, hardness, and wear resistance [120, 131, 136]. As stated previously, energy density can easily be adjusted via manipulation of the power or scan speed. The width and quality of tracks can also be connected to the laser power and scan speed, along with hatch spacing and layer thickness, and Averyanova et al. proposed a unitless parameter to describe the shape of a fused track, which is inevitably connected to surface quality [137]. The resultant microstructure of

laser deposited Ti-6Al-4V has also been shown to be responsive toward increasing power levels, with higher power levels partially causing a shift from the typical columnar structures seen in layer by layer AM systems to a more equiaxed structure, due to a decrease in the thermal gradients from an increase in solidification rates, an effect which is amplified by a change in component size scale [138]. As stated previously, however, there are both upper and lower limits for the energy density in which the material is favorable, and maximizing this factor is not necessarily beneficial, as Figure 2.10 shows even higher porosity at the higher energy density tested by Kasperovich et al. than at the lowest value [139]. This is especially evident when (a) scan speed,  $v$ , is the variable used for adjusting energy density, and although less evident, the same tendency toward a gradual increase in porosity with the rising energy density (after reaching a minimum) can be seen when (b) hatch spacing or (c) power are manipulated [139]. This suggests not only dependencies of the energy density on each variable, but also interactions between them which may merit further study. Of note, pore shapes were also found to differ at high and low energy densities in this study.

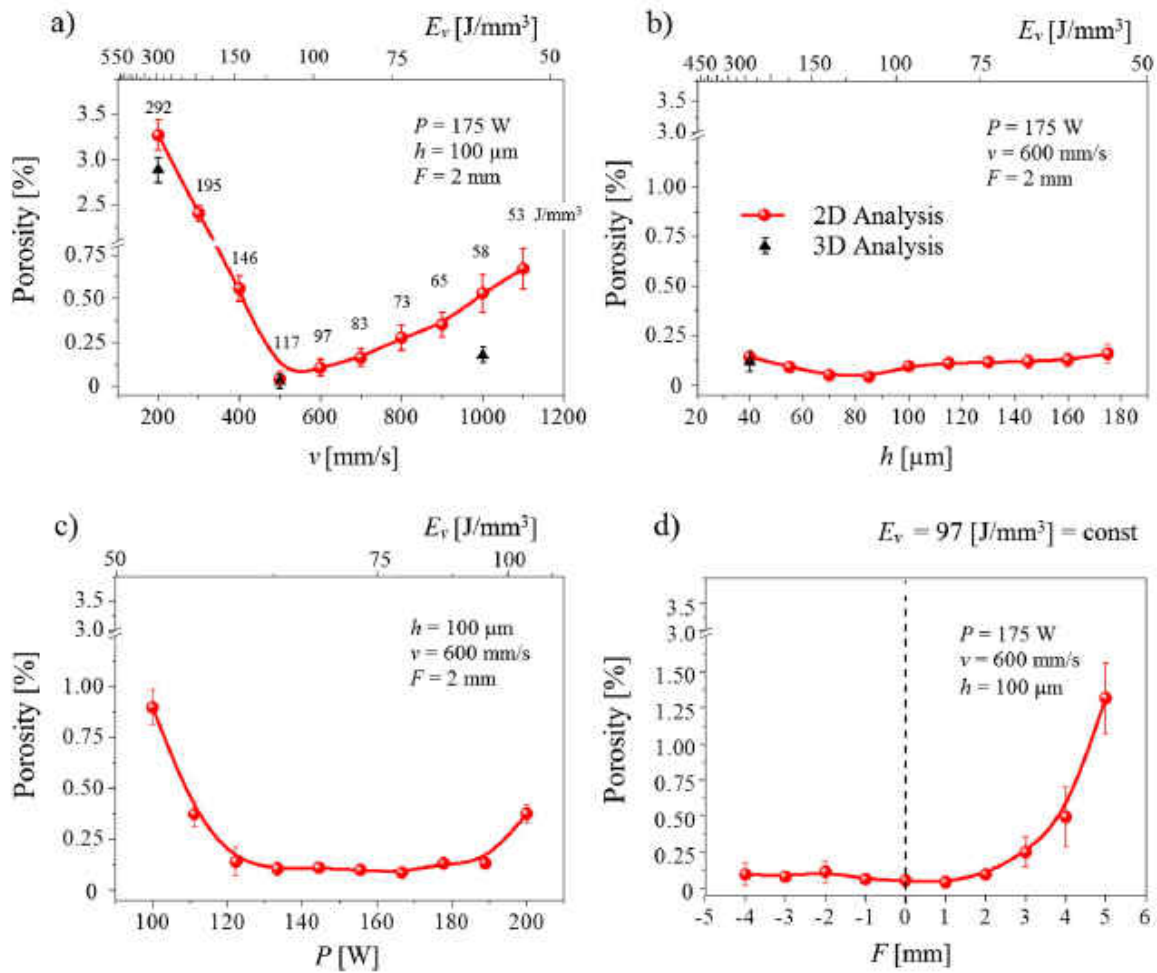


Figure 2.10 - The effects of the (a) scan speed, (b) hatch spacing, (c) laser power, and (d) focus distance on the resultant energy density and the effect of its variance on porosity [139].

Several other parameters which have been investigated and found to be of consequence in literature could be said to be intrinsically tied to the energy density, though not directly through the final calculation for volumetric energy density. As noted earlier, the evolution of the energy density has gone through several phases, one which had units of J/mm<sup>2</sup>, which is the ratio of power to the combination of scan speed and hatch spacing. This relationship can be rewritten as the Andrew number, which combines the overlap to a parameter known as the fluence [111]. The

overlap can be calculated as the ratio of the laser radius,  $\omega$ , and the hatch spacing,  $HS$ , as shown in Equation 2, which was originally described by [140].

$$O = \frac{\omega}{HS} \quad (2)$$

The fluence, developed by [141], is defined as the ratio of the laser power,  $P$ , to the combination of the laser radius,  $\omega$ , and the scan speed,  $v$ .

$$f = \frac{P}{\omega v} \quad (3)$$

As noted previously, combining these two parameters yields the Andrew number,

$$A_n = f \cdot O = \frac{P}{\omega v} \cdot \frac{\omega}{HS} = \frac{P}{HS \cdot v} \quad (4)$$

Which is the expression given earlier for “nominal laser power density.” As such, this measure, and the subsequent volumetric energy density measure, can be said to be influenced by both the laser spot size and the overlap. It has been shown that laser energy density increases with a decrease in spot size, when other factors are kept constant [109]. It was also shown, however, that an increase in spot size can increase material density and strength when held independent of energy density, that is to say, when the value of laser energy density is held constant by the variation of other factors [111]. In this case, the enlarged radius of the laser effectively gives a larger overlap of the current scan track with the previous scans, increasing bonding between them. Excessive overlap due to very small hatch spacing can also have slightly detrimental



effects on material density, however [108]. Additionally, the amount of cooling between each layer can have a similar effect. A slower cooling rate between layers, which can be achieved by reducing the delay between layers, results in an effective increase in the energy density and an aging effect, leading to higher strength and material density; the same effect of a reduced cooling rate has also been shown by manipulation of the scanning strategy employed [111, 142].

The laser scanning pattern, which is characterized by the angle or direction that the laser follows for subsequent layers, has also been shown to produce significant differences in part strength. Variations in scanning strategy during laser cladding have caused variations in material properties, including anisotropy and high deviations in strength and ductility [143]. This could be linked to the relationship between scanning pattern and energy density, as repeated passes lead to increased energy absorbed by the powder and increased interlayer bonding, with decreased chances of voids and cracks caused by unmelted powder particles. An optimized scanning pattern can reduce the delay between reheats of previously melted layers, increasing the strength of the bond between layers as well as the surface quality, including the effect of material balling [126]. The variation of direction and angle of the scanning pattern and its effect on the material density can be seen in Figure 2.11, which shows that although high density (>99%) can be achieved regardless of scanning pattern, the optimization of it causes density to further approach 100%, regardless of some of the other process parameters and in spite of the energy density [119, 120]. Others have argued that an island scanning approach is beneficial to reducing texture, where small (2x2mm to 7x7mm) square sections are scanned at a time with adjacent islands are rotated 90° and subsequent layers are shifted 1mm. The in-layer rotation can aid in reducing the occurrence of elongated grains from continuous scan tracks but can be affected by the occurrence

of cracks [87, 107, 144]. Fractal scan strategies which further shorten the scan vector length have also been found to be beneficial in increasing density, and thus reducing the occurrence of defects, especially as pertaining to difficult-to-weld high  $\gamma'$  superalloys [145]. While various scanning strategies have been employed, however, a simple 90° alternating back-and-forth, or bi-directional, scan strategy has often been found to provide minimization of defects while maximizing homogeneity within the microstructure [87, 132, 146]. The increased strength and ductility of the bi-directional pattern shown in Figure 2.11 can be attributed to an increase in the homogeneity of melting conditions and resultant grain size, orientation, and distribution; that is, the columnar structure typical of SLM parts can be decreased by using a multi-directional pattern, which causes an increasingly homogenous distribution of small grains [119, 137, 147]. Additionally, integrating laser re-melting into the scanning routine via scan path or by using a larger laser radius resulted in significant decrease of surface roughness, increasing the quality of the surface, and reducing residual stresses [83, 119].

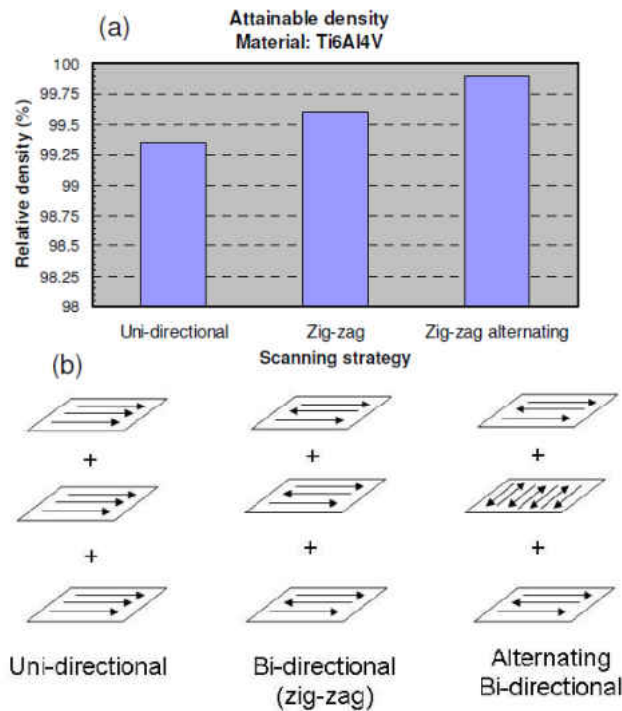


Figure 2.11 - Increased variation in (b) scanning strategies has shown a positive correlation with (a) higher relative density [119].

Some studies have also explored the topic of the environment in the build chamber, as it is responsible for the regulation of heat, cooling layers as they are created. Irregularities or inconsistencies in the gas flow over the build surface can then cause irregularities or distortion within samples, due to differences in heating gradients and cooling rates. Although it has been shown that, with other factors optimized, the type of gas environment with which the build space is purged when considering the typical purging gases of Argon and Nitrogen does not significantly affect component strength, gas flow and distribution does [98, 113, 122]. The velocity of the gas and the laser scanning direction in relation to the gas flow have been found to have a high effect on powder spatter from the melt pool, which in turn affects material properties and surface finish as spattered powder can form pores and defects, with increasing speeds

resulting in increasing strength, to a point, as did scanning against the direction of gas flow [148]. The use of Helium or Hydrogen as a protective gas and the attempt to use Hydrogen as a deoxidizer to provide additional protection both deteriorate finishing quality, as relative density was greatly reduced via the introduction of significant porosity, as seen in Figure 2.12; mixing the deoxidizer with any of the other protective gases had little or no effect [149]. The presence of oxygen, however, above acceptable limits can cause increases in oxidation, surface finish, and porosity, and is inclusive of oxygen which can be released from the powders during melting to directly affect the melt pool [123]. The homogeneity of the temperature distribution and cooling rate caused by the gas flow and part layout was found to highly influence deformations in parts, which in turn will affect part strength and variance in material properties [21]. It has also been shown that given homogenous gas distribution in the build chamber, part placement on the build plate had little effect on strength [148].

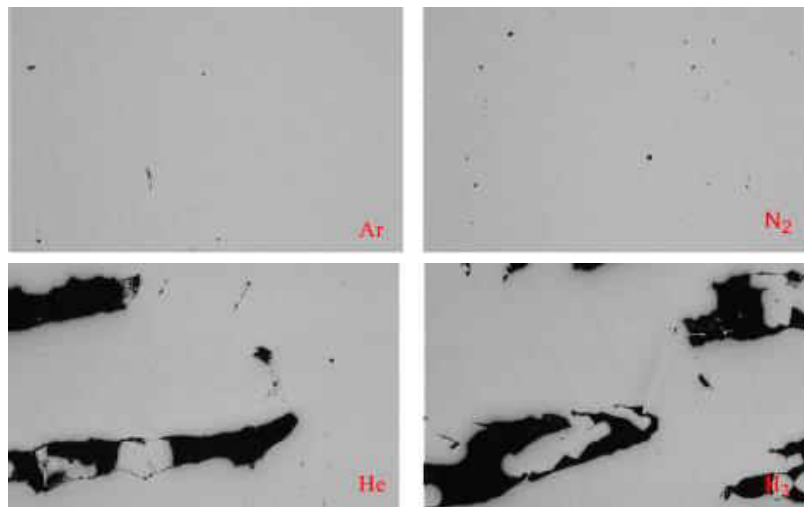


Figure 2.12 - The substitution or mixing of the typical Argon or Nitrogen environments with other protective gas environments has been shown to have detrimental consequences on component density [149].

The build plate can also be considered an environmental factor. All other parameters kept constant, preheating of the build volume, inclusive of the build plate, has been shown to be influential in producing fully densified parts. In said scenarios increasing the temperature of the build plate has been shown effective in reducing the formation of defects of 316L stainless steel SLM samples, increasing density to higher than 99.5% before post-processing, simultaneously reducing residual stresses and part deformation while promoting higher tensile strength and Young's modulus [149]. This is, in-part, due to the reduction of the temperature gradients which exist in SLM components, though the effect does have some interactions with component geometry [83]. In fact, a reduction of as much as 40% of the residual stresses of SLM 304 stainless steel can be achieved though preheating of the build plate [150]. The use of a heated build plate to relieve stresses has been shown to be effective in preventing warping of components upon removal [151].

#### **2.2.4 Post-processing Effects**

The layer-by-layer manufacturing of SLM produces microstructures unique to additively manufactured components, and although the specifics of the microstructure and the behavior of its constituents depends on the alloy and the specific process used, some traits are universally present. Manufacture via SLM produces very small crystals in the microstructure, along with columnar structures which are dependent on the direction of melting. The resultant components are typically more brittle than counterparts produced utilizing more traditional methods such as casting or machining from wrought materials. The columnar structures and very small crystals present in the microstructure dictate the strength and behavior of the material. While the very

small crystals promote high strengths often above those seen in traditionally manufactured materials, the columnar microstructure and layer-wise construction impose a directional dependency on said strengths. As such, material properties can show directional dependency and scatter based on manufacturing conditions. Processing parameters utilized during SLM can have a high effect on the resultant microstructure, particularly grain size and distribution, which in turn directly affect the mechanical properties [152]. Additional to those effects, processing parameter selection and optimization determine features such as the presence of microcracks, pores, and surface roughness, which all have a direct effect on material properties. While very high density can be achieved by optimization of said processing parameters, often it is very difficult to achieve full density or even near-full density due to the presence of said porosity and microcracking. It has been shown that post-processing can help to alleviate the effects of the structures that are intrinsic to layer-wise manufacturing, improving material properties and anisotropic behavior [88, 153, 154]. Processes such as hot isostatic pressing and heat treatment ranging from stress relief to extensive recrystallization have been studied on AM components and are reviewed here, specifically those related to SLM and their effects on microstructures and material properties.

Regardless of the optimization of processing parameters to minimize manufacturing defects, the presence of microcracks and voids in SLM and similar AM processed components is well documented. Failure can often be linked to surface defects and internal features which may create weaknesses, and fracture surfaces can be linked to crack paths following features such as voids or microcracks. Many of these defects and their successive effects can be eliminated via the application of a Hot Isostatic Press (HIP) cycle, during which the component is uniformly

subjected to high heat and pressure levels which induces closure of cracks and porosity, along with some level of recrystallization [155, 156]. While HIP has been shown to eradicate many of these problematic pores, some can also remain untreated due to the presence of features such as trapped gas [157]. Fracture surfaces of IN718 components created using direct laser deposition displayed significant areas of un-melted powder and porosity, with failure being directly linked to these [142]. Application of a HIP cycle has been shown to produce parts with a theoretical full density and reduced pores to below detection limits in SLM Ti-Al6-V4 and to below 0.5% porosity in IN738L [99, 152]. Microstructural changes resulting from the HIP treatments have been observed, where some grain growth and coarsening has been linked to an increase in ductility and hardness, but with a slight reduction in material properties as compared to as-manufactured SLM materials [98, 142, 158]. The recrystallization and increased bonding which occurred in HIP materials, rather than the closing of porosity, are typically credited for any enhancements in ductility, monotonic material properties, and the reduction in the anisotropy seen in those [142, 158]. However, fatigue and fracture properties have been shown to be highly responsive to reduced porosity in SLM materials, as HIP materials have displayed significantly higher fatigue strengths and lives than as-manufactured materials, as well as improvements in fracture strength and crack growth similar to those reported in literature for conventional materials [152, 158, 159]. These improvements were accompanied by a significant reduction in the anisotropy of both fracture toughness and fatigue strength. The four point bending fatigue life of Hastelloy X was improved by application of high-temperature HIP treatment, along with an improvement in the fatigue limit, and a reduction in scatter [115]. In Ti-6Al-4V SLM samples, a trend of increasing cycles to failure during high cycle fatigue testing at room temperature

corresponds with an increase in the heat treatment temperature, with the high temperature HIP treated samples displaying the highest cycle count [160]. An almost 20% increase in the fatigue limit was seen in high-temperature HIP treated 316L stainless steel over the as-manufactured condition, with a higher temperature being chosen specifically for causing recrystallization and is within the solution annealing temperature range. The effects of the solution heat treat HIP can be seen in Figure 2.13, where (a) depicts the as-manufactured microstructure, (b) shows some reorientation due to stress relief, and porosity is clearly evident, and in (c) that porosity is nearly eliminated, and grain shape and distribution is restructured [161]. The color distribution shows that implementation of a proper HIP cycle can close detrimental porosity and contribute to grain restructuring and distribution.

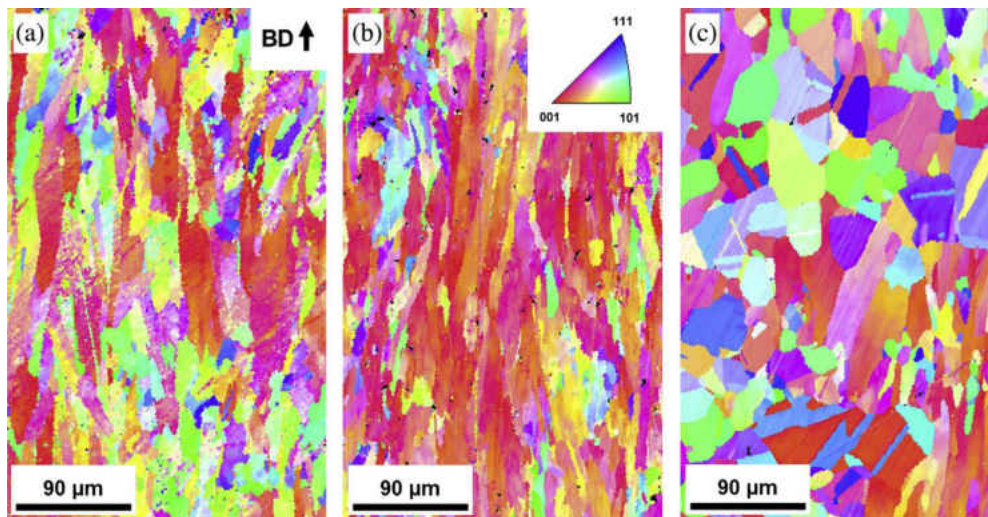


Figure 2.13 - The effects of post-processing are evident as the (a) as-manufactured microstructure responds to (b) stress-relief heat treatment with some reorientation and (b) solution heat treatment hot isostatic pressing with grain growth and pore elimination [161].



The implementation of the recrystallization-HIP cycle also improved crack growth and nearly eliminated anisotropy between build directions. Figure 2.14 shows that with both as-built and stress-relieved conditions (a) and (b), fracture behavior is dictated by the orientation of the elongated grains along the build direction. After the implementation of a high temperature HIP cycle (c), crack growth is found to be independent of build direction [161]. This is due to the normalization of grain shape and distribution regardless of build direction, as shown previously.

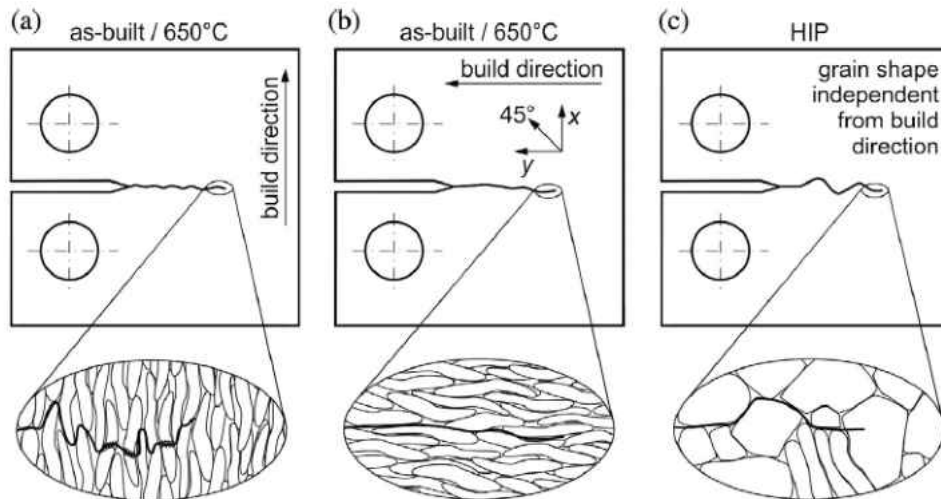


Figure 2.14 - Fracture behavior of as-built specimens is dependent on the build direction, but is independent of it once a suitable HIP cycle is employed [161].

Several other stages of heat treatment can be utilized provide varying microstructural effects to SLM materials. Microstructural changes vary based on both temperature and duration, and differences in cooling have been shown to affect phase volume fractions [105]. A low temperature stress relief cycle, which is typically short in duration, is employed primarily for eliminating residual stresses inherent to SLM components due to the temperature gradients in the SLM build, so as to prevent warping in parts upon HIP removal from the build plate, and has also

been shown to improve crack growth [151]. While implementation of a low temperature stress-relief heat treatment has been shown to significantly reduce measurable strain in parts after removal from the build plate, there is no discernable pattern which corresponds with rising temperature when kept within a certain range [160]. A similar stress-alleviating effect could be achieved by heating the build plate, though the effects of this are limited as temperatures are not as high and the build height to which this is effective is limited, so for taller parts the reduction of residual stresses is incomplete as a heat gradient is still present [83, 150]. Additionally, this cycle has been shown to cause precipitation of carbides at grain boundaries of SLM alloys in multiple studies, including an alloy similar to the proprietary alloy Hastelloy X and EOS stainless steel 17-4, which made more prominent the columnar structure, though it did not restructure it and therefore did not alter material properties [102, 162]. However, a study of SLM Commercially Pure Grade 2 Titanium by Lipinski et al. observed higher values for fatigue limits of limited life tests with stress relieved samples when compared to as-manufactured samples, but for cases of  $10^7$  cycles or more, stress relieved samples suffered a decrease in fatigue strength of about 11% when compared to as-manufactured samples [163]. This is in direct contrast to the findings shown previously of the effects of HIP on fatigue and is likely due to the lack of recrystallization occurring in purely stress-relieved samples.

The existence of residual stresses within the microstructure, however, have been cited as being the catalyst for recrystallization during heat treatment [134]. Recrystallization occurs once sufficient thermal activation energy is recovered through heat treatment to eliminate residual stresses [81]. Literature shows profound and varying effects depending on the method, temperature, and time of heat treatment employed, and evidence strongly suggests the need for

specially developed post-processing regimens for SLM materials independent of those employed for their traditionally produced counterparts. Heat treatments for traditionally manufactured components have been shown to be unreliable and unpredictable in their effects on SLM components made of the same materials, due to the fact that the starting microstructure varies greatly from that for which the procedures were established for [105, 164]. For example, the onset of recrystallization for SLM IN718 samples was shown to begin at 1100°C, while that of wrought IN718 occurs at 1020°C. In SLM materials, a fine, dendritic crystal structure is formed caused by the rapid cooling in manufacturing, along with microsegregation of Nb and Mo constituents to form Laves phase [85, 165]. The characteristic dendritic structure is recrystallized during heat treatments and coarse, curved grain boundaries are formed [159]. The Laves phase, which is detrimental to ductility, can also be dissolved through careful selection of heat treatment parameters to achieve homogenization, and depending on the material these parameters will likely differ from those used for traditionally produced materials [85, 166]. A popular material employed for SLM applications is Inconel 718 (IN718), and several studies have explored its use and optimization through both processing parameters and post-processing. As traditionally produced versions of this alloy have shown, variations of post-processing conditions can have important consequences on microstructural composition and resultant material properties, including creep and fatigue performance [54, 167]. In a solution treatment at 980°C the  $\gamma'$  and  $\gamma''$  dissolved into the matrix and the  $\delta$  phase was precipitated at the grain boundaries, while double aging further dispersed the gamma phases into the alloy, strengthening it [159]. Popovich et al. showed the evolution of microstructure and phase composition of SLM

IN718 through several stages of production, beginning with the powder, as seen in Table 2.3 [168].

Table 2.3 - Phase composition of SLM IN718 during different states of processing [168].

SLM IN718 Sample State	Phases Present	Percent Composition (%)
Powder	$\gamma$ - Ni	90.0
	$\gamma'$ -Ni <sub>3</sub> Al	3.5-3.9
	$\gamma''$ -Ni <sub>3</sub> Nb	4.3-4.5
	$\delta$ -Ni <sub>3</sub> Nb	1.8-2.0
SLM As-manufactured, no heat treat	$\gamma$ - Ni	86.8
	$\gamma'$ -Ni <sub>3</sub> Al	1.9
	$\gamma''$ -Ni <sub>3</sub> Nb	8.0
	$\delta$ -Ni <sub>3</sub> Nb	3.3
SLM after homogenization heat treat	$\gamma$ - Ni	90.1
	$\gamma'$ -Ni <sub>3</sub> (Al, Ti)	1.9
	$\gamma''$ -Ni <sub>3</sub> Nb	8.0
SLM after homogenization and aging heat treats	$\gamma$ - Ni	67.3
	$\gamma'$ -Ni <sub>3</sub> (Al, Ti), Ni <sub>3</sub> Al	25.2
	$\gamma''$ -Ni <sub>3</sub> Nb	4
	$\delta$ -Ni <sub>3</sub> Nb	3.5

As-manufactured SLM samples are nearly identical to bulk powders in terms of composition, with the biggest change being seen in the percentage of detrimental  $\delta$  and  $\gamma''$  phases nearly doubling from around 1.8% to 3.3% and 4.4% to 8%, respectively. After solution heat treatment at 1065°C, or homogenization as referred to here, the most notable change is that the  $\delta$  phase is eliminated, and the gamma precipitates are dispersed, the implication here when comparing to the previously cited work is that this process is very sensitive to temperature changes. Adding aging to the solution heat treatment restores the  $\delta$  phase to pre-heat treatment levels, reduces the  $\gamma''$  back to 4% and dramatically increases the  $\gamma'$  strengthening phases to a total of 25.2%. The increase and homogenous distribution of these secondary  $\gamma$  phases is credited

for the large increase in strength and ductility in comparison to as-manufactured samples, which are comparable to those of hot-rolled IN718 and exceed those of the cast material in strength [168]. Homogenization has also been shown to reduce scatter significantly between identically manufactured components, even when the initial microstructure is preserved [85, 89]. However, while the stress relief and aging temperature regimes increase hardness, higher temperatures in the solution range have been shown to quickly lower it, though higher temperature heat treatments have also been shown to increase precipitation and recrystallization, with slightly higher ductility to correlate with the reduction in hardness [81, 169]. The increased ductility associated with higher temperature heat treatments correlates with a reduction in delta phase precipitates and a subsequent improvement in dislocation mobility [81]. Similarly, heat treatment of Ti-6Al-4V and iron SLM components has shown concurrent increases in material properties. The ductility of the Ti-6Al-4V and the yield strength of the iron components increased up to 10% and 38%, respectively, from an as-manufactured state, though with a decrease in Young's modulus seen in the iron components [134, 160]. These improvements are attributed to a release of residual stress resulting in grain refinement and recrystallization eliminating the columnar structure and increasing grain mobility. The increase in hardness and ductility of Ti-6Al-4V can also be achieved by increasing the duration of heat treatment, as it correlates with an increasing decomposition of the  $\alpha'$  phase, but which results in a loss of strength [164]. As such, optimized heat treatments in studies such as the aforementioned are typically chosen as those which result in a balance between strength and ductility, with neither time or temperature being maximized. A study of SLM Al-12Si shows the drastic changes which can occur in a material from the as-manufactured state, as heat treatment raises the ductility from around 4% in the as-manufactured

state to 25% when heat treated, but lowers strength from just over 350MPa to around 175MPa [170]. The graph in Figure 2.15 illustrates this concurrent dependency of both ductility and strength on annealing temperature of Al-12Si due to a coarsening of the as-manufactured microstructure. This often leads to choosing a compromise between the two as being optimal, which, as can be seen, will still exceed the properties of the cast counterpart in both strength and ductility [106].

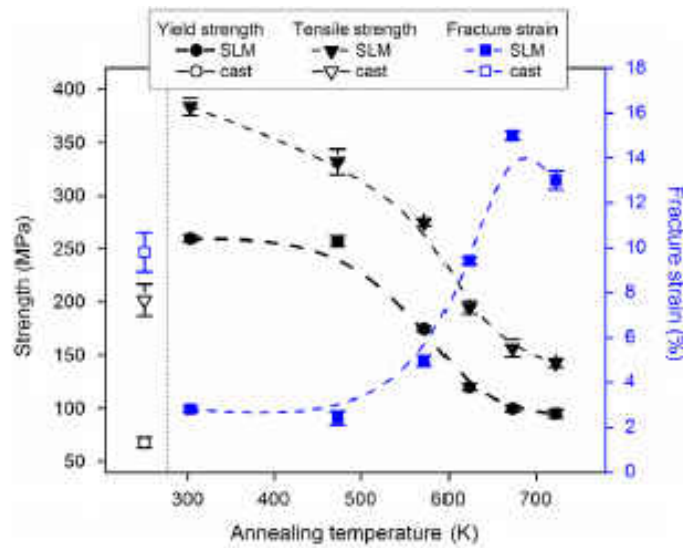


Figure 2.15 - Tensile properties after heat treat depend on the temperature used for the anneal [106].

Similar results have been seen elsewhere in literature, where after aging the yield and ultimate strengths of SLM IN718 both rose to above those of wrought material, and when combined with a solution treatment, those values rose further due to increased recrystallization and redistribution of precipitates [98, 142]. The material properties of SLM and laser-deposited IN718 in various states of processing can be seen in Table 2.4, which clearly displays the effects

of several processes. Solution and aging increase strength from as-manufactured condition, and while scatter is decreased, as is ductility, HIP is shown to increase ductility to a limited extent.

Table 2.4 - Mechanical properties of AM IN718 through several stages of post-processing.

<b>Material</b>	<b>Condition</b>	$\sigma_{ys}$ (MPa)	$\sigma_{uts}$ (MPa)	<b>Elongation/ Reduction in area (%)</b>
SLM IN718 [168]	As-SLM'd	569-646	851-1002	9.8-31.7
	Solution + Age	1160	1350	17.6
SLM IN718 [159]	As-SLM'd	889-907	1137-1148	19.2-25.9
	Solution + Age	1102-1161	1280-1358	10-22
SLM IN718 [98]	As-SLM'd	830	1120	25
	Anneal + HIP	890-930	1200	27
Laser deposited IN718 [142]	As-deposited	650	1000	38
	Aged	1204	1393	13
	Solution + Age	1257	1436	13
	HIP + Solution + Age	1155	1380	20

Comparable results have been seen in other materials in the Inconel family, such as IN738LC and IN939, where solution heat treat and aging caused a dispersion of  $\gamma'$  in the material while eliminating the columnar structure, and combination with HIP encouraged further precipitation [99, 103]. In the case of the IN738LC, the solution and aged material resulted in several material properties averaging around 20% higher than cast material. Taking into account grain growth induced by conventional heat treatment routines, grains in SLM materials, (a) and (b), are still considerably smaller than (c) as-cast materials, as shown in Figure 2.16 [103]. Although some reduction is seen, anisotropy between the two primary orientations, (a)  $0^\circ$  and (b)  $90^\circ$ , is still present, which enforces the notion that post-processing techniques must be

specifically developed for SLM materials to aid in uniform grain growth and distribution. This is especially true considering that aging, and especially over-aging, can result in high losses of ductility due to the formation of the precipitates which are responsible for large increases in strength after heat treatment, and dissolution of Laves phase back into material matrix can be achieved with proper selection of temperature and time during heat treatments, thus increasing boundary and location mobility which increases ductility [21, 99].

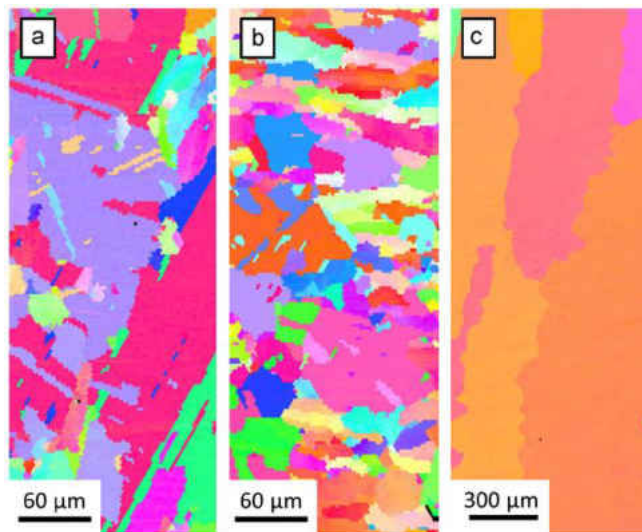


Figure 2.16 - Aging of SLM IN939 shows grain growth between (a) 0° and (b) 90° manufactured samples, though anisotropy between the two persists, and grain are still significantly smaller than (c) as-cast material [103].

Aging of as-manufactured materials has been shown to increase hardness dramatically, more so when combined with even a short solution heat treat, though the increases are less pronounced [85, 171]. An especially significant change was seen in SLM manufactured maraging steel 300, where a short aging cycle lead to dramatic increases in ultimate strength and hardness of 70% and 45% over the as-manufactured condition, respectively, but ductility was



reduced by 88%, as elongation at rupture changed from 13.3% in as-manufactured condition to 1.6% after aging [107]. There was also evidence that overaging could then lead to the decline of said material properties. A reduction in fatigue life has also been linked with precipitate growth during aging [103]. Optimized heat treatments, however, have shown the capability to practically eliminate typical SLM textures and homogenize the microstructure, including differences from orientation and subsequent directional features [172]. Moreover, the combination of optimized post-processing with optimized process parameters tested in this study showed an increase in fatigue resistance and neutralization of directional differences in fatigue life.

Despite the obvious drawbacks of the high anisotropy present within SLM structures and the benefits of the ability to reduce or eliminate said microstructural anisotropy while improving material properties, some studies have shown the ability to increase properties through gradual decomposition of precipitates while deliberately preserving the SLM microstructure [90, 105]. Such a case is seen as advantageous for creep tests, while the equiaxed structure is favored for tensile and fatigue tests. This effect is due to an interaction between the heat treatments employed on an SLM part and the processing parameters used to produce it. When IN718 parts were produced with a significantly higher powered laser (1kW in comparison to the typical 200-500W laser), heat treatment produces a different effect [90]. Short (1h) annealing treatments ranging from 550-1050°C failed to alter the as-built microstructure, though hardness and yield strength still showed a dependency on the treatment temperature, peaking at 700°C and then dropping again, though addition of an aging cycle prevents the drop and instead shows a steady increase with annealing temperature. As in other instances, the increase in strength leads to a corresponding drop in ductility, though again the combination of an aging cycle helps to improve

the ductility with increasing temperature. Creep rates were improved by an order of magnitude when comparing as-processed and aged to annealed and aged components, which is attributed to the ability of being able to preserve the microstructure even through the heat treatment. This is achieved through the use of a high power laser in combination with high temperature anneal and aging to increase strengthening phases and partially dissolve the Laves phase, the presence of which is increased by the use of a high power laser [90]. Post-heat treatment recrystallization of IN718 also shows an interaction with the scan strategy employed, as samples produced with an alternating scan path exhibited more uniform grain size and distribution than those produced with a single scanning direction, directly correlating to the distribution of residual stresses. The improved ductility of the sample produced with an alternating scan path is attributed to said increase in the homogeneity of the grain size and distribution [147]. Additionally, grain growth during post-processing heat treatments has been shown to be affected by processing parameters such as scan size and spacing, which ultimately determine the amount of overlap during each laser pass. In a study of SLM Al-12Si Prashanth et al. showed microstructures of as-manufactured components to be composed of large regions of circular morphology banded by thin regions of much finer, columnar grains [106]. This is due to the overlap between scans in the larger regions causing a partial direct heat treatment which evolves the microstructure, while the thinner, smaller grained bands remain in an as-manufactured state. When subjected to post-processing heat treatment, though both regions showed growth, the regions where overlap occurred were consistently characterized by larger grains than the thin boundary regions, which had no scan track overlap. Additionally, the increase of segregation and agglomeration of Si, which occurs with increasing temperature, is exaggerated in the scan overlap regions so that the

difference in morphology and resultant anisotropy is preserved to an extent. This is in contrast to studies such as that by Vilaro et al., where samples of Ti-6Al-4V were produced with a 50% overlap setting, so that each scan track overlaps exactly half of the track preceding it, and each track is scanned twice for a direct heat treatment effect [105]. The resultant morphologies found in the as-manufactured samples in [105] are much more uniform throughout the sample than those seen in [106] due to the difference in overlaps, and the general difference between the respective microstructures persists even after heat treatment.

As SLM technology continues to mature, it is being employed with a growing number of materials and applications. The layer-wise manufacturing method, like other AM methods, produces a distinct, columnar grain structure which can be detrimental to material properties due to intrinsic anisotropy. Proper selection of processing parameters and post-processing heat treatments can help to optimize the distribution of alloy constituents and grain sizes. This allows for production of consumer-quality components with added complexity that meet or exceed the material properties of conventionally-produced counterparts.

### **2.3 Small Punch Testing**

Small punch testing (SPT) is a testing methodology which has been experiencing wider application in recent years due to the ability to use very small, thin samples to assess the mechanical properties of a material. The method was originally developed in the 1980s by Manahan and colleagues [173, 174]. The advantages of such a test make it an attractive option for material evaluation for numerous alloys in various industries, one such being the energy industry and its many different facets, from steam to nuclear. These methods are especially

significant in nuclear power settings where many plants are reaching their end-of-life predicted ages and the long-term effects of neutron radiation are unknown [173, 175-181].

### **2.3.1 Introduction to Small Punch Testing**

As the small punch test employs very small samples, it is not only a good alternative where source material is scarce, but it is also useful in evaluating and tracking the evolution of material properties of a component that has been in service. As such, used components can be tested to gauge the effects of their working environments on the material properties, including the effects of radiation in nuclear power plants or the cyclic high-heat conditions to which a thin-walled turbine vane may be subjected. Small punch test samples are thus designed to be incised from existing structures with minimal impact to the integrity of the mechanism and with much less material than traditional testing procedures allow, giving a clear picture as to the remaining lifetime of components [9, 10].

The small punch test is designed to subject a small test coupon to combined bending and stretching. The test configuration consists of an upper and lower die to hold a small, thin sample and a punch with a spherical head or ball to contact and deform the specimen, as shown in Figure 2.17. The use of a ball in place of a machined punch allows for replacement of the ball after each test to prevent accumulation of damage to the punch affecting subsequent tests. The setup is adapted to a load frame which controls the punch displacement and measures the load,  $P$ , via a load cell, and a displacement gage is attached to accurately measure sample deformation due to displacement,  $\delta$ .

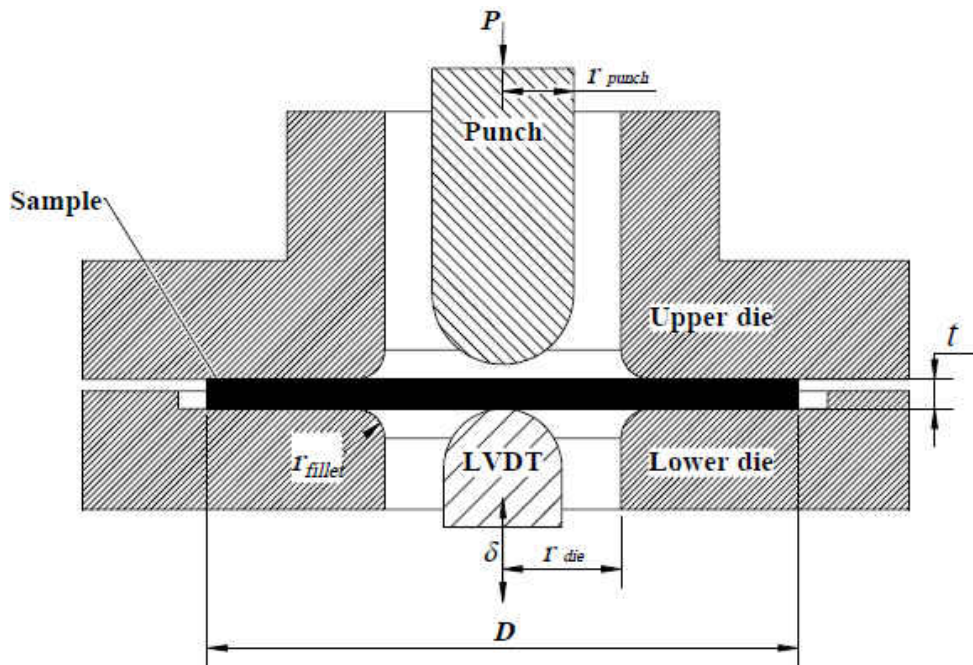


Figure 2.17 - Schematic of typical SPT setup.

The response of a small punch test takes the form of the force-displacement ( $P$ - $\delta$ ) curve. As shown in Figure 2.18, it is typically divided into four sections of distinct behavior of I) elastic bending, II) plastic bending, III) membrane stretching, and IV) plastic instability, these are typically differentiated by inflection points between the regions such as  $P_{II-III}$  [182, 183]. A fifth region is defined at the tail end of the fourth zone denoting the failure of the sample. As the exact point of failure can often be difficult to distinguish, its definition can vary from being taken as the entire region of the curve after the max load, as the region only after a certain amount of load drop, or it can occur as a sudden rupture [15, 184]. Transitions between zones of the  $P$ - $\delta$  curve are typically denoted by inflection points which are used in formulations for equating SPT results with traditional stress-strain results to acquire material properties, as will be detailed later in this

review. These include the slope of the elastic portion of the curve,  $k$ , the yield load,  $P_y$ , the maximum load,  $P_{max}$ , the deflection at maximum load,  $\delta_m$ , and the deflection at fracture,  $\delta^*$ . The response shown in Figure 2.18, however, is an idealized force-deflection curve and the divisions at which the regime changes and points of importance, such as  $P_y$ , the yield load, are not always as distinct as shown here.

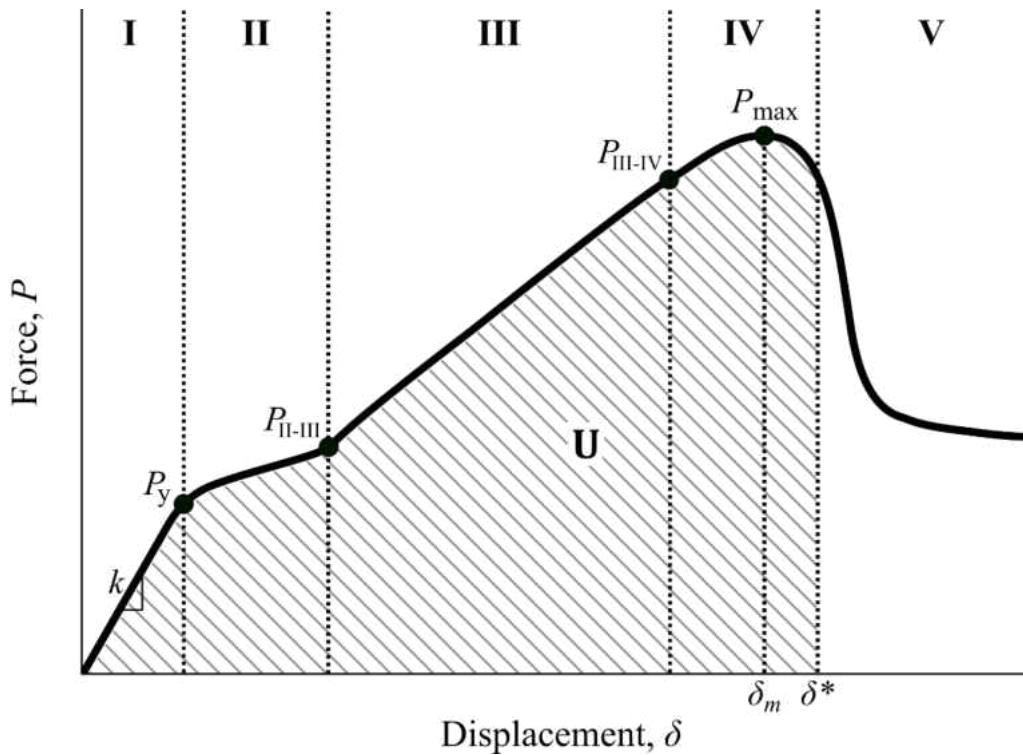


Figure 2.18 - Typical SPT load-displacement curve with important inflection and correlation points denoted.

Small punch tests are practical where source material is expensive and large quantities are hard to acquire. One such example is in the testing of precious metals, such as in testing gold alloys [11]. Cicero and co-authors utilized SPT to evaluate the tensile and fracture properties of

24 and 18 karat gold, with good agreement to results found through traditional tensile testing techniques. Small punch testing is also of interest, then, where producing samples solely for the purpose of destructive testing is costly not just in terms of material but also in manufacturing, as can be the case with samples produced via selective laser melting (SLM). Due to the high costs associated with AM material evaluation [8], utilizing miniaturized testing techniques such as SPT can cut down on costs in all aspects involved in new material evaluation, if evaluation methods equivalent to traditional testing techniques can be proven.

Traditional tensile test samples, as described by ASTM E8 [185], feature a gage section that is 50mm long and 12.5mm in diameter, for a volume of  $6136\text{mm}^3$ , without including material outside of the gage, including the radius from the gage to the support and the support sections, which can double the total length. This also means a significant amount of material is lost in the manufacturing process while grinding down the gage section of the sample. In contrast, however, SPT samples can be fabricated as square plates or thin discs, the former of which being the larger of the two with sides of 10mm and thickness of 0.5mm for a volume of  $50\text{mm}^3$ . As such, SPT samples require less than 1% of the volume of the gage section alone. Small punch tests have successfully been used to define material properties at varying temperatures, including yield and tensile strength, fracture toughness, and ductile to brittle transition temperature (DBTT), which is normally determined using extensive impact testing and consumes significant amounts of material, as well as the effects of degrading environments and varied conditions on these [186-188]. Although testing and specimen design are simplified with SPT, property acquisition is complicated by the complex states as compared to established conventional test practices, and furthermore by the differences arising from experimental design

variations [189-191]. The primary objective of current SPT research, then, is to simplify the process of acquiring material properties from small punch tests.

Given that widespread standardization does not exist for SPT, however, these methods of acquiring material properties are not as well as understood or utilized as traditional testing techniques. The only active ASTM standard for small punch testing is ASTM F2977, used for small punch testing polymeric biomaterials used in surgical implants, as a similar standard specific to ultra-high molecular weight polyethylene, F2183, was withdrawn in 2017 without replacement [192]. International standards include emergent standards or similar documents for working practices from Europe, the CWA 15627, the Chinese standard GB/T 29459, and some similar work in Japan, though no single standard is universally accepted, all three have strong similarities, and additional work has been proposed for all three to make official standards, as well as an ASTM work item for the same, WK47431 [193].

### **2.3.2 Basics of Small Punch Testing**

Although standardization of SPT is an ongoing effort, in 2004 the European Committee for Standardisation (CEN) released a workshop agreement in order to develop a set of guidelines so as to direct the growing interest of the use of SPT in a uniform manner [194]. The resulting workshop agreement, CWA 15627, which was later updated in 2007, established guidelines for testing and translation of data into tensile, creep, and fracture properties, and is more widely utilized than the other standards. The CEN code of practice recommends round specimens of 8mm in diameter with 0.5mm thickness, using a lower die opening of 4mm and a punch diameter of 2.4mm [194, 195]. These parameters are typically used in literature with some modifications



sometimes being present, such as the variation of specimen width, with 10mm round or square specimens also being common [25, 196-198]. Along with working parameters for the setup and testing of samples, the CWA 15627 also describes several relationships for relating SPT data to traditional test data. The following sections will be dedicated to exploring these relationships, among others found to be relevant by consequent research efforts.

Recent studies have shown that displacement is most accurately measured directly from the sample by placing an LVDT opposite the indenter, rather than using crossbar displacement, in order to minimize compliance effects [199, 200]. Much like traditional tensile tests, most SP tests are displacement-controlled with a constant displacement rate, which is typically recommended to be in the range of 0.2-2mm/min, though those equivalent to traditional creep tests are typically load controlled with a constant force [19, 195]. Measurement of displacement at a location other than directly below the sample, such as from the cross bar, can cause compliance errors in the resulting load-displacement curves, as shown in Figure 2.19. Although the general shape of the curve is preserved, both the load at the transition point from elastic to plastic and the total displacement are overestimated. This is due to small shifts in the load frame cross bar as it displaces, which in turn cause a shift in the resultant curve, due to the tight tolerances required for experimentation and relatively low load and displacement levels, as compared to conventional tests. Compliance effects have also been shown to be present when considering the stiffness of the loading system, frame, and geometry of the dies [195, 201]. These issues often dictate the necessity for compliance correction in the results, as will be presented in the following sections, if such is not accomplished through hardware modifications.

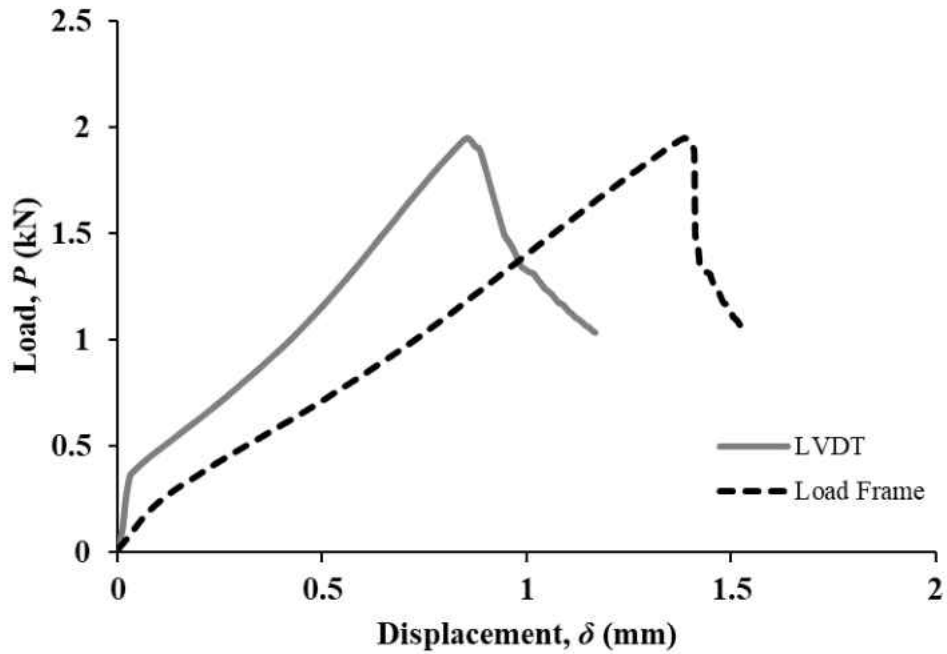


Figure 2.19 - Compliance effects in load-displacement curve from measurement of displacement via crosshead as compared to direct contact deflection transducer.

Test responses can differ strongly depending on the type of material used, how it has been treated, testing conditions, and how it behaves according to these, whether brittle or ductile in nature. As shown in Figure 2.20, load-displacement curves for brittle and ductile materials differ greatly in size and definition [202], with the sections outlined previously being somewhat more difficult to distinguish than in an idealized case, as are the relevant inflection points necessary for material property calculation to be discussed in the following sections. In these cases, as is indicated in the plot, fracture initiation occurs at very different times, whereas for the ductile case the fracture initiation is part of the stable plastic deformation regime and does not interrupt its progress, in the brittle case crack initiation also dictates peak load and failure.

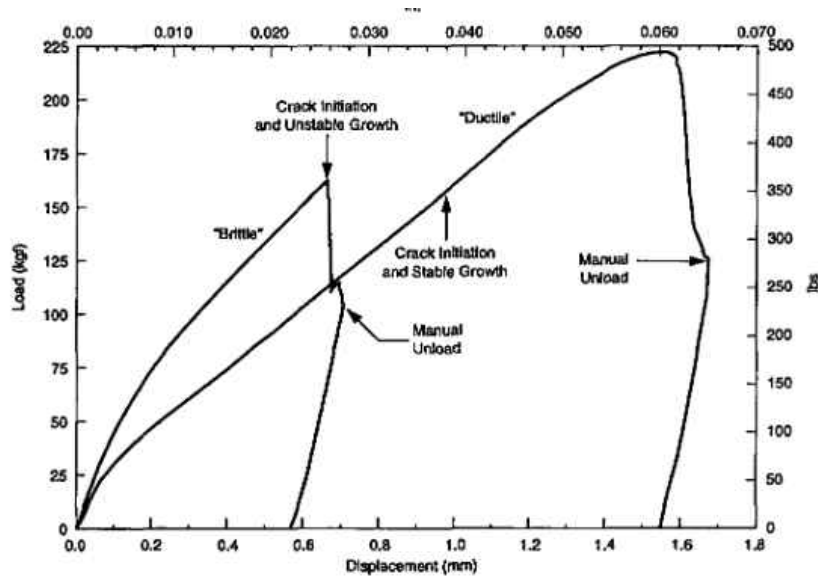


Figure 2.20 - Load-displacement response of a brittle vs. a ductile material [202]

### 2.3.3 Direct Correlation with Tensile Properties

Determination of tensile properties from small punch tests is an issue which has been of debate since the miniaturized test method was first introduced. As such, several differing approaches and formulations have been suggested and tested over the years for evaluating various material types [203, 204]. Some guidelines for testing and translation of data into tensile, creep, and fracture properties have been established [194]. The CEN CWA 15627 workshop agreement suggests several relationships for converting the load-displacement data directly into material properties typically established using stress-strain curves acquired from conventional testing. The correlations for determining material properties from small punch test data show dependencies on variables such as sample thickness, and use several inflection points of the curves, such as  $P_y$  and  $P_{max}$ , for determining material properties. These points coincide with

changes between the  $P$ - $\delta$  regimes as outlined in Figure 2.18. It has been shown [194], for example, that normalization of yielding load,  $P_y$ , by the square of the original specimen thickness,  $t$ , is a reliable method for estimating the 0.2% offset tensile yield strength via the use of a correlation constant,  $\alpha$ , e.g.

$$\sigma_{ys} = \alpha \left( \frac{P_y}{t^2} \right) \quad (5)$$

The determination of where  $P_y$  actually occurs is of some debate, with several definitions having been proposed. The various methodologies of determining the yield load are shown in Figure 2.21. These range from the use of tangents to offset displacements of 1% or 10% of the original thickness,  $t$ , with the original slope of the curve, and each method has support and contention in literature [12, 203, 205].

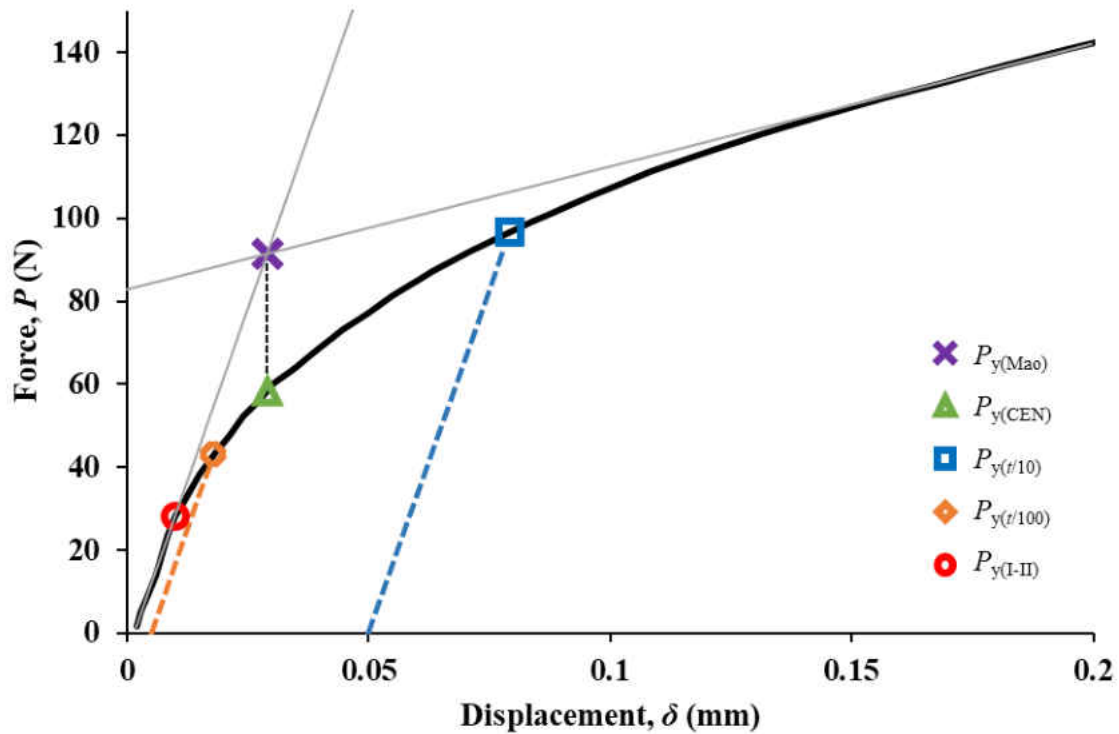


Figure 2.21 - Various methods for determining the yield load,  $P_y$ , of the load-displacement curve of SPT, created using AW6016 T4  $P$ - $\delta$  data from [206].

Mao and Takahashi [16] originally defined the location of this value,  $P_{y(Mao)}$ , by drawing a tangent of the initial stiffness and a tangent of the steady-state plastic stretching, previously defined as zone 3 in Figure 2.18, and finding the point of intersection. This method has been shown to be sensitive to material and testing conditions [207-209]; [207] presented variations of the Mao and Takahasi expression for samples which had undergone plastic deformation prior to testing which depended on whether the material had experienced tensile or compressive stresses. It is also worth noting that because of the variability in the determination of  $P_y$ , however, Isselin and Shoji proposed a method of evaluating the small punch yield using the energy up to the beginning of plasticity, known as the elastic deformation energy [208]. Determination of the

yield load has also been shown to be sensitive to experimental testing conditions, such as specimen thickness and support mechanisms [209]. Later, a new method was adapted in [194] by projecting the intersection point found by the method suggested by Mao and Takahashi vertically downwards onto the coinciding point,  $P_{y(CEN)}$ , of the load-displacement curve. Taken at a literal sense, Lacalle and co-authors suggested the use of the first inflection point,  $P_{y(inf)}$ , of the curve where zone I changes to zone II as the location where the initial stiffness changes to define the yield point [11, 210]. Finally, the offset method has been suggested akin to that which is used to find the 0.2% offset yield strength,  $\sigma_{ys}$ , on stress-strain curves, by using a straight line parallel to the initial stiffness to find the point of intersection. Different offset amounts have been suggested for use with this method, including the use of 1/100<sup>th</sup> ( $P_{y(t/100)}$ ) of the original thickness or using a larger offset of 1/10<sup>th</sup> ( $P_{y(t/10)}$ ) of the original thickness [25, 211]. Each of these is shown in Figure 2.21. Although the two-tangent method and the modified version of it are highly-cited in literature [26, 207, 212], [12, 213] show that the  $P_{y(t/10)}$  approach displays the strongest correlation with yield strength of those in Figure 2.21 when using a correlation value equal to 0.346, i.e.

$$\sigma_{ys} = \alpha \left( \frac{P_{y(t/10)}}{t^2} \right) \quad (6)$$

The constant in this relationship, like other correlation coefficients to be presented throughout this paper, are typically determined through a linear regression fit of the conventionally established mechanical properties of various materials plotted against the values of the equivalent SPT formulations, such as the yield strength plotted against  $P_y/t^2$ . Similarly,  $P_{max}$ , the maximum punch load in a  $P$ - $\delta$  curve, has been shown to have a linear correlation with

the ultimate tensile strength,  $\sigma_{uts}$ . Garcia et al. also showed that although the expression for ultimate tensile strength of

$$\sigma_{uts} = \beta_1 \left( \frac{P_{max}}{t^2} \right) + \beta_2 \quad (7)$$

and variations of it have been successfully used [11, 25, 200], a more recent expression of

$$\sigma_{uts} = \beta_1 \left( \frac{P_{max}}{\delta_m t} \right) + \beta_2 \quad (8)$$

where  $\delta_m$  is the punch displacement at maximum load, provided more accurate results when compared to conventional test [10, 12, 195, 203]. The coefficient  $\beta_1$  was found to have a value of 0.277, with  $\beta_2$  being negligible, for effective calculations with a variety of metals, including several grades of high strength, stainless, and structural steels, aluminum alloys, and magnesium alloys, and is less dependent on the material tested than the previous formulation [12, 214]. The preceding equations for determining yield strength and ultimate tensile strength can then be used with the Ramberg-Osgood hardening law in order to determine the hardening exponent,  $n$ , and generate true stress-strain data [215].

As achieving consistent, uniform thickness for numerous samples can be difficult on such a small scale, and due to the high effect of thickness variations on resultant SPT curves and material property calculations, Lacalle and co-authors proposed a normalization process to reduce the effect of varying thickness on results from otherwise identical samples [19, 198]. While the expression describing the earlier part of the curve stems from plate plasticity theory [216], it was determined that the normalization equation needs to be split into two regions, as

SPT curves generally deviate from plate theory behavior at the inflection point,  $P_{II-III}$ , where deformation transitions from plastic deformation, zone II, to membrane stretching, zone III. The expressions were proposed which can normalize test loads,  $P_{test}$ , to loads from a theoretical sample with a thickness of 0.5mm,  $P_{0.5}$ , regardless of actual sample thickness,  $t$ , for more direct comparison between curves, and with increased accuracy in the latter part of the curve [198, 207, 217], e.g.,

$$P_{0.5} = 0.5^2 \frac{P_{test}}{t^2} \quad P_{test} < P_{II-III} \quad (9)$$

$$P_{0.5} = 0.5 \frac{P_{test}}{t} + \frac{0.5P_{INF}(0.5 - t)}{t^2} \quad P_{test} > P_{II-III} \quad (10)$$

Presumably, all further calculations conducted with these normalized curves would assume a sample thickness of 0.5mm and have an ingrained adjustment on the determination of the  $\sigma_{uts}$  from  $P_{max}$  due to the expression for the latter part of the curve. Comparison through normalization of the curves in [198] also facilitated the deduction of the influence of sample or material orientation, which is especially relevant to anisotropic materials, and which was shown to be highly influential.

The theory of plates [218] has also been used to describe correlations very similar to those previously presented, along with a method of finding Young's modulus,  $E$ , which involves a summation of the different stiffness values of the various components of the SPT rig and the sample itself [11]. This is in line with an expression presented by Giddings and co-authors, who used a straight-forward methodology involving an FEA model to determine the correlation



between the initial stiffness of the load-deflection curve and the Young's modulus [13]. The small punch test technique was combined with various previously validated finite element models to evaluate the evolution of the Young's modulus of polymethylmethacrylate (PMMA), a commonly utilized bone cement, under varying conditions and temperatures. The equation directly relates  $k$ , the initial stiffness in the  $P$ - $\delta$  curve, to  $E$ , the Young's modulus, via,  $\lambda$ , a proportionality constant related to Poison's ratio and the frictional characteristics of the material in question. This relation was later normalized by dividing the initial stiffness,  $k$ , by  $t$ , the original specimen thickness, to mitigate differences to the resultant Young's modulus stemming from variations in sample thickness and produce more accurate correlations [15, 213, 219], e.g.,

$$E = \lambda \left( \frac{k}{t} \right) \quad (11)$$

Although the proportionality constant,  $\lambda$ , has shown some material dependence, a proportionality constant suitable for a variety to of metals may be found by using a similar fitting methodology with the SPT responses and Young's moduli of several materials together, as was done to determine constants in relationships described earlier. The tensile elongation of ductile materials has shown direct correlation with the displacement at maximum load, but has also shown high material dependence, and a universal correlation factor with a good fit was not found [12, 25, 30, 220]. To circumvent this issue, Chica et al. suggested introduction of an unloading/loading cycle to the SPT, and using the slope of this factor to determine the Young's modulus, as the initial portion of the curve,  $k$ , can be affected by the plasticity properties of a material [221].

Case studies on a unique material processing method, powder metallurgy, which uses powdered metal product pressed into component shapes followed by a sintering process, have been conducted by utilizing some of the aforementioned relationships [29, 222]. The nature of this manufacturing process leads to variability in the mechanical properties within components due to the variation in porosity and cooling rates of the different regions of the component [223, 224]. The inherent porosity usually leads powdered metal products to be considered as brittle, in comparison to conventionally produced materials, as reflected in the SPT response shown in Figure 2.22, with comparison to a common structural steel [30]. The fracture patterns in these two samples are very distinct, with the powdered metal fracture occurring and growing radially from the center of the sample as it was continually displaced, and the structural sample tearing around the center of the sample, growing as this area continuously stretches and thins with displacement.

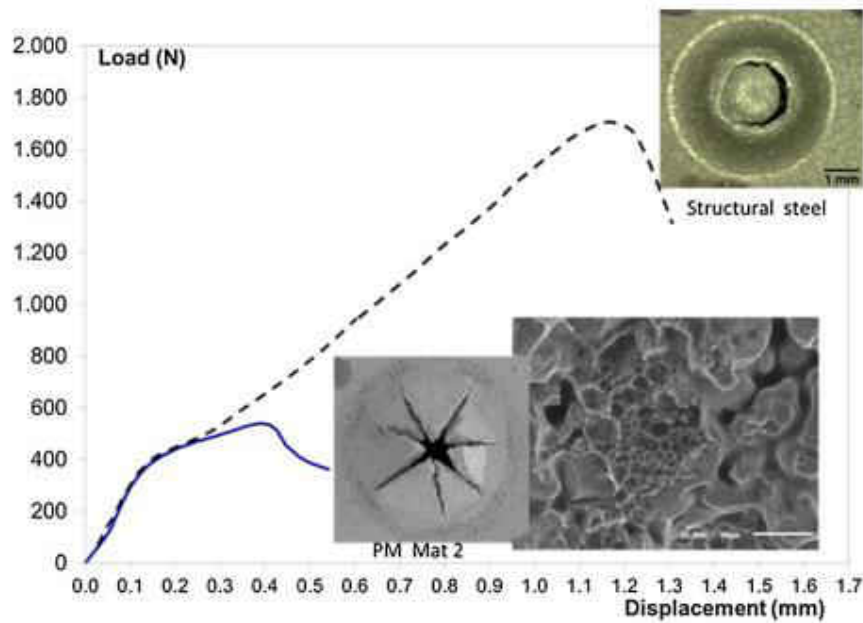


Figure 2.22 - Comparison of SPT response and fracture of powdered metal as compared to structural steel [30].

The analyses carried out in the canon of literature of SPT show that regressions comparing tensile and SPT results using the linear correlations presented earlier had an 80-90%  $R^2$  correlation fit for the yield strength, ultimate strength, and elongation. A slight adjustment to the constants provided an even more accurate fit, inclusive of the data presented in that work and the present study. It is also worth noting that SPT samples extracted from several different positions of the powdered metal bars produced for the acquisition of both SPT and tensile test samples for the present study correlate to the variability in porosity of these mentioned earlier. As such, even in a porous material, an SPT sample serves as a valid representation of a component, or even a localized region, and the strength variations associated therein. This is of critical interest when considering functionally graded or directionally dependent materials such as those produced with additive manufacturing techniques [25, 26, 222]. Additional support for analyzing these types of materials was shown by testing IN713C cast samples with columnar grain structures which displayed directionally dependent material properties and fracture behaviors, akin to those in additive manufacturing materials [184].

### **2.3.4 Creep Testing**

A variety of studies have leveraged the SPT to procure creep deformation and rupture properties of materials [18, 225-228]. Creep, which is a monotonic test, features a constant load application at elevated temperatures for prolonged periods. Milicka and Dobes established the existence of a linear correlation between the force of small punch creep tests and the stress from conventional creep tests which resulted in an identical time to rupture [19, 226, 227]. Strong dependencies of the rupture time on testing conditions such as sample thickness, load level, ball

diameter and type, temperature, and atmosphere have been shown; in the case of sample thickness, for example, achieving a similar time to rupture as a 0.3mm thick samples with a 0.6mm sample required over double the applied force [18, 19, 228-230]. As such, it was established that the stress in a conventional creep test and the force in an SPT creep test can be relate linearly with the use of a proportionality constant for a material at a certain temperature. A correlation has been developed between the small punch creep results and the conventional creep results as a ratio,  $\Psi$ , of the SPT force divided by conventional stress combined with the deflection at fracture, giving the relationship

$$\Psi = \frac{P}{\sigma} = \left[ \frac{A_C}{A_S} \right]^{1/n} \quad (12)$$

where  $P$  is the constant force applied during the small punch test,  $\sigma$  is the stress from the conventional test results, and where the constants  $A_c$ ,  $A_s$ , and  $n$  are described by the following relations which are driven by the time to fracture,  $t_F$ , and combine the power law and the Arrhenius exponential law [226], i.e.,

$$A_C = \frac{t_F}{\exp\left(\frac{Q}{RT}\right) \sigma^n} \quad (13)$$

$$A_S = \frac{t_F}{\exp\left(\frac{Q}{RT}\right) P^n} \quad (14)$$

In these equations,  $Q$ , the activation energy in kJ/mol, and the stress exponent,  $n$ , preserve their value across conventional creep tests and SPT. The variable  $t_F$  represents the time

to fracture, which needs to be identical for both tests for the validity of the formulation,  $R$  is the universal gas constant, and  $T$  is the absolute temperature. A modification to Equation 12 was made substituting  $P$  with  $(P/\delta^*)$ , where  $\delta^*$  is the deflection at fracture, reduced results dispersal of the ratio  $\psi$  as it accounts for variability in ductility of the material and thus it was suggested that the force in the SPT divided by the deflection at fracture is proportional to stress in a conventional creep test [226]. Additional modifications were suggested for compensating for differences in temperature, which produced high overlap of the time to fracture between conventional and SPT creep tests.

The CEN workshop agreement [194] established guidelines for exploring creep properties using SPT based on the theories established by Chakrabarty on the stretching of materials over hemispherical punch heads [231, 232]. This equation, which correlates the force of the small punch test,  $P$ , to conventional creep stresses,  $\sigma$ , which was previously defined as the ratio,  $\Psi$ , is given as

$$\frac{P}{\sigma} = 3.33k_{sp}r_{die}^{-0.2}r_{punch}^{1.2}t \quad (15)$$

where  $r_{die}$  is the radius of the opening of the lower die,  $r_{punch}$  is the radius of the punch,  $t$  is the thickness of the sample, and  $k_{sp}$  is a creep correlation factor. The constants were established through a regression fitting of several tests conducted via round robin. The correlation constant  $k_{sp}$  can be assumed to have the value of 1 initially, though to get a more accurate result a comparison with conventional uniaxial testing must be done [9, 194, 231]. It is worth noting that often the calculation of  $k_{sp}$  yields values which do not deviate very much from unity, and as such use of the value of 1.0 can give reasonable estimates [233]. Utilization of this formulation aids in

selection of the load,  $F$ , when designing SP creep tests with an equivalent time to rupture as a conventional creep test conducted at stress level,  $\sigma$  [9]. This method has also been shown to be reliable via verification using the Larson-Miller and Orr-Sherby-Dorn parameters to establish the same relationship [197].

The relationship established by CWA 15627 has been used in several subsequent studies. Zhao et al. used SP creep tests at 650°C with a constant load ranging from 225 to 350N on four different zones in a P92 chromium steel welded joint to explore deviations in the weld area [27]. Comparisons between SPC results and conventional results as well as FEM results showed good agreement. Small punch creep results have been shown to be representatively equivalent to conventional creep results, with bending being the principal mode of deformation in the primary creep region, while the secondary and tertiary stages are mostly characterized by membrane stretching [228, 234].

The SPC test and the relationship between SP results and creep stress have been shown to be effective for unique materials as well. Adaptability and suitability of use with single crystal and anisotropic materials has been shown, though with some limitations; directionality and temperature have been shown to affect correlations [201, 233, 235]. A study by Bruchhausen et al. also utilized the  $k_{sp}$  relationship, but with directionally different materials and noted differences based on the testing direction in reference to the extrusion direction [233]. Due to the material anisotropy the  $k_{sp}$  value was left at 1.0, as there was difficulty in evaluating the longitudinal material direction, due to the biaxiality of the stress field in SPT. The anisotropy is evident in the SPT creep results, and neither data set matches directly with traditional tests. This study also showed that SPT results follow the Monkman-Grant relationship, while others have

shown that the Larson-Miller law and Dorn equation for calculating load exponent and activation also work well [19, 227, 228, 233, 236]. Additionally, the Wilshire rupture model and logistic creep strain prediction equation have been used in conjunction to a high degree of accuracy [237].

### 2.3.5 Fracture Properties

Several formulations have also been proposed to estimate the fracture properties of materials from SPT results. Primarily, the methodologies relevant to determination of fracture properties stem from the utilization of an equivalent fracture strain for membrane stretching of blanks over a rigid punch. The equivalent fracture strain, proposed by Chakrabarty [232] and confirmed by several researchers [16, 176, 180, 238, 239], is defined as

$$\varepsilon_{qf} = \ln\left(\frac{t}{t_f}\right) \quad (16)$$

where  $t$  is the initial sample thickness and  $t_f$  is the final sample thickness in the area in which fracture occurred. As with others, a linear relationship was established with the fracture toughness by testing of specific materials such as different grades of CrMo alloys and carbon steels [239-243] or with several different materials such as in [12] using the equation for equivalent fracture strain which utilizes direct measurement of sample thickness at the fracture, given as

$$J_{IC} = A\varepsilon_{qf} + B \quad (17)$$

The relationship, with constants  $A$  and  $B$  of 1695 and -1320, respectively, was considered valid for alloys with an SPT biaxial strain at fracture,  $\varepsilon_{qf}$ , of greater than 0.8, though it was not considered valid for brittle materials [12]. However, measuring sample thickness at fracture can be difficult to accomplish and lead to inaccurate results. As such, the equation for equivalent fracture strain was used by Mao et al. [16, 239, 244] to develop the expression

$$\varepsilon_{qf} = \ln\left(\frac{t}{t_f}\right) = \beta\left(\frac{\delta^*}{t}\right)^p \quad (18)$$

where  $\beta$  and  $p$  are constants determined to be 0.09 and 2.0, respectively, for a disc with a diameter of 3mm and thickness of 0.25mm, and  $\delta^*$  is the deflection at fracture of the sample center, as shown in Figure 2.18, sometimes correlating to the maximum load, and thus  $\delta_m$ . These expressions can then be used to solve for fracture toughness,  $J_{Ic}$ , as established by Mao, which takes the form of Equation 17 but with first and second constants valued at 345 and -113, respectively, and applying to a range of materials [16, 239]. However, Kumar et al. [245] established quadratic equations for determining the value of constants  $\beta$  and  $p$  dependent on the original sample thickness,  $t$ , to determine the equivalent fracture toughness,  $\varepsilon_{qf}$ , by testing various thickness samples using an FEA analysis and implementing an exponential fitment curve. Comparative fracture toughness results for 2.25Cr-1Mo between the original constants determined by Mao and those determined using the quadratics established by Kumar et al. showed a reduction in error of 8-20% over Mao's constants using the quadratic constants when the fracture toughness obtained was compared to that found using CT specimens.

Ha et al. [186] tested the methods of Joo et al. and Afzal Khan et al. [246, 247], the latter of which is an Elastic-Plastic Fracture Mechanics (EPFM) approach, involving the calculation of



the energies of the different stages of deformation seen depicted in an SPT curve. The EPFM approach, though rather complicated in its formulation, gave results consistent with those found using Charpy impact tests. The methods presented by Joo et al. were shown to work consistently for materials in cold conditions to estimate fracture toughness, specifically once the material has crossed below the ductile to brittle transition temperature, but not for ductile materials [186, 246]. A sharp-notched central pre-crack of length  $a$  was introduced into the design of the SPT specimen while applying this methodology, as seen in Figure 2.23(c) and was successful in creating a stress concentration to replicate results congruent with those in other studies for the lower shelf energy region [248]. This method showed accuracy dependency on temperature and thickness, and has the disadvantage of having to know the point of crack initiation, which can prove to be of some difficulty with SPT. Similarly, Tanaka et al. utilized CrMoV cast steel SPT specimens with fatigue pre-cracked center notches to evaluate fracture toughness at high temperature [249]. In this study, electrical potential drop was used to indicate the beginning of unstable crack growth to determine the load at crack initiation, though locating the inflection point of the electrical potential curve proved difficult. Additionally, this method utilized FEA to obtain fracture toughness from the SP test using master curves of creep damaged materials. This requires previous knowledge of the material from tensile testing to program the behavior into the FEM analysis to produce said master curves. It was also noted that this method may be dependent on the toughness of the material, as high fracture toughness correlated with high error.

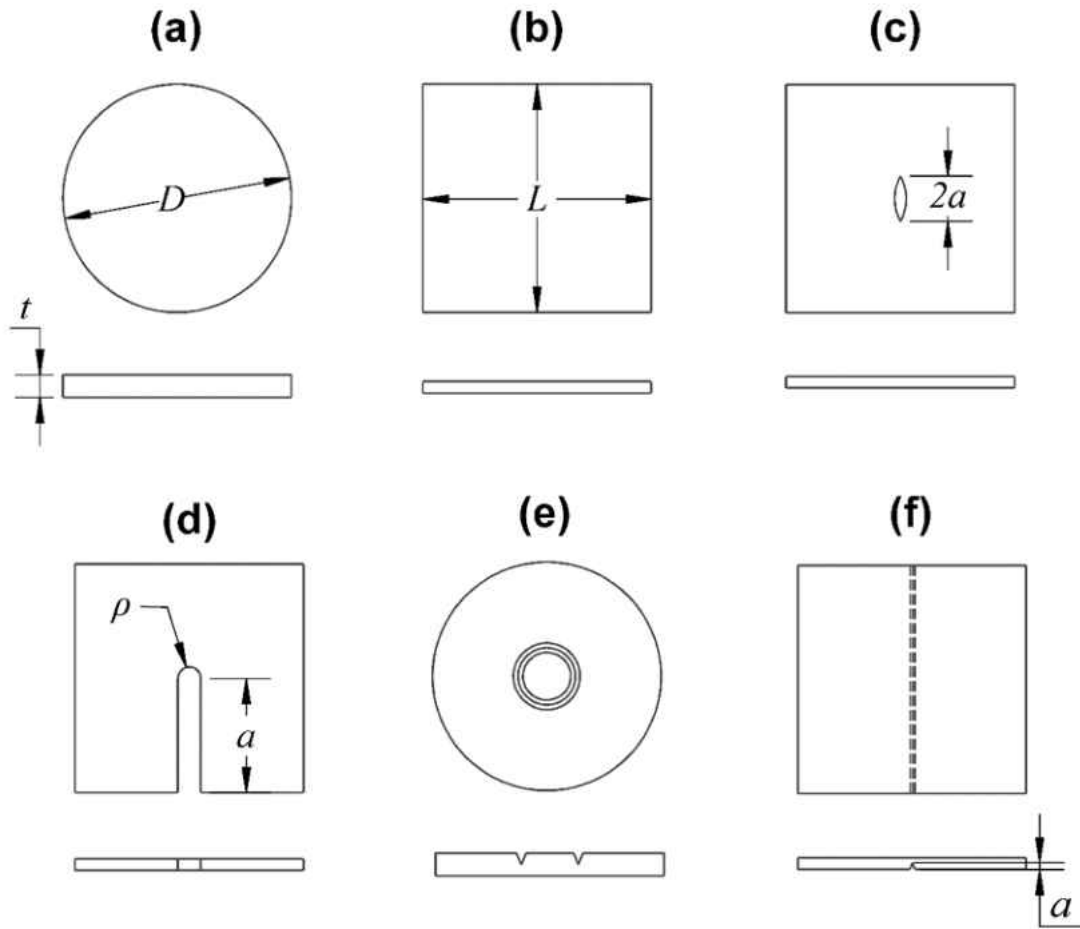


Figure 2.23 - Examples of specimen geometries utilized in SPT fracture studies including (a) standard round, (b) standard square, (c) central notched [248], (d) single edge notched [250], (e) circumferentially notched [251], and (f) lateral cracked [252].

Concurrently, Lacalle et al. developed a method based on traditional fracture testing standards using SPT samples with a simple lateral notch along one edge, similar to a single-edge notch tension test (SENT), of varying lengths in order to obtain the *J-R* curves [250, 253, 254]. This method was later verified by [196]. A sketch of the samples used, which are of the common configuration of 10x10x0.5mm, is shown in Figure 2.23(d). The initial notch length, *a*, is varied from 4-6mm in length, and the radius,  $\rho$ , was around 75-100 microns, and was cut using a laser

micro-cutting technique. Using this method the areas under the various curves corresponding to the different length of cracks are measured to obtain a set of J-integral values defined as

$$J = \frac{CU}{tb} \quad (19)$$

where  $U$  is the strain energy under the curve of interest,  $t$  is the specimen thickness,  $b$  is the remaining width from the tip of the crack, and  $C$  is a coefficient of material flow stress and notch length with a built-in geometry dependent factor [11, 250], e.g.,

$$C = 0.12 + \frac{58(a - 3.0)}{\sigma_Y} \quad (20)$$

Here  $\sigma_Y$  is the flow stress, given in MPa, and the expression  $(a - 3.0)$  is the effective notch length in mm calculated by subtracting the part of the specimen clamped by the dies from the total notch length. The flow stress is calculated as an average between the yield stress and ultimate tensile strength. Figure 2.24 shows a comparative response between two samples with varying initial notch lengths of  $a_1$  and  $a_2$ , with strain energies of  $U_1$  and  $U_2$ , respectively. Using the differential area between two subsequent curves, valued as strain energy, with different initial crack lengths gives the energy to extend the crack from one size to the next, taking the point of maximum loading to be the moment of fracture [196]. Calculating the strain energy to get from one notch to the next notch, that is, with two otherwise identical specimens with differing crack lengths to obtain the  $J$ -integral values, a composite fit curve can be fit to the plot of the  $J$  data points, which has been shown to correlated well with conventional results [196, 250]. This method has been used to find the fracture resistance of materials under plane stress to be verified,

or analyzed for the first time for materials which are more difficult to procure enough of in quantities sufficient for traditional methods, such as gold and its alloys [11]. A study utilizing nanocomposite films used the area under the load-displacement curve up to the break point to estimate the fracture toughness, with acceptable results, though the samples in this study did not utilize the multi-specimen approach, which is key to accurately modeling the  $J$ - $R$  curve to estimate fracture toughness [219]. In a study [196] comparing the SENT method with two others, the SENT method proved the simplest and most reliable, minus the drawback of requiring multiple specimens with different crack sizes. The other two methods, though also providing reasonable results, had significantly greater drawbacks. The first, based on crack tip opening displacement formulations, required multiple interruptions of tests to find the exact instance of fracture initiation and SEM access to measure crack opening. The second is based on using complex numerical simulation methods employed for simulating traditional notched fracture samples to calculate the  $J$ -integral which requires large deformations and therefore extensive calculations.

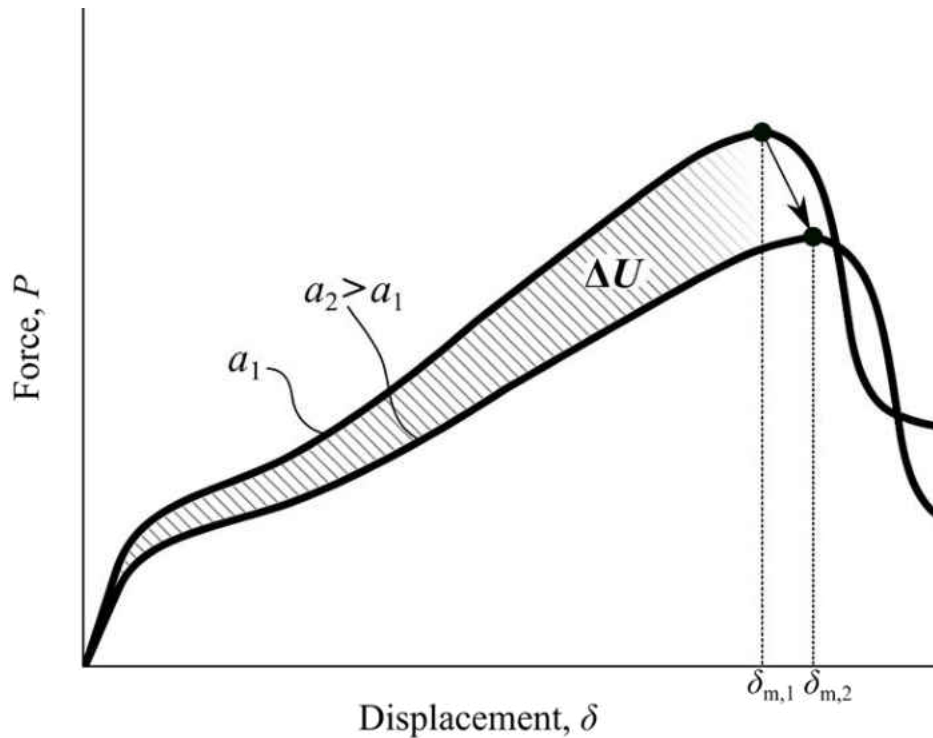


Figure 2.24 - Energy difference method for calculation of  $J$  integral.

Several other notched specimen types have also been proposed to characterize fracture strength using SPT [217, 251, 252]. In order to overcome the limitation presented by the SENT method of representing only situations of plane stress, Turba et al. [251] presented a new style of circumferentially notched SPT specimen, the details of which can be seen in Figure 2.23(e). This design is purported to approximate a plane strain condition for materials which exhibited fully brittle fracture, rather than ductile or mixed-mode fracture. Fracture energy in this case was measured up to a displacement corresponding to a 20% drop from the maximum load, which was where the specimen was considered as fractured. The main limitations of the circumferentially notched specimen are the presence of mixed-mode loading as opposed to pure Mode I loading and the difficulty presented in introducing a fatigue pre-crack to improve said limitation. Cuesta

and Alegre [252] conducted a study using a Charpy-like laterally pre-cracked specimen along with FE models to numerically simulate the pre-cracked specimen to obtain estimates of the fracture toughness, the geometry can be seen in Figure 2.23(f). Although complex, due to requiring varying depth cracks and extensive modeling, results were found which were within the valid variability range established by Charpy impact tests. A subsequent study from Cuesta et al. [217] using similar specimens showed the effects of crack shape and quality on the results. Although the methods did not have a direct effect, the overall shapes of the cracks and their uniformity affected the repeatability and quality of results, emphasizing the need for accurately machined pre-cracks with high stress concentrations to increase reliability. Further complications arise when considering the numerous notched samples proposed, as notch configuration, size, tip radius, and quality affect the fracture response, and furthermore the severity of the response is dependent on sample thickness [255]. A study by Martínez-Pañeda et al. studied the effects of notch configuration and quality, as imparted by the chosen machining method, while also introducing a cross-notched configuration derivative of that shown in Figure 2.23(f), where another crack is machined perpendicular and centered to the lateral crack shown [255]. The different configurations were also modeled to study the damage behavior for the use of determining Gurson-Tvergaard-Needleman model constants.

A thorough literature review by Abendroth et al. also noted significant contributions by several other researchers to this area of SPT research [256-258]. Misawa et al. determined a linear relationship for fracture toughness similar to those noted earlier in this article, in which the single constant relating  $J_{Ic}$  to the equivalent fracture strain is both material and geometry dependent, and has units of  $\text{kJ/m}^2$  [256]. Other notable contributions include calculation of  $J_{Ic}$

and ductile-to-brittle transition temperature via the use of the calculated small punch energy by Bulloch, similar to the work cited earlier by Alegre et al [258]. Abendroth et al. were then able to propose a parameter identification process with FEA and constitutive material models to describe both ductile and brittle behaviors, one of the few processes to claim as such [257]. Brittle materials were evaluated using a Weibull statistical failure analysis, which was shown to be effective with varying compositions of carbon bonded alumina ceramic.

A study by Altstadt et al. [24] on oxide dispersed strengthened steels using SPT showed the effects of anisotropy on fracture results, which is especially relevant so SLM materials. The anisotropic nature of the crystal growth leads the material to act like a layered structure, with different directions behaving differently under SPT loading. This study showed that when loading direction was parallel to each layer the layers would delaminate, while samples loaded perpendicular to layers tended to arrest growth of the crack each time in encountered a new layer. This translates to the load peaking, dropping suddenly, and then continuing to rise, often repeating this behavior multiple times. Results from this investigation arising from this behavior led to the determination of transition and ductile-to-brittle transition temperatures to be inconsistent from traditional results with SP tests yielding much higher transition temperatures, with differences over 400°C present. The effects of these behaviors on determination of other material properties are unclear.

Overall, SPT has been shown capable of characterizing the fracture behavior of various materials. Results show sensitivity to microstructural differences, and test results display response to differences in sample temperature and thickness. Samples with machined or fabricated fracture notches show some promising similarities to traditional notched sample

testing, but dependence on material type and condition as well as sample geometry and preparation makes these approaches less reliable. Though a large body of literature exists, direct inferences on fracture behavior have been shown to be highly dependent on several factors, and as such various approaches have been studied, though no single method has strong confirmation, making direct correlations with conventional results difficult.

### 2.3.6 Shear Properties

A variant of the SPT is utilized for determination of shear properties which utilizes a flat punch rather than the typical rounded punch, known as shear punch testing (ShPT), and was derived from blanking operations used for metal forming [259, 260]. This varies slightly from the small punch test, which is the primary focus of this paper, when considering formulations for determining material properties from ShPT test data, but has been shown analogous to uniaxial tension [260]. While the dimensions of most of the components are typically very similar, the rounded punch or ball is replaced with a flat punch of the same diameter which causes the primary deformation mode to be one of shearing in the sample along the edges of the punch. The shear stress,  $\tau$ , can be calculated from the load-displacement data as

$$\tau = \frac{P}{2\pi r_{avg} t} \quad (21)$$

Where  $P$  is the applied load,  $t$  is the initial specimen thickness, and

$$r_{avg} = (r_{punch} + r_{die})/2 \quad (22)$$



where the variable  $r_{punch}$  denotes the radius of the circular, flat-tipped punch, while  $r_{die}$  represents the radius of the opening of the lower die. This method of calculating shear stress from shear punch data is widely utilized in literature as providing accurate results [175, 260, 261]. This is one of the more straightforward conversions of punch test data to traditional data that is reliably present in literature. Conversion of load-displacement data to shear data via the use of this equation allows for more direct calculation of material properties in shear.

Linear relationships have been proposed for determination of tensile properties such as yield strength, ultimate strength, and strain hardening exponent from shear punch testing [262, 263]. It has been agreed upon that a linear relationship exists between the primary yield point of the shear-displacement curve and that of the tensile yield strength. However, such as is the case with the small punch test, the determination of where the yield point occurs is a topic of considerable debate, with a few methodologies having strong experimental support behind them. The relationship for determining the tensile yield strength,  $\sigma_{ys}$ , from the shear-displacement curve can be given as

$$\sigma_{ys} = \alpha\tau_{ys} \quad (23)$$

where  $\tau_{ys}$  is the shear yield determined from the shear-displacement curves developed from the force-displacement results using Equation 21. The primary method used for determining the point of shear yield was by using the point of first linear deviation from the shear-displacement graphs as the point where shear yield occurs [264, 265]. This method, however, is somewhat arbitrary and the point is not always well defined, making this method difficult to use. Consequently, after a redesign of typical SPT fixtures incorporating some compliance correction

by adjusting the location of displacement measurement, a 1% offset shear strain method was suggested for defining the shear yield stress, where the shear strain,  $\gamma$ , can be calculated as

$$\gamma = \delta/c \quad (24)$$

where  $\delta$  is the punch displacement and  $c$  is the clearance, defined as the difference between the radii of the punch and die when using a flat-faced shear punch [263]. This method showed a marked improvement when compared to FEA simulation results relative to older methods [199, 263].

Guduru et. al tested various alloys and suggested a variation to the 1% offset shear strain method previously used [261]. In order to mitigate sample thickness effects associated with this method, they implemented a normalization factor when plotting the shear-displacement curves, normalizing the displacement by dividing it by the sample thickness and using a 1% offset to find the corresponding yield point. The correlation constant was then found by plotting the known 0.2% offset yield stress values of the various metals tested versus the shear yield values found with SPT. A correlation value of 1.77 was determined, so that the equation for correlating tensile yield stress and shear yield stress begins to approximate the von Mises yield criterion which utilizes a correlation factor with a value of 1.73 when the deformation mechanism is dominated by shear. Later, FEA models were similarly utilized to support this correlation against experimental results by using the von Mises yield criterion as a basis for comparison. FEA results indicated that much smaller offsets were necessary, with the difference between the correlation factor found and that given by the von Mises yield criterion being attributed mainly to compliance effects from the SPT test rig [266, 267]. Originally, experimenters incorrectly

assumed the crosshead displacement correlated with the punch displacement. It was later shown that flex in the components of the load frame and of the small punch apparatus actually invalidate this assumption, and SPT force-displacement curves had to be offset in order to mitigate punch compliance effects [265]. As such, a measurement device was placed parallel to the punch in later studies, which helped to mitigate these effects which were especially apparent in high strength materials [261, 263].

Additional support was given by SP testing electrodeposited copper samples, the properties of which were not included when determining the correlation factor or the subsequent FEA analysis, and comparing values determined using the correlation factor of 1.77 to miniaturized tensile testing results [266]. The correlation factors used for calculating tensile yield and ultimate strength produced values that were within 6% of the measured values from tensile tests [266]. It was later shown that compliance issues could be further eliminated by measuring the displacement of the sample itself, as it is represented in an FEA [264, 265]. As was the case for the small punch test, this was accomplished by locating a linear variable differential transformer (LVDT) directly below the sample, and was shown to be highly successful [199, 200]. In fact, in the case of the shear punch test, the offset using this correction with additional information gleaned from elastic loading tests reduced the necessary offset to 0.2%, matching earlier FEA simulations and changing the linear relationship definition to one which matches the von Mises shear yield criterion [199, 266, 267], e.g.,

$$\sigma_{ys} = 1.73\tau_{ys} \quad (25)$$

Similarly, a linear relationship has also been determined for calculating the ultimate tensile strength. A relationship was proposed stemming from the manufacturing process of blanking to which the shear punch test is akin, where the maximum shear load was related to the ultimate tensile strength by way of a factor dependent on the strain hardening exponent [268, 269]. However, this required previous knowledge of the strain hardening exponent in order to be utilized, typically requiring tensile tests to characterize, thus rendering the ShPT redundant. Subsequent studies eliminated the need for previously established constants and proposed a more direct relationship [199, 269, 270]. This relationship can be expressed as

$$\sigma_{uts} = \beta \tau_{uts} \quad (26)$$

where  $\tau_{uts}$  is the ultimate shear stress value, the maximum load determined from the shear-displacement graph and  $\beta$  is the correlation factor. This equation is an adjustment from the original which included an additional offset parameter on the right side, to improve the overlap between shear punch and conventional uniaxial data and which varied with the class of alloy [264]. This offset parameter was subsequently eliminated by the aforementioned correction of compliance issues which made the data sets from SPT and conventional tests overlap more accurately [262, 263]. In [261], experimentation with a variety of materials led to a suggested universal correlation value of 1.8 for the constant  $\beta$ . Subsequent support showed that this correlation also works well for a material not included in their primary study, electrodeposited Cu [266]. Other studies, however, while confirming the form of the relationship, found differing correlation constants for the UTS relationship based on the material, and the use of a single constant for all materials provided unreliable results [179, 199]. Rabenberg et al., for example,

found correlation factors for the shear yield and ultimate shear strength of 1.5 and 1.4, respectively, in addition to utilizing a 2.2% offset to determine the shear yield point, all of which differ from several studies presented earlier, though it falls within a large range that they found present in literature [179]. Their correlation factors were established through a series of tests with samples of aluminum, stainless steel, and Inconel of varying treatment conditions, and validated with irradiated 304SS; however, the LVDT used in this study to measure displacement was attached to the crosshead, rather than below the sample, which lends credence to the higher need for compliance correction, as seen in works cited earlier.

### **2.3.7 FEA of SPT**

Finite element models and simulations of small punch tests have been extensively utilized to validate SP tests in order to evaluate material properties. Many of the studies reviewed have utilized FE models to varying degrees in order to acquire results and material correlations. Though some investigations utilize 3D models, 2D axis-symmetric models have been shown to be sufficient for most studies [271]. Simulations are often employed to determine material properties via the inverse method. The FEA for the solution of the inverse problem involves using the results of SPT to inversely solve for the stress-strain curve. A simulated SPT curve is assembled in a piecewise manner using assumed values for material model constants, adjusting them iteratively until the curve up to a particular point matches that of the experimental output. This is repeated until the output of the simulation matches that of the experiment, after which the acquired curve can be used to characterize an equivalent stress-strain response and thus establish material properties. Efforts have been made to speed the curve-fitting optimization process using

a number of different algorithms to calculate the numerous iterations, including least squares, neural networks, and pattern searches, among others [272-275]. This approach is often useful when not much is known about the material. Husain et al. used this iterative approach on the elastic portion of SPT curves to determine the elastic moduli and corresponding stress-strain relationships of three different steels, with promising results versus traditional tensile tests [276]. A comprehensive study using the inverse method was conducted by Campitelli et al. in order to assess the true stress-strain relationship [277]. The model which was developed showed the necessity for splitting the strain hardening into two stages for increased accuracy. The importance of the effects of compliance, friction, specimen thickness, and constitutive modeling were all verified. A model constructed by Egan et al. showed the importance of basing material property variance based on deformation shape [272]. The elastic-plastic behavior was found via three plasticity coefficients which were optimized using a pattern search curve fitting algorithm, cutting down on manual computation efforts. Similarly, Linse et al. combined the computing power of neural networks with an optimization routine using an axis-symmetric model for the prediction of load-displacement curves by limited variation of material properties [273]. Results for identifying the hardening coefficients of reactor vessel steels with the optimization routine showed results correlated well. A study using PMMA bone cement by Giddings et al. corroborated the findings of previous studies to evaluate the relationship between the initial stiffness of the SPT test and the Young's modulus by varying the value of the modulus and the corresponding set of initial stiffness values [13]. The proportionality constant was found by utilizing an FEA model with an assumption of the Poisson's ratio value and variation of the elastic moduli to note the initial stiffness then applying a least-squares fit. In this way a

correlation factor between the two was determined for future predictions. This same method has been used with metals as well [278]. Kim et al. found correlation factors for determining the yield strength, Young's modulus, and hardening coefficient [212]. A comprehensive study conducted by Garcia et al. on determination of correlation factors for SPT to mechanical property relationships utilized a FEA model to evaluate several points on the force-displacement curve to find the best fit for the correlations for calculation of yield and tensile strengths [12]. This study extended into determining a correlation coefficient for fracture toughness for ductile steels. Additionally, Guduru et al. and others have used correlation simulations to find correlation factors between the shear strength data produced using the shear punch test and tensile strength and yield strength [261, 266, 267, 269, 270].

Simulations have also been used for evaluating creep properties in SPT, with suitable correlation to traditional creep tests having been found. Simulations, like traditional tests, have primary, secondary, and tertiary stages, and showed failure in the expected areas [234, 279]. Using P92 steel welded joints, Zhao et al. simulated creep damage and determined correlations between the applied load and stress levels [27]. A strain model was then used to relate the creep strain of SPT to determine a relationship between strain rate and stress. Zhou et al. similarly found good correlation of FEA creep simulations and experimental results, along with the significant influence of specimen thickness, load level, ball size, temperature, and test atmosphere [18].

Kim et al. calculated critical fracture stresses for low alloy steels at very low temperatures by comparing maximum loads from SP curves to FE results [212]. Tanaka et al. utilized a FEM analysis from a notched 3D model in order to obtain fracture toughness from SP

tests, in combination with the small punch energy value calculated from the force-displacement curve [249]. Master curves were created which relate the fracture toughness value  $J_E$  and the SP energy  $E_{SP}$ , which require the use of a traditional tensile test to obtain a stress-strain curve. Simulation of a small punch test is conducted to obtain relationships between  $E_{SP}$  and the strain energy density  $W_{SP}$  at the crack tip of the SP specimen. Similarly, a simulation of a traditional CT fracture test serves to provide the relationship between  $J_E$  and the strain energy density at the crack tip of the CT specimen,  $W_{CT}$ . The relationship of  $W_{SP} = W_{CT}$  is then used to relate  $J_E$  to  $E_{SP}$ , thus allowing the use of these master curves as references for future test curves to estimate fracture toughness. This process is similar to one utilized previously by Foulds et al. [280]. The results of this method were somewhat questionable, being dependent on certain limiting conditions. Similarly, Turba et al. used another novel fracture specimen previously described. In this case, FEA was used to optimize the notch size, calculate the stress intensity factor, and carry out an elastic-plastic analysis on said specimens. The stress intensity factor calculated using the FEA in combination with test results were then used to estimate a fracture toughness value [251]. Cuesta et al. utilized the Gurson-Tvergaard damage model to simulate SPT results up to fracture with good agreement [281]. In this manner, material properties were determined by matching simulation to experimental results. The model was separated into six stages and parameters were determined one at a time using the inverse method. Dutta et al. suggested a method to improve the numerical prediction of fracture initiation and overall fracture energy curve calculation using the Gurson-Tvergaard-Needleman material model with split parameters [282], which was shown to improve prediction and determination of J-integral vs crack growth data [215].



Similarly, damage parameters for the Gurson-Tvergaard-Needleman model have been used to precisely simulate fracture of notched SPT specimens of varying configurations [255].

Several studies have correlated experimental force-displacement curves with those produced by FEA models in order to determine compliance effects on experimental results. The FE simulation conducted by Egan et al. used experimental data to find the influences of maximum force depending on the material properties supplied and the sample geometry [272]. The effects of microdefects and microvoids were examined by Guan et al. [283]. Simulated curves with varied void sizes integrated in the models showed that although defects had little effect on the earlier parts of the curves, strength in the plastic region was affected and the defect produced large amounts of scatter. Hulka et al. analyzed the geometry presented in the CEN workshop agreement for sensitivity effects on results of inverse simulations which tested the influence of the mesh density, the modeling of the tools, the sample thickness, the material model used, and the effects of friction between the punch and sample and between the sample and the dies [284]. Similar studies have shown that sensitivity studies are useful for evaluating fracture properties as well, as [245, 285] showed model response and fracture location dependencies on sample thickness and friction, but an independence from mesh density. Sensitivity studies apply when modeling the shear punch test as well. Goyal et al., for example, explored the effects of several parameters on shear yield strength, such as effects of punch compliance, which was severe [286]. Less severe were offset effects and variations in lower die width and specimen thickness.

Simulations thus play an integral part in determination of material properties when utilizing small punch test, especially as the most accurate method of acquiring conventional data

from SPT test data is by utilizing the inverse solution method. In an effort to reduce calculation time due to the numerous iterations necessary when curve fitting via the inverse method, correlation factors are often used to determine material properties. However, these have been shown, often through the use of FEA models, to have dependencies on material, geometry, and other test factors. As such, FEA is and will remain an integral part of material characterization with small punch testing.

### **2.3.8 Fatigue**

The small punch test (SPT) has yet to be leveraged for thorough evaluation of the fatigue behavior of materials. This is due to the difficulty of applying reversed loading in an SPT setup, or even zero-to-load setups, as a return to the origin displacement of zero could cause punch alignment issues upon subsequent load cycles, as a gap forms between the punch and the sample surface due to plastic deformation of the sample. With the constricted space used in SPT, forming an SPT setup which can apply more than the typical downward load of a typical SPT setup presents a challenge. Several reviews which cover miniaturized testing summarily stated that small samples gave high correlation with full size sample S-N curves and as such sample size was found to have little effect on results, though otherwise lacked insight on the matter [231, 287]. Hirose et al. used miniaturized cylindrical fatigue specimens to show that size did not have a significant effect on fatigue properties [288]. Li and Stubbins conducted fatigue crack growth tests using miniaturized three point bending samples well within the dimensions of SPT samples [289]. These samples, with the dimensions of 7.9mm in length, 2mm in width, and 0.8mm in thickness, were pre-cracked with a 0.1mm deep notch made by electro-discharge machining and

cycled with a load ratio,  $R$ , of 0.1. The crack growth data corresponded very well with standard sized test specimens.

However, Prakash and Arunkumar presented a novel cyclic compression-compression small punch test routine which was inspired by monotonic and cyclic automated ball indentation for estimation of material properties, including fatigue life [15]. This method uses hysteresis energy of cyclic SPT as a parameter to quantify the fatigue life of materials. To quantify the fatigue damage, they defined a damage parameter as the difference between unity and the ratio of the plastic energy dissipated per cycle of damaged material to that of a virgin material. The determination of the damage parameter involves the summation of the plastic dissipation energy for damaged and virgin materials, in this case copper and stainless 304, by cycling materials at a frequency where the hysteresis is constant or stable. The load for cycling is a percentage of the maximum load determined by first conducting monotonic small punch tests. The typical cyclic loading regimen for small punch tests is thus as shown in Figure 2.25. Due to the design constraints, cyclic loading is applied to the top of the sample to a certain load level, with the deloading cycle going to approximately zero load, though maintaining contact is important due to alignment concerns.

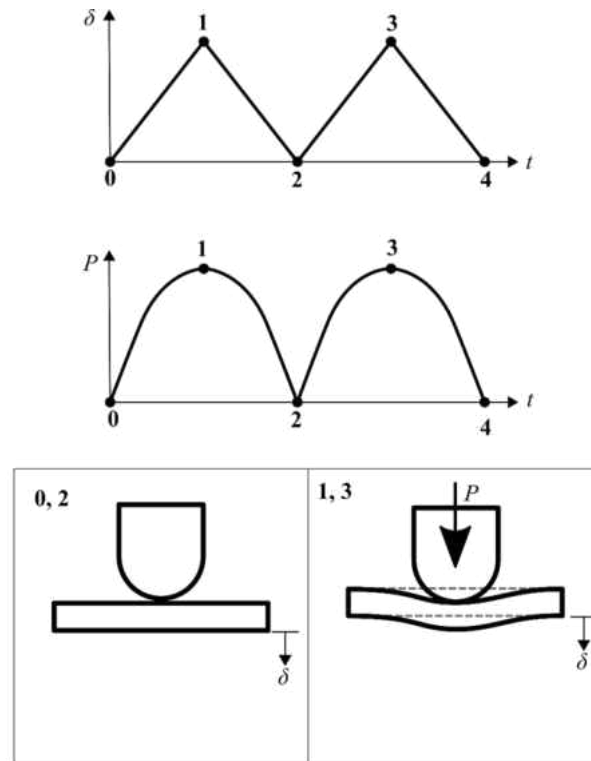


Figure 2.25 - Typical cyclic small punch test loading profile found in literature.

A significant effect was also found with variation of the frequency of cyclic loading, as thermal effects from excessively high frequency tend to alter material behavior and resultant hysteresis, emphasis was also placed on optimization of clamping torque, which varies based on the material being cycled [15]. The approach shows sensitivity to material condition and testing parameters with loads varying as little as 2N showing differences in life. The damage parameters of copper at different fatigue life states calculated via cyclic loading were compared with damage estimated from monotonic SPT as well as tensile tests, and while the cyclic parameters were generally higher, they were within 7% difference of both monotonic SPT and tension tests.

A cyclic SPT study based on using the standards for testing ultra-high molecular weight polyethylene (UHMWPE) for surgical implants, ASTM F2183, showed that cyclic SPT gave repeatable and reliable results [290]. Test results showed the differences in life for varying loads and varying aging conditions, with distinctions showing for different aging times versus virgin material. Samples were cyclically loaded at 200N/s with a triangular waveform, with loading between 2N and a maximum of 60-94% of the maximum load of monotonic tests so as to result in failures below 10,000 cycles. A similar study by Jaekel et al. using polyetheretherketone (PEEK) polymeric biomaterials confirmed that cyclic testing with SPT was sensitive enough to detect differences in manufacturing conditions for the materials, even while restricting loading to the elastic range of the load-displacement curve [14]. These studies show the sensitivity of the SPT to material variations due to both testing and manufacturing conditions, which is important for additive manufacturing materials as processing parameter variations to the resultant microstructure and material properties.

While these studies mainly show that SPT can detect differences in fatigue life due to differences in processing or treatments, it is unclear whether the results directly translate to traditional fatigue life prediction data. Additionally, the capabilities presented in literature for fatigue testing with SPT are limited to zero-to-tension loading. This type of loading, while useful, only gives a limited perspective on fatigue, as it provides no insight on reversed yielding or plasticity. A significant gap in SPT fatigue testing exists which needs a modified methodology capable of reversed loading in order to fill it, which present a large challenge given the confined dimensions of the test system. Regardless of its scarcity, however, the literature on this topic

shows the potential for fatigue testing with SPT, especially since sample size does not seem to have a significant effect.

## **2.4 Summary**

Additive manufacturing methods such as selective laser melting are being increasingly utilized in both research and industry. The general effects of process parameters and post-processing treatments with AM are well understood, as they have been thoroughly documented in literature, yet each material is unique in how it reacts to the processes and in the properties of the resultant microstructure. Nickel superalloys, specifically those of the Inconel family, display high strength which persist up to very high operating temperatures. As such, nickel superalloys are of high interest to SLM applications for energy applications, such as in the design and manufacture of steam turbine components with complex cooling geometries. These alloys are highly susceptible to processing and post-processing, due to the microstructural evolution of their constituents, and these effects are compounded by the manufacturing conditions present in SLM. Each alloy must therefore be thoroughly characterized before being employed for specific applications to ensure its suitability and to establish optimal SLM processing parameters and post-processing techniques. This can be both time consuming and expensive, as experiments must be carried out to assess the effects of varying numerous build parameters and post-processing treatments.

The small punch test, as a miniaturized sample test technique, is proposed as able to alleviate the time and cost of this process due to the simplified design of the sample and the experiment. As a consequence of this, however, the state of stress induced during

experimentation is more complex than that of a conventional test such as a tensile test. This necessitates the use of more complicated techniques in analyzing data to determine material properties. Several procedures are outlined to equate SPT data with conventional stress-strain data, and though lacking formal standardization, many of these methods are well established in literature. Correlation values for deriving material properties from SPT data have been shown material dependence in certain cases, but not others. Relationships exist with conventional testing techniques including tension, creep, fracture, and fatigue, as well as a variation of the small punch test known as the shear punch test for acquiring shear properties.

#### **2.4.1 Knowledge Gaps**

Although many of the methods outlined here have been explored widely in literature, variations between studies show sensitivity to experimental and material conditions. Correlation factors have shown material dependency, though some constants have been proposed to be widely applicable to a range of materials. It is unclear whether these constants will serve suitable to analyzing SLM materials, due to the intrinsic differences to conventionally produced materials, or if correlation factors need to be established based on material type, orientation, condition, etc. The most reliable method of deducing material properties from SPT data is through extraction of a stress-strain curve via the implementation of the FEA inverse solution method. The optimization is often done via least squares of error. It is unclear whether a model starting with conventional material properties will accurately match with the experimental force-displacement curves given the fundamental microstructural differences, and especially when

factors such as orientation are considered. As the literature highlighting the use of SPT with AM materials is limited, its suitability for characterizing SLM materials is relatively unknown.

Some areas of SPT as they correlate to conventional testing techniques have not been thoroughly established. Though strong equivalencies exist, there are numerous variations with establishing fracture properties, with no single approach being universally accepted, and dependencies on material type, condition, and orientation exist. Additionally, the use of the small punch creep test is prominent in literature and the relationship for determining the equivalent stress level necessary to achieve the same time to rupture at a certain force with SPT is well-established. However, this relationship has been shown to be sensitive to material anisotropy, a trait which SLM materials are well known to exhibit. Most prominent of the deficiencies in SPT research are those relating to fatigue. Research on cyclic loading in SPT is scarce and limited to zero-to-tension or tension-to-tension loading, with no studies having explored reversed loading equivalent to conventional tension-to-compression testing which is necessary for estimating component life, especially as related to energy production applications. These deficiencies make it difficult to utilize the small punch test to thoroughly characterize SLM materials to the extent achievable with conventional experimental techniques.

#### **2.4.2 Applicability of SPT to SLM**

Despite these deficiencies, evidence in literature suggests that SPT can be a valuable tool for optimizing SLM materials. The small punch test has been utilized to characterize some AM materials, and a number of welded specimens with heat affected zones with microstructures arguably similar to those of SLM materials. These include materials manufactured via selective



laser melting, direct laser deposition, and electron beam deposition. The small punch test has been shown to be sensitive enough to detect the characteristics and variations present in SLM materials and is thus a good candidate for optimizing processing parameters during manufacturing as well as in post-processing. The ability to assess the material properties of SLM materials with SPT is therefore somewhat questionable, but promising, and as such will be explored here. This will involve utilizing methods both novel and established within literature, in the hopes of advancing additive manufacturing techniques through the use of miniaturized testing techniques such as the small punch test, while enhancing the capabilities of the small punch test itself.

## **CHAPTER 3: EXPERIMENTAL PROCEDURE**

The main objective of this study is to assess the suitability of the small punch test to evaluate new materials for use with SLM, so this chapter will detail the process by which that is accomplished. As the literature has shown, SPT is sensitive enough to show the effects of anisotropy and the evolution of the microstructure as directly related to it, and SLM components are prone to anisotropy which can be affected by post-processing. This means that small punch tests should be able to accurately describe the material properties of a new alloy being used for SLM part construction, including being sensitive to the intricacies of the build process, so as to optimize process parameters and post-processing routines. It is of interest, then, to study whether the capabilities currently available with typical SPT studies are sufficient to evaluate SLM materials to the extent typically done with traditional testing, or if a modified methodology is necessary and can be achieved. The SPT matrix will therefore be adapted to meet the conditions of a test matrix which uses full-size samples. More specifically, due to the limited space in the design of an SPT setup, fatigue tests cannot currently be conducted in a fully-reversed mode and are relegated to the zero-to-tension region which provides a limited perspective, so it is of interest to determine if the capabilities of an SPT setup can meet those of a traditional test, or if SPT capabilities can be expanded.

### **3.1 Overview**

In order to assess the viability of the small punch test as a method of characterizing the material properties of the proprietary nickel superalloy IN939V, two comparable sets of test matrices have been designed. For all tests to be conducted with IN939V, samples were produced

in an SLM Solutions SLM 280HL machine at Power Systems Manufacturing, LLC (PSM). This machine features a build volume of  $280 \times 280 \times 365\text{mm}^3$  and the possibility of several configurations of single or multiple IPG fiber lasers at possible power levels of 400W, 700W, and 1000W in an inert Argon gas environment. The system is flexible in terms of powders and is capable of using various alloys for building components, including nickel superalloys and proprietary formulations such as IN939V.

Optimized processing parameters established previously via design of experiments for this combination of machine and material were employed to produce the samples at orientations where loading occurs both parallel and perpendicular to the layer stacking direction, which were subsequently subjected to full post-processing including recrystallization, HIP, and heat treat. Optimized processing parameters were determined previously at PSM via the implementation and analysis of test matrices using design of experiments with the objective of minimizing defects such as microcracks and achieving uniform component porosity of 0.2% or less throughout. Figure 3.1 explains the terminology used herein for relating loading and layer stacking. Samples constructed with the long direction vertically (in reference to the build plate) will experience loading parallel to the layer stacking direction (perpendicular to the layer surface), and may be referred to as longitudinal, and those built with the long direction built horizontally will be loaded perpendicularly to the layer stacking direction (parallel with layer surface) and may be referred to as transverse. In terms of directions, it can be said that transverse samples are loaded in the [100] direction as relating to layer surfaces, while the longitudinal samples are loaded in the [001] direction in reference to the layer surfaces, which will correspond with the direction of the columnar grains typical in as-built SLM microstructures.

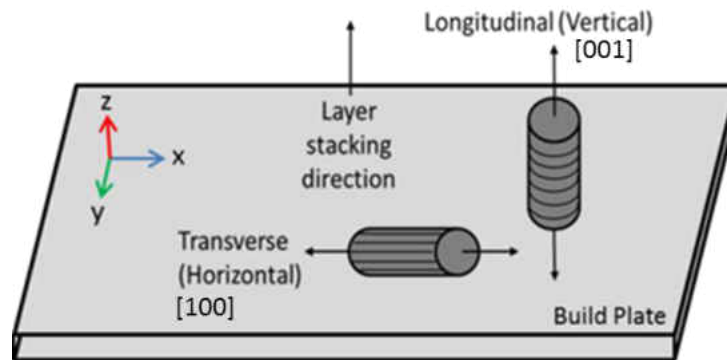


Figure 3.1 - Build orientation terminology diagram.

Test coupon design was dependent on orientation and intended use. Bars with the length produced parallel to the build plate (transverse samples) were shaped hexagonally to improve surface finish, reduce warping, support construction and removal, and improve overall build quality due to intrinsic limitations inherent to the system. These limitations do not apply for samples built with the length perpendicular to the build plate (longitudinal), so the majority of these were round in shape to minimize material waste when machining test samples from the as-built SLM bars, Figure 3.2 shows both types of samples, along with SLM blocks produced for machining of fracture testing samples. For conventional tests the SLM bars were machined and polished according to pertinent standards. For SPT samples, bars were machined to size and sliced using pertinent methods as detailed in section 3.3.



Figure 3.2 - Hexagonal transverse and round longitudinal bars produced for full-sized tension samples and blocks produced for fracture tests, all of which were utilized for SPT samples.

### **3.2 Post-processing**

Test bars were stress relieved while still attached to the build plate to prevent warping and then removed from the SLM build plate through the use of wire electrical discharge machining (wire-EDM) to make precision cuts and reduce material waste. A high-temperature recrystallization cycle was implemented so as to encourage crystal growth and reduce the effects of anisotropy, as anisotropic properties can make component life prediction much more difficult. Following this, SLM samples were treated to a Hot Isostatic Press (HIP) cycle and several subsequent heat treatment cycles designed to redistribute alloy constituents and reduce anisotropy within the microstructure.

#### **3.2.1 Recrystallization Cycle**

The recrystallization temperature was chosen based on the results of a differential thermal analysis (DTA) conducted on the material to find its phase transition temperature, in this case the melting temperature, and use a temperature just below it, in which recrystallization occurs. A

preliminary study was conducted to gage the effects of differences in time and temperature of the recrystallization cycle on the resulting microstructure and anisotropy effects on material properties, including Young's modulus, yield stress, and tensile strength. The immediate measure of the efficacy of the heat treatment would be the modulus in both directions, strength in both directions, variations in microhardness within and between samples, and, to a degree, the physical size of the grains. The recrystallization cycle effects study is defined in Table 3.1 with these purposes in mind. The table also denotes the level of post-processing that each sample was subjected to, and the averages hardness and the variance of each after application of the recrystallization cycle but prior to the heat treatment, to be discussed later in this section. After their designated recrystallization treatment, each of the tensile samples were subjected to hot isostatic pressing and a full heat treat regimen which included a solution and stabilization heat treat, a secondary heat treat, and a precipitation heat treat. These are the standard treatments which are utilized for cast components made from the same material. Due to the high cost and time required to produce, post-process, machine, and test each specimen, the minimum number of specimens possible was chosen to determine if the heat treat was successful, though this limited sample size could skew results and prevents confirmation of an optimal recrystallization having been found. The limited number of specimens available and the cost of fatigue and creep testing made it prudent to perform these tests before committing a large number of specimens to the recrystallization heat treatment for a full factorial test matrix.

Table 3.1 - Test matrix for recrystallization study

Sample	Geometry	Orientation	RX Temp	RX Time	Heat Treat	Response
1	Tensile	Horizontal	T <sub>RX</sub>	Base	RX, HIP, HT	Modulus, Microstructure
2	Tensile	Vertical	T <sub>RX</sub>	Base	RX, HIP, HT	Modulus, Microstructure
3	Tensile	Horizontal	T <sub>RX</sub>	3X Base	RX, HIP, HT	Modulus, Microstructure
4	Tensile	Vertical	T <sub>RX</sub>	3X Base	RX, HIP, HT	Modulus, Microstructure
5	Slice	Vertical	T <sub>RX</sub> -10°C	Base	RX	Microstructure
6	Slice	Vertical	T <sub>RX</sub> +10°C	Base	RX	Microstructure
7	Tensile	Horizontal	None, sent As-is to HIP and HT		HIP, HT	Modulus, Microstructure
8	Tensile	Vertical	None, sent As-is to HIP and HT		HIP, HT	Modulus, Microstructure

As stated, samples 1-4, 7, and 8 were tensile tested in ambient conditions after being heat treated, while samples 5 and 6 were small slices taken from bars utilized for other purposes, of which the originals could not be recovered. As such, these two samples served only as references for microstructure and hardness comparisons when the heating temperature fluctuates within the available controllable range of the furnace used for the recrystallization treatment. The tensile responses of full-sized samples are depicted in Figure 3.3, along with a more detailed view of the elastic portions of each. The first trait of note is that any level of recrystallization reduces strength as compared to a non-recrystallized sample of the same orientation. Additionally, all samples show a directionally dependent variance in strength and elastic moduli. Closer

inspection shows some effects of the recrystallization time difference. Applying a recrystallization cycle of any time reduces the difference in between the elastic moduli of the two directions. Continued heating time further decreases the anisotropy between the two build directions, reducing the difference in modulus between them. Though there is still a difference in strength between the two directions, and both times are below the non-treated strength, the increased time does not cause a further decrease in strength. Additionally, all trials were found to exceed the specified minimum value given for the elongation, tensile strength, and yield strength of the cast material. The stress-strain curves show the samples treated for the 3X base time converging in strength, as shown by the arrow, although they will not fully merge. It is doubtful that increased time in the recrystallization cycle would fully eliminate the anisotropy, and as highlighted in the literature, would likely induce embrittlement of the microstructure, reducing ductility of the material and therefore life.



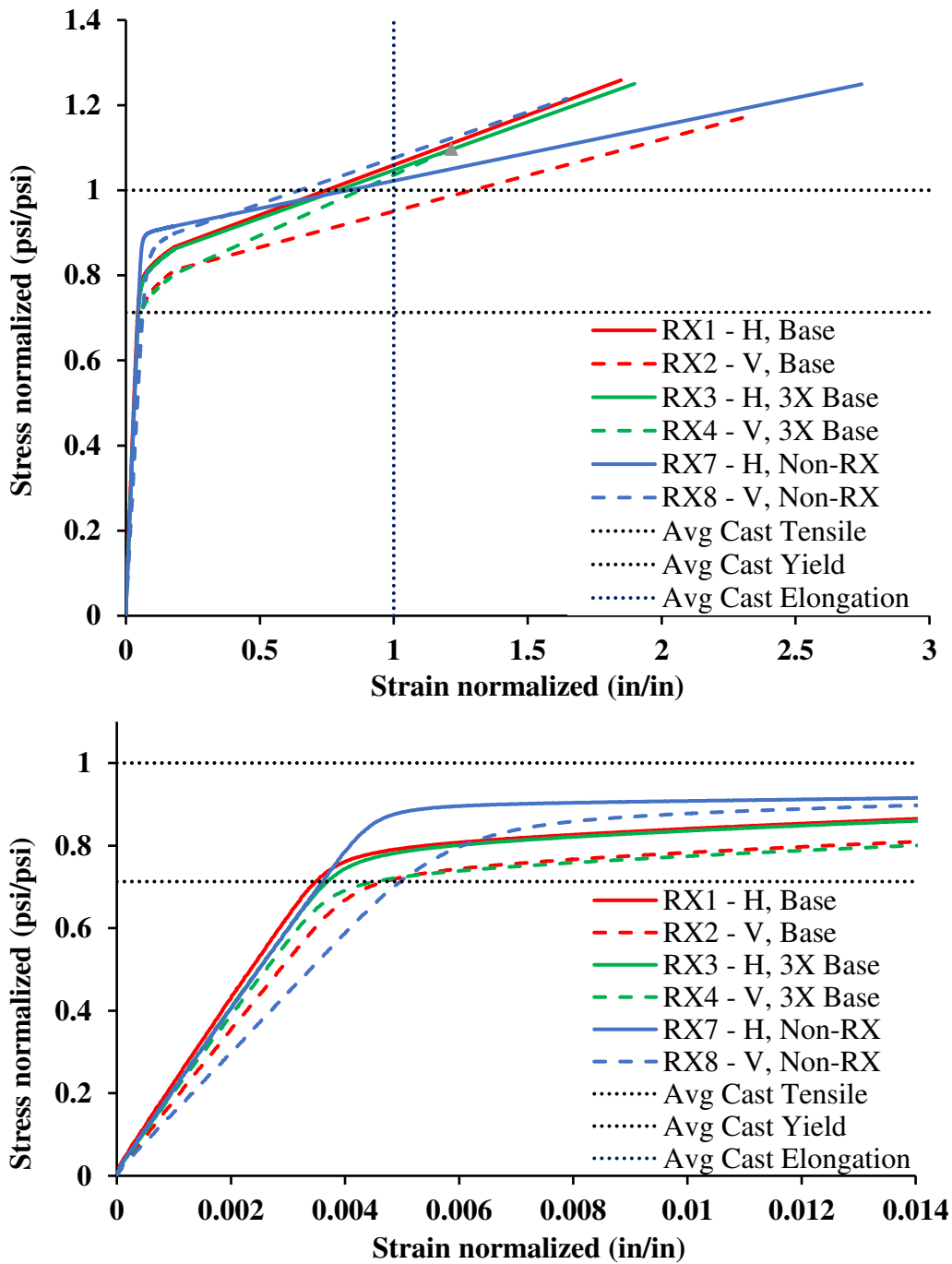


Figure 3.3 - Recrystallization study tensile test results, with a detailed view of the elastic sections.

To preserve the proprietary status of the material, the mechanical properties determined from this preliminary study have been normalized using the response typical to a cast sample and show desirable trends. Results are portrayed graphically in Figure 3.4. The graphical representation of the tensile test results shows that both of the 3X Base samples exceed the given elastic modulus that is typical of cast to size specimens, while the vertical samples for the untreated and Base cases did not. However, all SLM samples, both treated and untreated, exceed ultimate tensile and yield strength specified minimum required (SMR) values as well as those for a typical response for cast IN939V. It can be seen that although increased time reduces strength, it also reduces anisotropy. Also of note, is that recrystallization also reduced elongation (or ductility), though all trials still exceed typical cast values. Increased time further reduced elongation, and though it cannot be said that it reduced anisotropy as well in the 3X Base samples as it did in the Base samples for elongation, the reduction in area is nearly equal. Results show that an extended recrystallization cycle leads to a greater reduction in anisotropy while still producing favorable material properties. However, this does not necessarily mean that a longer cycle time would work better, as there is no guarantee that the material would ever reach full isotropy or suffer otherwise.

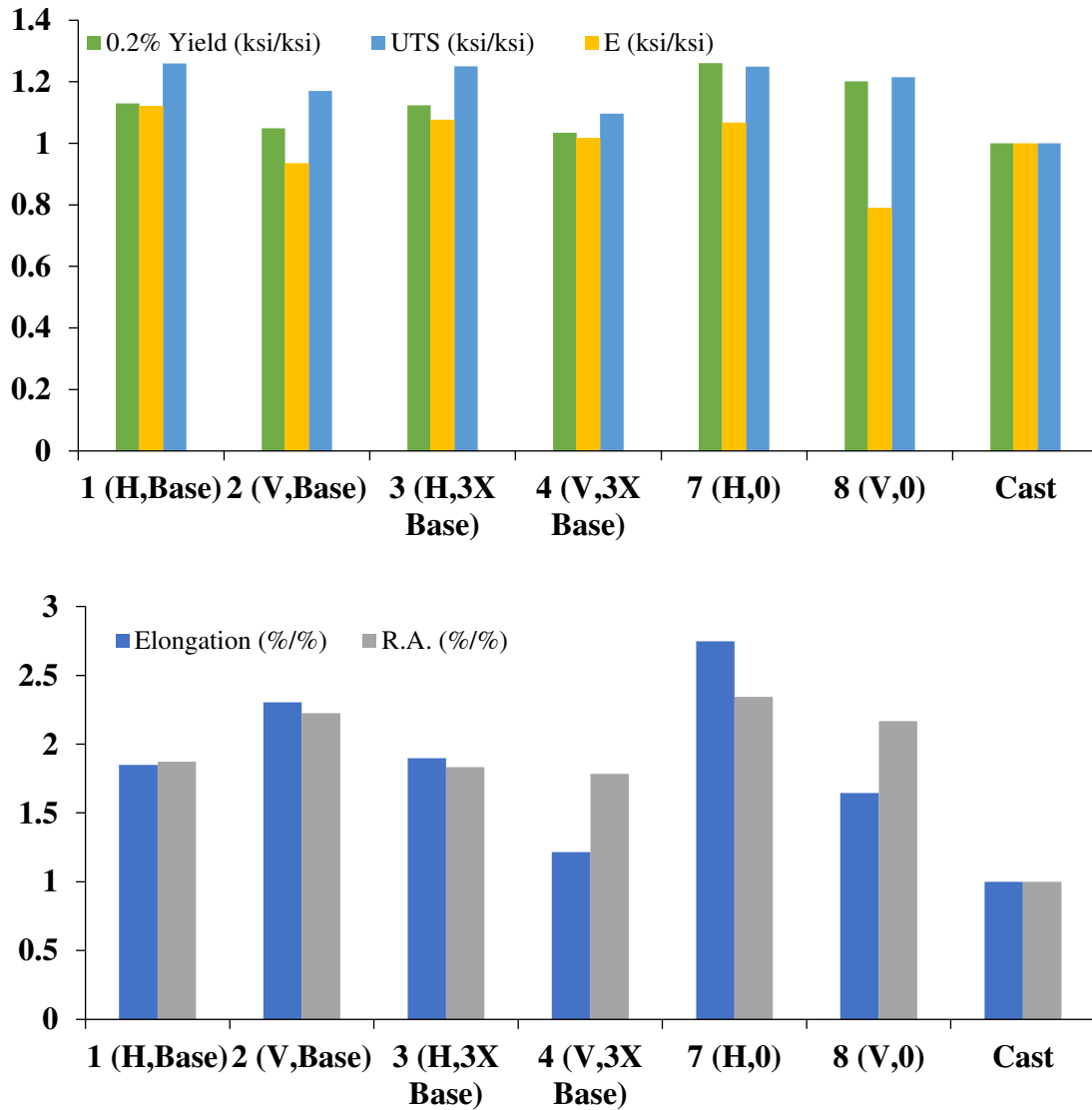


Figure 3.4 - Comparison of material properties from tensile tests between different treatments.

Microscopic inspection of the various samples did not indicate any abnormal growth from extended heating time. There is some difference in grain size resulting from using an increased (or decreased) temperature within the certified furnace limits, but distribution remains normal. Inspection of the slices of bars 6 and 7, which did not have enough material for tensile

testing, showed no abnormal grain growth with minor fluctuations in recrystallization heating temperature within the  $\pm 10^{\circ}\text{C}$  of control available in the furnace utilized to carry out the recrystallization cycle. To facilitate a comparison between the full-size samples and those with limited material, hardness testing was conducted on cross-sections of each. Over 40 points were hardness tested for each sample in Table 3.1 on a Vickers hardness tester and converted to Rockwell C hardness values, and the average hardness values were calculated. Of note, these samples were restricted only to recrystallization treatments; none of the subsequent treatments that the samples went through before tensile testing were applied at this stage, which means samples 7 and 8 were tested in an as-received condition. In all cases the variance is below 4%, so variations within samples do not indicate any abnormalities within the grain structure. Although the hardness results indicate that recrystallization treatments decrease hardness by a few points, variations between treatments and directions are minimal, and on average the variance for the recrystallized samples is somewhat lower than those of the as-manufactured samples, suggesting that the recrystallization cycle reduces scatter in material properties within SLM components. That is, it cannot be said that variations in time, temperature, or orientation had any largely significant effects on hardness testing results related to microstructural changes. Given these results, the 3X Base time recrystallization cycle was chosen as achieving the best compromise in resulting material properties when combined with the other heat treatments employed due to the large decrease in anisotropy and small loss in strength, despite the loss in ductility.

### 3.2.2 Heat Treatment

Following recrystallization, the SLM bars were subjected to the full heat treatment used for cast components manufactured from IN939V. This includes hot isostatic pressing (HIP) to close any remaining internal pores and cracks and reduce the scatter of material properties across samples that are otherwise identical. The HIP process, however, will not close any surface defects, as all of the surface, including defects, will be at the same pressure. As such, test bars for the full-size components which the SPT samples will be compared to are machined and polished to avoid the effects of surface defects on mechanical performance. Finally, the full standard heat treat routine to which conventionally cast IN939V components are subjected to was implemented in order to optimize the microstructural composition and constituent distribution of the alloy. The heat treatment routine is based on the standard heat treatment utilized for cast IN939V, which was primarily based off of that used for IN939 and conducted in four stages including various cycles of solution and aging heat treatments, as listed in the literature review portion of this document in Chapter 2. This includes a solution heat treat to bring carbides and intermetallics into a solid solution, a heat treatment to stabilize the solution, and secondary heat treatments cause precipitation of carbides for grain boundary strengthening and precipitation of the  $\gamma'$  strengthening phase within the grain structure. Samples were also produced and tested with the material at varying stages of processing, from as-manufactured to partial or full implementation of post-processing steps. Tests conducted at intermediate stages are used to determine the effects of processing routines and optimize the conditions of such, while showing the capabilities of SPT to track material evolution.

### **3.3 SPT Sample Preparation**

To produce SPT samples, SLM test bars were machined to round bars of 10mm diameter or square bars 10mm x 10mm wherever appropriate. Originally, individual SPT samples were cut from the machined bars using a Buehler Isomet low speed cutting saw to a thickness of roughly 1.5mm, taking special attention to remove burrs and lips resulting from the cutting operation. Samples then needed to be ground and polished to a final thickness of 0.5mm, which was achieved using a Buehler single-force head auto-polisher. Temporary sample holders were utilized to aid in the polishing process, but shear forces caused the samples to slip from the sample holder. Samples were then mounted in an epoxy casting system, polishing one side completely. The samples were then removed from the epoxy molds, cleaned, flipped, and re-cast to repeat the process on the other face, so that both surfaces are polished to a mirror finish and free of defects that might otherwise affect strength and fracture behavior. Due to variations in cuts and a limited amount of movement built into the polisher to maintain contact with the polishing plate, samples would often end up with uneven thicknesses which could vary significantly. Due to the scale at which SPT is performed, variations at a tenth of a millimeter represent a 20% variation in sample thickness, which causes complications with testing as they affect stress distribution.

Finally, to circumvent the issues arising from variations in sample thickness, samples were cut using wire-EDM (electrical discharge machining) to a thickness of just over 0.5mm, using cutting settings which minimize the severity of the re-cast layer. This precise cutting process produced samples of uniform thickness which required minimal grinding and polishing. Slices were then manually polished to a mirror finish using several grades of silicon carbide sand

paper and polishing cloths on a rotating plate with a variety of lubricants such as water and several grades of diamond polishing suspensions to a mirror finish. Factors such as plate rotation speed, lubricant grade, and pairing and order of lubricants and pads were determined via the use of polishing guidelines supplied by Buehler, adjusted accordingly for manual use rather than with the auto-polisher head.

### **3.4 Planned Experimental Matrices**

As stated previously, two sets of test matrices were designed for the completion of this study. The first set of tests composed of full-sized specimens, which were subjected to conventional testing techniques under varying conditions for the characterization of the material for subsequent use in life prediction models following standards noted previously. In this study, this matrix primarily served as a model and standard of comparison for the second matrix, which is the focus of this study using the SPT. These tests included conventional tensile, creep, fatigue, and fracture tests at varying testing conditions. These will evaluate mechanical properties of IN939V to establish a basis by which the efficacy of the following SP tests may be evaluated. Material mechanical properties such as Young's modulus, yield and ultimate tensile strength, creep rates, and more will be determined at varying temperatures on samples manufactured in both horizontal and vertical orientations.

The second matrix, designed for small punch tests, has been subdivided by the equivalent conventional test types for each SP test, as outlined in the following tables, and will use similar conditions to those of the traditional test matrix, but adapted to the limitations of the small punch test. Desktop test controls were provided through the use of MTS software package Testworks

Elite, implementing controls for force or displacement as required by the test matrix. A displacement rate of 0.5mm/min was used, which is in the range of what is commonly seen in literature and dictated in the CWA 15627, 0.2-2.0mm/min. The matrices are divided by the tests to which they are equivalent; tension, creep, and fatigue, with a variation of conditions for each of these. Heading each of these matrices are trials listed as using conventionally produced 304 stainless steel. Tests with this material serve as verification runs of the capabilities of the SPT rig with both the monotonic and cyclic functions. This is necessary especially given the novelty of the design for incorporating reversible loading, as significantly greater amounts of data are available for traditionally produced 304 stainless, facilitating comparison of test results. The feedstock material from which these samples are taken was certified for composition and material properties by the manufacturer. Selective tests which are representative of the traditional tests conducted were used for constructing the SPT matrix utilizing the SLM samples in order to show the suitability of SPT to evaluate SLM material evolution and SLM materials in general. In order to do so, some tests will be repeated with materials in various stages of post processing as well as different material types from both the machine at Power System Manufacturing (PSM) and from other sites. This includes several trials using samples taken from the grip sections of the tensile specimens produced by PSM and used for the recrystallization study presented earlier in this chapter, in which materials were tested at various stages and variations of heat treatment. Additional studies listed in the test matrices previously given include other popular SLM materials. These include GP1 stainless steel samples, for which the feedstock material is manufactured by EOS specially for their DMLS machines with the equivalent composition to 17-4PH, manufactured at Central State University, and IN625 samples manufactured by Solid



Concepts. These add variability in terms of both materials and SLM machines used, to ensure those do not present additional factors that affect test results when gauging the suitability of SPT for evaluating SLM materials. Finally, samples produced from IN718 on an EOS 270 machine with the manufacturer optimized settings will provide further additional test pieces and variability. This will provide a factor of variability within the test for different materials, to show that SPT is viable for more than one type of SLM material. These additional samples were mainly tested with monotonic SPT, comparing results to traditional tensile test results available in literature, and source data from traditional testing conducted at PSM, where available and applicable, as well as with conventional tests completed for this purpose, with samples manufactured from the same stock as the SPT samples. Test conditions for additional tests replicated those already existing within the test matrices shown in Table 3.2 to provide comparisons between materials.

Table 3.2 - Tensile test equivalent SPT matrix.

<b>Test No.</b>	<b>Temp. (°C)</b>	<b>Orientation</b>	<b>Material</b>	<b>Condition</b>
<b>T1</b>	21	-	SS 304	As-received
<b>T2</b>	21	Long	IN939V	RX, HIP, HT
<b>T3</b>	21	Trans	IN939V	RX, HIP, HT
<b>T4</b>	21	Long	IN939V	RX 3X Base, HIP, HT
<b>T5</b>	21	Trans	IN939V	RX 3X Base, HIP, HT
<b>T6</b>	21	Long	IN939V	RX Base, HIP, HT
<b>T7</b>	21	Trans	IN939V	RX Base, HIP, HT
<b>T8</b>	21	Long	IN939V	No RX, HIP, HT
<b>T9</b>	21	Trans	IN939V	No RX, HIP, HT
<b>T10</b>	21	Long	IN939V	As-manufactured
<b>T11</b>	21	Trans	IN939V	As-manufactured
<b>T12</b>	300	-	SS 304	As-received
<b>T13</b>	427	Long	IN939V	RX, HIP, HT
<b>T14</b>	427	Trans	IN939V	RX, HIP, HT
<b>T15</b>	21	Long	IN625	As-manufactured
<b>T16</b>	21	Trans	IN718	As-manufactured
<b>T17</b>	21	Trans [100]	EOS SS GP1 (17-4)	As-manufactured
<b>T18</b>	21	Trans [010]	EOS SS GP1 (17-4)	As-manufactured

Table 3.3 - Fatigue test equivalent SPT matrix.

Test No.	Temp (°C)	Material and Condition	Cycle/Min	R ratio	Hold (s)	Range
<b>F1</b>	RT	304SS	20	0	0	0.1-1kN
<b>F2</b>	RT	304SS	20	0	0	0.15-1.5kN
<b>F3</b>	RT	304SS	20	-1	0	±0.5kN
<b>F4</b>	RT	304SS	20	-1	0	±0.5mm
<b>F5</b>	200	304SS	20	0	0	0.1-1kN
<b>F6</b>	200	304SS	20	-1	0	±0.5kN
<b>F7</b>	200	304SS	20	-1	0	±0.5mm
<b>F8</b>	427	IN939V Long. Full HT	20	0	0	0.04-0.4kN
<b>F9</b>	427	IN939V Trans. Full HT	20	0	0	0.04-0.4kN
<b>F10</b>	427	IN939V Long. Full HT	20	0	0	0.05-0.5kN
<b>F11</b>	427	IN939V Trans. Full HT	20	0	0	0.05-0.5kN
<b>F12</b>	427	IN939V Long. As-man.	20	0	0	0.05-0.5kN
<b>F13</b>	427	IN939V Trans. As-man.	20	0	0	0.05-0.5kN
<b>F14</b>	RT	GP1 x-axis As-man.	20	-1	0	±1.9kN
<b>F15</b>	RT	GP1 y-axis As-man	20	-1	0	±1.9kN
<b>CF1</b>	200	304SS		-1	15	±0.5kN

\*Initial cycles of samples F14 and F15 were conducted as tensile equivalent trials T17 and T18.

The variability of tests in terms of materials and manufacturing ensures that the test is robust and sensitive enough to detect any differences these variables may present, rather than gauging the suitability with a single material, IN939V, in the same state of processing. Samples were subjected to small punch testing and the accompanying analyses as detailed in the literature

review to determine how well the properties and constants determined correlate with those of the traditional test matrix for tensile, creep, and fatigue test. Previously published correlation values from the various literature reviewed were tested to expand the existing literature and support or oppose the use of the published correlation factors. Updated correlation factors will be proposed as necessary. Although, tensile tests were directly adapted from traditional tests using SPT with monotonic loading, fatigue tests were modified to accommodate the test limitations. This includes cyclic loading in only one direction as previously seen in literature, and a novel modified cyclic testing mechanism able to test reversed cyclic loading. The use of this novel mechanism design allows for reversed loading via application of twin punches on either side of the sample, producing the loading history seen in Figure 3.5. The tests in Table 3.3 with an R value of -1 utilize this configuration, and the range denotes whether control for each trial is imparted using peak load or deflection.

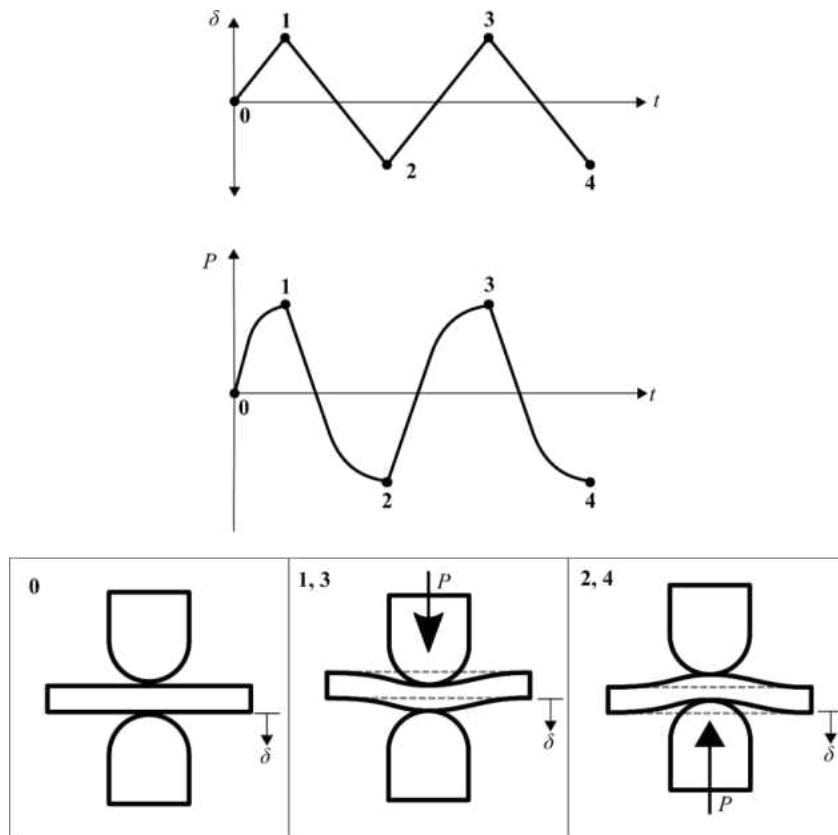


Figure 3.5 - Reversed cyclic loading as imparted by dual-punch SPT configuration.

Additionally, the fatigue test matrix also includes cyclic loading with the inclusion of a hold time at loading, which is representative of creep-fatigue loading as defined by ASTM E2714, which, as of this writing, has not been studied with SPT. The creep-fatigue and reversible-loading fatigue tests were conducted using load-control, while the single-punch fatigue tests were conducted using displacement control to achieve testing at specified strain ranges. The test matrices designed for this study test the viability of SPT as a test method for evaluating the material properties of components produced via SLM with its inherent directional property dependence, as well as its suitability for evaluating Inconel alloys. These tests will

evaluate how well SPT can track changes in material properties due to operating temperature, build orientation, and post processing variations. As such, an additional assessment for the use of SPT as a method for optimizing processing parameters can be also indirectly conducted. If so, this determination alone could reduce process parameter and post-processing optimization time and costs considerably from current practices.

### **3.5 Reliability and Error**

A series of load-unload (L-UL) tests were conducted using fully heat treated IN939V samples in both longitudinal and transverse orientations. These tests were conducted at room temperature with a loading rate of 0.5mm/min, as was used in the monotonic tests. The time period of each cycle was this adjusted accordingly to preserve the loading rate. Two samples manufactured in the longitudinal orientation and one sample manufactured in the transverse orientation were subjected to cyclic monotonic loading in increasing increments of 0.05mm, returning to 0mm displacement each time. The displacement range chosen for these tests extends into the third zone of the  $P$ - $\delta$  response, as dictated by the results of the monotonic tests with identical conditions and material manufacturing state. The results of one of these tests can be seen in Figure 3.6. The repeated loading and return to zero tests the reliability of the fixture by evaluating the distribution and development of the modulus ( $k_{UL}/t$ ) over time. The  $k_{UL}$  values are taken as the steady slope of each loading step of each L-UL cycle, omitting the non-linearities at the top and bottom of each cycle and normalizing them against the corresponding sample thickness so as to evaluate them together. The non-linearities are more evident at the lower displacement cycles as there is added elasticity in this range. As the loading program continues

and the sample progresses into the third zone, the sample enters into a steady plastic stretching regime, and the unloading behavior represents a constant elasticity. The use of multiple samples and orientations expands this to conditions of sample mounting and loading between tests.

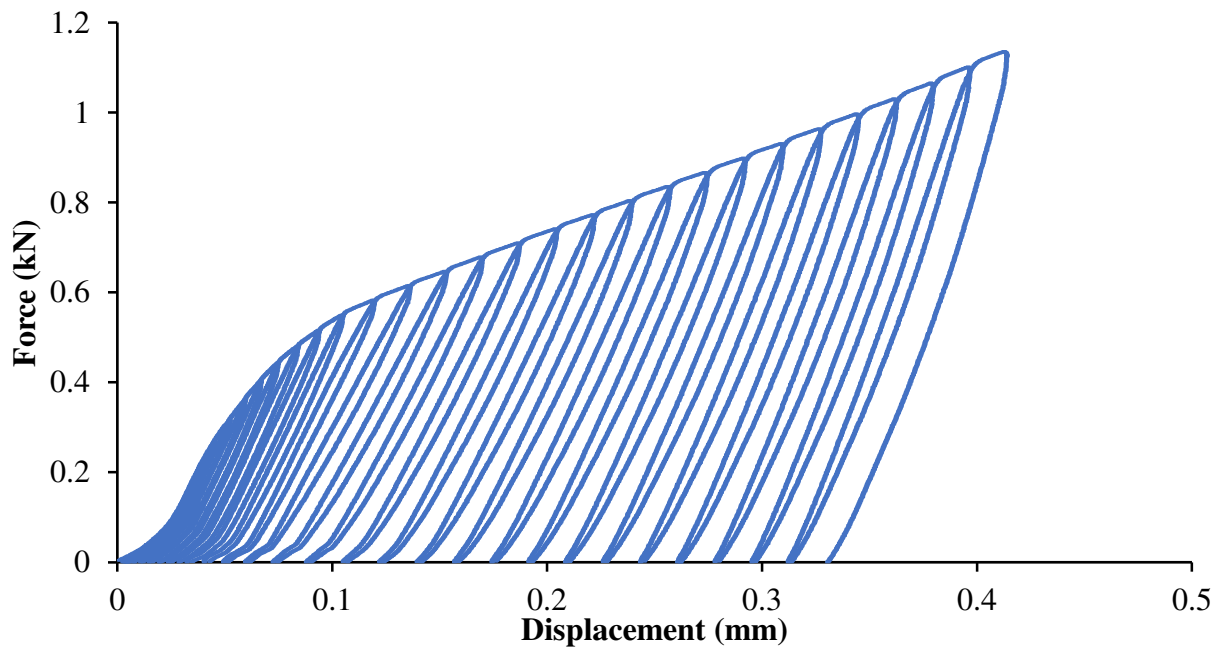


Figure 3.6 - Load-unload cyclic history of IN939V sample.

There is a general increase in stiffness as the L-UL cycles progress and displacement increases. However, the increase is minimal and the  $k_{UL}$  values tend to remain within a normal range for the entirety of the tests. The combined results of the three L-UL tests are plotted against a normal PDF created using a statistical analysis of the test data, as shown in Figure 3.7. The mean stiffness of the unload cycles,  $k_{UL}$ , is 22.41 with a standard deviation of 2.69. As seen in Figure 3.7, the data fits well within a normal distribution, with the majority of the data clustered within the center portion of the PDF. This indicates a high level of reliability for the

test system, as the loading step experienced by the cycles is shown to be highly consistent, though some deviation does occur due to differences in plasticity levels in the different  $P-\delta$  zones. This is especially true for the higher displacement levels, where plastic stretching is in effect. Due to this development of stiffness, a lognormal distribution may be shown to provide a minor increase in fit. Overall, this instills high confidence in the reliability and consistency of the methodology and test setup used in this study.

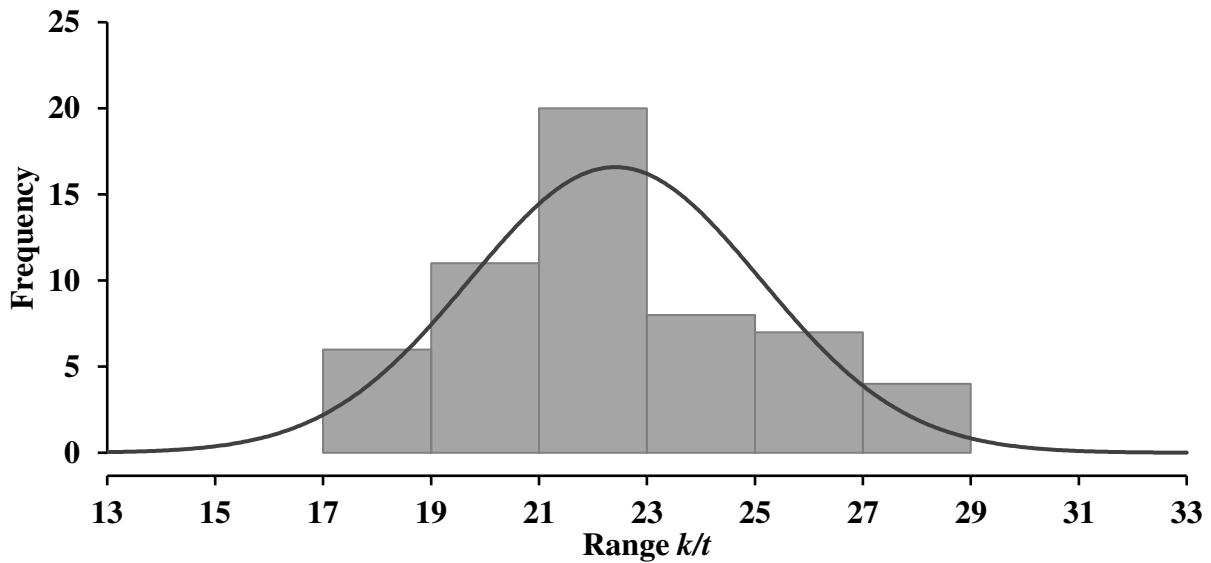


Figure 3.7 - Normal distribution and histogram of  $k/t$  values for collective results of L-UL cyclic tests.

Uncertainty values given within the results section were calculated via the use of the propagation of error method, whereby the error of each function calculated is based on the sum of the individual errors of the instrumentation used. In general, this equation can be written as



$$U_f = \sqrt{\sum_{i=1}^N \left( \frac{\partial f}{\partial x_i} u_{x_i} \right)^2} \quad (27)$$

Where  $f$  is the function in question, and  $u$  is the uncertainty associated with the variable  $x$  to which you take the derivate of  $f$  with respect to. The uncertainties,  $u$ , are mainly derived from the given uncertainty values of the load cell, LVDT, and micrometer. It is important to note that this does not include operator error or errors which are from irregularities in the materials, as AM materials are prone to having. As such, the tolerances given later in the results make results seem typically highly accurate, but this is really a reflection on the instrumentation errors only. This is done for the relationships relating SPT results with tensile material properties, including the relationships for  $E$ ,  $\sigma_y$ , and  $\sigma_{uts}$  given previously throughout section 2.3. As these relationships involve variables which are themselves functions of other variables, the same was calculated for the initial stiffness,  $k$ , and for  $P_y$ . The relationship for  $P_y$  was initially established using the Ramberg-Osgood equation, which will be shown to accurately describe the behavior of materials in the SPT in Chapter 4. The variables of the Ramberg-Osgood relationship were replaced with the corresponding variables for SPT  $P$ - $\delta$  responses and rearranging to solve for  $P_y$  to get

$$P_y = \frac{P}{\left\{ \frac{10}{t} \left( \delta - \frac{P}{k} \right) \right\}^n} \quad (28)$$

However, this relation is dependent on the hardening exponent,  $n$ , which is not typically known, and is of indeterminate error. This was rectified by establishing the formula of  $P_y$  as

$$P_y = k\delta_y - \frac{kt}{10} \quad (29)$$

Where  $\delta_y$  is the displacement at yield and is considered a known quantity. This is derived as determining the point of intercept of the offset line of  $t/10$  with slope  $k$  used for finding  $P_y$ , projecting downward to the displacement axis to find  $\delta_y$ .

### **3.6 SPT Assembly**

An MTS Criterion Model 42 tabletop electromechanical screw-driven load frame equipped with a 5kN load cell was used with the SPT setup, the ends of which were designed to fit this model, an example of which can be seen in Figure 3.8. The SPT test setup that was designed for this study is shown in Figure 3.8. A 90mm long load cell extension was designed and machined from 303 stainless steel to provide the clearance necessary to fit all of the components for the SPT device and the attached furnace due to the configuration of connectors between the MTS device's loading arm and load cell. The clearance afforded by the load cell extension protects these sensitive electronics from the heat of the furnace utilized for high temperature tests. This extension arm also serves as an adapter between the load cell and the components of the SPT device.

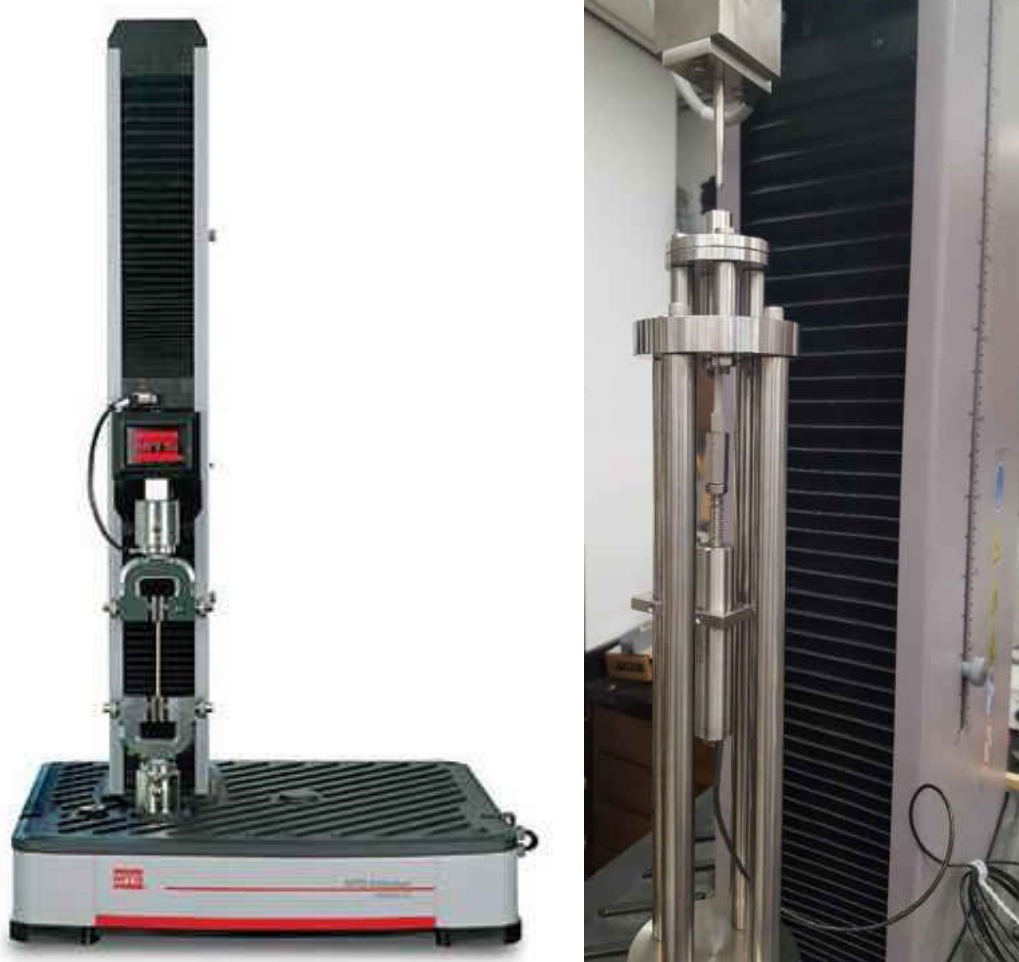


Figure 3.8 - Example of MTS Criterion Model 42 [291], to which the small punch test jig attached to load frame in single punch configuration used for monotonic style tests.

The SPT device consists of upper and lower dies with openings of 4 mm, an opening radius of 0.5mm, and a punch ball with 2.5mm diameter. Though for the initial design of the upper die hole was designed as a nominal clearance hole of 2.5mm diameter to guide the punch, it was modified to mirror the specs necessary for the lower die opening that adhere with the CWA 15627 so that when reversible cyclic loading is implemented the bending against the upper die mirrors that of the lower. The upper die also has a shank extending from the upper surface

which gradually increases the diameter slightly from the bottom to the top of the shank, acting as a guide for the tapered punch, which is inversely angled. This ensures that the punch is centered and straight when it makes contact with the sample, which will be especially crucial for the application of cyclic loads, ensuring the point of contact is constantly maintained. The dies are constructed from hardenable 4140 steel which lends itself to machining but can easily be hardened and has a high temperature resistance. The lower die has a pocket machined into the face to securely hold the sample, with radial cuts at the corners which aid in machining and as access points for extracting the deformed sample after testing. The upper and lower dies are held together by four bolts which run through the dies, standoffs, and the die support and are held on by nuts tightened using a digital torque wrench to 5Nm, clamping the sample between them. The constant use of 5Nm torque to tighten the bolts ensures that sample clamping pressure is not a factor in the results across different tests.

The punches are cut and threaded from 4.7625mm (3/16") diameter stainless steel rods which can be threaded onto the mechanism, the upper punch threading directly into the load cell extension. Additional efforts were expended to study the adaptability of the SPT fixture shown here to fully-reversed loading in fatigue. As shown in the literature review, the body of research utilizing SPT for studying fatigue properties is severely limited, with reversed cycling having been previously unexplored. As such, the design shown includes adaptability for use as a single punch monotonic or cyclic test and as a cyclic test with reversed loading featuring a second punch below the sample attached via an adapter system. Adapter plates and threaded shafts are designed to fit around and on top of the core components necessary for the monotonic testing setup, rather than as substitutes, with just a change of the bolts used to join components. The

lower punch is of the same specs as the upper punch traditionally employed in SPT, though rather than threading directly into the adapter it threads through it and is held in place by a pair of nuts and locking washers on each side of the adapter plate, which is connected to the upper adapter plate via bored and threaded 101.6mm (4in) long by 6.35mm (0.25in) diameter shafts, which also add rigidity to the system. This punch design allows for a measure of adjustability when adapting the system to a dual punch setup and facilitates the mounting of such. Shafts used in the setup are all certified for straightness, including those used between the base and die support, those utilized for the dual punch adapters, and that which provided the stock for machining the punches, ensuring direct load application and precise load and displacement measurement, minimizing compliance error effects. Closer views of the dual punch configuration and dies can be seen in Figure 3.9. The punches are tapered gradually from the 3/16" diameter at the threaded end to the 2.5mm indentations ends of the punches, which are machined with a radial depression matching the diameter of the hardened steel punch balls so as to securely hold them in place when loading or unloading the samples, and distribute loading over a higher surface of the punch balls. This also allows the punch balls to be treated as an expendable commodity, to be replaced periodically to ensure the punch tip is not damaged and consistently delivers uniform loading throughout. Although shorter punches are often used to reduce the risk of bending or buckling, the punches used in this setup are longer so as to provide distance for sensitive components such as the load cell and displacement sensor from the heat source, and rigidity is ensured by using a larger initial diameter with a gradual taper.

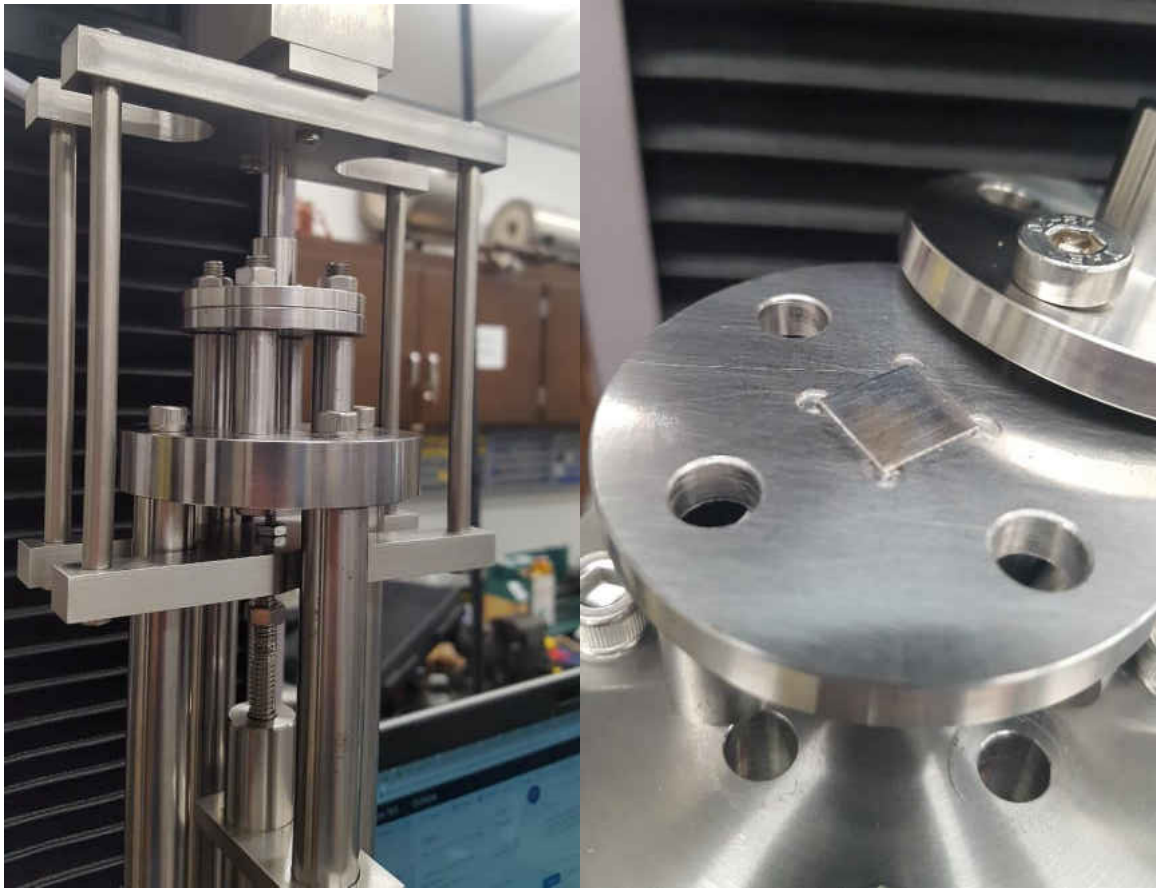


Figure 3.9 - Detailed views of the dual punch configuration and sample dies with a 10x10mm sample in place.

Standoffs between the dies and the support structure isolate the dies from the rest of the structure for the purposes of reducing heat conduction between them when the furnace is used. The furnace used for high temperature creep and fatigue tests is an Industrial Heater Corp. B74772 ceramic band resistance furnace. This furnace has an upper continuous operating temperature of 760°C, an inner diameter of 57.2mm (for which the dies were designed), and a height of 63.5mm and is powered and controlled using a Lightobject JLD-612 PID temperature controller which utilizes a K-type thermocouple to monitor the temperature of the sample and

provide feedback for the internal PID controls. The furnace is supported in place by a frame constructed of square 80/20 aluminum slotted tubing which allows for careful adjustment of the furnace in X, Y, and Z directions to optimize furnace placement and heating. Flexible ceramic insulation at the top and bottom of the heater and a heat shield constructed of sheet metal lined with insulation surrounding the circumference of the heater minimized heat loss from the dies and helped protect the rest of the components, specifically sensitive electronics such as the LVDT and load cell. Figure 3.10 shows the furnace mounted to the 80/20 frame and fitted to the SPT setup, as well as a complete operational setup showing the insulation and air cooling used to isolate heat to the dies and protect the rest of the setup. Additionally, cooling of assembly components not intended to be heated was achieved via cooling utilizing directed air streams from a laboratory air supply. A 30-minute soak time was implemented after reaching the objective temperature to ensure the entire sample was heated thoroughly and homogeneously before commencing testing.

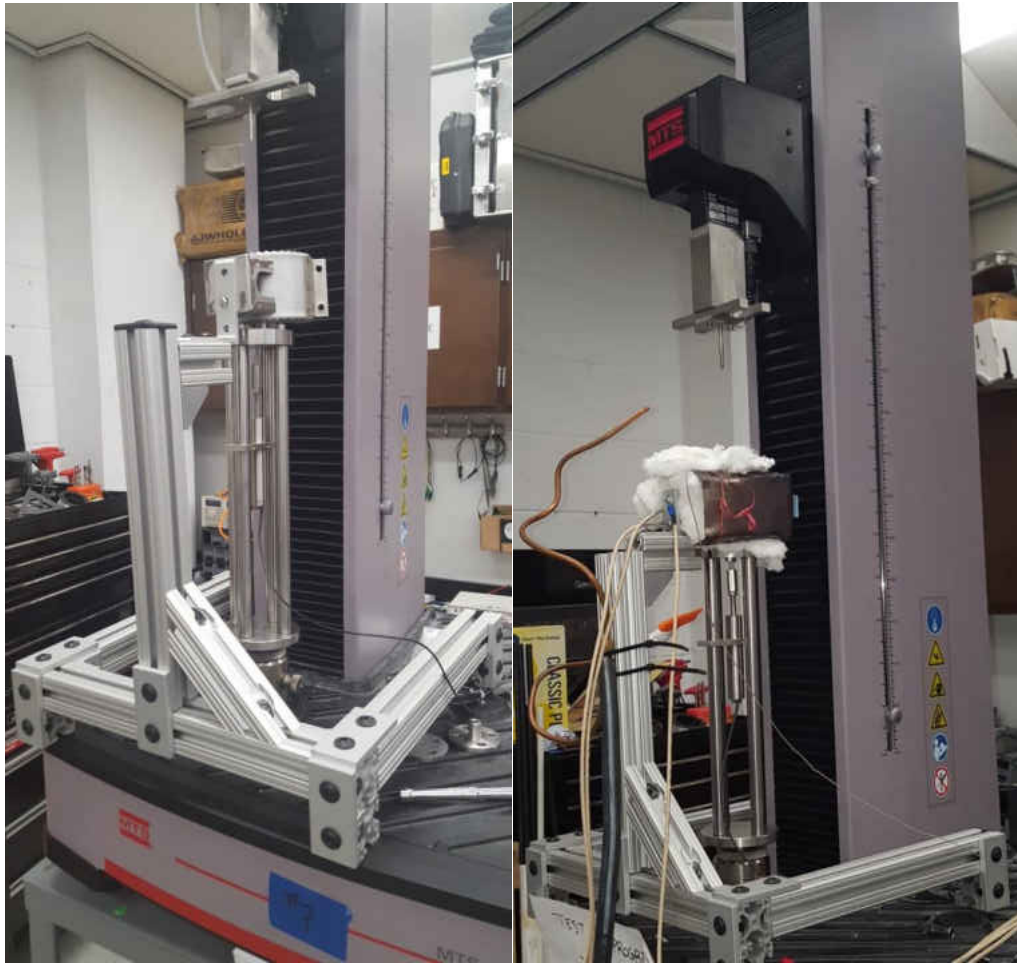


Figure 3.10 - Industrial Heater Corp. B74772 furnace mounted to a custom 80/20 frame, shown (a) as designed to fit SPT rig, and (b) fitted with insulation, heat shield, and directed air cooling used during operation.

An Omega LD621-5 linear variable displacement transducer (LVDT) with 5mm of high sensitivity travel is located directly below the sample to measure sample displacement and reduce the effects of compliance errors stemming from indirect displacement measurements. Bored and threaded shafts 305mm (12in.) long hold the die support apart from the base which adapts to the load frame fixture and a tight tolerance clamping block holds the LVDT sensor parallel to the support beams directly below the sample for accurate displacement measurements.



An alumina rod is adapted as an extension of the LVDT sensor between the sample and the sensor to protect it from the heat generated by the furnace, preventing heat conduction that would occur with direct contact of the sensor and heated samples. Displacement measurements from the LVDT help to eliminate compliance errors from flexure in the load frame or plastic deformation imparted to the sample, which would reduce the overall displacement of the sample. To establish the capabilities of the cyclic configurations and the effects of compliance errors, experimental trials were conducted using 1040 carbon steel samples, measuring displacement with both the crosshead and the LVDT, as shown in Figure 3.11. The outputs of the two measurements show significant differences, stemming from compliance errors. The most notable of these differences is that the crosshead displacement measures the full range of the programmed displacement of  $\pm 1.0\text{mm}$ , with the cycles overlapping nearly perfectly for the entirety of the test, while the LVDT shows a very different response. The LVDT displacement extends to about  $0.06\text{mm}$  in either direction, and continued cycling shows a gradual increase in force and a shift in the displacement to the left toward larger negative values and lower positive values for the peak of each cycle. Along with compliance effects, the difference between the two sets of measurements may also be due in part to the formation of a small gap between the sample surface and the punch. Once the initial indentation deforms the samples, a small gap forms between the surface of the sample the punch contacts and the face of the punch as it returns to the origin position of zero displacement. The changes in force and displacement indicate an evolution of the material, with the increased load demonstrating work hardening of the material as the punches create indentations on the surfaces of the sample. The crosshead does not detect the difference in the programmed

displacement versus that actually experienced by the sample, which would lead to errors in estimating material properties.

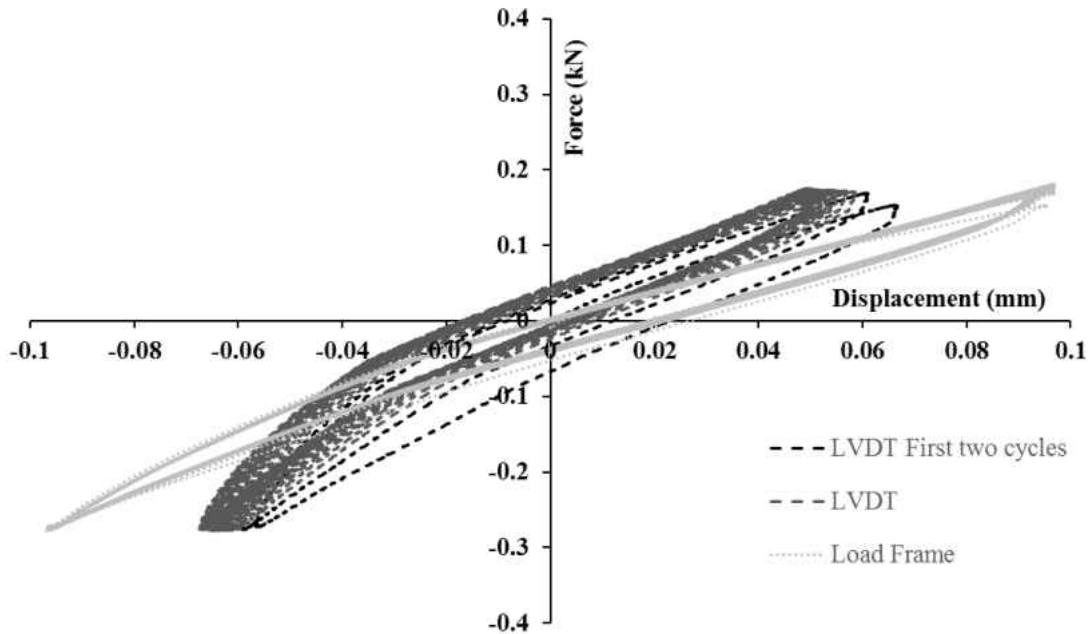


Figure 3.11 - Reversed loading of 1040 steel with a displacement range of  $\pm 1.0$ mm measured with both the load frame crossbar and LVDT.

The novel small punch test experimental setup presented here is capable of executing tests equivalent to conventional tension and creep tests as shown in literature and has been designed to expand on the current limitations of fatigue testing. The setup has been designed so that experiments mainly follow the guidelines established by the CWA 15627, with an LVDT for directly measuring sample displacement to reduce compliance errors and increase accuracy of material property estimates. A variety of materials produced via SLM and at various states of

processing will be evaluated with SPT to gage its ability to track the property differences between materials and processing states.

### **3.7 Microscopy**

Inspection of deformation to samples was conducted with the use of several microscopes including a Dino-Lite AM7013MZTS digital microscope and a UNITRON metallurgical optical microscope. The Dino-Lite is equipped with a 5MP CMOS and an adjustable polarizing lens allowing for detailed photography of reflective metallic surfaces without a glare, and is capable of magnification up to 240x depending on the adjustable working distance and focus adjustment. This makes it ideal for inspection of SPT samples and fracture surfaces without the need for extensive sample preparation. Each sample was photographed on both faces along with profile shots to characterize the indentation and fracture surfaces. The UNITRON metallurgical microscope is equipped with magnification lenses of up to 100x, and a Leica EC3 3.1MP digital camera attached to the viewfinder to record the images. Both cameras can interface with a computer for live viewing and image capture. Cross-sections of tested samples were made by the same process and tools used to section said samples from feedstock, including sectioning with Buehler Isocut slow-speed saw, mounting in epoxy, and polishing with a Buehler Ecomet polishing plate and center force polishing head, using successive grades of polishing media and lubricants to achieve a mirror finish on the sample surface. Etching of polished sample surfaces was achieved by immersion of samples into a Kalling's 2 etchant solution for around 60 seconds immediately after completion of the final polishing step. Inspection of microstructures of etched

samples was achieved through the combined use of a Zeiss optical microscope and a Phenom G1 SEM desktop microscope.



Figure 3.12 - Optical and digital microscopy station for sample inspection.

### **3.8 Data Post-processing**

Post-processing of data was necessary to organize and analyze results. As raw data is produced in the form of text files, the text files were imported into Microsoft Excel for processing, including plotting of the  $P$ - $\delta$  curve and calculation of relevant inflection points, these included the yield load,  $P_y$ , the maximum load,  $P_{max}$ , the initial stiffness,  $k$ , and other relevant values were then used in conjunction with the relationships discussed in the literature review to

assess the suitability of correlation constants established in literature. Data acquired from conventional tests were used as the measure of efficacy to which SPT data was compared. Additional evaluations of SPT data were conducted utilizing a numerical model. Where necessary, statistical analysis of the data was conducted using the SigmaZone QuantumXL software in conjunction with Microsoft Excel.

Simulations were carried out in ANSYS as necessitated by the testing array to help determine mechanical properties via the inverse solution method and to determine correlation factors to establish the framework for evaluation of SLM materials. A curve fitting method was designed and employed in order to match simulation results to experimental force-displacement curves so as to determine material properties via the inverse method. A sensitivity study was also conducted to determine the effects of varying several material properties such as Young's modulus, the strength coefficient, and the strain hardening exponent on the resulting force-displacement curves produced by a simulated SPT. Details of the model, the curve fitting methodology, and the FEA sensitivity study will be detailed further in Chapter 4.

### **3.9 Data Management**

Organization and retention of test data is of the utmost importance for successful analysis of data and continuation of this course of study. Copies of raw data and processed data files were kept in multiple instances on different computers to ensure redundancy and prevent loss of data. This includes raw data on the computer connected to the load frame, and copies of raw and processed data on a 4-terabyte hard drive with cloud connectivity, this keeps the data safe by minimizing the risk of damage to the drive while also keeping it accessible. Data files are

organized by test type and material, in single and combined files where necessary to make comparisons. Files and samples were named via an alphanumeric code where the first digit is the letter corresponding to the test type; T for tensile, C for creep, and F for fatigue, and the second and third digits correspond to the run number as designated in the test matrices. A simple naming scheme and organized storage structure ensures that data is easily accessible and comprehensible, in case the data is necessary for subsequent studies by other investigators.

## CHAPTER 4: NUMERICAL APPROACH

Finite element analysis of SPT models have been shown to be an integral part in conducting material studies, validating SP models and helping to determine material properties. The use of 2D axis-symmetric models has been shown to give reliable, replicable results in place of more complex, time-consuming 3D simulations, which offered no distinct advantages in most cases [271]. However, sensitivity studies have shown the reliance of models on several factors, such as force, the presence of voids, sample thickness, mesh parameters, friction factors, and compliance effects when compared to experimental results [272, 283, 284, 286]. Using the inverse solution method, the curve produced by an FEA model of a SPT is fitted in a piecewise manner to that produced by an experiment of the same parameters by altering the properties of the model one at a time. Once the model fits the experiment, material properties can be determined via the extraction of true stress-strain response. Studies have been done to calculate properties such as Young's modulus and yield strength and material constants in the plastic region such as strain hardening coefficients [272, 273, 276, 277]. The repetitive calculations involved in iteratively determining the values can be very costly in terms of time and computing power. As such, several studies have made efforts to automate the process. Automation of the curve fitting process has previously been completed with curve fitting algorithms and neural networks which automatically vary material properties within a certain range [272, 273]. This chapter will therefore focus on the creation, verification, and implementation of the numerical model utilized for equating experimental small punch test results to conventional material property data.

#### **4.1 FEA Model**

The model created for this study was primarily verified via comparison to a proven model established by Campitelli et al. using similar experimental parameters, with additional verification against other experimental and simulated studies [277, 292]. A 2D axis-symmetric model was utilized within ANSYS to carry out the simulation, using a static structural analysis, as shown in Figure 4.1. The upper and lower dies were modeled as rigid, fixed structures. The sample and punch were meshed with quadrilateral elements, with refinements on the edge of the punch and in the center of the sample where the majority of the deformation occurs. The elements at the center of the sample were later modified to be much denser from the center of the sample and extending this region to the majority of the free portion of the sample between the punch and the dies, so as to increase coverage in the area where the punch makes contact, with sides sized to approximately 0.035mm, and a gradual refinement increasing this size to the clamped edge of the punch. A friction factor of 0.1 was applied between the specimen and each die, to keep the sample in place during deformation, simulating the clamping contact present in the experiment. Contact and friction of 0.05 was used between the punch and specimen, for contact between the polished punch and polished sample, and represents the higher end of the friction range for lubricated materials [277]. A displacement rate of 1mm/min was employed, which is roughly equivalent to 0.02mm/sec, which is commonly employed in experimental setups following the CWA 15627 guidelines with a recommended rate of 0.2-2mm/min [195]. The model utilizes regular elasticity with a multilinear isotropic hardening model for plasticity. The model developed was compared to several literature sources to gauge reproducibility and



accuracy, as well as with a variety of materials to test its adaptability to various material types. Necessary adjustments were made for later analyses.

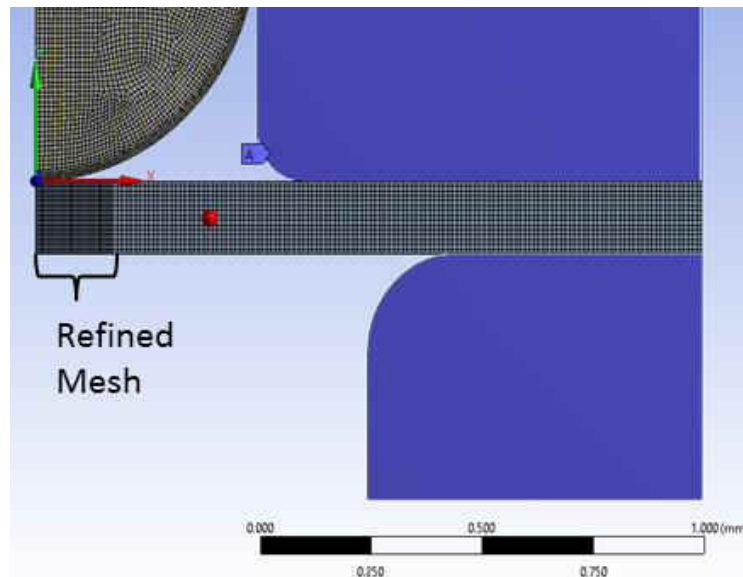


Figure 4.1 - Axis-symmetric small punch test modeled in ANSYS.

Simulations comparing the model shown in Figure 4.1 to that originally referenced by Campitelli et al. matched well in terms of the physical model deformation and strain distribution, which is shown in Figure 4.2. As the punch displaces the sample, strain begins to build up directly below the punch on the bottom of the sample, as the rest of the sample begins to bend at the radius of the bottom die. As the displacement increases the portion of the sample below the punch will begin to compress and stretch, while the portion of the sample between the punch and the lower die begins to stretch, as seen in Figure 4.2, which shows the plastic strain distribution in a 0.5mm sample of 316L at a displacement of 0.1mm.

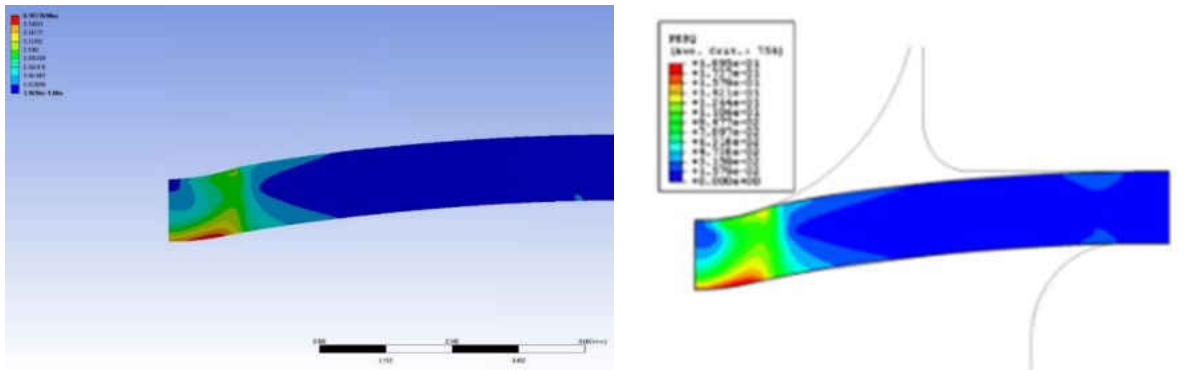


Figure 4.2 - Strain distribution within the SPT sample at a displacement of 0.1mm, as compared to [277].

The strain distribution match between the simulation and that from which it was modeled, by Campitelli et al., shows a strong correlation. Stretching and necking typically occurs most in the free area between the punch and the lower die, concentrated at the area near the punch. Figure 4.3 shows the response of an element in this region at low strain levels showing a correlation with the stress-strain response of a tensile test conducted in [277] on the same material. This correlation occurs as this section undergoes nearly continuous stretching, similar to a tensile test.

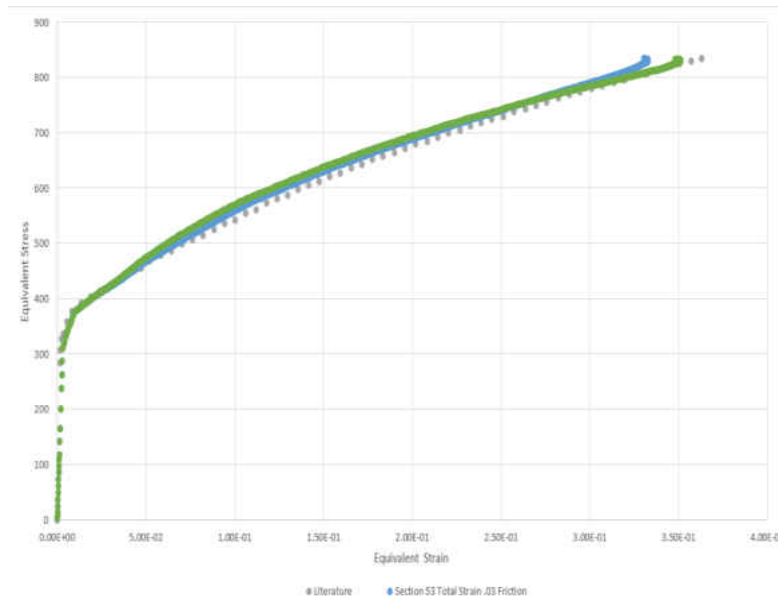


Figure 4.3 - Stress-strain response from single element in free area of sample between punch and dies as compared to actual tensile results [292].

The area directly below the punch will continue to stretch and eventually fracture, the position of the fracture will depend on the material in question and its microstructure, which will be especially relevant for the layered structures present in SLM materials. A similar experimental response using SLM materials may be expected to that shown in Figure 4.4, which shows the effects of microstructural orientation on the fracture of SP specimens extracted from extruded steel with a directional microstructure [233]. Figure 4.4(a) shows a sample where the extrusion direction is perpendicular to the surface of the sample and Figure 4.4(b) shows the longitudinal sample, where the extrusion direction is parallel to the face of the sample, and is loaded perpendicular to it, thus fracturing is parallel lines along the elongated boundaries of the grains which grow in the direction of extrusion. The transverse specimen has much more symmetric fracture as the load is applied along the direction of grain growth, though the model will not reflect these grain orientation-driven differences, especially given that the level of fracture

shown in these images represents rupture at high deflections from high temperature creep testing, and is not typical of tensile-equivalent SPT samples. The fracture behavior will have an effect on the resultant SPT curves, which will in turn affect curve fitting efforts. Modeling this type of damage accumulation requires a much more advanced model, such as those in [255, 293], but will not be studied here as fracture development is not a primary concern of this study.

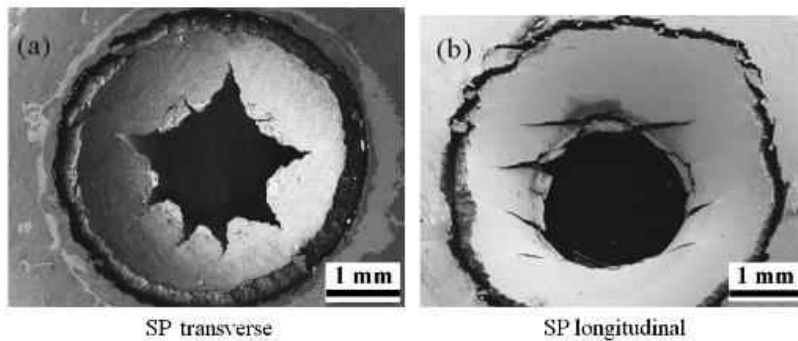


Figure 4.4 - Fracture morphology based on directional grain growth orientation [233].

The model was then tested for flexibility with material choice against another set of published experimental SPT results by Cuesta et al. [206] which utilized Aluminum 6016-T4, as shown in Figure 4.5. The force-displacement results match very well for the majority of the length of the curves but begin to diverge at the peak load and continue to do so with further displacement. This is an indication that the plasticity and damage models utilized do not properly characterize the behavior in the regime and should be modified. Similar results were seen when comparing calculated results to those seen in [277], in which the plasticity models were varied in order to provide a better match between simulations and experiments. Although most of the relevant material properties would still be able to be approximated with the model output

depicted in Figure 4.5, some level of error would be experienced when determining peak load and total displacement, which subsequently affects estimation of ultimate tensile stress and ductility.

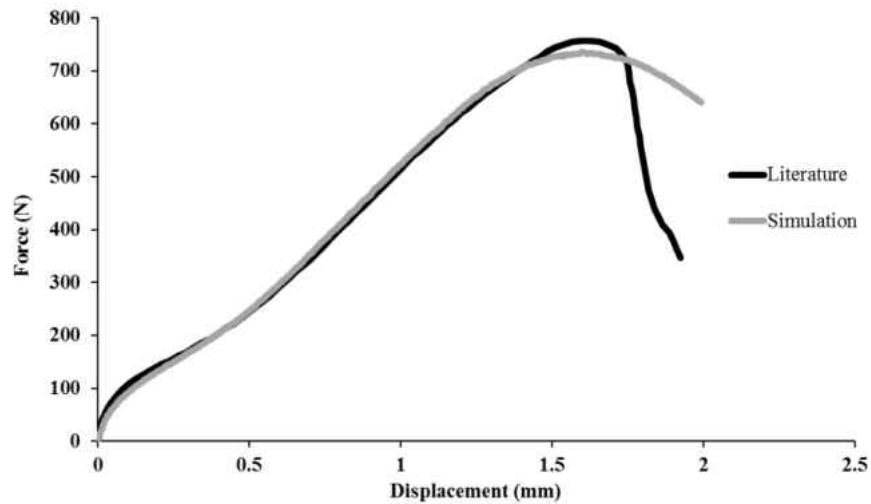


Figure 4.5 - Simulation compared to published experimental results of AL 6061-T4 [206, 292].

Additional testing of the model shows adaptability to different types of materials. The plot in Figure 4.6 shows the varied response of the model to both a ductile material, aluminum 6061-T6, and a comparatively tougher, more brittle material, AISI S7 tool steel. The material properties of the aluminum 6061-T6 and the AISI S7 tool steel were programmed into the ANSYS model using the published values and stress-strain response curves in [294, 295]. The load-displacement responses of simulated SP tests for these materials show drastically different responses, with the AISI S7 tool steel supporting a much higher load, but much lower displacement than the aluminum 6061-T6. The different sections of the SPT response curve are notable to varying degrees with each type of material, though the inflection points separating

each section which are important for calculating material properties can almost be inferred visually for both materials. The T6 curve shows significantly more stretching after the peak load, which occurs at a significantly lower load than that of the S7, but at a similar, slightly higher displacement. Although it can be difficult to distinguish from the plot, peak load responses occur at different levels of displacement; peak loading occurs at 1.4349mm and 1.4905mm for the AISI-S7 and 6061-T6, respectively. The failure region of the T6 curve extends significantly longer than that of the S7, indicating extensive stretching and thinning of material in the free region between the punch and the dies due to the higher ductility of the material.

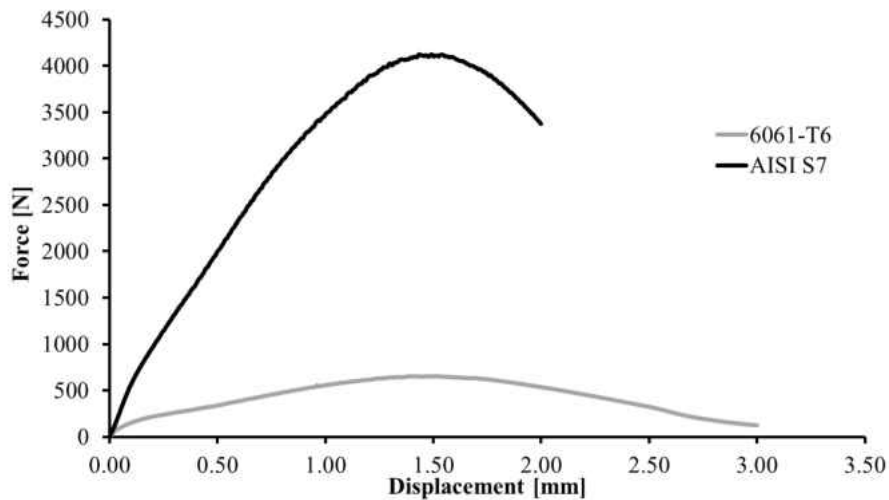


Figure 4.6 - SPT responses of comparatively tough and soft materials, AISI S7 and AL 6061-T6 [292, 294, 295].

The comparative studies conducted show the capabilities of the initial FEA model. The model has been shown capable of matching, to an extent, with experimental results when using the same material. Additionally, variation of responses can be seen when testing different classes of materials, speaking to the flexibility of the model. In order to aid in efforts to employ the

model for its intended use, the inverse solution for matching FEA results to experimental results, the sensitivity of the model to material variations needed to be further explored, and a parametric study was implemented to do so.

## **4.2 Cyclic Modeling**

As the experimental setup includes an adaptation for a dual-punch setup for conducting cyclic reversible-loading, a variation of the model was made to reflect this capability, as well as that of cyclic loading with a single punch. Concurrent to the experimental trials conducted using 1040 carbon steel samples used to verify the capabilities of the setup, the model was modified to reflect the experimental conditions, as shown in Figure 4.7. The model shows twin dies and punches of diameters 4mm and 2.5mm, respectively. The punches move in unison to a range of  $\pm 0.06$ mm displacement at a rate of 1mm/min, as was done in the experiment conducted for comparison between the experimental outputs and the simulation. On the initial displacement in each direction, the surface of the sample is plastically deformed. Beyond this initial deformation, however, there is little damage to the contact surfaces upon repeated loading during cycling, but the sample continuously bends at the edges of the dies.

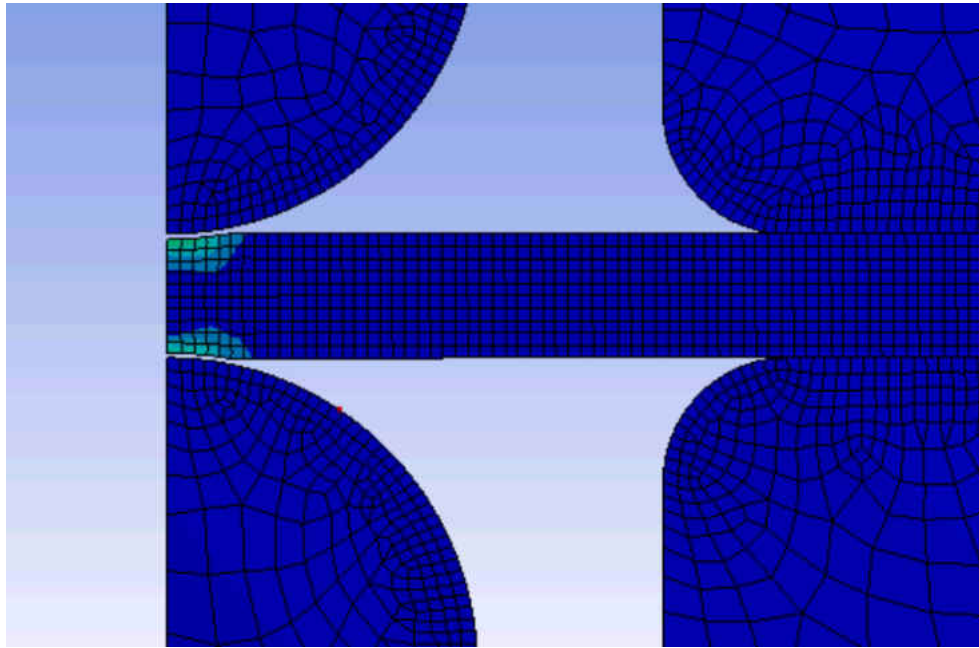


Figure 4.7 - Dual punch configuration for reversed-loading cyclic testing.

Notable differences can be seen in the responses between the experimental measurement with the LVDT and the simulation output. The load response in Figure 4.8 is significantly higher for the simulation than that of the experimental responses. This is likely due to the material profile used for the 1040 in the simulation not matching the actual properties of the sample used for the test. The other notable difference between the experimental and simulation responses is the level of hysteresis occurring in the experimental data but not in the simulation. This is due to the displacement and force measurements in the model being sensed at nodes on the tips of the punches, so that displacement is being registered even as the load is removed from them due to the loss of contact with the sample surface due to the sample thinning from the plastic deformation caused by the initial indentation.



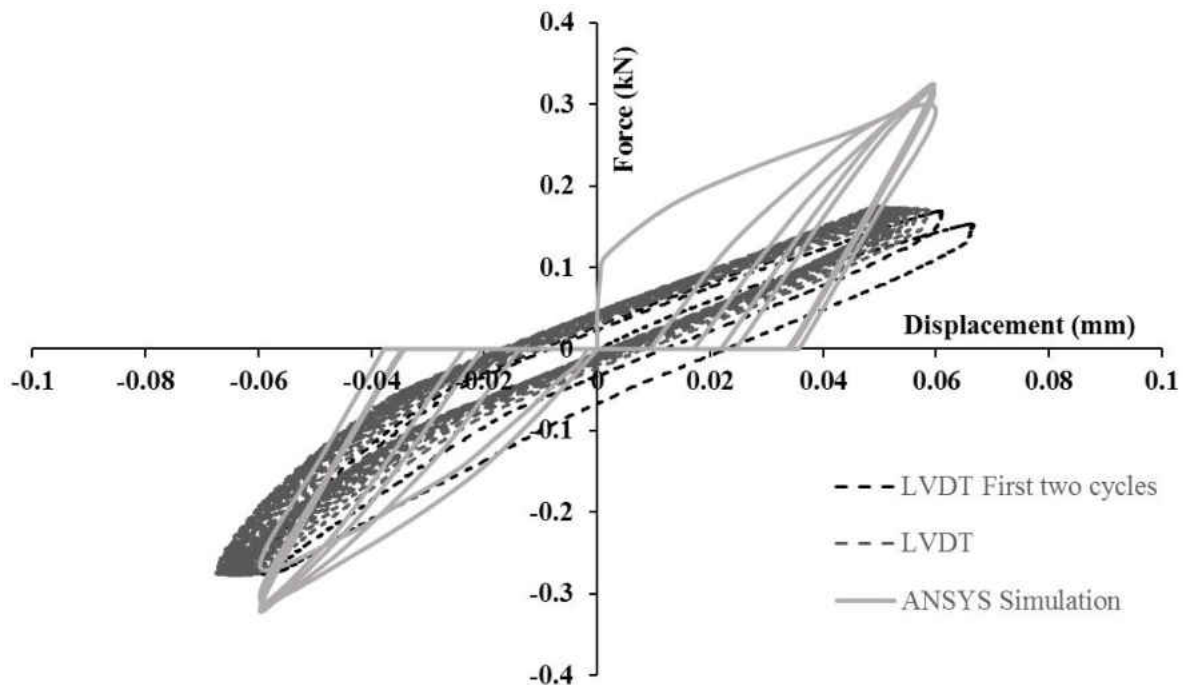


Figure 4.8 - Cyclic test data acquired with an LVDT using 1040 carbon steel with reversed loading as compared to FEA simulation output.

The results of the cyclic model show strong correlation with experimental results. The curves of both the experimental and cyclic trials show similarities, but also significant differences. Improvement of the model will aid in predicting fatigue behavior of SPT materials and correlating results with conventional testing results.

### **4.3 Parametric Study**

A full-factorial experimental matrix was designed to establish the effects of the Young's modulus,  $E$ , the strength coefficient,  $K$ , and the hardening exponent,  $n$  on the resulting force-displacement curves of otherwise identical experiments [292]. This will aid future curve fitting

efforts for approximating simulation results with experimental results, minimizing error between them. The factors  $K$  and  $n$  come from the relationship for true stress and true strain.

$$\sigma = K\varepsilon^n \quad (30)$$

This relationship, Hollomon's law, helps to describe what happens in the plastic region when a material deforms and undergoes strain or work hardening. The strain hardening exponent,  $n$ , is used to describe the plasticity of a material, ranging from 0 to 1, with 0 being described as perfectly plastic and 1 as perfectly elastic. Combined with Hooke's law, which describes the elastic portion of a material's behavior, the formulation of the Ramberg-Osgood relationship is established, which can describe the entirety of the stress-strain curve for a strain-hardening material.

$$\varepsilon = \frac{\sigma}{E} + K \left( \frac{\sigma}{E} \right)^n \quad (31)$$

These factors are well suited for use in studying the model sensitivity as related to changes in material properties. Determining the influence of these factors will help to tune the influences of each so as to refine the results and improve the accuracy of simulations as compared with experimental results, in order to determine material properties of materials tested with SPT.

The median values for these factors (Level 3 in Table 4.1) were chosen as the approximate mean mechanical properties of IN939 from various sources at room temperature, being the material basis for future studies [55, 56, 296, 297]. Each factor was then varied by  $\pm 10$

and 20% from the median value, a common practice when utilizing DoE and ANOVA, to establish a total of 5 levels for each factor, as shown in Table 4.1, for a complete test matrix of 125 experiments. The factors and levels were input into the SigmaZone QuantumXL statistical software to design the full-factorial study, which provided the factor levels necessary for each run. As the tests conducted were simulations, multiple replicates were not necessary.

Table 4.1 – Factor levels for full factorial parametric design study.

	<b>Level</b>				
<b>Factor</b>	<b>1</b>	<b>2</b>	<b>3</b>	<b>4</b>	<b>5</b>
<b>E (MPa)</b>	160000	180000	200000	220000	240000
<b>K</b>	880	990	1100	1210	1320
<b>n</b>	0.08	0.1	0.12	0.14	0.16

The experiments were programmed into the ANSYS model for evaluation and the effects of each case were determined by analyzing the effects on several points throughout the load-displacement curves, which correspond to either specific inflection points or were chosen as being representative of each region of the curve as denoted earlier in the experimental section, and are named after those regions as designated in [15, 273]. The design was then analyzed using ANOVA, and a regression was run to analyze the effects of each factor. The contributions of each of the independent factors are shown in the Pareto plot in Figure 4.9 in terms of percent contribution. It is important to note that since this graph only accounts for the main factors, and does not show the interactions of these factors, each set may not equal unity. The points are

ordered in terms of their appearance on a  $P$ - $\delta$  curve in terms of stages from left to right, showing the trends of factor influence as deformation increases.

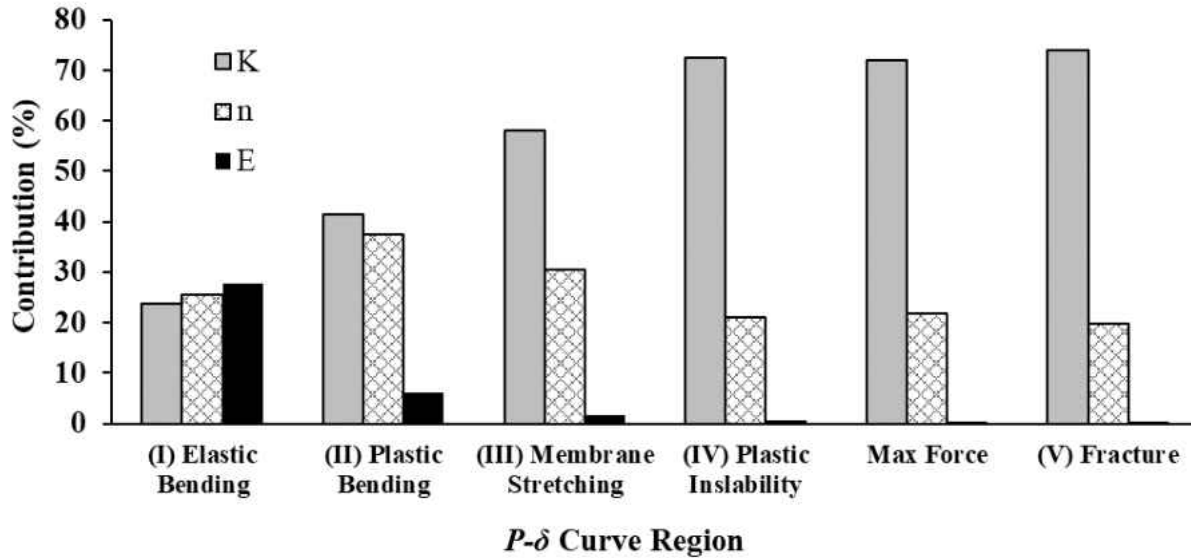


Figure 4.9 - Percent contribution of main factors to the various sections of the SPT force-displacement curve.

The normalized percentage values show that for the majority of the force-displacement curve the strength coefficient,  $K$ , is the dominant factor, and nearly always by a wide margin. The hardening coefficient,  $n$ , is always second most influential, though the effect varies depending on the section of the curve in question, while Young's modulus,  $E$ , is largely ineffectual. The exception to this, of course, is in the primary, elastic portion of the curve, where although  $E$  affects the outcome the most,  $K$  and  $n$  each have an almost equal effect as  $E$ . These trends are to be expected, as the power law in which  $K$  and  $n$  are used to describe material behavior pertains solely to the region of plastic deformation, while the elastic region is primarily

described by Hooke's law, in which only  $E$  is present. However, this contribution by  $K$  and  $n$  to the elastic portion of the  $P$ - $\delta$  curve indicates that this region is not wholly elastic, and so as was suggested in [221] a universal constant using the slope of this region to determine a correlation may not be viable. There is also a small notable effect from the Young's modulus to the plastification region, and a nearly negligible contribution to the hardening region, which sequentially follow the elastic portion of the force-displacement curve. Logically, a trend can be seen in the diminishing influence of  $E$  as displacement progresses and damage transitions from elastic to fully plastic, with a combination of the two occurring somewhere in the plastification region. It is also worth mentioning that for all but the elastic and plastification zones, the interaction between  $K$  and  $n$  has a larger effect than  $E$ . As mentioned, this is not the case for the elastic zone since  $E$  is the dominating factor there and the interactions of  $E$ - $K$  and  $E$ - $n$  are much more relevant than  $K$ - $n$ . However, for the plastification zone, even though it is the zone with the second highest effect from  $E$ , contribution from the interaction between  $K$  and  $n$  is nearly equal to that from  $E$  alone. Select responses of this study as detailed in Table 4.2 to aid in the visualization of the variations of the responses caused from altering the parameters and the different combination of such. The runs selected represent cases with varying combinations, from all high values to all low values, with varying combinations in between, to give a full spectrum of possible responses by which to gauge the effects of each variable.

Table 4.2 - Factor levels of select runs for comparison of effects.

	<b>Run</b>				
<b>Factor</b>	<b>5</b>	<b>13</b>	<b>21</b>	<b>75</b>	<b>76</b>
<b><i>E</i> (MPa)</b>	200000	200000	200000	240000	160000
<b><i>K</i></b>	880	1100	1320	1320	880
<b><i>n</i></b>	0.16	0.12	0.08	0.16	0.08

The responses of these runs are visualized in Figure 4.6, which the complete curves and a detailed view of the initial linear portions of such. The responses vary widely from the linear portions to failure, regardless of the values of the factors used. Specifically, the variation in the initial liner response shows its dependence on all three factors, even though the Young's modulus has been shown to be the dominant factor, as runs 5, 13, and 21 all share the same value for  $E$  but display highly varied responses based on the combinations with the designated values of  $K$  and  $n$ .

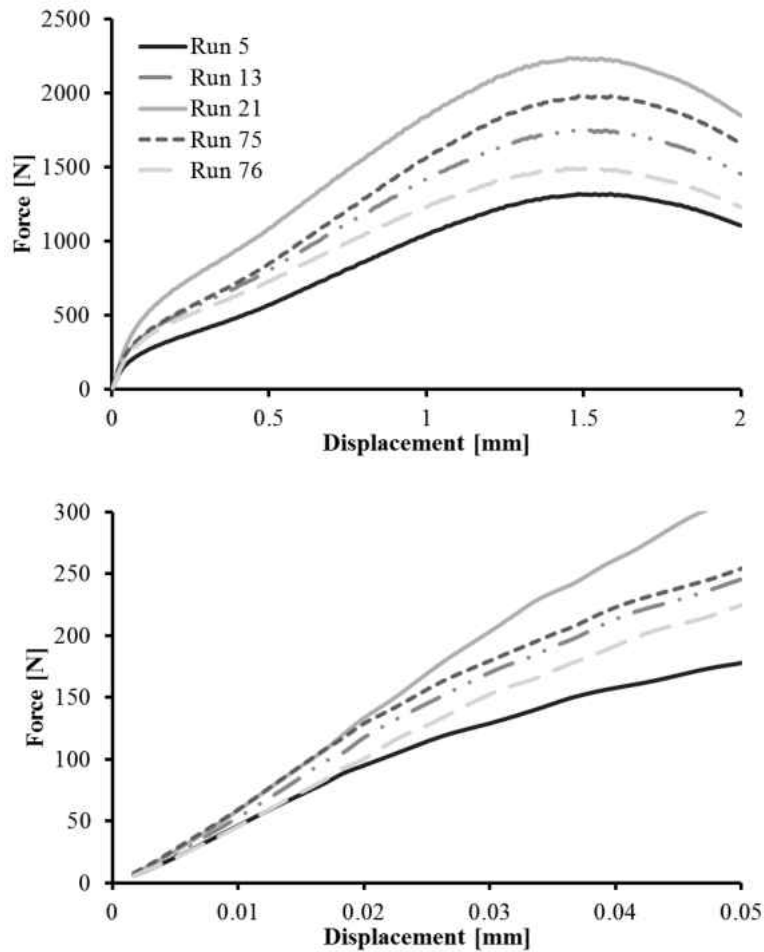


Figure 4.10 - Select curves from the parametric study, and the linear portions of such [292].

The curves in Figure 4.10 represent several varied cases within the study: run 13 correlates with the Level 3 settings in Table 4.1, with all of the median values for IN939 at room temperature, run 75 correlates with the Level 5 settings with the high end values for all factors, and run 76 correlates with the Level 1 settings where all factors are set to the low values. Comparing these three sets the combined effects of altering the factors can easily be seen, beginning almost in the elastic range. The slope of the elastic region increases with increasing factor values, and a continuous divergence of the three curves occurs as displacement increases.

Runs 5 and 21 keep the Young's modulus,  $E$ , at the median value combined with a low  $K$  and high  $n$  or high  $K$  and low  $n$ , respectively. These two cases represent the extremes in this plot in terms of response. The initial, elastic portions of the curves match very well with the cases correlating with the Level 1 and Level 5 settings. Run 76, in which all factors are set to low, and run 5, which has a low  $K$  and high  $n$  match in the elastic zone and quickly diverge, with the gap between them staying nearly equal. Note that the combination of low  $K$  and high  $n$  lowers the force levels of this response throughout, a logical response to a material with a lower strength coefficient and higher hardening constant. On the other end of the spectrum are Run 75, which has all of the factors set to the high values, and Run 21, which combines the median value of  $E$  with a high  $K$  and a low  $n$ . In this case the two elastic portions again match but for a slightly larger displacement level, with a more pronounced difference occurring throughout the lengths of the curves, with the difference escalating slightly with increasing displacement. This more pronounced difference, the highest of which occurs at the peak load, occurs due to the low hardening coefficient allowing for more of a divergence between the two. This small selection of curves shows how prominent the effect of changing these factors and their interactions are on material response. Interesting to note is that the most extreme responses here are elicited by the combinations of the opposing extreme values of  $K$  and  $n$ , rather than by those on the same end of the tested range.

As the microstructures and material properties of AM materials, such as those from SLM, have been shown to be highly sensitive to both processing parameters and post-processing conditions, the advantages of utilizing the small punch test to evaluate them become immediately evident [128, 142]. As the changes in SLM material microstructures can range from minor to



major depending on the variations employed in processing or post-processing, tracking them with a very sensitive method is of high importance. As SPT has been shown to be sensitive to minor changes in small volumes, this then becomes a highly attractive option for optimizing processing parameter settings and post-processing routines. The Pareto plot and the resultant curves from the parametric curves show that the model implemented here is in fact sensitive enough to track these changes as well, which is necessary in implementing the model for its intended use.

#### **4.4 Intended Use: Inverse Solution Method**

A case has been made for the use of the small punch test to evaluate selective laser melted materials. An FEA model was constructed in ANSYS and tested with varying material types, and a subsequent parametric study was designed to test the sensitivity of the model to varying material conditions. As such, the subtle changes that will arise in SP testing various SLM samples with minor processing variations can be evaluated by using the model presented here with the inverse solution method so as to extract stress-strain data and subsequently the relevant material properties. This allows for tracking the evolution of an SLM material through changes in processing parameters and through the various stages of post-processing. Recent studies reviewed here and the adaptability and sensitivity of the model presented here show that the small punch test is a suitable method for optimizing SLM materials and processing.

The model will primarily be employed for the implementation of the inverse solution method to determine material property values from experimental data of small punch tests conducted here, as outlined in the literature review. This will allow for a direct and more

accurate comparison against results established with conventional tests, as well against estimates made using correlation factors as outlined in the literature review. The inverse solution in this case is accomplished via the use of sum of squares of error, also known as the residual sum of squares, using minimization of this as a target within ANSYS workbench for optimization of the simulation response based on the factors  $E$ ,  $K$ , and  $n$ . The residual sum of squares (RSS), can be described by the equation:

$$RSS = \sum_{i=1}^n (y_i - \hat{y}_i)^2 \quad (32)$$

where  $y_i$  is the predicted  $i^{th}$  value of the variable being estimated and  $\hat{y}_i$  is the corresponding  $i^{th}$  value of the experimental results. That is,  $y_i$  represents the force values of the simulation and  $\hat{y}_i$  represents the corresponding force values of the experimental results. Thus, the sum of squares of error targets the force response of the simulation and compares it to the experimental response input into the system, working at 10% intervals up to the force corresponding to the maximum displacement, adjusting  $E$ ,  $K$ , and  $n$  to systematically adjust the curve to minimize the difference in the responses between the simulation and the experimental data. Once the optimization program within ANSYS determines the  $RSS$  value has been minimized as much as possible, the material model in the SPT simulation produces a force-displacement curve equivalent to that of the experimental result to which it was matched. That same material model can then be used to extract a true stress-true strain plot, which is used to analyze material properties such as yield strength, ultimate strength, and Young's modulus, which are compared to conventional test results to gage accuracy. The iterative process by which this is done, matching the simulation to the experimental results in a piecewise manner, is explained graphically in Figure 4.11, showing

the similar process utilized by Husain et al., which proved successful for extracting accurate stress-strain curves from SPT results for a variety of steels [276]. As was noted in Figure 4.9, the effects of the factors considered for executing the curve fit depend on the point of the  $P$ - $\delta$  of interest. In Figure 4.11, these points are denoted by the corresponding occurrence of the load  $P_x$ , with  $x$  being the order at which the load occurs, with an increase in  $x$  denoting an increase in total displacement. By using ANSYS to carry out these calculations, the time expended by investigators is economized, as factor adjustments and fit calculations are carried out automatically.

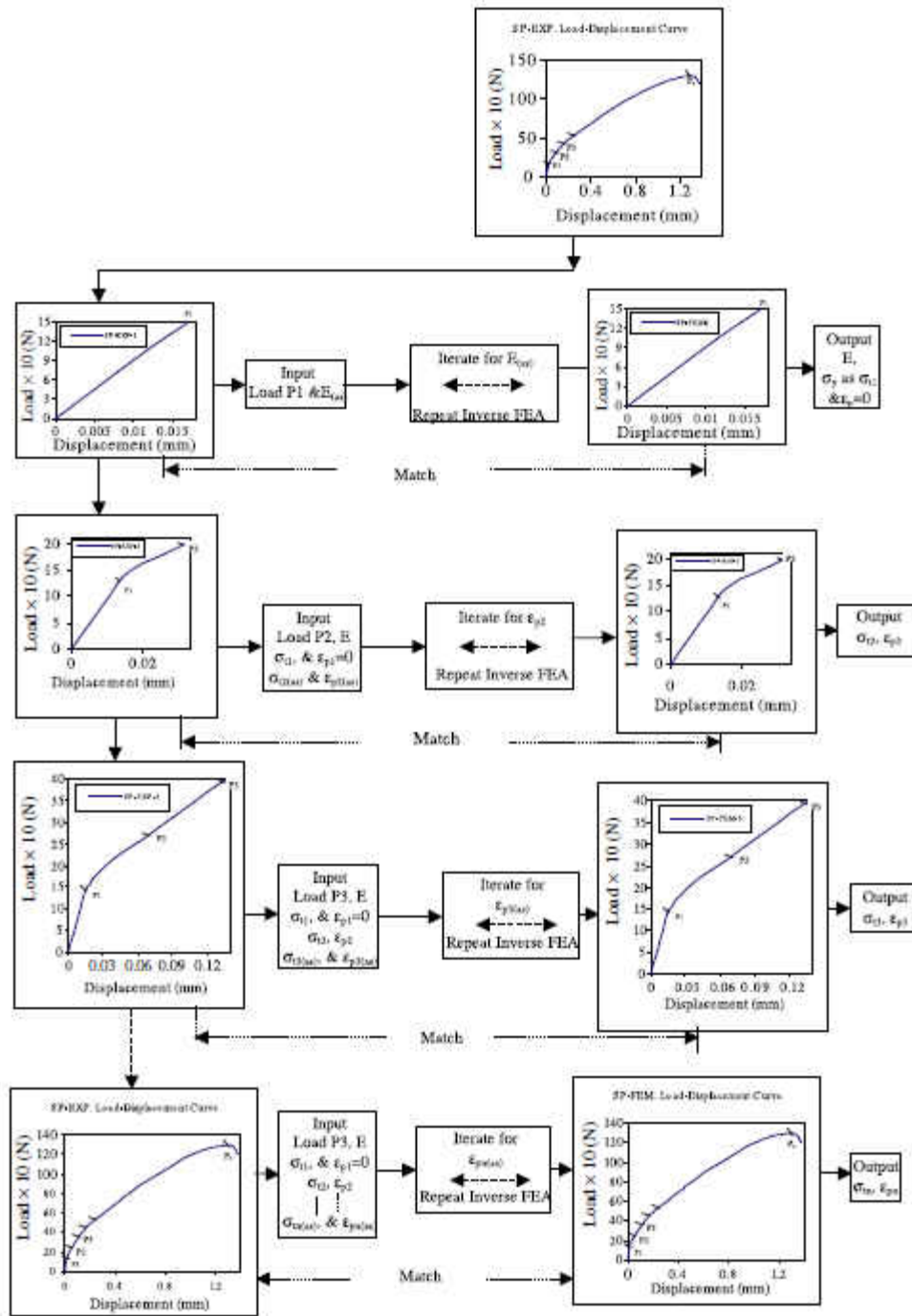


Figure 4.11 - Graphical representation of the piecewise manner in which the inverse solution method is used to match the simulated response to the experimental response [276].

The creation and verification of the FEA model against experimental results will play a key role in determining the material properties of samples tested with SPT. Although general trends can be established by examining the  $P$ - $\delta$  results, the inverse solution provides the most accurate and dependable approach to determining the true stress-true strain behavior. This is necessary for determining material properties to the extent of being able to compare SPT results to those acquired via conventional testing.

## **CHAPTER 5: EXPERIMENTAL RESULTS**

The experimental results for the several test types explored in this study will be presented here. A detailed analysis of small punch test results and comparisons of these will be included, closely examining the effects of manufacturing and testing variations. Correlations between experimental results and simulations will help to establish material property values using the inverse solution method. Finally, observations from microscopy will be utilized help to explain differences between trials.

### **5.1 Small Punch Test Results**

This section will explore the results of the small punch tests conducted as outline in section 3.4. Test results will be presented in a number of subsections based on the differences present between the trials being compared. In this manner, several subsections will follow exploring the effects of both testing variables and the sensitivity of test results to material processing variables such as orientation and heat treatment. By doing so, the effects of several variables can be established in order to determine the suitability of SPT for evaluating SLM materials, while simultaneously expanding the known capabilities of the small punch test.

#### **5.1.1 Effects of Post-Processing Routines**

Several of the trials listed in Table 3.2, T4 through T9, are designed to use samples sourced from the tensile tests conducted in the recrystallization study outlined in Table 3.1, and are meant to mimic those tests. These tests are designed specifically to evaluate the ability of the small punch test as a means to track gradual changes in microstructure due to variations in the

recrystallization implemented in the post-processing of IN939V to reduce the anisotropic characteristics of the as-manufactured material. The responses shown in Figure 5.1 show the  $P$ - $\delta$  curves of these samples, while the equivalent tensile responses can be seen in Figure 3.3. These curves show a variation in the response depending on the post-processing recrystallization cycle implemented on the samples, and are labeled by their respective recrystallization study designation, with RX7 and RX8 having forgone the recrystallization cycle and instead received only the hot isostatic pressing and successive heat treatments and serve as a basis for comparison of the effectiveness of the recrystallization cycle treatment. Samples for RX1 and RX2, trials T6 and T7, respectively, were treated for a base recrystallization time at the recrystallization temperature,  $T_{RX}$ , while samples for RX3 and RX4, trials T4 and T5, respectively, were treated for a time of 3X base in otherwise identical conditions.

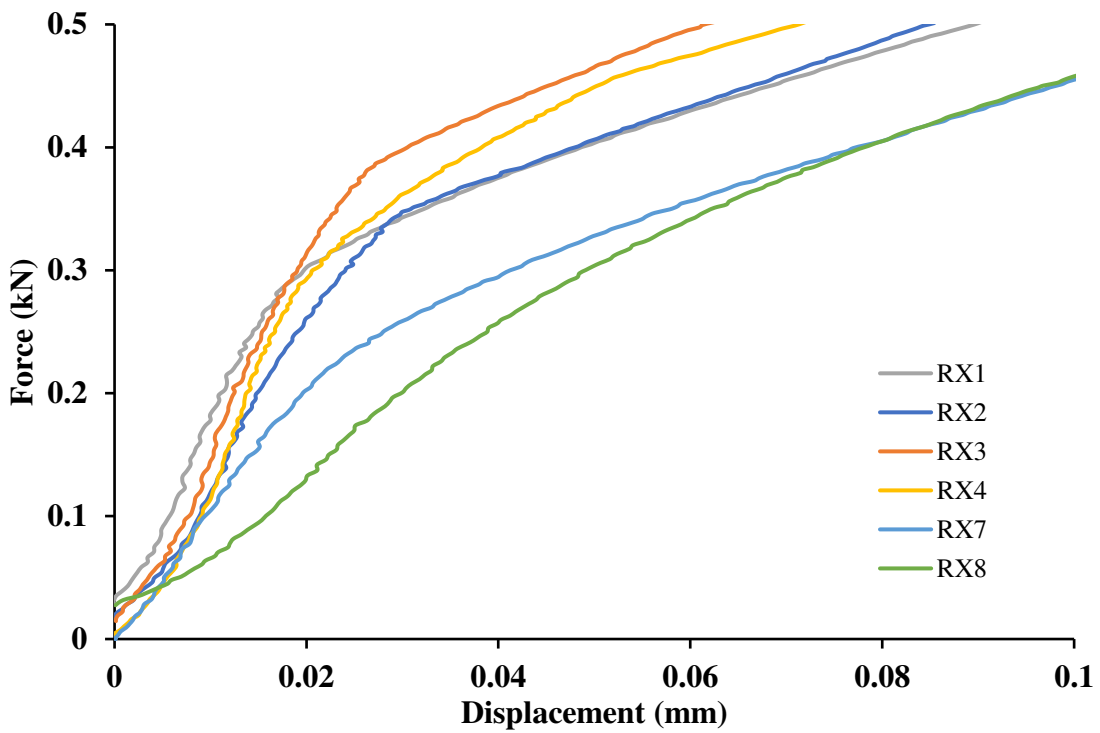
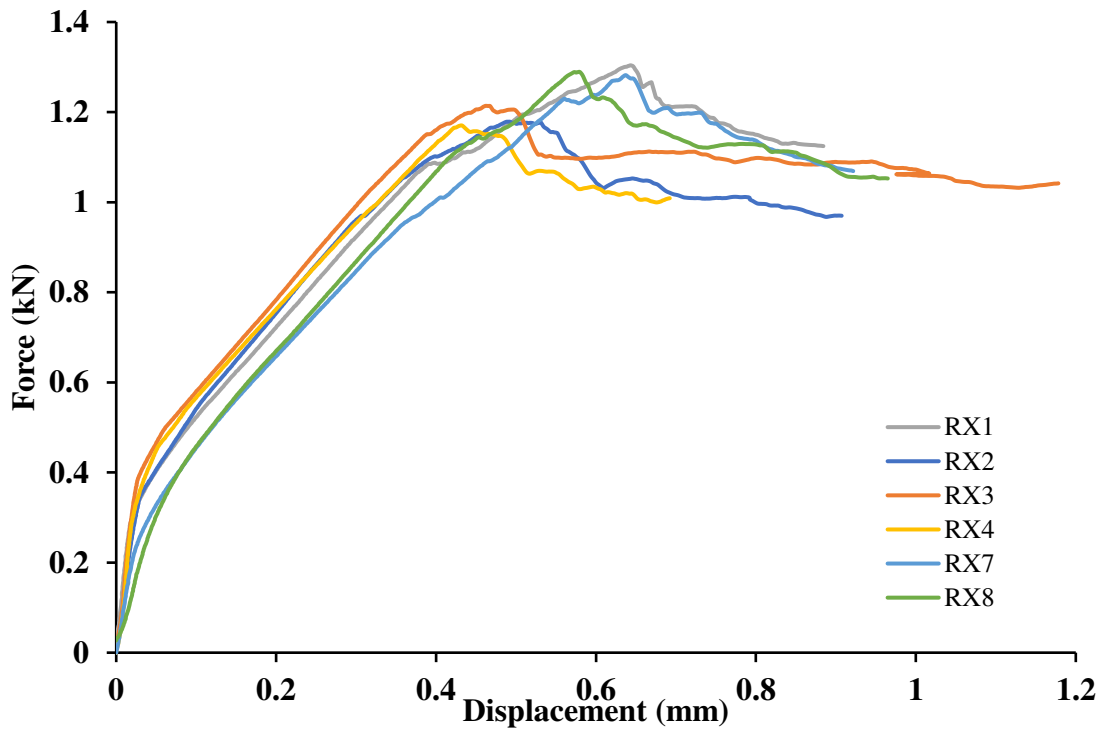


Figure 5.1 - Small punch tech test response of samples sourced from tensile tests conducted during the recrystallization study outlined in section 3.2.1.



The most prominent feature of note when simultaneously comparing all six trials is an evidentiary reduction in strength, which corresponds to the occurrence of  $P_{max}$ , with the implementation of a recrystallization cycle. This seems to continue as the recrystallization time increases, as  $P_{max}$  generally occurs at lower values and also earlier on, at a lower value of  $\delta_m$ . The samples which were not recrystallized, RX7 and RX8, diverge in the first and second regions, overlap for most of the third region, then diverge and switch position during the latter portion of the third region, of which RX8 has a longer duration, as the sample for RX7 has a longer plastic instability region, the fourth zone of the  $P$ - $\delta$  curve. Sample RX8, however, peaks earlier and at a higher level than RX7, and the two seem to converge again later in the failure region, suggesting similarities in the failure region and latter stages of ductility. To aid in inspection of the fractures of each specimen and ascertain their differences, however, samples were not tested until total failure, but stopped after a significant load drop indicating the appearance of a fracture and a limited amount of growth of the crack. Closer inspection of the elastic regions of these curves reveals a notable difference in their slopes, much larger than any of the other equivalently-treated pairs of differently-oriented samples. Given the collective differences in elasticity, strength, and ductility, a significant amount of anisotropy can be deduced to exist between the two directions.

Samples from RX1 and RX2, treated with a Base recrystallization cycle, conserve some of the behaviors of those displayed by the non-recrystallized samples. In the primary section of the responses of RX1 and RX2, the elastic portion, the gap is considerably reduced from that between RX7 and RX8, the non-recrystallized tests. The slopes of these portions of the curves appear almost parallel, which would make the elastic moduli equal, though they diverge somewhat in the latter portion of the elastic zone, prompting an assumption that they are not. The

two curves begin to merge at the end of the elastic zone, but then begin to diverge soon after, as they cross and diverge early in the third region, then cross again as RX1 resists instability and fracture for much longer than RX2, as  $\delta_m$  for RX1 occurs at 0.64mm, as opposed to 0.49mm for RX2, accompanied by a higher strength at 1.30kN for RX1 versus 1.18kN for RX2, though the rate of increase in the third region, and thus the plastic behavior up to the instability zone just before fracture seems to be equal for both orientations. This is akin to the behavior displayed by samples from RX7 and RX8, as both RX1 and RX7, which were manufactured in the transverse direction, have a higher  $\delta_m$  than their longitudinally-manufactured counterparts, suggesting higher ductility and resistance to loading. A comparison of these two sets of trails also indicates that the recrystallization heat treatment initially impacts the strength of the longitudinally-manufactured samples more so than the transverse ones, as the elastic portion and the peak load of RX2 change more dramatically when compared to RX8 than RX1 does when compared to RX7.

This is continued, logically, when inspecting the curves of RX3 and RX4, which were recrystallized at a 3X Base time, relative to RX7 and RX8, as they are now nearly overlapping and remain parallel in the elastic region, suggesting equal moduli. The elastic regions persist for a longer range of displacement than those of either RX1 and RX2 or RX7 and RX8, and the modulus also appears higher for the longer treatment, reinforcing the direct correlation between the increasing modulus with treatment time, and a reduction in the anisotropy of such, as the initial slope of the  $P$ - $\delta$  curve has been linked as a direct correlation with the Young's modulus. In a macroscopic view, the two curves match up very well, with only a small gap separating them for the majority of their length, with the peak loads being only 3.5% different, from 1.214kN for

RX3 to 1.171kN for RX4, and a difference of only 4.3% when normalized with respect to thickness and displacement. This indicates a significant reduction in anisotropy between the two directions, when compared to the un-recrystallized samples of RX7 and RX8, and even in comparison to the shorter Base treatment times undergone by the samples for RX1 and RX2. There is also, however, an overall considerable reduction in strength when compared to RX7 and RX8, and another smaller further reduction of the transversely-built samples between the Base and 3X Base trials (RX1 vs. RX3). The successive reductions in strength, however, are crucial to the reduction in anisotropy, as the recrystallization treatment affects the transversely-built samples more dramatically than the longitudinally-built samples, closing the gap between the two directions over time. This suggests the possibility of a limit to the effectiveness of the recrystallization cycle for reducing anisotropy, and it's unclear whether a further extension of the cycle time would lead to any further homogenization of the two directions, or just continue to reduce strength while maintaining a difference between them.

It must be considered, however, that the correlation of  $P_{max}$  with the ultimate strength of a material has been shown to be dependent on the displacement,  $\delta_m$ , at which  $P_{max}$  occurs as well as the thickness,  $t$ , of the sample. In effect, this will work to reduce the differences in strengths when peak loads between two samples occur at very different values of  $\delta_m$ . As such, Table 5.1 more directly quantifies the differences between the samples as they occur in the  $P$ - $\delta$  curves shown in Figure 5.1. These values show similar trends to those ascertained by visual comparison of the curves but show significant differences dependent on sample thickness and the value of the displacement at maximum load.

Table 5.1 – Relevant inflection points and normalized values corresponding to material properties for small punch tests of recrystallization study test samples.

	<b>RX1</b>	<b>RX2</b>	<b>RX3</b>	<b>RX4</b>	<b>RX7</b>	<b>RX8</b>
$P_{max}/\delta_{mt}$ (MPa)	4269.1 ± 0.046	5237.7 ± 0.058	5566.6 ± 0.060	5807.8 ± 0.063	4265.8 ± 0.046	4734.9 ± 0.051
% diff.		-22.70		-4.33		-11.0
$P_{max}/t^2$ (MPa)	5778.8	5643.9	5449.1	5367.1	5754.2	5837.1
% diff.		2.34		1.50		-1.44
$k/t$ (GPa)	37.31 ± 0.384	33.48 ± 0.304	41.45 ± 0.366	46.63 ± 0.351	21.77 ± 0.232	12.58 ± 0.152
% diff.		10.26		-12.50		42.22
$P_{y(u/10)}/t^2$ (MPa)	2068.9 ± 0.010	2383.1 ± 0.007	1659.0 ±0.008	1467.8 ± 0.008	1903.6 ± 0.006	2288.8 ± 0.004
% diff.		-15.18		11.53		-20.23

Inspecting the values in Table 5.1 and the percent differences between the directions for each set of treatment reveals similarities and differences to the visual trends. A notable reduction of  $P_{max}$  is seen as recrystallization time is implemented and with the increase in time. The implementation of the cycle also increases the anisotropy, but the extended duration reduces the difference between orientations. This trend continues when the values are normalized, though normalization with respect to thickness and displacement shows a much higher difference than those normalized with the square of the thickness, which are included here solely for the sake of showing this disparity. Considering the  $P/\delta_{mt}$  values reveals some inconsistencies, as these values actually denote an increase in strength with increasing recrystallization time, as well as a dominance in strength favoring the vertical orientation. Normalization with respect to thickness only shows a general trend of decreasing strength with respect to increasing treatment time, indicating either errors in the displacement values or an incompatibility of AM materials tested in SPT with the normalization techniques which utilize this metric. Inspecting the normalized

values corresponding to the modulus and yield strength shows a general reduction in anisotropy with implementation and extension of a recrystallization cycle. Notable is that both of these traits seem to switch in terms of the dominant orientation when considering the extended recrystallization cycle as opposed to the base cycle or the non-recrystallized samples. This is denoted by a change in sign from negative, which indicates higher values for vertical samples, to positive, which indicates higher values for horizontal samples.

The effects of post-processing can be better assessed by comparing samples produced from uniform donor geometries, such as those acquired from the large blocks. Using these, samples for each condition can be sourced from the same donor for both orientation, so that geometry and its effects on initial and post-processed microstructures are not a factor, as they are in the recrystallization study, where the transverse samples were produced with the long direction parallel to the build plate and the longitudinal samples were produced with the long side perpendicular to the build plate. As seen in section 5.2.2, donor geometry differences such as these induce differences in cooling rate between layers, which will inherently affect microstructure and resultant material properties. The responses of monotonic room temperature tests for samples sourced from large blocks in both the as-manufactured and fully post-processed states are shown in Figure 5.2. Like in the recrystallization study trials, there is a severe indication of anisotropy in the as-manufactured samples, which is significantly reduced after heat treatment. As established previously in the tensile RX study, samples labeled as fully heat treated herein will have been treated with the longer recrystallization cycle, in an effort to reduce anisotropy as much as possible.

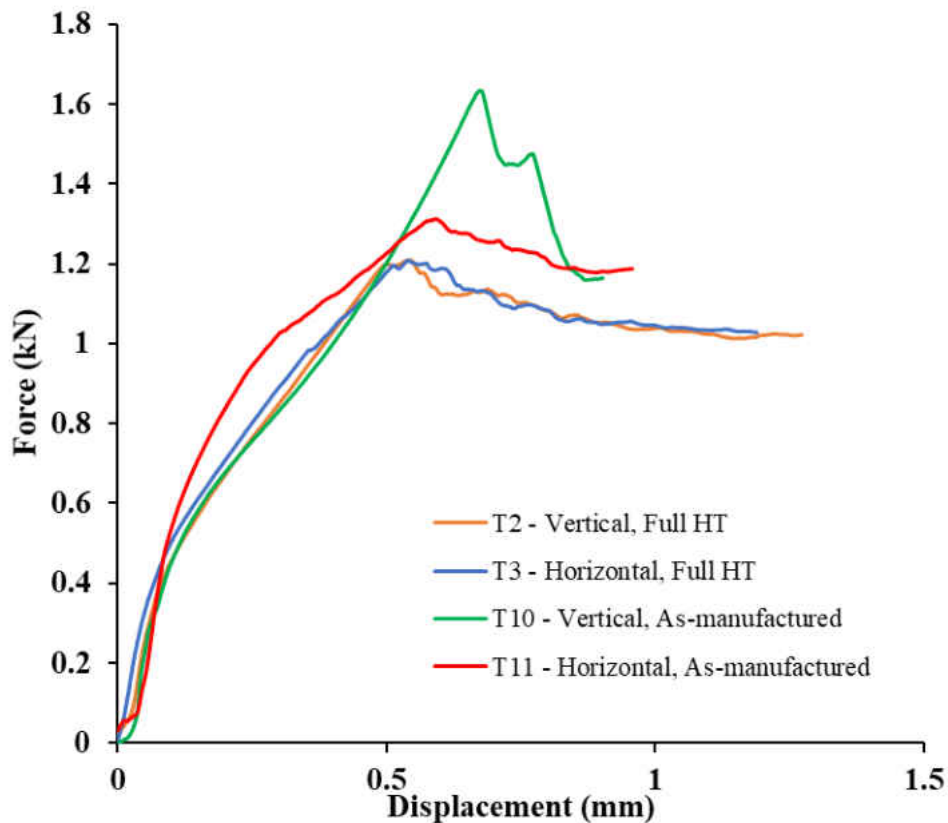


Figure 5.2 - Monotonic SPT responses of SLM IN939V samples tested at room temperature in as-manufactured and heat-treated conditions for transverse and longitudinal orientations.

Upon primary inspection of the curves, further notable traits include similar moduli for all trials, distinguished by varied responses in the plastic region and significantly higher strength for the as-manufactured samples. The as-manufactured samples, T10 and T11, show higher strength throughout the entirety of the curves, with the horizontal sample displaying increased resistance to the onset of plastic deformation up to peak loading, absorbing a larger amount of strain energy in the early stages of displacement than the vertical sample. After the horizontal sample peaks, however, the vertical sample continues to steadily increase in load and deflection, highlighting a large disparity in directional strengths. Considering normalization factors

emphasizes the anisotropy present in the as-manufactured samples, and the effectiveness of the post-processing routine for reducing it, as shown by the values in Table 5.2. There is a marked difference when considering normalized and percentage difference values for strength and moduli. Normalization shows an increase in ultimate strength for the transverse orientation, with a reduction for the longitudinal orientation, and a decrease for both in yield when normalized using the  $t/10$  offset method, and moduli are increased for both orientations. Percent difference between orientations is reduced for all properties for the post-processed samples to the range of 2.7-3.2%, as compared to the as-manufactured absolute difference ranging from 13-17%. This shows the effectiveness of the post-processing routine in homogenizing the microstructure and the minimization of scatter due to the reduction in anisotropy. Of note, as differences are calculated using an error formula with longitudinal values as the base, some are calculated as negative, indicating higher values in the horizontal orientation. For the sake of comparison, discussions are typically done in absolute values of these. It can also be deduced, whether or not considering absolutes, that percent difference between directions, and thus anisotropy, is greatly reduced when donor geometry is kept constant between orientations, as the percentages for the samples sourced from the large blocks, regardless of manufacturing condition, are consistently lower than those sourced from the bars produced for the recrystallization study.

Table 5.2 – SPT material property value results of SLM IN939V samples tested at room temperature in as-manufactured and heat-treated conditions for both orientations.

	<b>T2 long. HT</b>	<b>T3 trans. HT</b>	<b>T10 long. as-man</b>	<b>T11 trans. as-man</b>
$P_{max}$ (kN)	1.2089	1.2081	1.6353	1.3114
$P/\delta_{mt}$ (MPa)	4832.3 ± 0.053	4701.3 ± 0.048	5144.5 ± 0.055	4473.5 ± 0.046
% diff. $P/\delta_{mt}$		2.71		13.04
$k$ (kN/mm)	5.16	5.16	3.60	3.13
$k/t$ (GPa)	11.21 ± 0.123	10.86 ± 0.082	7.63 ± 0.107	6.32 ± 0.114
% diff. $k/t$		3.16		17.07
$P_{y(t/10)}/t^2$ (MPa)	2520 ± 0.003	2450 ± 0.003	2710 ± 0.003	3100 ± 0.004
% diff. $P_{y(t/10)}/t^2$		2.86		-14.43

### 5.1.2 Effects of Testing Temperature

The effects of testing temperature were examined by comparing several otherwise identical test trials. This included both conventionally and additively manufactured materials. As is seen in conventional tests, testing temperature affects material properties such as strength and ductility, and the extent of which can be shown to interact with other sample variations. The variations in materials properties between room temperature (RT) and elevated temperature test trials due to SPT response will be shown here, and comparisons to equivalent tensile testing data will be drawn in Chapter 6, using percentage differences for context.

Tensile equivalent monotonic tests which were conducted with stainless steel 304 at room and elevated temperature served as a basis for testing of the thermal capabilities of the SPT fixture developed for this study. Elevated temperature monotonic testing of 304 stainless was conducted at 300°C, with test parameters otherwise matching those of the room temperature test. The responses of these trials, T1 and T12, are shown in Figure 5.3. Additionally, the response of the initial loading cycle of test F5, which was cycled at 200°C with R=0 to 1kN, is given. This is



done to facilitate comparison of temperature effects on test response due to the irregularities in the response of the 300°C monotonic sample in the initial portions of the curve. Upon inspection of this curve, it is evident that there are irregularities present in the initial stages of deformation, as the response depicts a higher Young's Modulus and yield strength than that of the room temperature samples, along with a very sudden transition to the plastic zone rather than the gradual transition usually seen, depicting an exceptionally stiff material. The response of the 200°C curve, contrastingly, follows a logical trend when considering the typical behavior of metals at elevated temperatures. Though the elastic responses of the room temperature and 200°C curve appear equivalent, the onset of plastic deformation and transitions into zones II and III of the SPT curve appear earlier, trending towards a lower maximum load (as this was a load-controlled curve with a maximum of 1kN, max loading is not readily discernable from this curve). This confirms the irregularities in the 300°C response, though the cause of such is not clear. However, the latter portions of the 300°C curve appear to follow a logical trend, as the curve shows more gradual crack formation following a reduced maximum load level, which is expected as the elevated temperature allows for added plastic deformation in the form of stretching while the crack forms, whereas the RT sample fractures quickly after the load peaks.

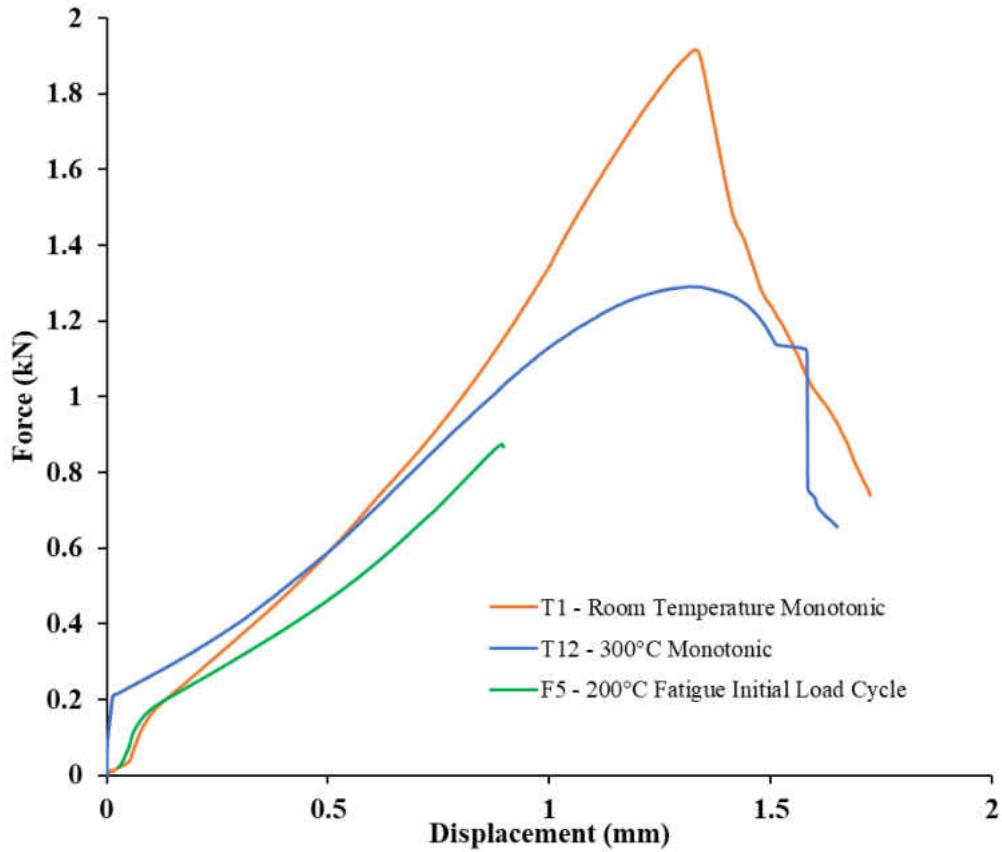


Figure 5.3 - Monotonic SPT responses of 304SS samples tested at room temperature and 300°C, with initial loading of 200°C fatigue test shown for additional comparison.

The variation in material properties due to test temperature can be quantified as percentage difference between room temperature and elevated temperature responses. The normalized values of inflection points  $P_y$ ,  $P_{max}$ , and  $k$ , which have been shown to directly correspond to material properties  $\sigma_y$ ,  $\sigma_{ult}$ , and  $E$ , respectively, are given in

Table 5.3 for T1, T12, and F5, where applicable. Once again, the disparity of values between the two monotonic tests is readily visible. Although the drop in maximum strength seems feasible, the difference calculations indicated an increase in yield strength of almost 6% and a staggering increase in Young's modulus of almost 240%, the negative signs indicating the

increase over room temperature properties. Comparing the room temperature values to the values determined from the initial loading curve of the F5 fatigue test at 200°C contrasts directly with the results for T12, as this run shows a reasonable decrease in yield strength and Young’s modulus of 12% and 13%, respectively. This serves to highlight the error in the 300°C curve while showing the ability of the small punch test to track changes in material due to operating temperature. Additionally, this enforces the need for additional test trials, as results indicate that testing at such a reduced scale are highly susceptible to minor deviances and errors.

Table 5.3 – Property values of 304 stainless steel samples tested at various temperatures.

	<b>T1 RT</b>	<b>T12 300°C</b>	<b>F5 200°C</b>
<b><math>P_{max}</math> (kN)</b>	1.9165	1.2915	-
<b><math>P/\delta_{mt}</math> (MPa)</b>	$3100.3 \pm 0.034$	$2077.9 \pm 0.022$	-
<b>% diff. <math>P/\delta_{mt}</math></b>	-	32.98	-
<b><math>k</math> (kN/mm)</b>	3.06	10.47	2.71
<b><math>k/t</math> (GPa)</b>	$6.58 \pm 0.037$	$22.19 \pm 0.395$	$5.70 \pm 0.044$
<b>% diff. <math>k/t</math></b>	-	-237.2	13.34
<b><math>P_{y(t/10)}/t^2</math> (MPa)</b>	$1050 \pm 0.001$	$1110 \pm 0.010$	$917 \pm 0.001$
<b>% diff. <math>P_{y(t/10)}/t^2</math></b>	-	-5.63	12.42

In general, SPT results show sensitivity in response to testing temperature, as material properties are reduced with increasing temperature. There is a significant degree of anisotropy present when considering directional response of the SLM produced IN939V samples at elevated temperatures, especially when placed in contrast to the room temperature samples of otherwise identical processing, as shown in Figure 5.4. In contrast to the room temperature responses, the curves for T13 and T14 for samples tested at 427°C deviate considerably with regard to orientation. Behavior is highly altered from that of the room temperature samples, as the change

between zones in the early stages of deformation generally occur earlier and plastic changes occur more abruptly. Additionally, the transverse sample shows signs of hardening, as the load peaks, starts to decrease, and then steadily rises until peaking again to a value above the first peak. It is difficult to say if this is the case for the longitudinal sample as well, due to premature test interruption.

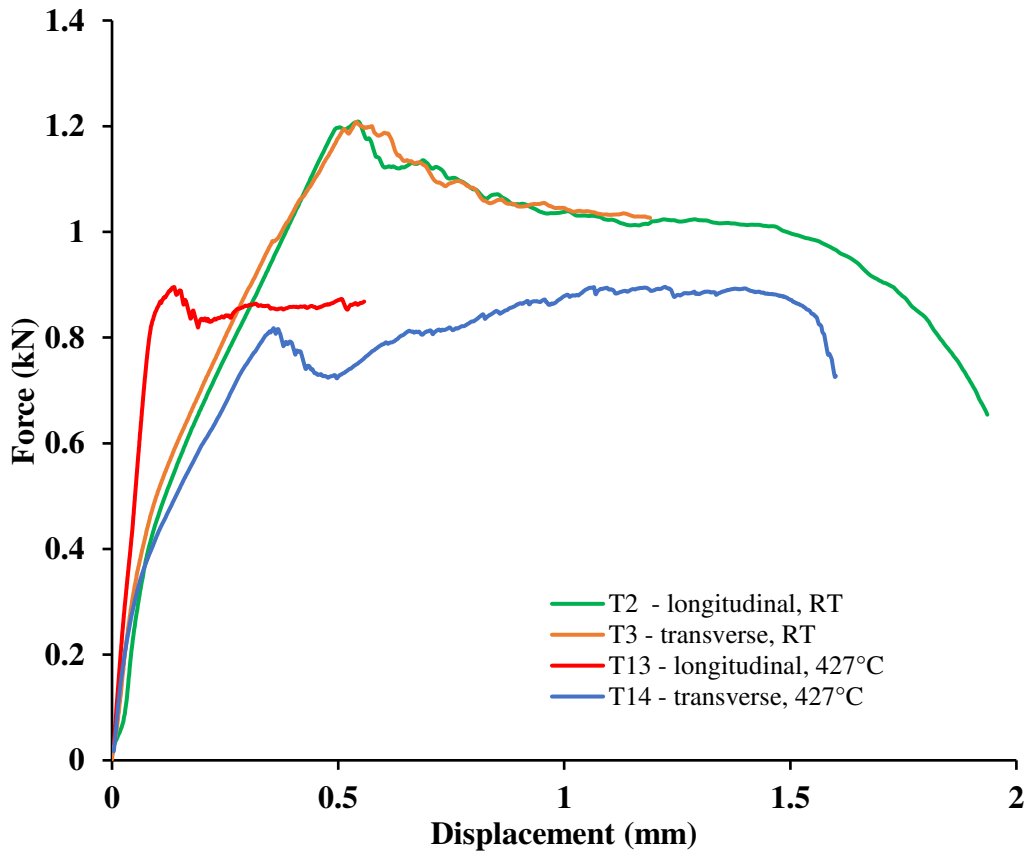


Figure 5.4 - Monotonic response of SLM IN939V varies by orientation when subjected to elevated temperature.

Whereas the material property responses for the room temperature samples from T2 and T3 vary by around only 3%, the corresponding values for tests conducted at 427°C vary

significantly more. This is shown in Table 5.4, where once again, the difference values have been calculated with respect to the longitudinal direction. Of note, the strength calculations for T14 were conducted using the primary peak in the data, so as to be comparable to the T13 data, which was cut short; utilization of the secondary peak changes the directional percent differences for  $P/\delta_{mt}$  and  $P/t^2$  to 88.2% and -9.1%, respectively. The high difference calculated between the two orientations at 427°C is partly due to the behavior of the longitudinal sample in the early stages of deformation, as the curve displays distinctly high stiffness, with a modulus exceeding that of those it is compared against by a wide margin. This not only causes erroneous calculation of the moduli for the heated samples, as they exceed those of the room temperature samples, but a high difference between the two directions. This translates into additional errors in calculating the offset yield load, for which the 427°C samples again give distinctly higher values than the room temperature samples, along with a high degree of anisotropy at a difference of 49%. The strength values also show a high degree of anisotropy for the heated tests when utilizing the  $P/\delta_{mt}$  normalization technique, and some degree of error as well, as the normalized strength values for the heated test again exceed those of the room temperature values. This reveals an error in the displacement outputs, due either to measurement or setup techniques, as the high temperature values should not exceed those of the room temperature samples. While a higher degree of anisotropy is expected at elevated temperatures, it is also necessary to consider that the errors outlined previously are affecting these results. This is shown by comparing the directional difference values given using two different normalization techniques,  $P/\delta_{mt}$  and  $P/t^2$ . Whereas the room temperature samples, T2 and T3, show a modest increase from 2.7% to 6.3% when using  $P/\delta_{mt}$  and  $P/t^2$ , respectively, the heated samples T13 and T14 show a drop from 63.2% to

0.4%. This shows not only a high sensitivity to normalization techniques but also reinforces the theory of the presence of errors in the displacement data for the heated tests, necessitating the revision of testing procedures at elevated temperatures.

Table 5.4 – Comparison of directional variation of monotonic responses of SLM IN939V at room temperature and 427°C.

	<b>T2 - long., RT</b>	<b>T3 - trans., RT</b>	<b>T13 - long., 427°C</b>	<b>T14 - trans., 427°C</b>
$P_{max}$ (kN)	1.2089	1.2081	0.8956	0.8959
$P/\delta_{mt}$ (MPa)	4832.3 ± 0.053	4701.3 ± 0.048	13818.2 ± 0.150	5087.1 ± 0.018
% diff. $P/\delta_{mt}$		2.71		63.2
$P/t^2$ (MPa)	5713.1	5354.5	4054.3	4038.1
% diff. $P/t^2$		6.28		0.401
$k$ (kN/mm)	5.16	5.16	11.04	8.71
$k/t$ (GPa)	11.21 ± 0.123	10.86 ± 0.082	23.49 ± 0.242	19.35 ± 0.194
% diff. $k/t$		3.16		17.7
$P_{y(t/10)}/t^2$ (MPa)	2520 ± 0.003	2450 ± 0.003	4020 ± 0.007	2050 ± 0.005
% diff. $P_{y(t/10)}/t^2$		2.86		49.1

### 5.1.3 Effects of SLM Sample Donor Geometry

Sample geometry effects on material properties of SLM materials have been documented in literature, as the sample geometry can affect the heating gradients present in SLM parts as they are being manufactured. Different geometries which present different surface areas for laser scanning will undergo varying period of cooling between scans, altering the heat gradient in the component, which in turn affects the resultant microstructure. As donor components for SPT samples can vary from large components from which they may be extracted to small, purpose-built samples made to test specifications, documenting the effects of microstructural variation stemming from geometrical differences of SLM donor components is of high importance.

The majority of the IN939V samples used in this study were sourced from large blocks originally intended to be machined into crack toughness (CT) samples. The tension samples used in the recrystallization study outlined in section 3.2.1, however, were manufactured as either hexagonal transverse or round longitudinal bars, depending on the orientation of interest, and machined to size. The SPT samples corresponding to the study in section 3.2.1 were then sourced from the grip sections of the tension samples utilized in this study. As such, a comparison of otherwise identically processed samples to gauge the effects of geometry on  $P$ - $\delta$  data is both possible and prudent. Results from small punch tests on samples manufactured in the longitudinal and transverse direction sourced from both the CT blocks and the recrystallization study (RX study) tension test bars are shown in Figure 5.5. Comparing the transverse samples and the longitudinal samples to each other shows a consistent gap between the samples sourced from the CT blocks and those from the RX study bars, regardless of orientation. The gap is smaller for the transverse samples, likely due to the cooling differences between the CT block and the vertical bar being more pronounced than those between the CT block and the horizontally manufactured bar. This is likely also responsible for the difference in peak loading present in the longitudinal samples which is not present in the transverse samples, which peak at similar load levels, as can be seen in Table 5.5.

Table 5.5 - Maximum load and displacement at maximum load for fully post-processed samples in longitudinal and transverse directions sourced from RX study tension bars and CT block.

	<b>Trans., from RX</b>	<b>Trans., from CT</b>	<b>Long., from RX</b>	<b>Long., from CT</b>
<b><math>P_{max}</math> (kN)</b>	1.2140	1.2081	1.1705	1.2089
<b><math>\delta_m</math> (mm)</b>	0.46	0.54	0.43	0.54
<b><math>t</math> (mm)</b>	0.472	0.475	0.467	0.460
<b><math>P/\delta_{mt}</math> (MPa)</b>	$5566.6 \pm 0.060$	$4701.3 \pm 0.050$	$5807.8 \pm 0.063$	$4832.3 \pm 0.053$

Although the samples tested here are not shown to full fracture in order to preserve the fracture pattern, the increased rate of load drop for the longitudinal sample from the RX study as compared to the longitudinal sample from the CT block also reinforces the differences brought about from the geometry of the donor component as an increase in ductility can be inferred. Additionally, differences in  $\delta_m$  show higher ductility and loading resistance in the CT samples, both between and within each orientation. Finally, strength variations manifesting from differences in orientation are more pronounced in the RX study bars than in the CT samples, as in the CT samples the differences arising from orientation have been mostly eliminated by the implementation of the full post-processing routine, and both directions have been sourced from the same sample. Since the samples from each direction from both donors are very close in thickness to each other, the differences in load and displacement can easily be attributed to microstructural differences resulting from sample donor geometry, as the differences between the two transverse samples is 15.5% and the difference between the two longitudinal samples is 16.8%. This suggests an interaction between donor geometry and orientation. Interestingly, the higher strength values in this case are both from the RX samples. This suggests that the smaller geometry achieves higher strength due to the decreased cooling time between layers due to its



smaller cross-section, recalling effects seen elsewhere in literature [111, 142]. Of note, the percent differences between the two directions for the two donors vary by little more than 1%, 4.15% for the RX samples and 2.71% for the CT samples. This suggests that microstructural growth may be consistent between them despite donor geometry, though a lower initial level of anisotropy in the CT-sources samples is likely responsible for the difference that is present.

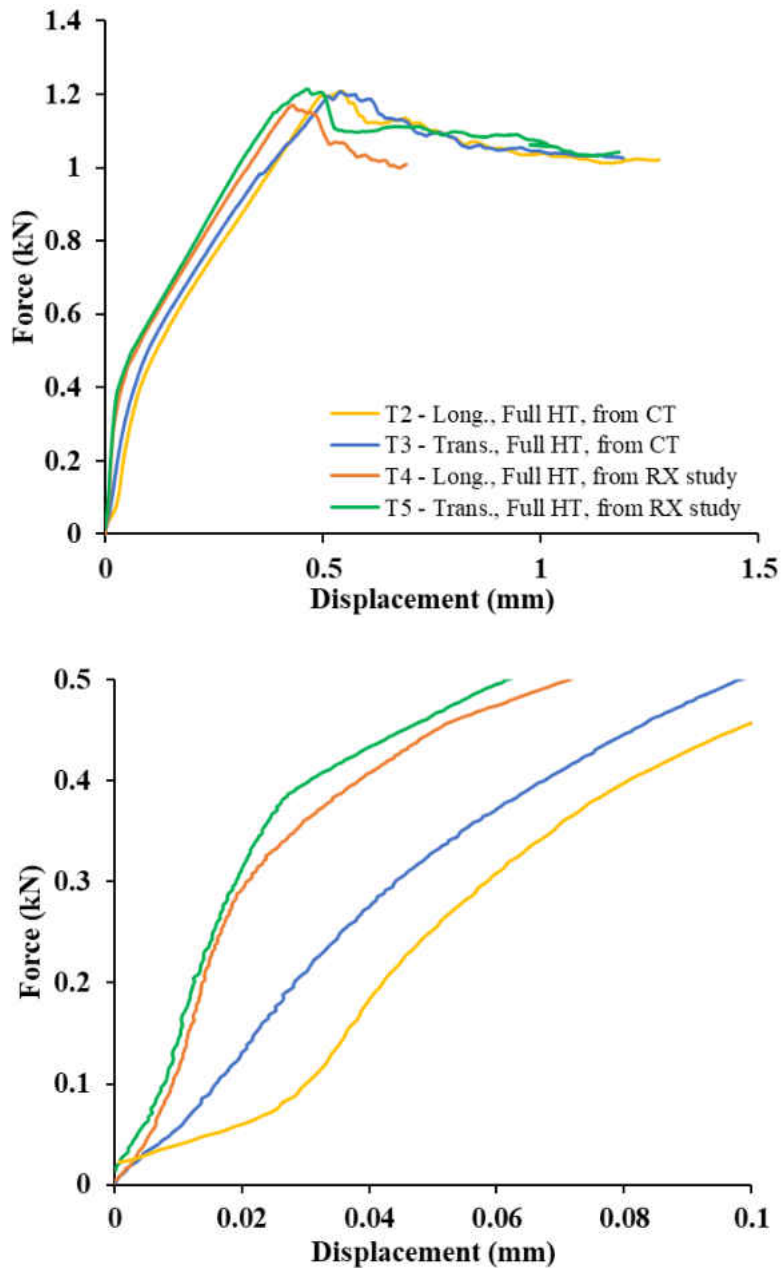


Figure 5.5 - Comparison plots of transverse and longitudinal manufactured samples sourced from both CT blocks and tension test bars.

While the differences presented from sample donor geometry are not extreme, they are notable and detectable by the SPT. This shows the importance of consistent sample geometry when utilizing SPT to optimize SLM processing parameters, as some trends will persist

regardless of geometry, but others may not, and as such geometry should be kept constant to minimize interactions with other parameters.

#### **5.1.4 Effects of Manufacturing Orientation**

Manufacturing orientation has been cited as highly influential to the resultant properties of SLM materials, as shown in Chapter 2 and as exemplified in the preceding sections, and can have varied interactions with other factors. In section 5.1.3, for example, the severity of anisotropy arising from manufacturing orientation, or sample orientation as is the case for the samples sourced from the CT blocks, varies depending on the initial donor sample geometry, as given in Table 5.5. Despite identical manufacturing and post-processing treatments, the samples sourced from the CT blocks have a difference of 2.7% in strength between orientations, while otherwise identically treated samples sourced from the RX study samples have a difference of 4.2%. When considering the results of section 5.1.1, a dependency on orientation can be seen in how the recrystallization cycles implemented affect the material properties. Though the severity of such varies depending on the cycle length or normalized material property considered, the recrystallization generally affects samples manufactured in the longitudinal direction more so than their transversely-manufactured counterparts. Finally, considering the differences present between identically manufactured samples at different temperatures as given in section 5.1.2 shows a directional sensitivity to testing temperature. Comparing the room temperature and 427°C values of the longitudinally-manufactured samples T2 and T13, respectively, shows a drop of 29% when using the  $P/t^2$  technique (as this is the only value which is not affected by erroneous displacement measurements for the heated samples). The transverse counterparts, T3

and T14, have a difference of 25%, indicating a somewhat lower sensitivity to testing temperature than the longitudinal samples.

In addition to the aforementioned sensitivity to orientations due to the application of the load with respect to layer direction, variation in material response can also be seen due to in-plane rotation. That is to say, the orientation of the long axis of a transverse sample with respect to the build plate can alter material response, as shown in Figure 5.6, which shows the response of two as-manufactured samples produced from GP1, a derivative of 17-4PH stainless steel produced by EOS for additive manufacturing. The response of the two curves for T17 and T18 show sensitivity to in-plane rotation when otherwise identical samples are oriented along the x-axis and y-axis, respectively. These curves, however, do not show the max load of the material, as the material strength exceeds the capabilities of the small frame to which the SPT apparatus was adapted. The portions of the curves which were acquired depict very similar behavior, with only slight variations at the early and late portions of the curves, while the majority of the curves overlap.

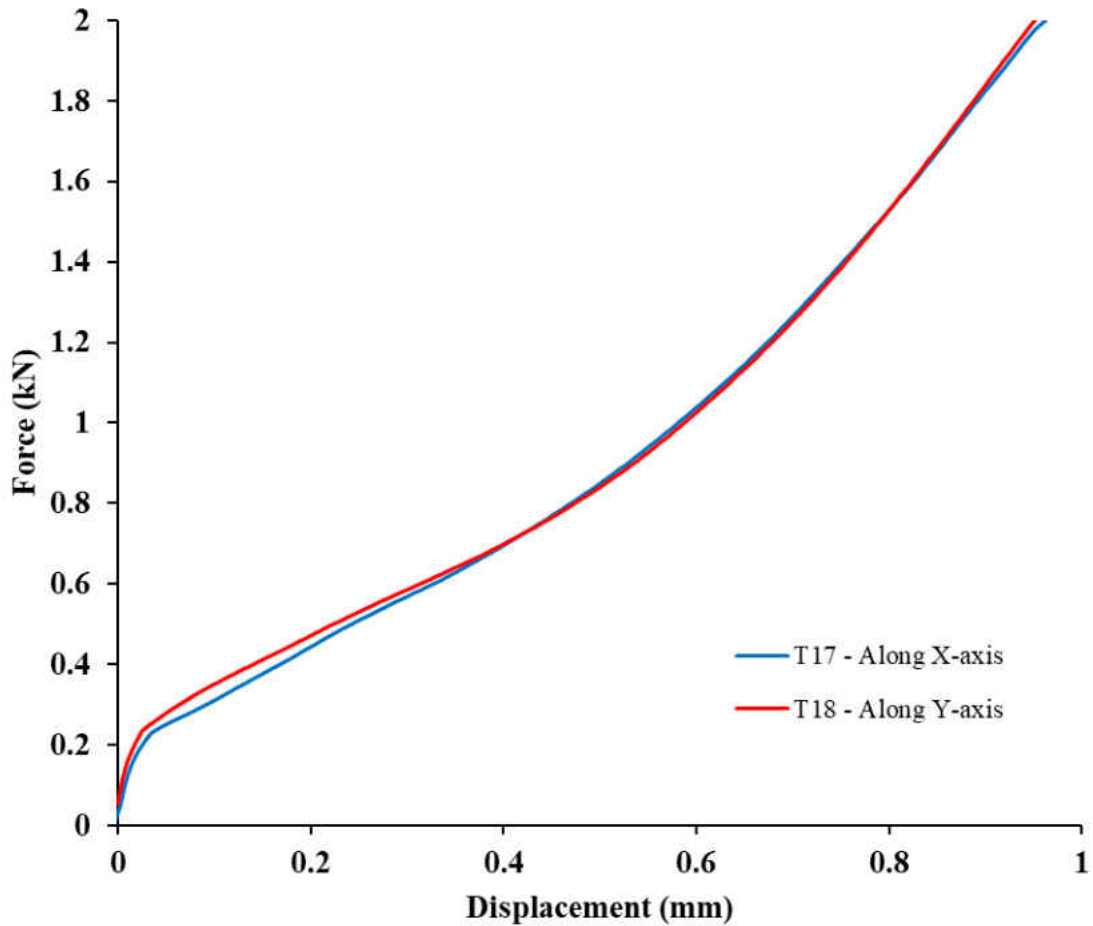


Figure 5.6 - Monotonic room temperature test responses of transverse GP1 samples built with the long axis rotated with respect to the build plate axes.

The calculated differences between the two transverse samples of as-manufactured GP1 from tests T17 and T18 show that in-plane variation can be significant once response values are normalized. Although response differences appear minimal when inspecting the curves, the variations between them are more significant when quantified, as shown in Table 5.6. Although the slopes of the elastic portions of the curves appear parallel, the curves diverge quickly after their respective inflection points, indicating the divergence between them. This difference

propagates into the transition zone, in which yield occurs. As such, the comparison between the sample produced along the y-axis produces higher values for the yield and elastic modulus by 12% and 19%, respectively, than that manufactured along the x-axis. Although the curves converge for the majority of the late second and early third zones, divergence occurs again at the end of the available curves, indicating a likely variance in the max strength. This is corroborated by the difference in displacement at which the maximum load, 2kN, occurs, which causes a 2% difference in the values of  $P/\delta_{mt}$ . These disparities indicate the existence of dependency on in-plane rotation when producing transverse samples as the rotation of the part alters the scan path, which is akin to the differences seen in the literature for tensile samples tested with varying scan patterns, as reviewed in section 2.2.3 [119, 137, 147].

Table 5.6 – Property variation of transverse GP1 samples with dependency on in-plane rotation.

	<b>T18 GP1 Y-axis</b>	<b>T17 GP1 X-axis</b>
$P_{y(t/10)}/t^2$ (MPa)	1411.6 ± 0.011	1243.4 ± 0.007
% diff $P_{y(t/10)}/t^2$		11.92
$P/\delta_{mt}$ (MPa)	4427.7 ± 0.047	4347.5 ± 0.046
% diff. $P/\delta_{mt}$		1.81
$k/t$ (GPa)	23.384 ± 0.419	18.913 ± 0.285
% diff. $k/t$		19.12

### 5.1.5 Other AM Materials

In addition to those tests highlighted above, the monotonic test matrix included other SLM (or DMLS) materials in order to add variety and substance to the efforts to establish correlation factors. These include IN625 manufactured by SolidConcepts (currently of Stratasys) and IN718 manufactured by EOS, using the respective materials and recommended processing

settings of each manufacturer. The IN625 was manufactured in a longitudinal orientation and the IN718 was manufactured in the transverse orientation. The SPT responses of these are provided in Figure 5.7 and Table 5.7. These will serve for comparison to published material properties as given by the respective manufacturers in Chapter 6 and will aid in determining correlation factors for AM materials, comparing these to those of conventionally-manufactured materials as reviewed in Chapter 2.

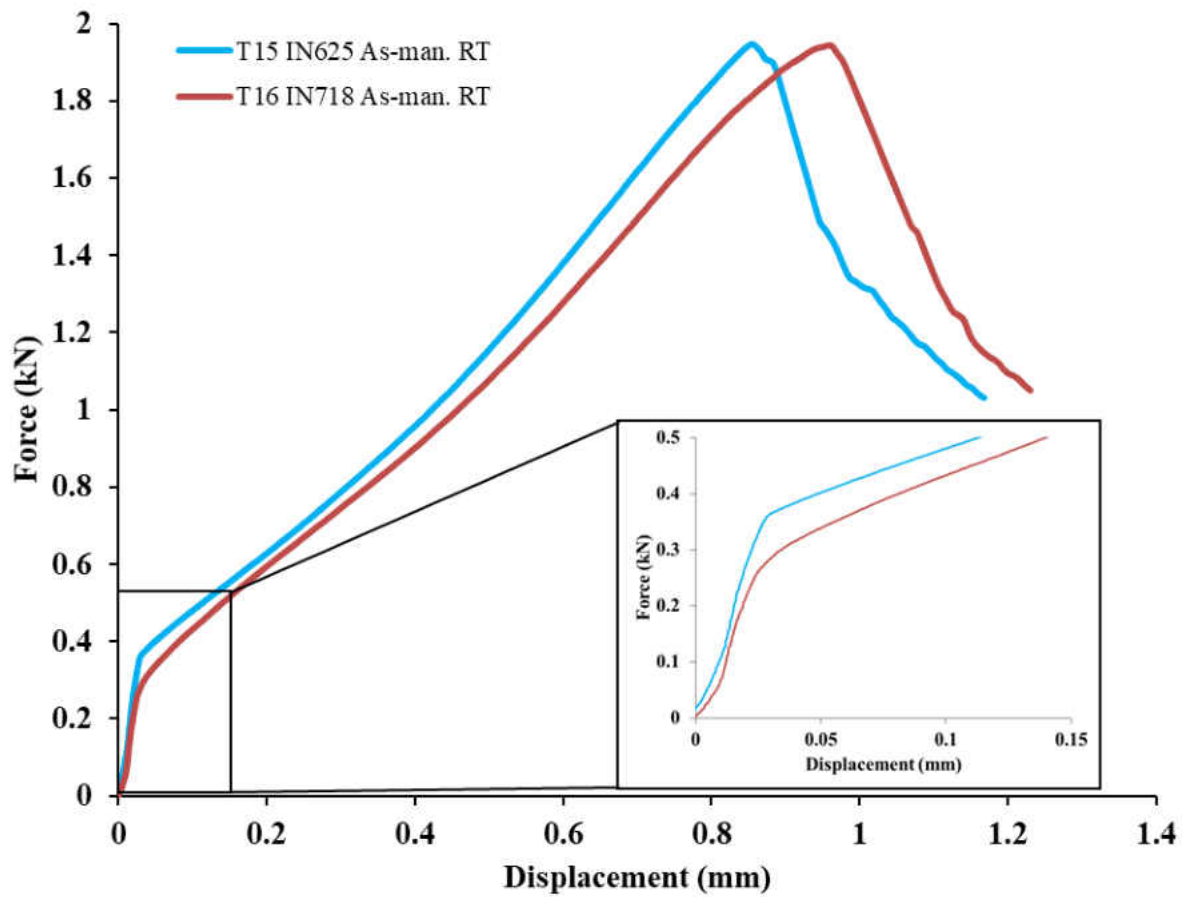


Figure 5.7 - SPT responses of as-manufactured IN625 and IN718.

The curves show similar behavior for the two materials, for which the samples were of a similar thickness, though the values in Table 5.7 indicate a significant advantage in strength and modulus for IN625 over IN718 due  $\delta_m$  value of IN718, a relationship which is not supported in literature, as IN718 is typically a much stronger material than IN625 due to a higher Al and Ti content [298]. Though some variation in material properties is to be expected when considering AM manufactured materials versus their conventional counterparts, the general trends when comparing the two materials should be upheld as these differences are primarily associated with material composition. A level of error in determining the modulus and yield may be associated with determination of the initial slope due to the shape of the curves, but the difference in maximum strengths cannot be attributed to this, and so error must also lie elsewhere, either in testing or sample manufacture. Additionally, it may be considered that the difference in manufacturing orientation for these materials may be significant enough to cause this discrepancy, as both were tested in an as-manufactured state, and thus vulnerable to directional dependencies as previously shown.

Table 5.7 – SPT material properties of AM IN625 and IN718.

	<b>T15 IN625 long.</b>	<b>T16 IN718 trans.</b>
$P/\delta_{mt}$ (MPa)	4881.1 ± 0.053	4301.2 ± 0.047
$P_{y(t/10)}/t^2$ (MPa)	2028.1 ± 0.007	1773.2 ± 0.006
$k/t$ (GPa)	42.513 ± 0.315	36.247 ± 0.244



### **5.1.6 Effects of Clamping Pressure**

Finally, a note on the importance of sample manufacturing accuracy and uniformity in terms of size and fit within the test apparatus is shown here. Due to a deviation in the original machining of the lower die from the specified dimensions, the sample pocket depth was initially larger than specified, and thus at a greater depth than the thickness of the majority of the SPT samples. This deviation lead to the free bending of SPT samples, rather than the constrained bending concentrated only at the punch site as intended. This causes bending of the entire sample, as shown in Figure 5.8, which shows the edges of the sample bending upwards, away from the bulge created by the punch, as the sample is slowly stretched and pushed through the lower die hole. The red lines inserted in Figure 5.8 show the extent of the warping which occurred. The vertical line is drawn parallel to the edge of the sample in the direction of the thickness, or parallel to the punch movement, and the horizontal line is drawn perpendicular to this vertical reference to the opposite lower vertical edge corner, allowing for a contrasting view of the continuous curvature inflicted on the sample from the unconstrained bending.

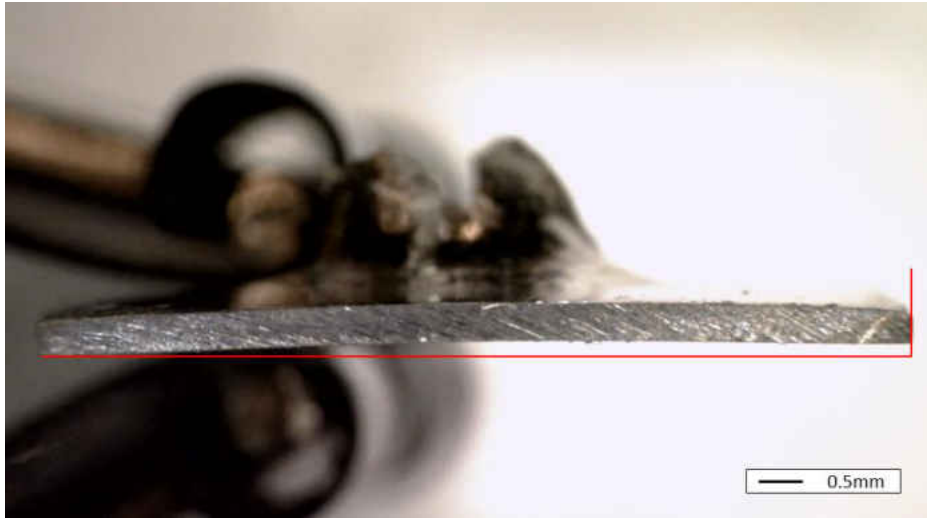


Figure 5.8 - Warping of sample edges resulting from unconstrained bending of samples due to excessive lower die pocket depth.

In terms of  $P-\delta$  results, the unconstrained bending of samples can result in several deviations when compared to a properly constrained sample of similar thickness. The  $P-\delta$  curves in Figure 5.9 show the numerous differences between an unconstrained sample and one which is properly clamped between the top and bottom die, with the four clamping bolts tightened to 5Nm using a torque wrench. The differences between these two test types are readily apparent, beginning with differences in the elastic regions offsetting the remainder of the curve. Though much of the stretching behavior between the clamped sample and unclamped sample (1) appear similar as the curves are parallel in the beginning of the plastic zone, the two begin to diverge and continue to do so as the clamped sample reaches maximum loading and subsequent failure. The unclamped sample, however, did not reach maximum load but rather continued to stretch and instead reached the maximum capacity of the equipped load cell, showing no signs of fracture initiation and instead warping the rest of the sample as was shown in Figure 5.8. The

secondary unclamped sample tested to verify this phenomenon, designated as Unclamped 304SS (2) in Figure 5.9, shows the extent of the variation possible, as the elastic region for this sample is greatly exaggerated and differs significantly from the clamped sample.

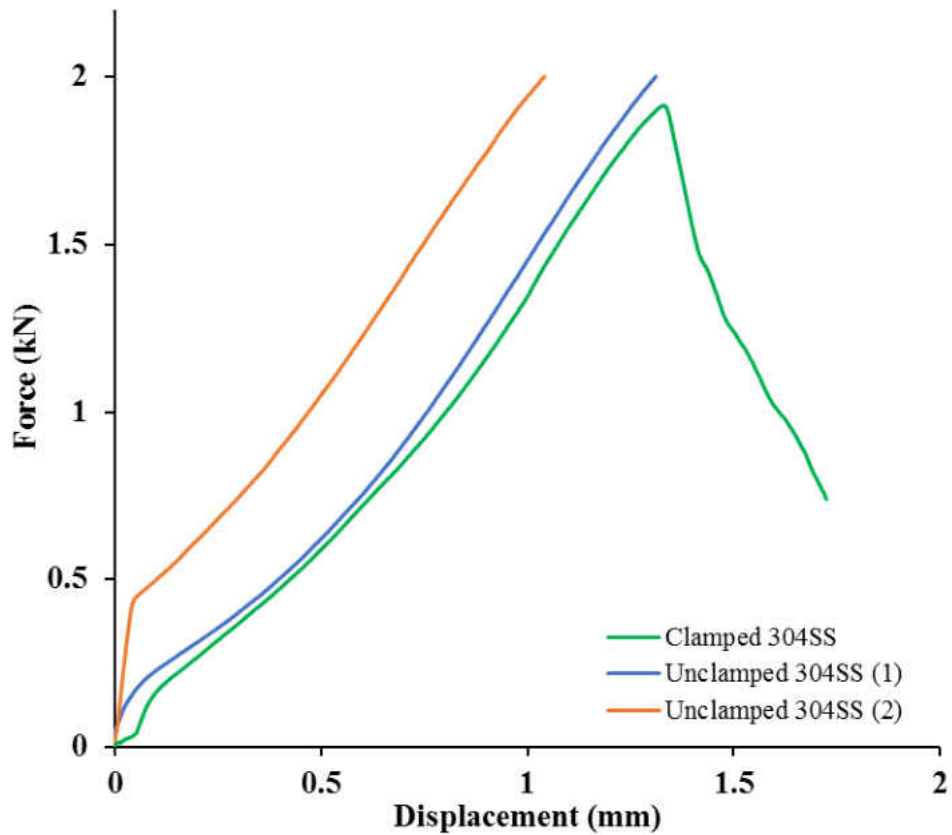


Figure 5.9 - The effects of clamping pressure on otherwise identically tested 304SS samples can be readily observed.

The variation in response between clamped and unclamped samples and further variation between otherwise similar unclamped samples highlights the importance of constraining samples in SPT. Fully unconstrained bending of the samples leads to large variations in resultant  $P-\delta$  data

which will affect inferences of material property variations due to manufacturing differences and the estimation of such.

## **5.2 Cyclic Small Punch Test Results**

Due to the prevalence of failure due to cyclic loading for the applications the materials of interest are often utilized in, a major motivator for researching this topic is in assessing the performance of such, so a number of tests were conducted using varying cyclic loading conditions. These include tests with a single punch using an  $R=0$  load cycle, in which parts are repeatedly loaded in zero to tension under a load which results in plastic deformation within the stable deformation range of the force-displacement curve, region 3. Additionally, several tests were conducted with a fully-reversed loading range of  $R=-1$  using the novel dual-punch design presented in Chapter 3, with control modes varying between load and displacement dependent. Load and displacement levels were chosen according to the monotonic response of the material, typically choosing a load or displacement which corresponds with the third region of the  $P-\delta$  curve. The results of these and comparisons of such will be presented in this section. Subsections will examine the effects of several test variations on the sample response, examining capabilities of the SPT to evaluate materials for varied cyclic loading applications. Comparisons are facilitated by presenting cyclic responses in the form of load or displacement versus cycles to failure, depending on the control mode, and are taken as equating to stress-life and strain-life responses, respectively, given the relationships established in Chapter 2. Several of the tests conducted in this section also utilized the conventionally manufactured 304 stainless steel. Use

of a conventional material aided in establishing best practices and isolating the effects of specific test conditions, without the complications and interactions that AM materials may present.

### 5.2.1 Differences from Load Level

The first condition tested on the cyclic response of 304 stainless steel was in choosing the load level for R=0 tests. Adhering to practices for traditional fatigue tests, the loads chosen for the majority of the cyclic small punch tests herein typically lie within the range of stable plastic deformation, zone 3 of the  $P$ - $\delta$  curve, so that each cycle imparts an equal amount of deformation until the onset of failure. In the interest of adhering to traditional test practices, however, two load-controlled tests with R=0 were conducted at loads which correlate to proportional levels of displacement. As such, one test was conducted to 1kN (F1), which produced a displacement of slightly less than 0.8mm under monotonic loading, and another was conducted at 1.5kN (F2), which produced approximately double that displacement. The displacement per cycle plot comparing these is shown in Figure 5.10. The increased load level of the 1.5kN test reduces the cycles before the onset of failure to a third of the 1kN test, from 3000 to 1000 cycles. However, a comparison of the stabilized hysteretic loops shows that both samples have a displacement range of approximately 0.04mm, so that reduction in strength is not necessarily caused by an increase in the stabilized strain range, but by increasing levels of damage accumulated due to the higher load level causing an increase in the plastic strain, or displacement, range. It is also worth noting that the 1.5kN load level falls close to the plastic instability zone, region 4, of the monotonic test response of 304SS, which could be the driving reason behind the increased plastic strain range in this test, which is not present for the 1kN test.

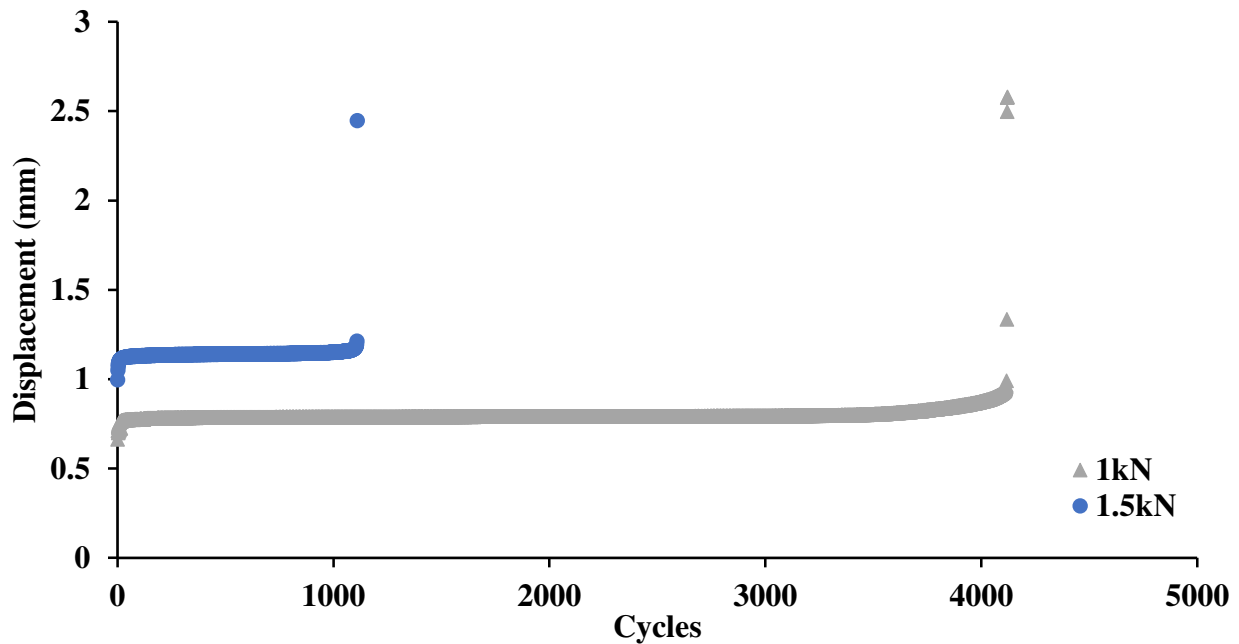


Figure 5.10 - Variation in response of 304SS tests F1 and F2, cycled at R=0 with loads of 1kN and 1.5kN, respectively.

### 5.2.2 Effects of Testing Temperature

Typical conventional fatigue studies are conducted at elevated temperatures corresponding to operating conditions in the application of interest. Three different test types of small punch fatigue tests were studied, and each of these was studied at both room and elevated temperatures to provide a baseline for cyclic behavior in SPT and the effects of temperature. Conditions between corresponding tests are otherwise identical, and samples with similar thicknesses were chosen for each set of test type to facilitate comparisons. For test evaluation purposes, samples utilized in these trials were made from wrought 304 stainless steel, rather than using the AM materials, the characteristics of which would interact with the test parameter changes to affect the responses.

The first cyclic loading mode studies follow those previously shown in literature, where loading is applied in zero-to-tension, with  $R=0$ . The curves in Figure 5.11 depict the response of 304 stainless steel cycled from 0.1kN to 1kN at room temperature (F1) and 200°C (F5). As can be expected, there is a higher mean displacement for the heated test due to increased malleability leading to a larger amount of deformation upon initial loading, but the two curves mostly show a similar trend of growth. Both the room temperature and 200°C responses remain at a steady level of displacement for over 2500 cycles, after which point the heated test undergoes a sudden increase in displacement, likely caused by the occurrence of a major crack. Following that, the displacement, and concurrent damage, increase slowly but steadily until a sharp rise indicating total failure. The room temperature sample, however, maintains a mostly constant displacement level for around 1000 more cycles, after which damage accumulation occurs much more quickly, showing exponential growth, until the indication of catastrophic failure via the large, sudden increase in displacement. Due to the lower level of malleability in the room temperature, crack growth and failure occurs in fewer cycles than in the 200°C trial.

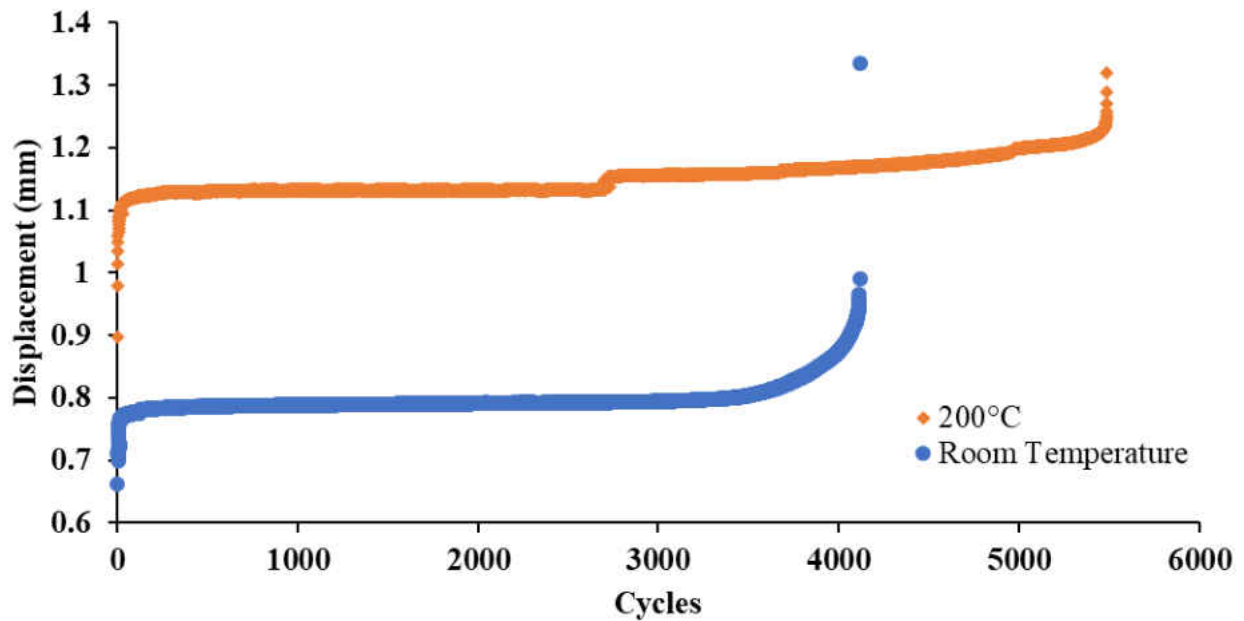


Figure 5.11 - Cyclic response of 304SS tests F1 and F5, tested with R=0 to 1kN at room temperature and 200°C, respectively.

The effects of testing temperature on load controlled cyclic tests are more pronounced when utilizing the fully-reversible dual punch configuration. The displacement-life results of 304 stainless tested with the dual punch configuration for an R=-1 with load control cycling between -0.5kN and 0.5kN at room temperature and 200°C are shown in Figure 5.12. The room temperature sample remains steady at around 0.5mm displacement for around 50 cycles, at which point damage begins to accumulate and crack growth causes a steady increase in the displacement level to about double this value, after which point it levels off again. Leveling off is likely due to the presence of a large fracture (hole) in the center of the sample at this point, after which further cycling of the sample does very little damage as the punch tips are no longer fully in contact with the sample, rather the sides of the punch are further deforming the periphery of



the punch contact area on the sample. Corroboration of the presence of this fracture can be seen later in section 5.4. The elevated temperature sample, when inspected alone, levels off for around 30 cycles after an initial increase to a nearly doubled value of displacement as compared to the room temperature sample. After this steady displacement region there is a sudden, exponential rise in displacement during which time damage accumulates rapidly and the sample fails catastrophically. This is followed by a similar period of steady displacement and a subsequent increase, where the failed sample is damaged further as portions of the deformed are displaced beyond damage that is typically seen.

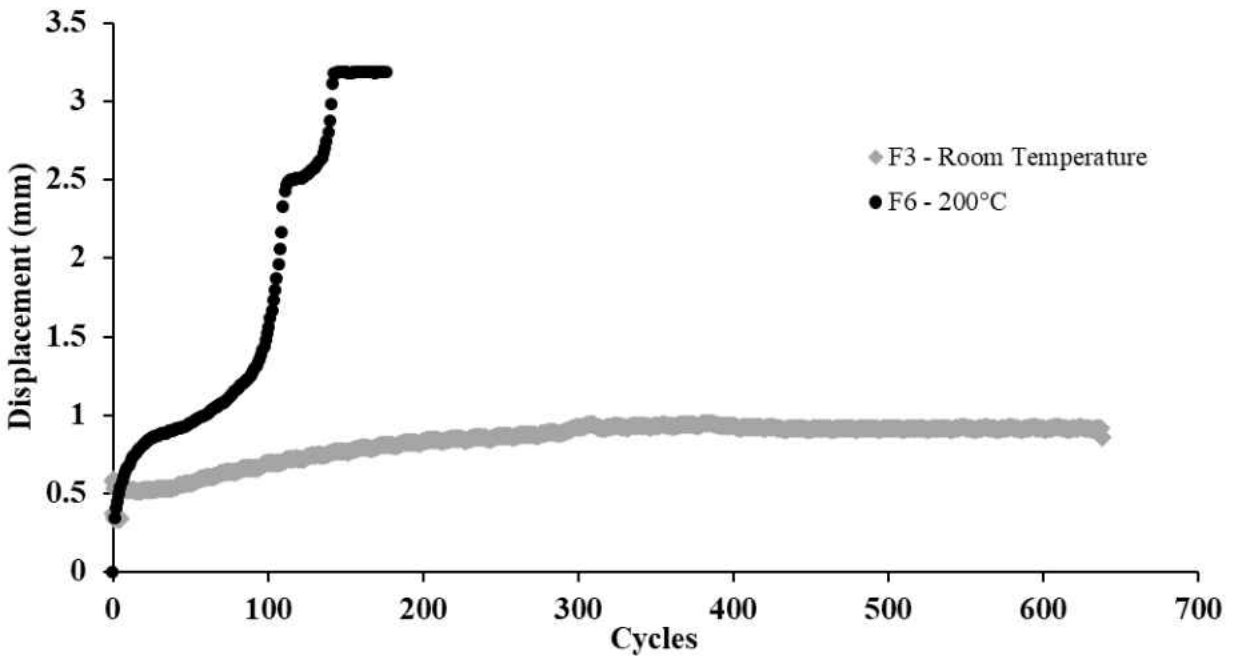


Figure 5.12 - Cyclic response of 304SS with R=-1 load controlled at -0.5kN to 0.5kN at room temperature and 200°C

Although the total loading range for the samples shown in Figure 5.12 is the same as for those shown in Figure 5.11, 1kN, the responses of these are vastly different. While for the single punch R=0 test life is shortened by roughly 33% before the onset of fracture for the heated test as compared to the room temperature test, for the R=-1 load-controlled tests life is shortened considerably more so, by 85% when comparing heated to room temperature. Additionally, the rate at which damage accumulates for the elevated temperature R=-1 test is significantly higher than that of the R=0 test, though proportionately they both occur at nearly double the cycle number of that which indicates the onset of failure. That is, for the R=0 sample the onset of fracture, which is visible in Figure 5.11 as a sudden, short increase in displacement, occurs at just over 2700 cycles, while failure occurs at around 5400 cycles. Similarly, for the R=-1 sample the onset of fracture in which the rate of increase of displacement increases greatly occurs just shy of 50 cycles, and the sharp increase in displacement denoting failure occurs at around 100 cycles.

The displacement-controlled R=-1 tests also feature a sharp contrast between the room temperature (F4) and 200°C (F7) trials, though the initial load levels for both trials appear to overlap for several cycles. The responses of these can be seen in Figure 5.13. Despite the initial similarity, however, the elevated temperature test accumulates damage and peaks very early, followed by a steady reduction in load supported and a divergence from the room temperature response, indicating a steady increase in fracturing and failure rate, as compared to the room temperature sample. The room temperature test features an early peak and drop of supported load that levels out after a period of steady decline, though with some deviation in the load level due to the control settings of the frame. Likely the steady decline occurred as the major damage to the sample accumulated, with the steady latter portion increasing the damage more slowly in the

area further away from the punch tips. Thus, as will be seen in fractography, the center of this sample features a hole where the punches repeatedly impacted and deformed the sample, while the areas surrounding it underwent repeated bending which lead to slower accumulation of plastic deformation and cracking. In comparison, the 200°C increase in temperature shows highly detrimental effects on the cyclic life of the samples, as the load drops much more rapidly for the heated sample, even though the two start at equivalent load levels (thickness was only marginally different for these samples, and of minimal effect). The increased malleability induced by the high temperature caused the damage to occur much more rapidly. It is difficult to say when catastrophic failure occurred with respect to cycles tracked, however, so it's difficult to know how much of the life of the room temperature sample that was tracked is actually fatigue of the area surrounding the circular hole caused by the punch tip. Despite the scatter present in the data, the maximum loads for the room temperature sample do not drop below the final value of the 200°C sample until at least 4x as many load cycles, indicting significant life reduction due to implementation of heat.

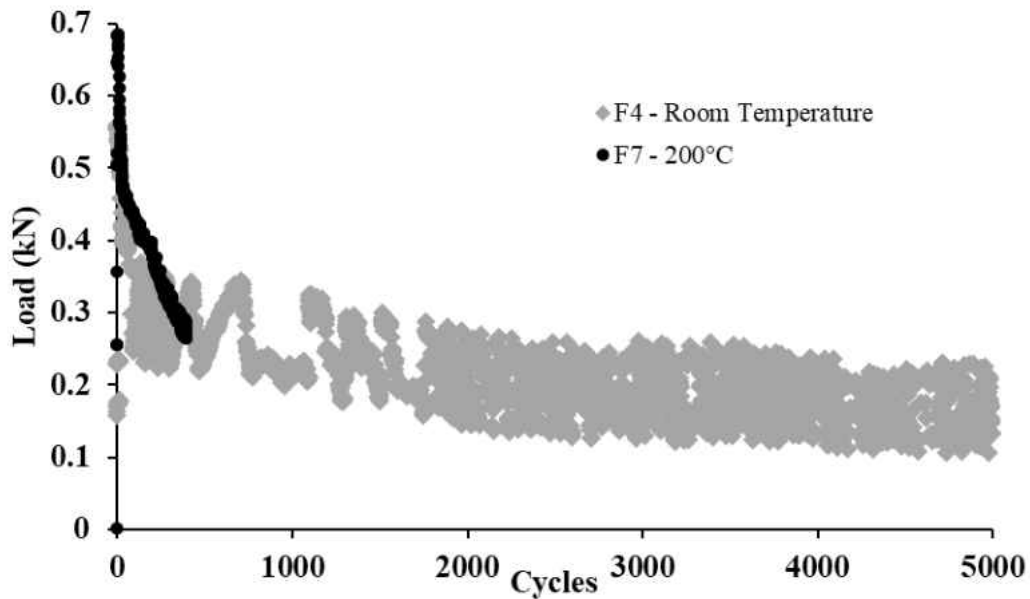


Figure 5.13 - Cyclic response of 304SS with R=-1 displacement controlled at -0.5mm to 0.5mm at room temperature and 200°C

### 5.2.3 Differences from Loading Type

In this study a novel method for evaluating fatigue behavior was proposed, in which a dual punch SPT setup could be utilized to achieve R=-1 reversible loading. The loading mechanism implemented in each test will affect the resultant behavior, and consequently the effects of other variables upon material response, as when comparing room temperature and 200°C tests. Referring again to Figure 5.11 and Figure 5.12 facilitates a comparison of the effects of loading type directly, that is R=0 with a single punch to R=-1 with dual punches, both of which feature a total loading range of 1kN. Though both maintain a ratio of approximately 2:1 for cycles at onset to cycles at failure, the scale at which this occurs is highly dependent on the loading mode, as the single punch configuration delivers significantly less damage over time to

the sample, and thus extends life. This is due to the fact that the  $R=-1$  configuration fully reverses the load in order to achieve the full loading range, imparting damage on both sides of the sample as the punches plastically deforms the sample in both directions with each cycle, whereas the  $R=0$  loading configuration simply builds on existing deformation to achieve the repeated loading, imparting minimal additional deformation to the sample with each cycle. Comparing the individual hysteresis loops of the two test types confirms this, as shown in Figure 5.14. The loop for the  $R=0$  to 1kN shown in Figure 5.14 (a) is characterized by a small displacement range, which is similar to the strain range of a traditional fatigue test, of less than 0.04mm, and appears almost entirely plastic. Contrastingly, the loop shown in (b) for the  $R=-1$  test from -0.5kN to 0.5kN has a displacement range of approximately 20x that of (a), with a significant portion of plastic strain being present, and a corresponding increase in plastic strain energy.

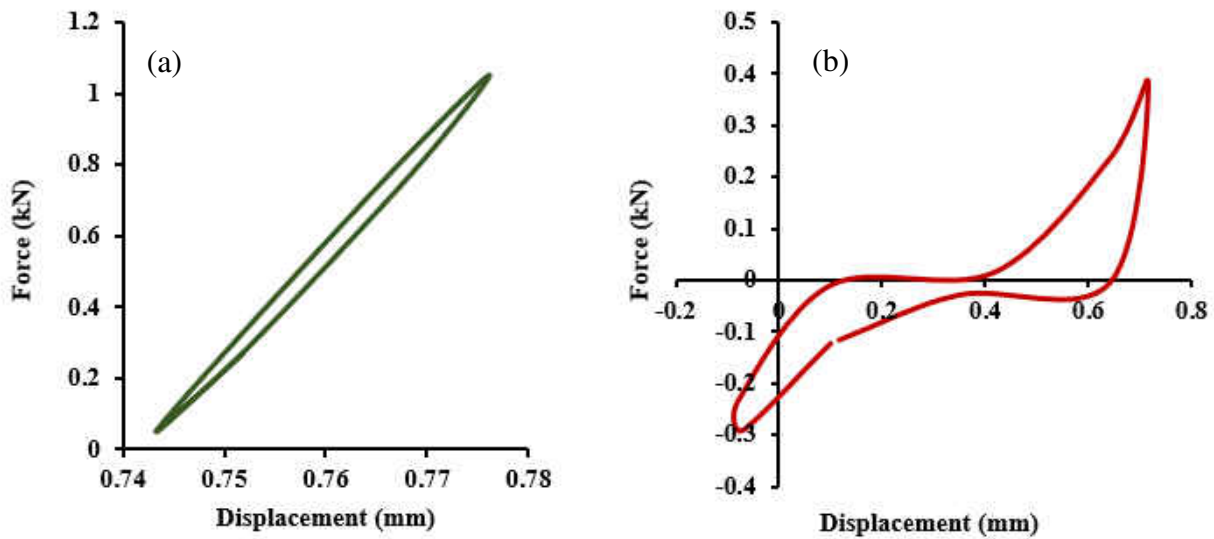


Figure 5.14 - Hysteretic responses of 304SS cycled at RT with (a)  $R=0$  to 1kN and (b)  $R=-1$  with a range of  $\pm 0.5$ kN.

#### 5.2.4 Differences from Reversible Control Modes

Conventional  $R=-1$  fatigue tests are typically strain controlled, yet the limited cyclic SPT studies documented in literature utilized a single punch  $R=0$  configuration which is load controlled. As such, an objective in the evaluation of the novel dual punch cyclic design is to determine which control type is best suited for use with the reversible loading test to acquire the most informative results, load or displacement. Single hysteresis loops from each control type with an  $R=-1$  ratio at room temperature are shown in Figure 5.15. Note that the output for the displacement-controlled test is recorded via LVDT, though input is established by the movement of the load frame cross head, which causes the resultant displacement level to not cycle at the input range of  $\pm 0.5\text{mm}$ . Despite this discrepancy, the resultant output works well for comparison to the load-controlled test, as levels of both load and displacement during stabilized cycling correlate significantly, with a similar strain range. There is, however, a difference in the values which correspond to the stress and plastic strain range. Additionally, the gap which exists in the middle of each loop, which corresponds to a gap in application of the opposing punch as one punch removes its load from the sample, is more pronounced in the displacement-controlled sample. When considering the entire span of life tested, the loops for the displacement-controlled test feature overlap better than those of the load controlled, which feature more pronounced ratcheting and build-up of plastic deformation.

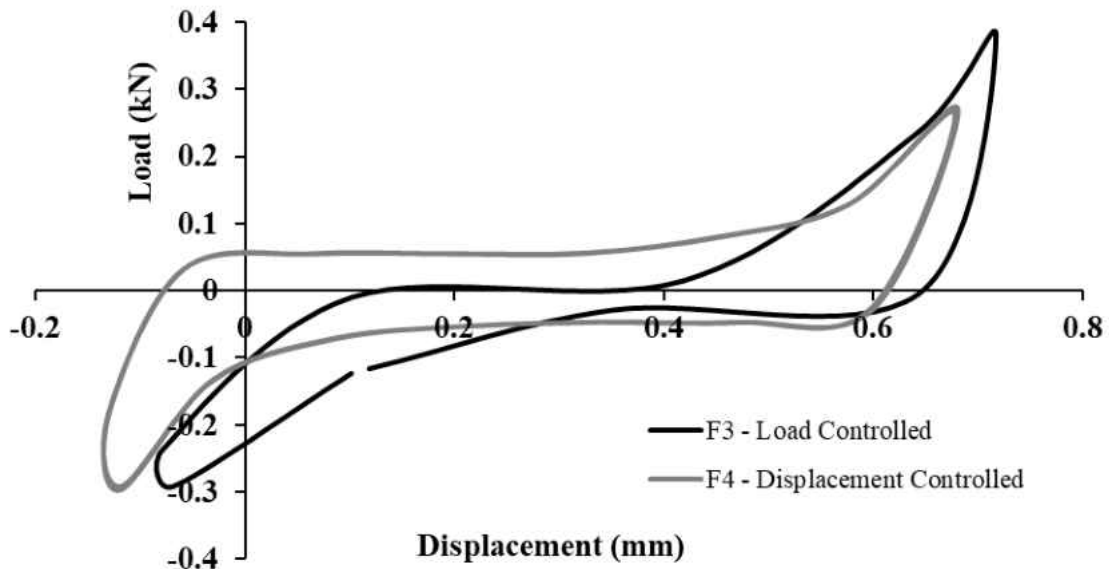


Figure 5.15 - Comparison of results for displacement and load controlled tests of 304SS when tested with  $R=-1$ .

The effects of control type also show an interaction with testing temperature. To facilitate comparison, both load controlled and strain-controlled tests of 304 stainless at room temperature and 200°C are plotted on the same x-axis in Figure 5.16. The load and displacement-controlled curves shown therein were cycled at  $\pm 0.5\text{kN}$  and  $\pm 0.5\text{mm}$ , choosing values within the steady-state plasticity region which produce responses roughly equal to each other. The room temperature tests both have a period of rapid increase in their respective response value level, and level off around 200 cycles. Both values at which cycling levels are set to, 0.5kN and 0.5mm, correspond to levels within the steady-state plastic deformation region of the monotonic response of 304 stainless at room temperature, indicating that similar trends can be seen for at least part of each test when adhering to this experimental design guideline regardless of control mode. Elevated temperature testing impacts load controlled samples more severely than

displacement-controlled samples, as the softer, heated material is able to support less load. Displacement increases quickly in order to achieve the 0.5kN load level to which it is being cycled, whereas the displacement-controlled sample undergoes a steady, gradual loss of strength as it is displaced the same amount, so the reduction in strength occurs due to a more gradual accumulation of damage. As such, it can be said that displacement control is best suited for comparison to conventional test results, as a likeness can be drawn to strain controlled tests, and a steady rate of damage accumulation can be achieved. However, a lower displacement level for cycling should be utilized in order to extend overall test duration and sample life, choosing a displacement at the beginning of the steady deformation zone, zone III, or perhaps even in the plastic bending zone, zone II.



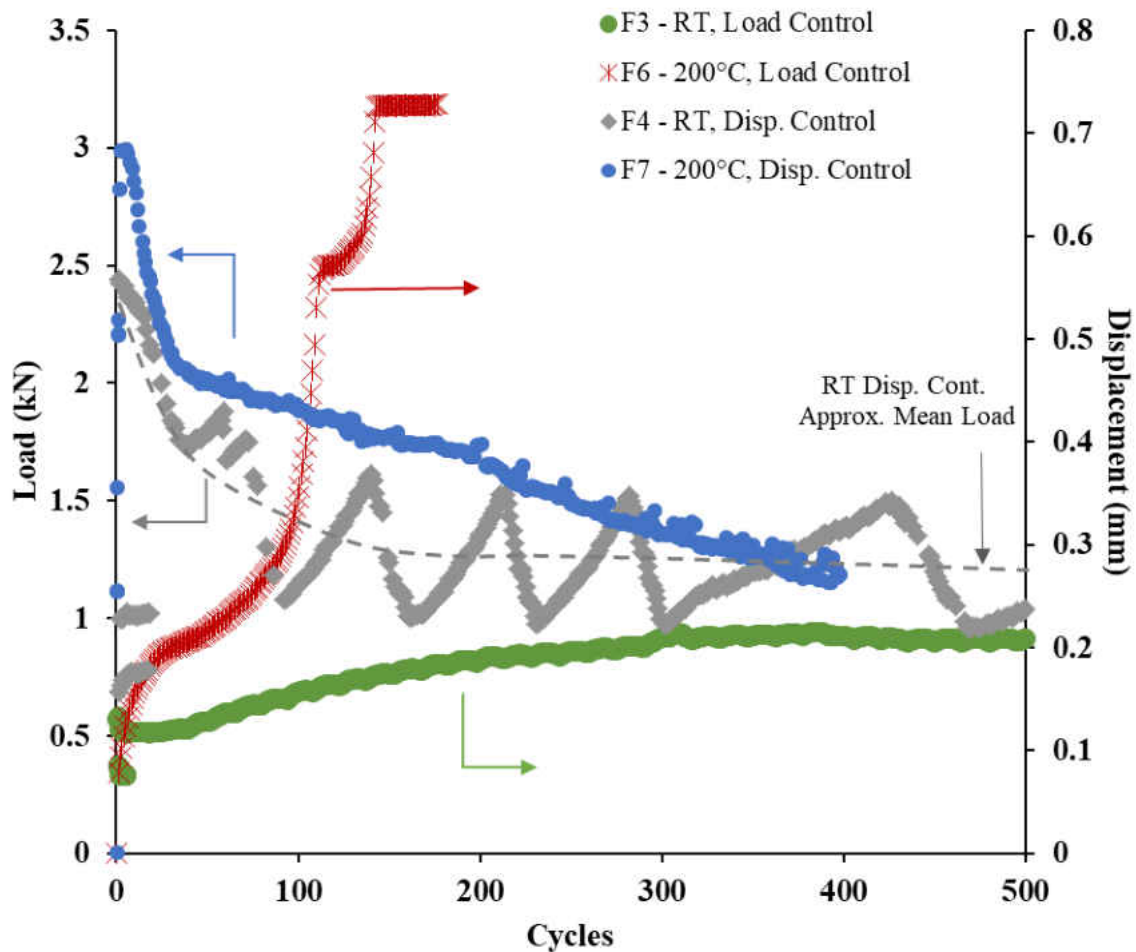


Figure 5.16 - Comparison of cyclic behavior of 304SS at RT and 200°C for samples tested with R=-1 utilizing both load and displacement controls.

### 5.2.5 Effects of Hold Time

A hold time was incorporated into one of the cyclic tests of 304SS with R=-1 at 200°C, to evaluate the effects of said hold time versus cyclic results without a hold, approximating creep-fatigue testing conditions. The response is shown in Figure 5.17. The sample was cycled with a load range of  $\pm 0.5\text{kN}$ , with a 15s hold applied at the +0.5kN hold, and the load and unload

segments applied at a rate equivalent to those of the other cyclic tests conducted at 20 cycles/min. The majority of the loops overlap with some small level of ratcheting as plastic deformation increases, though the latter stages of deformation show increasing level of plastic deformation during individual hold cycles until failure.

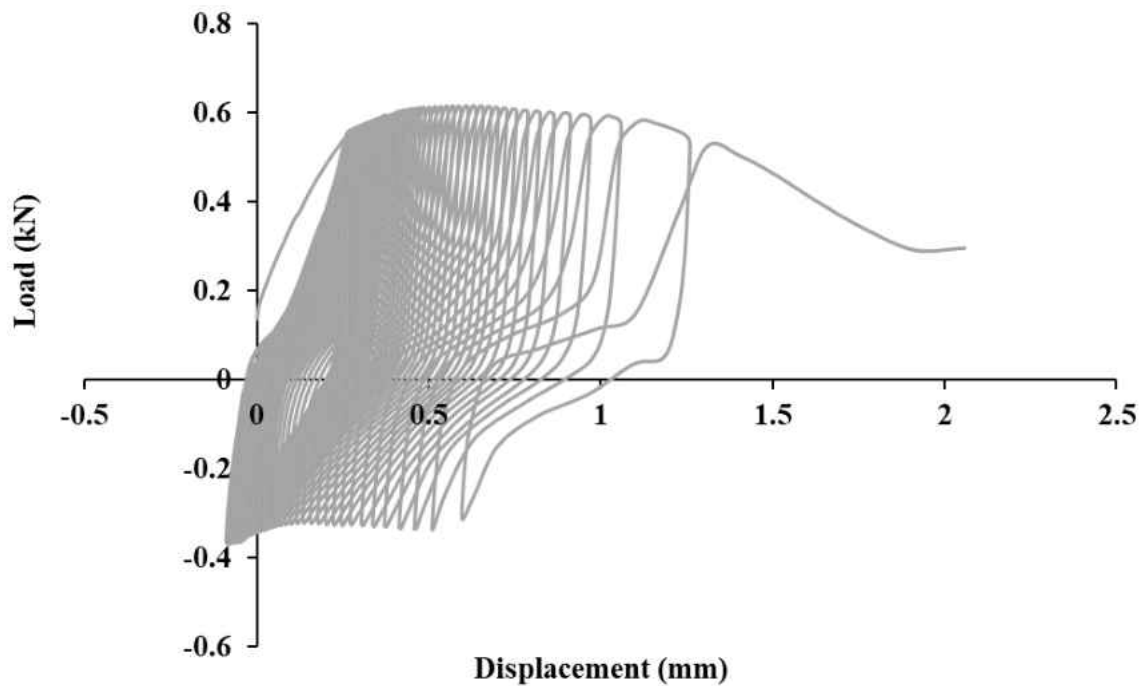


Figure 5.17 - Load-displacement response of 304SS cycled at  $R=-1$  with load control and a 15s hold time at 0.5kN.

As such, the measured life output is in terms of displacement with respect to cycles, as due to the hold time a comparison with respect to time is not very informative. In comparison to F6, the cyclic data with the hold time, CF1, shows significant damage due to the hold time, as overall duration is around 1/3 the number of cycles as the run without the hold time. For the creep-fatigue sample displacement progresses steadily until fracture sets in, at which point the

displacement rapidly increases until failure, whereas the steady-state portion of the sample cycled without the hold time is much longer, with gradual increases in both the initial and latter portions of the response. The hold time thus facilitates increasing levels of damage accumulation with only slight increases in displacement, as the steady-state portion of the creep-fatigue sample occurs at a displacement level of about 1/3 of that of the sample without the hold time but fails much sooner in terms of cycles. In terms of time, however, the hold cycle appears to facilitate slower accumulation of damage and over double the duration of life, as the hold cycle skews the scale in favor of the creep-fatigue test.

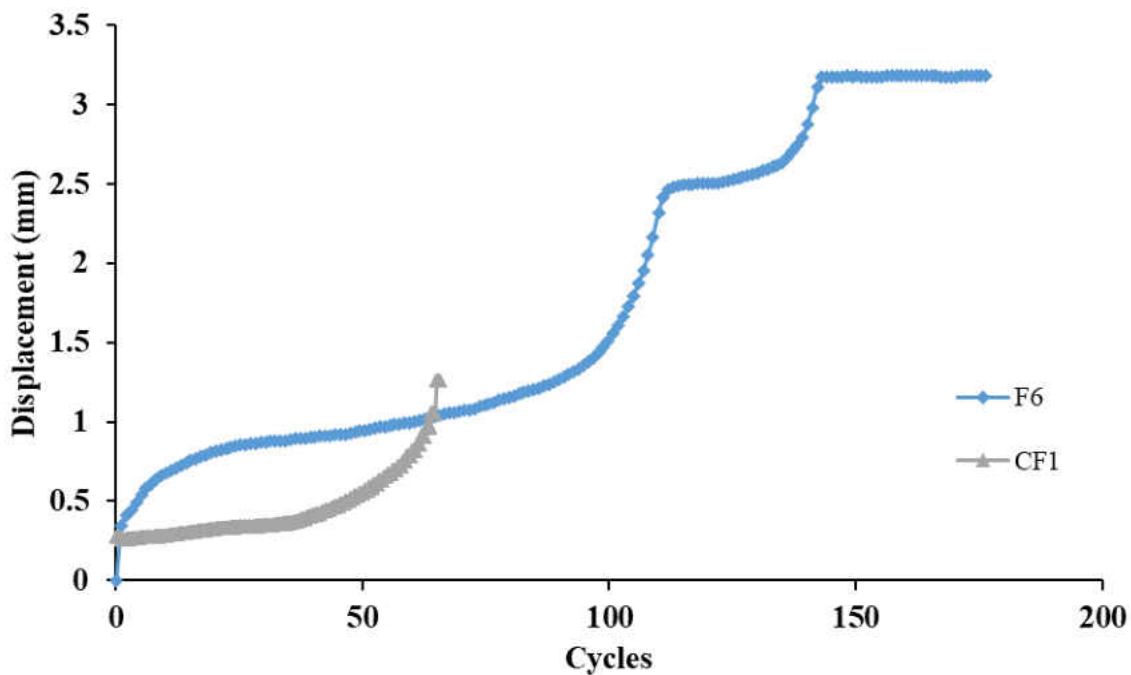


Figure 5.18 - Displacement vs cycle response of 304SS at 200°C cycled at R=-1 with  $\pm 0.5$ kN, with (CF1) and without (F6) a hold time.

### 5.2.6 SLM Materials and the Effects of Heat Treatment and Orientation

Utilizing the knowledge gleaned in the previously discussed cyclic tests on the effects of testing conditions on cyclic response, additional cyclic tests were designed for evaluating SLM materials. These tests also incorporated the traits and conditions unique to the SLM materials studied, such as the effects of manufacturing orientation and heat treatment. As these effects are intrinsically tied to one another, this section presents an overall examination of these tests as a whole, rather than attempting to isolate the singular effects of each condition in different sections, showing the effects of different variables both individually and as interactions where appropriate.

As with the monotonic tests, the response of IN939V to cycling at elevated temperatures varies depending on manufacturing orientation, processing, and testing conditions. The curves in Figure 5.19 show the cyclic responses of IN939V in various stages of manufacture and loading tested with  $R=0$  at  $427^{\circ}\text{C}$ . Most notable of these responses is that of F8, the vertical heat-treated sample tested to 0.4kN, which clearly does not follow the same general trend that the other samples seem to follow. While the remainder of the samples show a cyclic increase in displacement after an initial period of steady displacement levels, a consequence of strain ratcheting caused by softening, the response of F8 features a small drop in displacement at 3000 cycles, followed by a slow increase in displacement. This is likely due to a malfunction in the measurement equipment or other error in procedure, as the total final sample thickness from the tip of the bulge to the other side of the sample measures at 0.88mm, and the original sample thickness was 0.46mm. This means that the total sample deformation should be closer to 0.4mm, in the range of the horizontal sample. Due to this, it would seem that the 0.4kN-loaded samples

display more of a directional difference in response than the identically treated 0.5kN-loaded counterparts; however, this should be attributed mostly to the errors encountered in the vertical sample response. Chronologically, the 0.4kN samples were some of the earlier heated cyclic tests conducted, and the inconsistencies in the response of the vertical sample and shorter duration of the horizontal sample are attributed to the learning curve in working with the system.

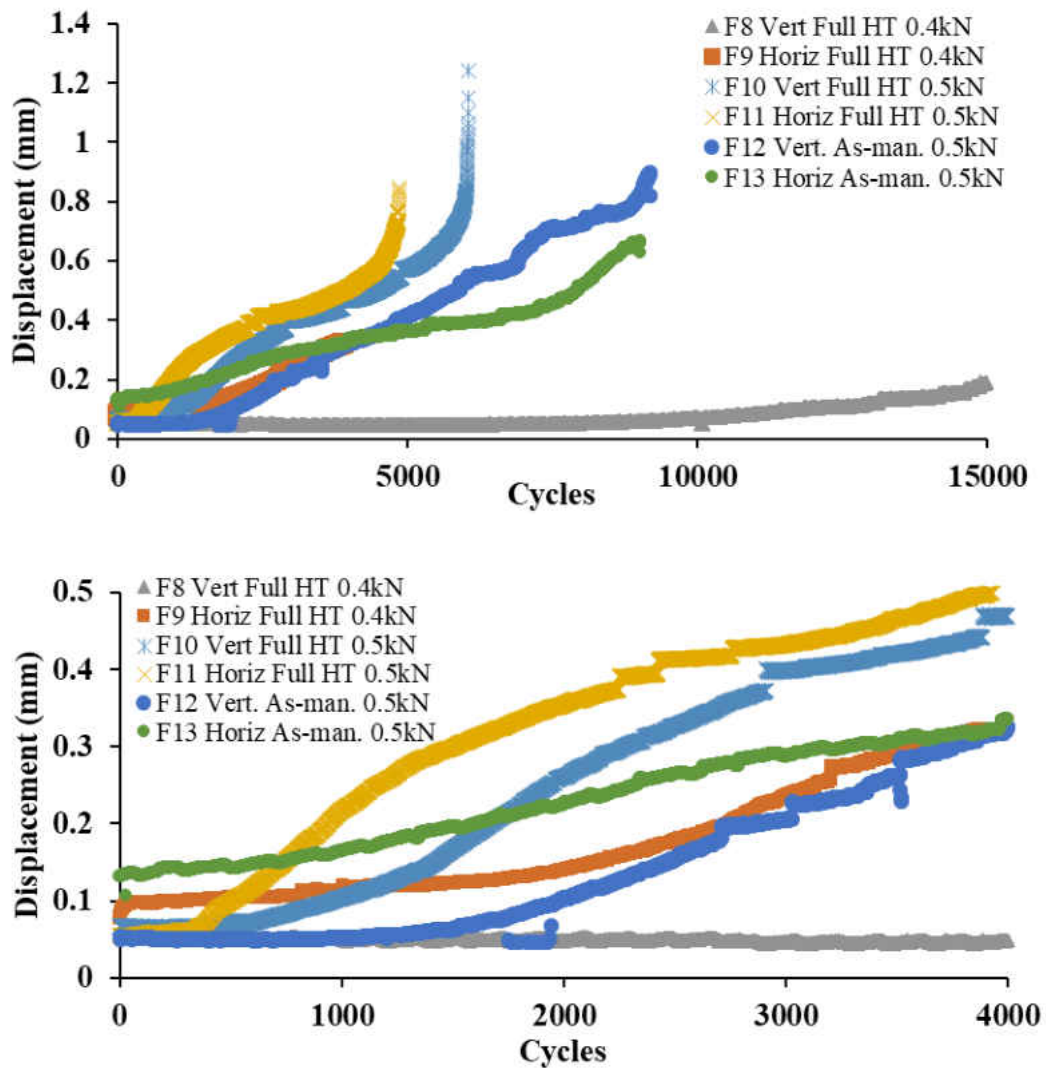


Figure 5.19 - Displacement-life responses for IN939V samples tested with various conditional variations at 427°C with R=0.

Despite the short duration of F9 (the 0.4kN transverse sample), several distinctions in behavior can still be surmised by using it for comparison to the other tests. There is a significant increase in displacement levels with respect to cycles present when considering a load increase of just 0.1kN between the horizontal samples tested at 0.4kN and 0.5kN, with a corresponding decrease in cycles before the initiation of fracture, as indicated by the presence of minor, sudden jumps in displacement. Additionally, the 0.4kN-loaded sample features a much longer initial period of near-constant displacement than the 0.5kN-loaded sample, as the onset of cyclic softening occurs much sooner for the 0.5kN-loaded samples. Cyclic softening is also initiated earlier when considering heat treated samples as compared to as-manufactured samples, as is the presence of shifts in displacement levels indicating the formation of cracks, due to the documented loss of ductility in SLM materials with the implementation of heat treatment [98, 142]. The increased ductility of the as-manufactured samples is also evidenced by the higher initial displacement level of the horizontal as-manufactured sample when compared to heat treated samples. Of the two load levels, the as-manufactured sample is more closely resembled by the 0.4kN-loaded sample, as they show similar initial trends for around 1500 cycles before the heat-treated sample displacement begins to increase quickly, whereas the 0.5kN-loaded sample undergoes a rapid change in displacement rate at only 500 cycles despite a lower initial displacement level. Notable as well when considering initial displacement levels is the tendency of horizontal samples to be affected more adversely by varying material and testing conditions, as the horizontal samples vary significantly more than the vertical samples, which vary in a range of only 0.015mm. In general, when inspecting the pairs for each set of conditions, longitudinal samples resist increases in displacement level for longer than transverse samples as well.

Although post-processing heat treatment of the material reduces overall life and increases the rate of softening, the anisotropy is significantly decreased for the heat-treated samples as compared to the as-manufactured samples due to the reduction in directional differences in the crystal structure. Post-processing also makes cyclic behavior more consistent between the two manufacturing orientations, as the heat-treated sample curves remain parallel for the majority of their duration, while the as-manufactured samples cross, as the vertical sample takes damage at a much faster rate than the horizontal sample despite a lower initial displacement, accompanied by an earlier, more exaggerated appearance of cracks. Despite the differences present between the 0.5kN-loaded heat-treated samples such as the earlier onset of damage and appearance of cracks, as well faster aggregation of such (jumps are closer together) of the horizontal sample, the damage rates appear to be identical. As such, it can be deduced that the implementation of post-processing heat treatment significantly reduces anisotropy in cyclic behavior.

Plotting single loops for each of F8-F13 also shows the level of anisotropy and its dependency on load and treatment condition. As seen in Figure 5.20, the responses of each sample vary, and although all of these are taken at 2000 cycles, the differences in initial displacement and rates of cyclic ratcheting cause the positioning of the various loops to vary greatly. Considering the effects of heat treatment when compared to as-manufactured, however, a reduction in anisotropy is notable as the loops for F10 and F11 for the heat-treated samples are positioned closer together than the loops for F12 and F13, the as-manufactured samples, as the deformation trends of the treated samples differ less between orientations, as shown in Figure 5.19. Visual comparison of the loops, although of overall similar shape for all but the erroneous vertical 0.4kN sample, reveals a general increase in the area within the loop, the strain energy,

for the horizontal samples as compared to their vertical counterparts. This is due to a higher width, which indicates higher levels of plastic strain energy, due to minutely increased plastic deformation with each cycle. The transverse, or horizontal, samples also show an increased displacement range and level as compared to their longitudinal counterparts, regardless of the load level.

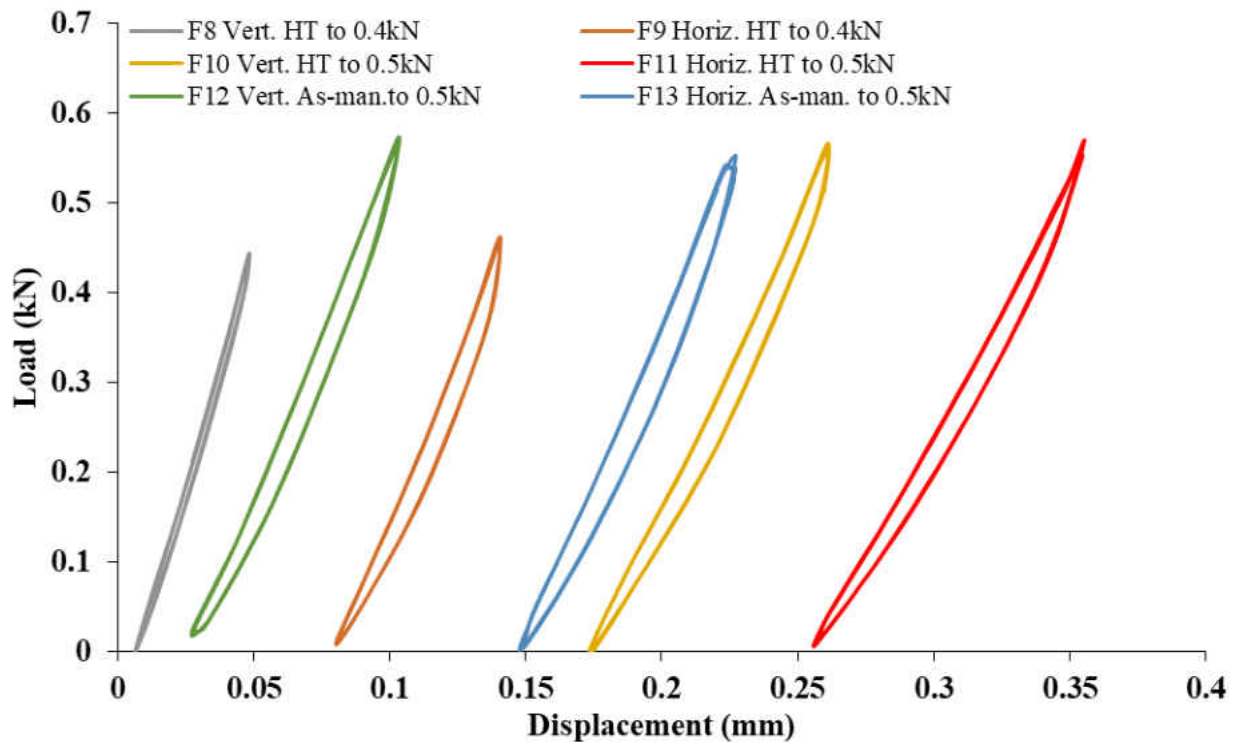


Figure 5.20 - Single hysteresis loops for IN939V samples tested with R=0 and various conditional variations at 427°C.

Additional effects on life due to manufacturing orientation variations can be deduced when inspecting the cyclic responses of an AM material manufactured transversely but with varying alignment of the longest dimension along different axes. The cyclic response of the GP1,



the EOS equivalent of 17-4PH stainless steel for use with their DMLS devices, shows a stronger dependency on orientation than the monotonic responses in Figure 5.6. Due to their strength exceeding the frame limit under monotonic testing, the samples tested in Figure 5.6 were cycled at  $\pm 1.9\text{kN}$  with  $R=-1$  using the dual punch setup. The cyclic response of these tests is shown in Figure 5.21. Due to the high load level used, featuring a total load range of  $3.8\text{kN}$ , these tests were very short in duration, which allows for a comparison of their entire life cycles. Overall, the two samples exhibit large similarities in the shapes of the hysteretic loops and how they evolve over time. It is evident, however, that the sample produced along the x-axis experiences a greater amount of plastic deformation than the one manufactured along the y-axis, as it is characterized by a larger total and plastic strain range.

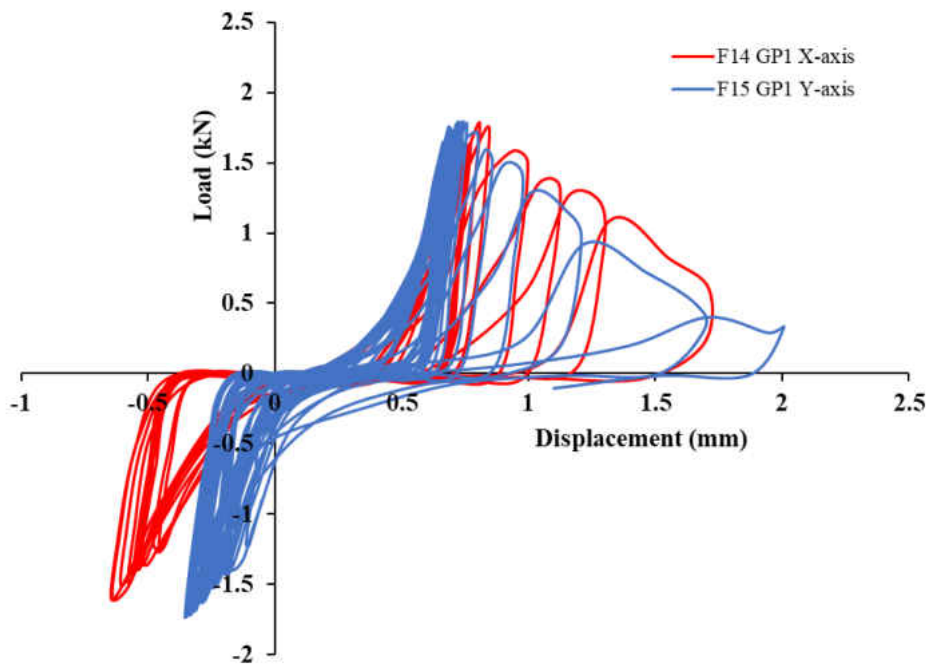


Figure 5.21 - Fully reversed, load controlled cycling of GP1 DMLS samples at room temperature after monotonic testing.

Due to this discrepancy in the cyclic strain behavior between the two transverse samples produced along different axes, a difference in life is manifested. A comparison of the maximum displacement with respect to cycles is shown in Figure 5.22. The x-axis sample maintains a marginally higher displacement level than the y-axis sample during steady cyclic behavior. Due to the increased displacement and plastic deformation experienced by the sample produced along the x-axis, the number of cycles before the onset of failure is half of that of the y-axis. The rate of failure, however, is identical between the two samples once the onset is achieved. This is corroborated by the distinct shape of the final loops shown in Figure 5.21 that the two samples share.

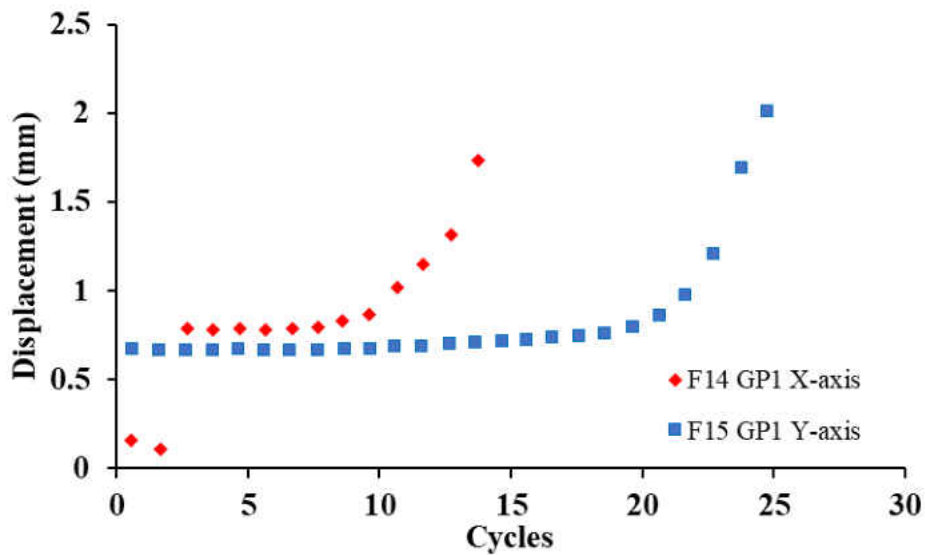


Figure 5.22 - Maximum displacement with respect to cycles of GP1 samples produced transversely along the x and y axes.

Overall, cyclic SPT responses of AM materials vary distinctly from those of conventionally tested 304. Many of the SPT conditions tested with the conventionally

manufactured 304 stainless steel feature responses which resemble those seen with conventional fatigue tests in overall response shape. This includes the responses of samples tested with  $R=0$  featuring load control which induces a steady displacement response for the majority of the sample life, as well as the  $R=-1$  tests with displacement control to a lesser extent. The  $R=-1$  tests with load control and especially the heated tests of those are more likely to feature a gradual increase in displacement leading to a sudden increase in change, with a staircase effect on the overall response. This is similar to the responses of the SLM samples, which in general feature an increase in displacement over time due to displacement, or strain, ratcheting. However, the SLM samples are less likely to develop a staircase effect on the overall response due to the appearance of sudden, small jumps in the displacement indicating the development of small fractures in preference to large deformation.

### **5.2.7 Summary of Cyclic SPT Results and Conditions**

It should be noted that many of the cyclic test results studied in this section featured varying degrees of ratcheting, as displacement or load were increased slightly over time, though at a steady rate. In conventional fatigue tests, this typically indicates a high mean stress or strain during cycling, resulting in excessive deformation. In the case of cyclic SPT, mean stress seems to be unavoidable, leading to ratcheting regardless of the setup, though with different levels of effect. This can lead to cyclic softening/hardening, which causes the constant increase in load or displacement, depending on the test being analyzed. When loading at  $R=0$ , mean stress is unavoidable, though the effects vary depending on the material and testing conditions. With the conventionally produced 304SS, ratcheting is largely absent at room temperature tests, as seen in

Figure 5.10, though the higher load level does show a slight increase of such. An increase in temperature also increases the sensitivity of such, as seen in Figure 5.11. Samples made from SLM materials, however, are much more sensitive to ratcheting, as shown in Figure 5.19, though the effects of such vary depending on the load level and manufacturing conditions. These materials would likely benefit from testing with lower load levels, despite the fact that tests were designed using the same rules as those preceding them and load levels lie within the same range of their respective curves. The tests utilizing  $R=-1$  with load control appear close to a zero-mean stress when inspecting curves, but overall have both a mean stress, or load, and mean strain, or displacement. The  $R=-1$  tests using displacement control, while appearing to cycle around zero, feature large vertical gaps in the hysteresis loops, so that the load level does not truly return to or oscillate about zero, as demonstrated in Figure 5.15. Instead, it could be said that these tests feature dual mean stresses, thus inducing ratcheting effects. As such, in the case of dual-punch reversed cyclic loading a displacement control mode is recommended, and load control is recommended for the single punch setup. Appropriate load/displacement levels may be determined by iterative processes, or the use of equations such as those presented in Chapter 2 for equivalent strain.

The differences in behavior between SLM and conventional materials have also been shown and can be attributed to the sensitivity to manufacturing and testing conditions, including orientation, post-processing treatments, and load level. Given the deviation of results, such as those seen in the comparisons of the various IN939V tests at  $R=0$ , it is clear that some refinement of test procedures is necessary. The response of the vertically manufactured sample cycled to 0.4kN diverges from the apparent trend that the other samples follow, as the

displacement does not develop progressively, but rather drops for a time before increasing again slowly. This is likely due to errors in measurement or setup procedures, as the depth of the deformation does not coincide with the displacement outputs. As such, refinement of the testing procedure is necessary, with constant vigilance kept on load and displacement readings during the heating and thermal soaking of the setup, so as to eliminate unintentional deformation due to thermal expansion of the constrained sample expanding against the punch. Additional data supporting this conclusion includes high stiffness during monotonic testing of both conventional 304SS at 300°C and additively manufactured IN939V tested at 427°C.

### **5.3 FEA Correlations**

A major component in being able to utilize the small punch test to evaluate AM materials is in being able to extract material properties via the inverse method. A model of the SPT and a curve fitting methodology were designed for this purpose as part of this study. As such, this section will present an overview on the goodness fit of simulated results as compared to experimental SPT data.

To deduce material properties from experimental data, a model of the setup was created within ANSYS, and simulations carried out for several cases studied here. The material properties of the sample were changed for each case with an approximation of a conventional counterpart found through literature, this aids to refine and shorten the simulation. As described in section 4.4, a sum of squared errors optimization was used to find the best fit approximation within ANSYS as a series of guesses were input at set intervals corresponding to points on the experimental curves with an objective to minimize error.

### 5.3.1 Simulations of 304 Stainless Steel

Experiments utilizing conventionally-manufactured 304 were replicated using the ANSYS simulation. These simulations help to refine the simulation and assess its efficacy against data acquired using the experimental setup designed for this study. The tests studied were compared to experimental data from F5, conducted at 200°C, and T12, conducted at 300°C. The curve of F5 was generated by combining the initial loading cycle up to 1kN with the peak load points of the subsequent cycles for use with the optimization program. The results of the optimization studies for the responses of the aforementioned are shown in Figure 5.23 comparing ANSYS outputs with the respective SPT experimental results. Although results vary, the  $R^2$  values for each of the optimizations are very high, indicating high goodness of fit. Visually, the curves overlap for significant portions, leading to the high  $R^2$  values, as determined by the error in optimizing the values of  $E$ ,  $K$ , and  $n$  for use in the Ramberg-Osgood equation for describing material behavior. The estimates for these values which produce the best fit, or smallest error, are given with the respective curves, and will be compared to conventional values in Chapter 6. Simulations are designed to end at or near the max load point of the SPT response, as the damage model employed cannot sufficiently model failure.

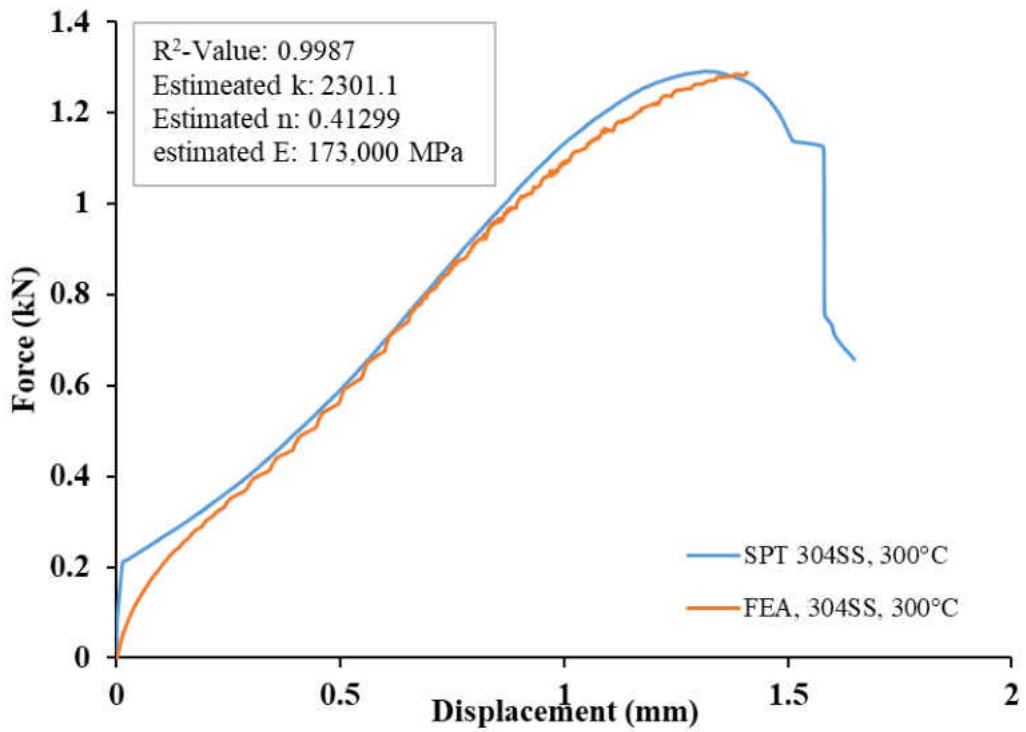
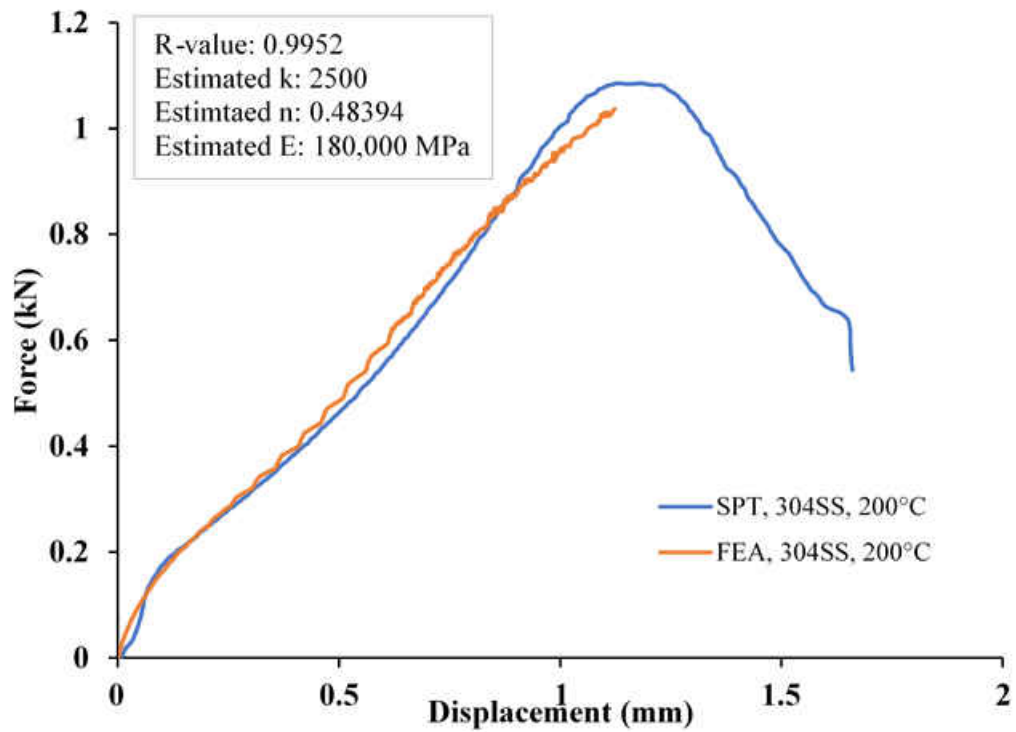


Figure 5.23 - Optimized FEA inverse solutions as compared to experimental results.

The approximations made by ANSYS are able to mitigate the errors caused by faults in testing or otherwise which are seen in the experimental results, such as in the initial portions of the curves. Specifically, there are deviations in the 200°C curve which causes the initial elastic portion to be very irregular in shape, but which the simulation creates a good fit for. For the 300°C curve, in which the initial portion displays unreasonable stiffness, as discussed in section 5.1.2, the simulation approximates a logical behavior which quickly converges on the experimental curve. The middle and latter portions have significant overlap, indicating a satisfactory approximation, though the simulations tend to diverge on approaching the maximum loads, as the damage model utilized lacks sufficient definition to properly model these stages. The use of the aforementioned portions of the curve, however, can be utilized to acquire an estimate of the stress-strain curve for each of the materials, from which material properties can be determined and compared to conventional data.

#### **5.4 Observations from Microscopy**

As a number of factors have been shown to affect material response to SPT loading, microscopy was conducted on each of the samples to aid in explaining differences between samples due to variations in sample preparation and test variations. Variations in fracture morphology can be used to help identify and explain differences in material response. The following will compare the fracture surfaces of select test samples, linking fracture behavior to sample responses. Unless otherwise noted, all samples fractured with the bulge on the bottom face of the samples, though there are a few fatigue samples utilizing the dual punch setup which fractured upwards, due to circumstances of the test and the setup, in which initial loading is



applied upwards rather than downwards. For fatigue samples with displacement controlled fully-reversed loading regimes the samples showed characteristically small bulges upon fracturing. These samples are identified with a mark on the top face of the sample, which may be visible on some of the photos, so as to facilitate analysis and comparison, but which does not otherwise affect the sample.

Component orientation during manufacturing has been one of the most influential parameters to AM material response, in both this study and in the general body of literature. As such, it is of high interest to explore the corresponding fracture pattern variations of AM materials as they pertain to orientation. Additionally, the effects of the orientation on the resultant material properties have been shown to be dependent on material and test condition, such as the extent of post-processing or test type the sample was subjected to. The various material types produced via SLM show distinct fracture patterns which are characteristic to layer-wise manufactured materials.

The SLM IN718 and IN625 samples tested in conjunction to the IN939V samples added variety to the study, but also helped to verify trends. These have exemplary fracture surfaces characteristic to SLM materials. These can be seen in Figure 5.24. The SLM IN718 sample, which was manufactured in a transverse orientation, shows a lot of distinct parallel striations on the surface of the bulge, as denoted by the arrows. These are unidirectional and parallel to the side of the large fracture, some of which have also developed into small cracks. The main fracture also appears to be very straight when viewed from the side. The orientation and shape of these features suggests that the sample is cracking along the boundaries of the layers, and the final fracture grew from one of these initial cracks.

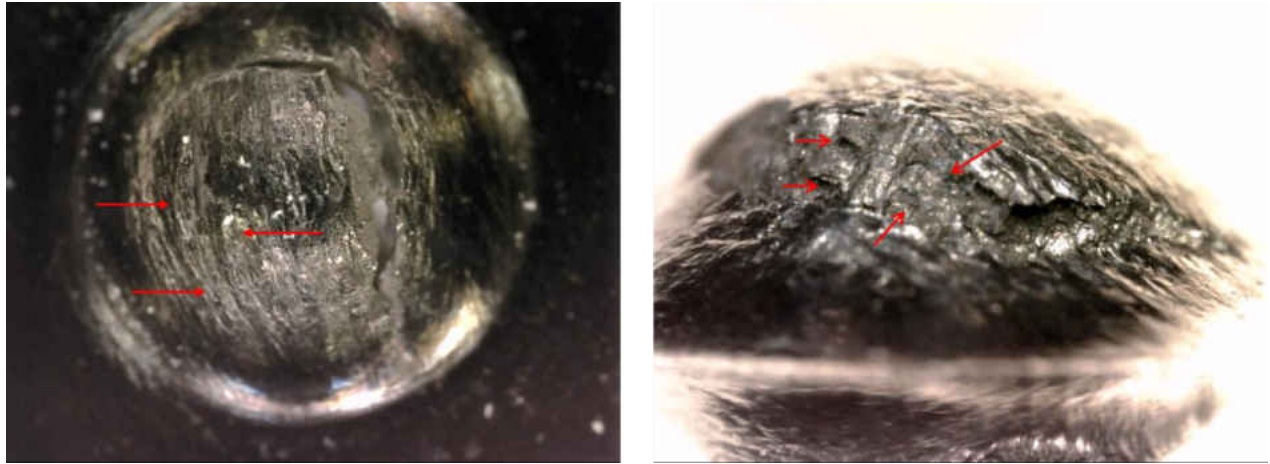


Figure 5.24 - Fracture surface of samples produced from SLM IN718 (left) and SLM IN625 (right) showing crack growth characteristic to layered AM materials.

Close inspection of the IN625 sample shows distinct striations (denoted by arrows) along the inner face of the fracture, running parallel to the surface of the sample. These are indicative of some level of separation or delamination occurring between the layers as the component fractures. This is suggestive of systematic component failure via fracture of individual layers, similar to a composite layered structure in a 3-point bend test, which undergo progressive failure from a mixture of tension and compression, fiber failure, and delamination [299-301]. The lack of stepping or multiple peaks in the data, however, suggests that these occur through progressive layer separation and crack growth, rather than sudden delamination or failure of individual layers that would cause quick drops in sample strength. The distinction between layers, then, is likely made visible as the crack grows along gaps or build defects, such as sites with incomplete layer adhesion or inconsistencies in the build.

Samples constructed from IN939V also show a dependency on orientation when tested in the as-manufactured condition. The monotonic loading samples shown in Figure 5.25 (a) and (b)

exhibit decidedly different fracture behavior. The horizontal sample, (b), can easily be identified by a long, straight central crack with several additional fractures stemming from this central crack and growing perpendicular to it. The vertical sample (a), however, is characterized by cracks which grow radially from a centralized point, rather than from a centralized crack. Though these features differ from those which characterize the IN625 and IN718 samples in Figure 5.24, they are distinct manifestations of orientation effects on fracture behavior.

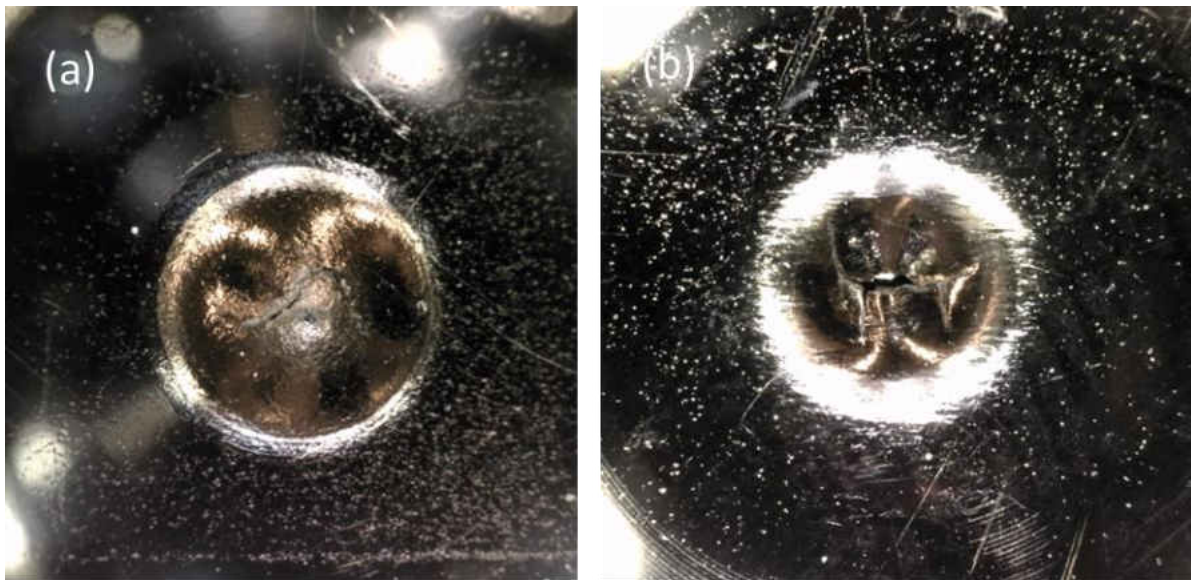


Figure 5.25 - Monotonic loading fracture behavior depends on orientation: (a) T10 is longitudinal and as-manufactured, (b) T11 is transverse and as-manufactured.

Analysis of the microstructures of the IN939V samples reveals links to fracture behavior differences. As the data suggests, the as-manufactured material is highly anisotropic in both behavior and microstructure. As the columnar grains grow parallel to the direction of heat application, the interaction of the load and the microstructure will differ depending on sample

orientation; longitudinal samples have load applied parallel to the columnar grain length, while transverse samples are loaded perpendicular to columnar grain growth. As such, the punch makes contact with two largely differing microstructures, as shown in Figure 5.26. The longitudinal sample, shown on the left, supports the load along the tops of the columnar grains, presenting a nearly isotropic appearance, though some directionality is evident in the alignment of grains towards the bottom right of this sample. The contact surface of the transverse sample, however, is characterized by highly directional elongated grains, which will induce directional material properties and affect fracture behavior. The presence of micropores is evident in both samples.

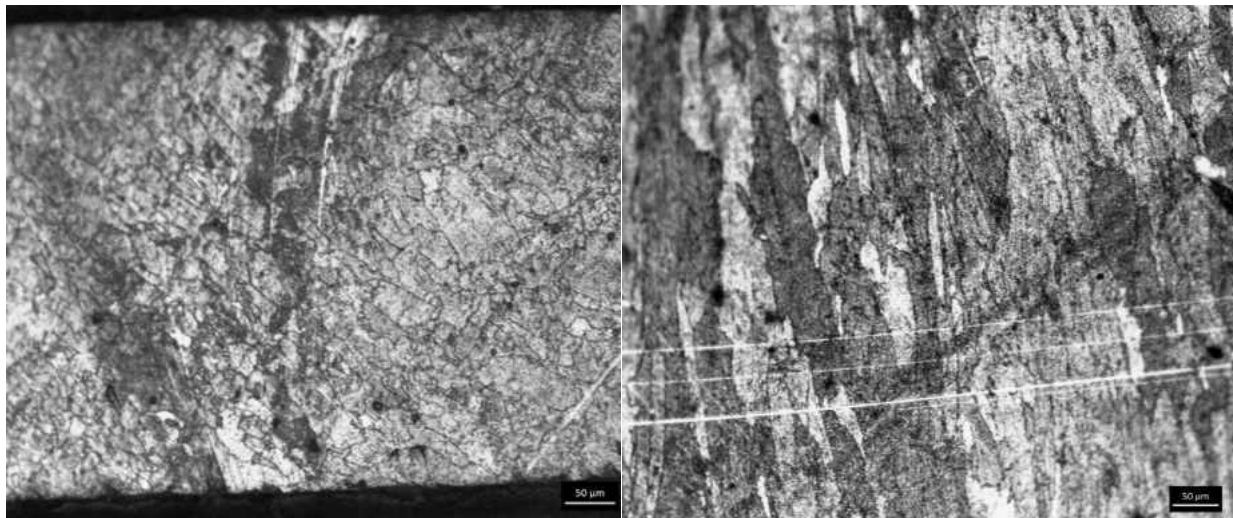


Figure 5.26 - Microstructures of as-manufactured IN939V sample loading surfaces for longitudinal (left) and transverse (right) samples.

Crack growth through the sample will also be affected by the directionality, however, as the textures shown in Figure 5.26 are reversed when considering the cross-sections of the two

sample directions. That is, the thickness (or cross-section) of the longitudinal samples is characterized by elongated grains, while that of the transverse samples is characterized by the smaller, more isotropic structure in one direction and the columnar grains in the other direction, with the lengths parallel to the sample face. Cross-sections of fractured surfaces of as-manufactured samples are shown in Figure 5.27, with the transverse samples having been sectioned perpendicular to the larger central fracture, cutting across its width. As has been shown by the FEA model, the highest stress and strain occurs on the sample face opposite the punch, as the sample is stretched, and this face is placed in tension, and thus the fracture originates in the site. Growth of fractures through and across the sample is then dictated by grain structure. The longitudinal sample shows crack growth through the sample thickness to follow the elongated grains. The transverse sample shows some small deflections, but crack growth is generally undisturbed, with limited deflections occurring due to the small, tight grain structure, similar to that seen on the face of the longitudinal sample in Figure 5.25, but on a reduced scale. As such, the propagation of fractures along the faces of the samples in Figure 5.25 can be related to the differences in the as-manufactured microstructure. The radial growth of the fracture of the longitudinal sample is then attributed to numerous deflections being caused by the small, tightly clustered grains which characterize the face of this sample. There is also evidence of secondary damage towards the center of the sample, to the left of the visible crack, suggesting formation of microcracks from the sample surface following along the direction of the columnar grains due to excessive deformation in this area. Moreover, considering the transverse sample in Figure 5.27 was sectioned perpendicular to the large, horizontal fracture seen in Figure 5.25, and is characterized by the tight microstructure which characterizes the face of the longitudinal sample

shown in Figure 5.26, it can be determined that the large fracture grows parallel to the columnar grains, while the smaller, perpendicular fractures likely form along the edges of the individual layers, suggesting the occurrence of delamination.

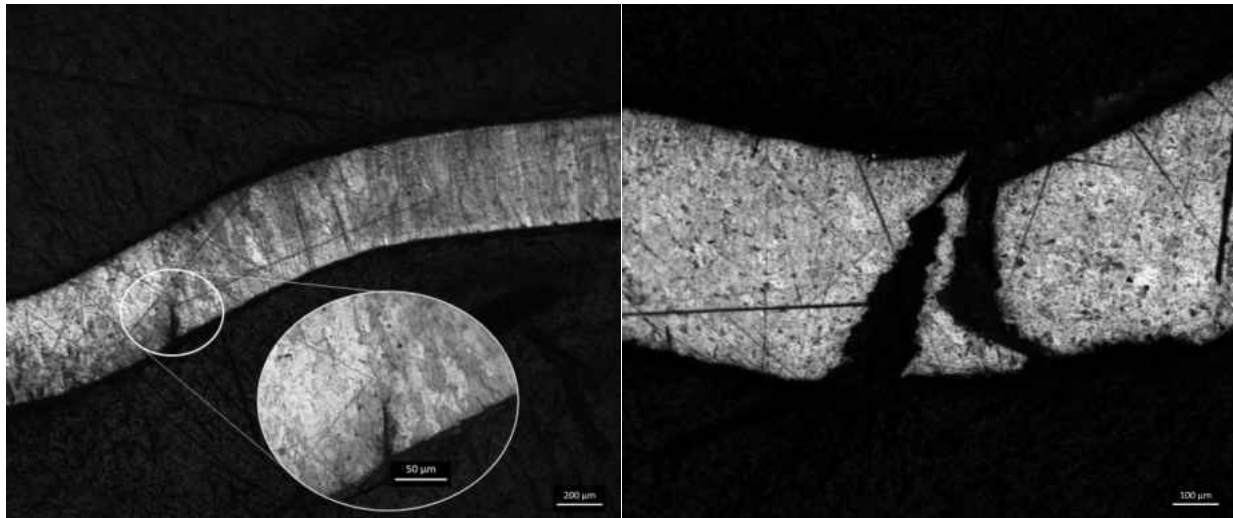


Figure 5.27 - Cross-sectioned fractures of longitudinal (left) and transverse (right) as-manufactured IN939V samples.

This same behavior is displayed by as-manufactured IN939V samples tested cyclically with the single punch configuration. The samples shown in Figure 5.28 (a) and (b) were tested with  $R=0$  at 0.5kN at 427°C in the as-manufactured condition, and display the same fracture patterns as the room temperature monotonic counterparts shown in Figure 5.25, and the differences are arguably more distinct. The longitudinally-built sample, (a), shows significant fracturing which extends radially from a central point, with smaller cracks stemming from these. Long, straight cracks on this sample likely follow separations or grain boundaries formed between laser pass scan tracks. The transverse sample, (b), is characterized by features very

similar to those of the monotonically loaded sample in Figure 5.25 (b), though more distinct in appearance, likely due to their more gradual growth. The inside of the fracture has interestingly straight lines (even more distinct than the bottom/outside face), with cracks growing perpendicular to each other and the sides. This indicates rack growth through the sample thickness is relatively undisturbed by the microstructure.

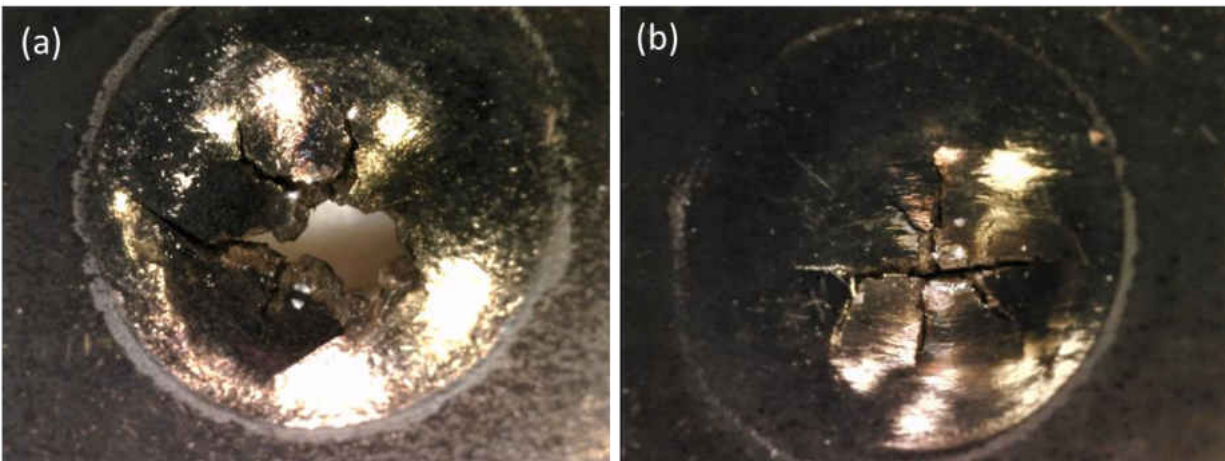


Figure 5.28 - Fracture surfaces of as-manufactured IN939V (a) vertical and (b) horizontal samples tested in cyclic conditions in the as-manufactured condition with  $R=0$  at  $427^{\circ}\text{C}$ .

Microstructural inspection of as-manufactured fatigue samples shows similar behavior to that of the monotonic samples, but with some key differences. As fracture propagation is much more gradual in these samples, the directionality of the microstructure thus has a higher influence on final fracture morphology. Cross-sections of the samples shown in Figure 5.28 are shown in Figure 5.29. These show similar behavior to the monotonic counterparts, though damage is exacerbated due to the gradual accumulation of damage and decreased strength due to heating. However, even considering the deflections of the cracks, overall the fractures present in

these samples are morphologically very similar to those in the monotonic samples, with growth being dictated by the directionality of the microstructure, and very few small deflections occurring, for overall very sharp fractures.

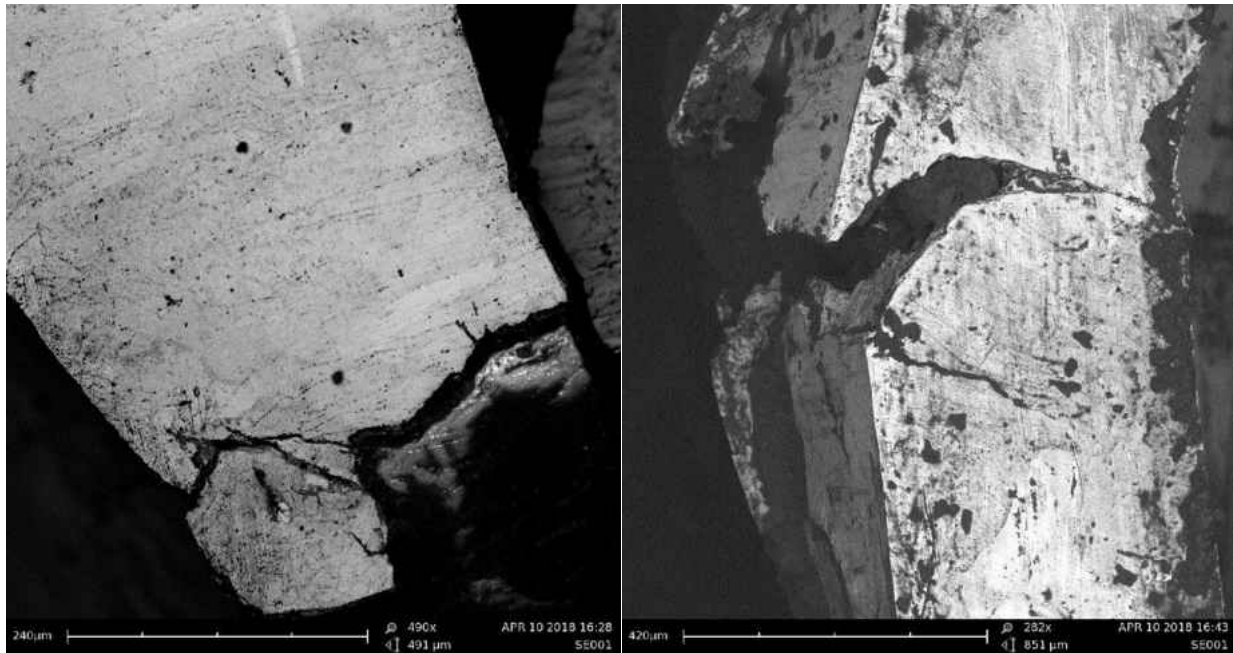


Figure 5.29 - Cross-sectioned as-manufactured longitudinal (left) and transverse (right) IN939V samples tested under cyclic loading with  $R=0$  to 0.5kN and 427°C.

The effect of manufacturing orientation on fracture behavior, however, is mostly mitigated by the implementation of a heat treatment cycle. Examining the fracture patterns of fully heat treated IN939V samples, as seen in Figure 5.30, subjected to cyclic loading with  $R=0$  at 427°C to a load level of 0.4kN reveals only slight differences in the crack morphologies between (a) longitudinal and (b) transverse-oriented samples. Both of these samples, though of different orientations, feature a centralized fracture from which several other cracks radiate, and



they seem to differ only by a small difference in the total amount of cracking, these minute differences are likely attributable to differences in test duration. As such, it can be said that the implementation of a suitably designed post-processing routine can sufficiently alter the microstructure so as to eliminate the tendency of samples to fracture along defects created from manufacturing features.

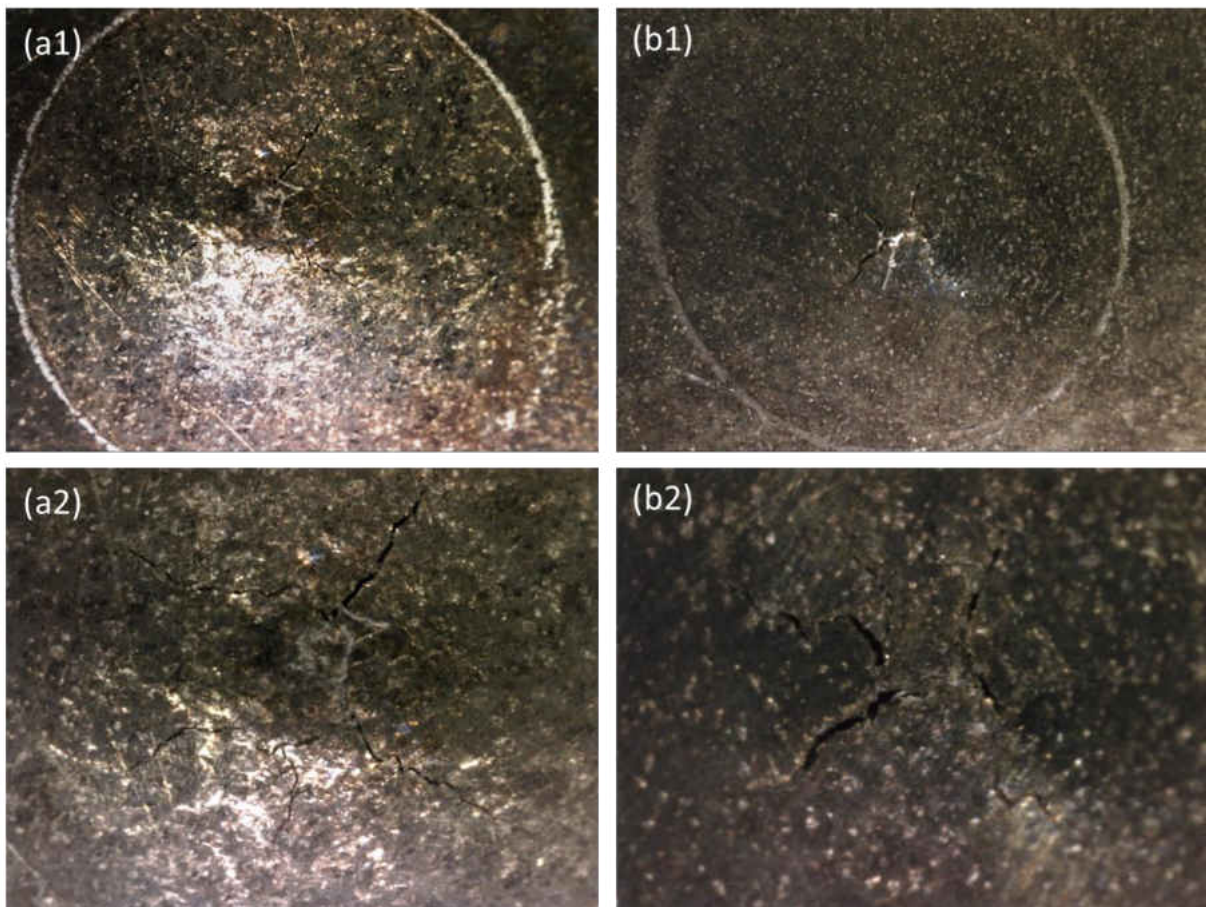


Figure 5.30 - Samples of fully heat treated IN939V tested with R=0 to 0.4kN at 427°C in (a) longitudinal and (b) transverse orientations.

The fully heat treated monotonic samples, however, do not fracture as uniformly as their cyclic counterparts seem to indicate they should. Figure 5.31 shows several fully post-processed examples of fracture resulting from monotonic loading. Both the longitudinal sample, (a), and the transverse sample, (b), were tested at room temperature to gauge the effects of the heat treatment on strength and anisotropy, as can be seen in earlier portions of the report. The fracture surfaces of these samples are very similar and devoid of the obvious signs of directionality, however, though when comparing the two orientations some differences can be seen. The longitudinal samples feature a circumferential crack around the bulge, while the transverse samples, on the other hand, feature a central crack with additional growth stemming radially from it. While the layer-oriented fracturing was eliminated via heat treatment, differences in fracture morphology between the two directions are still present. The fracture morphologies do not change, however, when samples are subjected to higher testing temperatures. Samples (c) and (d) in Figure 5.31 were tested at 427°C. Both the longitudinal samples, (a) and (c), and the transverse samples, (b) and (d), have strong resemblance to each other, regardless of test temperature. This indicates that up to the testing temperatures featured here, and perhaps beyond, there is little effect on fracture behavior.

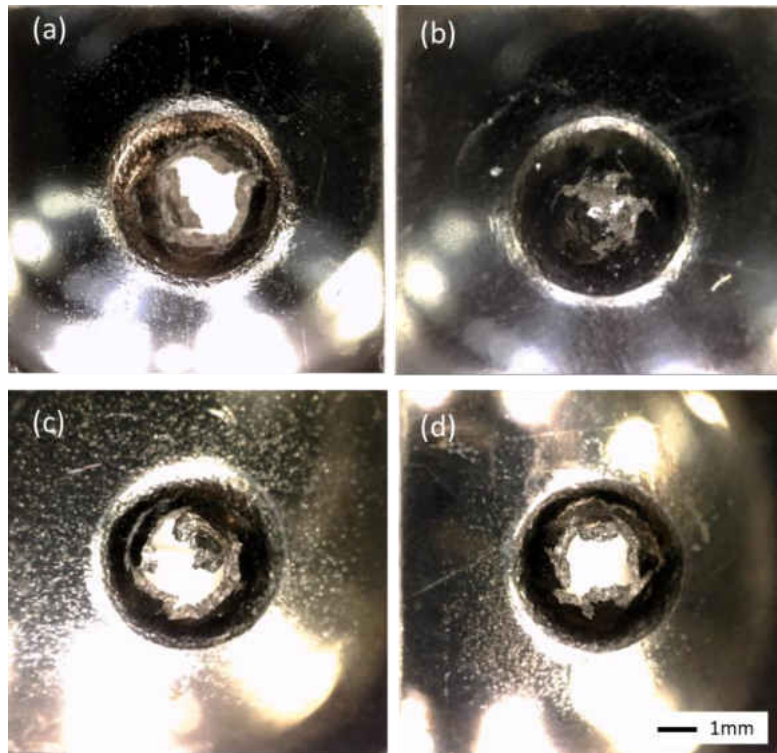


Figure 5.31 - Fracture surfaces of fully heat treated monotonic tests at room temperature (a) longitudinal (T2) and (b) transverse (T3) orientations and at 427°C for (c) longitudinal (T13) and (d) transverse (T14) orientations.

Microstructures of the fully heat-treated IN939V samples show substantial similarities in grain size and shape, and consequently on fracture morphology as well, indicating a reduction in anisotropy due to post-processing modifying the microstructure. Cross-sections of the monotonically loaded fully heat-treated IN939V samples can be seen in Figure 5.32. Both the longitudinal (left) sample and the transverse (right) sample show a significant decrease in directionality in terms of grain shape and distribution as well as in fracture morphology. Although some size difference is still evident between the two directions, the grains now appear very similar in shape and show no obvious signs of directionality. Both fractures are characterized by a significantly higher amount of deflection in terms of direction of growth when

compared to their as-manufactured counterparts. The enlarged grains concurrently cause a decrease in strength for the longitudinal samples and an increase in strength for the transverse samples.

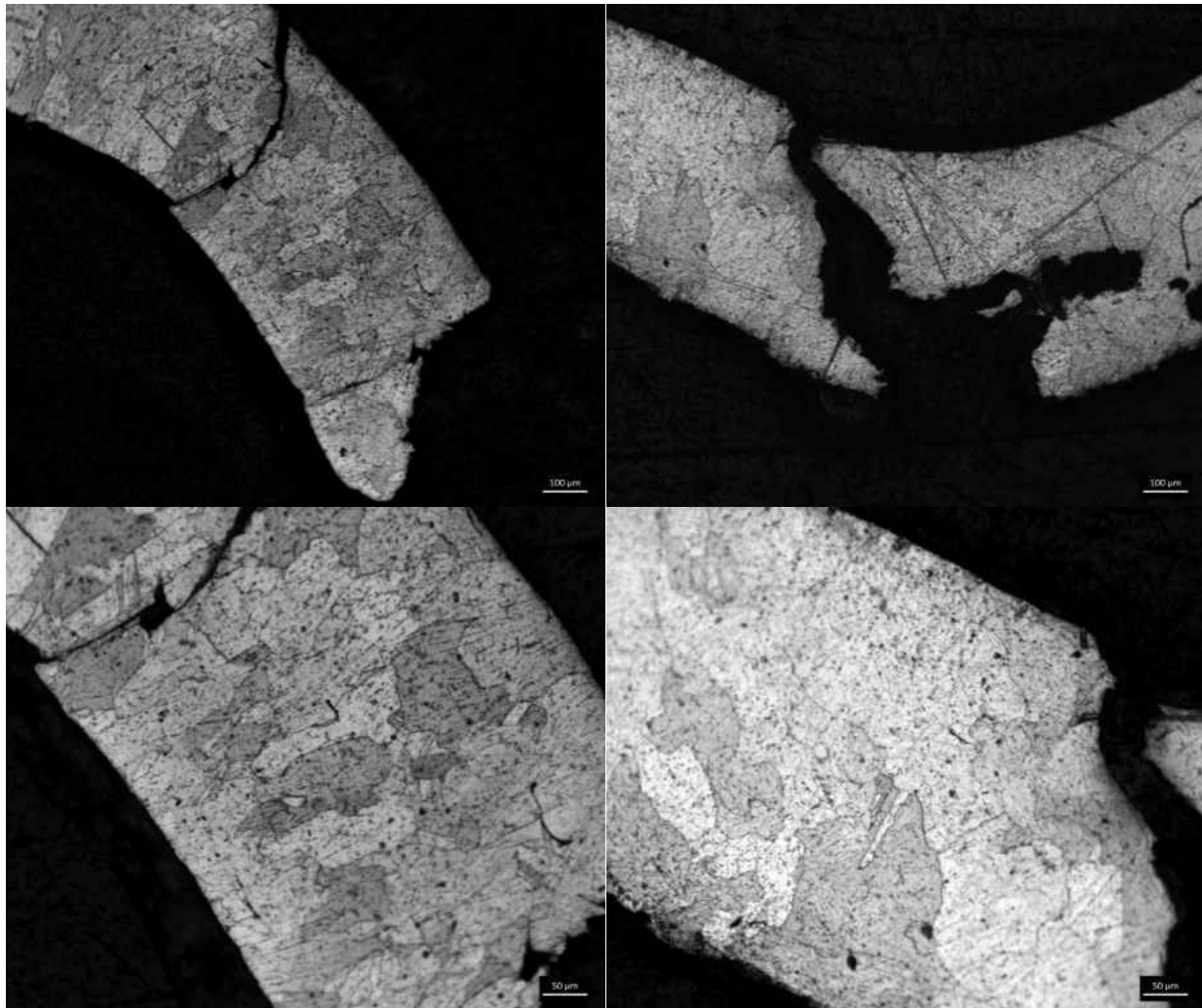


Figure 5.32 - Cross-sectioned views of fracture morphologies of fully heat-treated IN939V samples in the longitudinal (left) and transverse (right) directions.

The behaviors shown in the monotonic samples are also shown in the fatigue samples, again to an exaggerated level. The samples shown in Figure 5.33 show very similar fracture behavior between the longitudinal (left) and transverse (right) samples, with numerous small deflections due to grain morphology. The transverse sample shows a greater amount of damage as compared to the longitudinal sample, though some of this is likely due to the location of the cross-section, some also appears to be due to the coalescence of micropores and their contribution to the overall fracture behavior. As cyclic results favor the longitudinal direction in terms of life, it can then also be determined that the increased deflection in the transverse sample occurs due to sudden damage which ultimately lowers life.

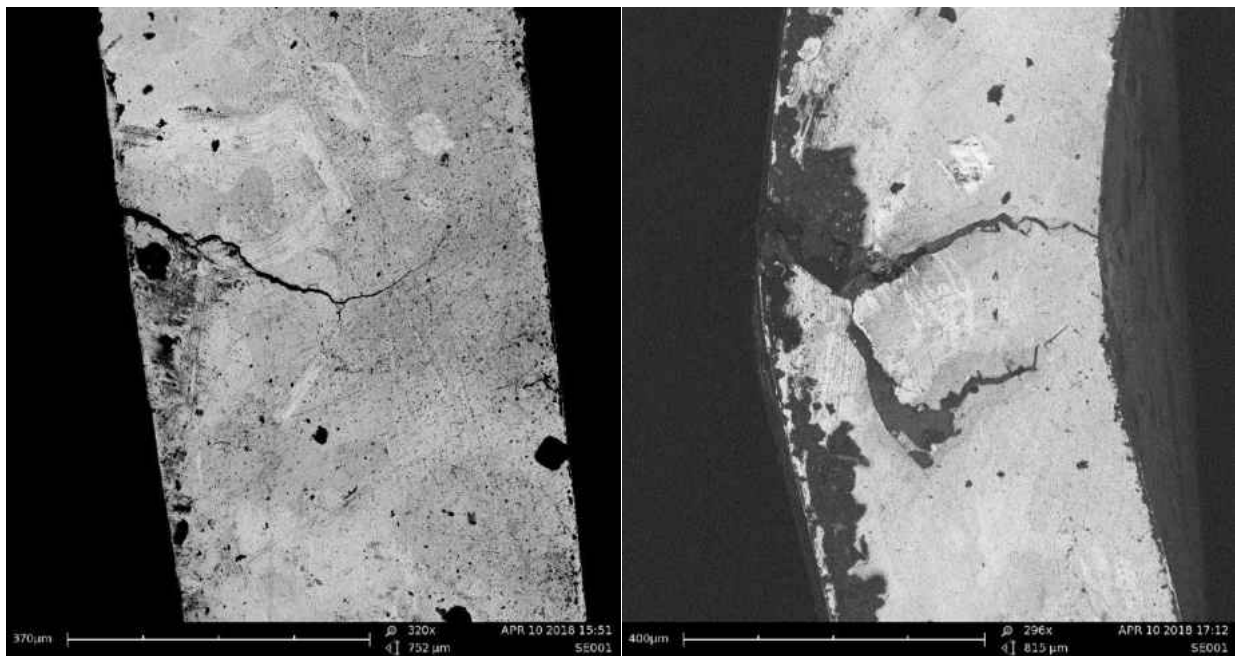


Figure 5.33 - Cross-sectioned fully heat-treated longitudinal (left) and transverse (right) IN939V samples tested under cyclic loading with R=0 to 0.4kN and 427°C.

The various recrystallization cycles implemented in trials T4-T9 do not show readily obvious signs of impacting the fracture behavior of the IN939V samples. Figure 5.34 shows the fracture surfaces of the six recrystallization study samples tested, each of which underwent a different recrystallization cycle, but all of which were subjected to hot isostatic pressing and heat treatment. Comparing (e) and (f), which did not undergo a recrystallization cycle, to (a) and (b), which were subjected to a short recrystallization cycle, respectively, shows very similar fracture patterns, neither of which shows the fracture patterns seen to be characteristic to the as-manufactured samples seen in Figure 5.28. This suggests that the heat treatment implemented on the samples induces sufficient recrystallization to largely mitigate the effects of the layer-wise construction process and the resultant microstructure to which the fracture patterns shown in Figure 5.28 are attributed. Closer inspection, however, reveals changes that are representative of the change to material behavior and characteristics as seen in earlier sections, such as the continuous reduction of anisotropy with increasing recrystallization.

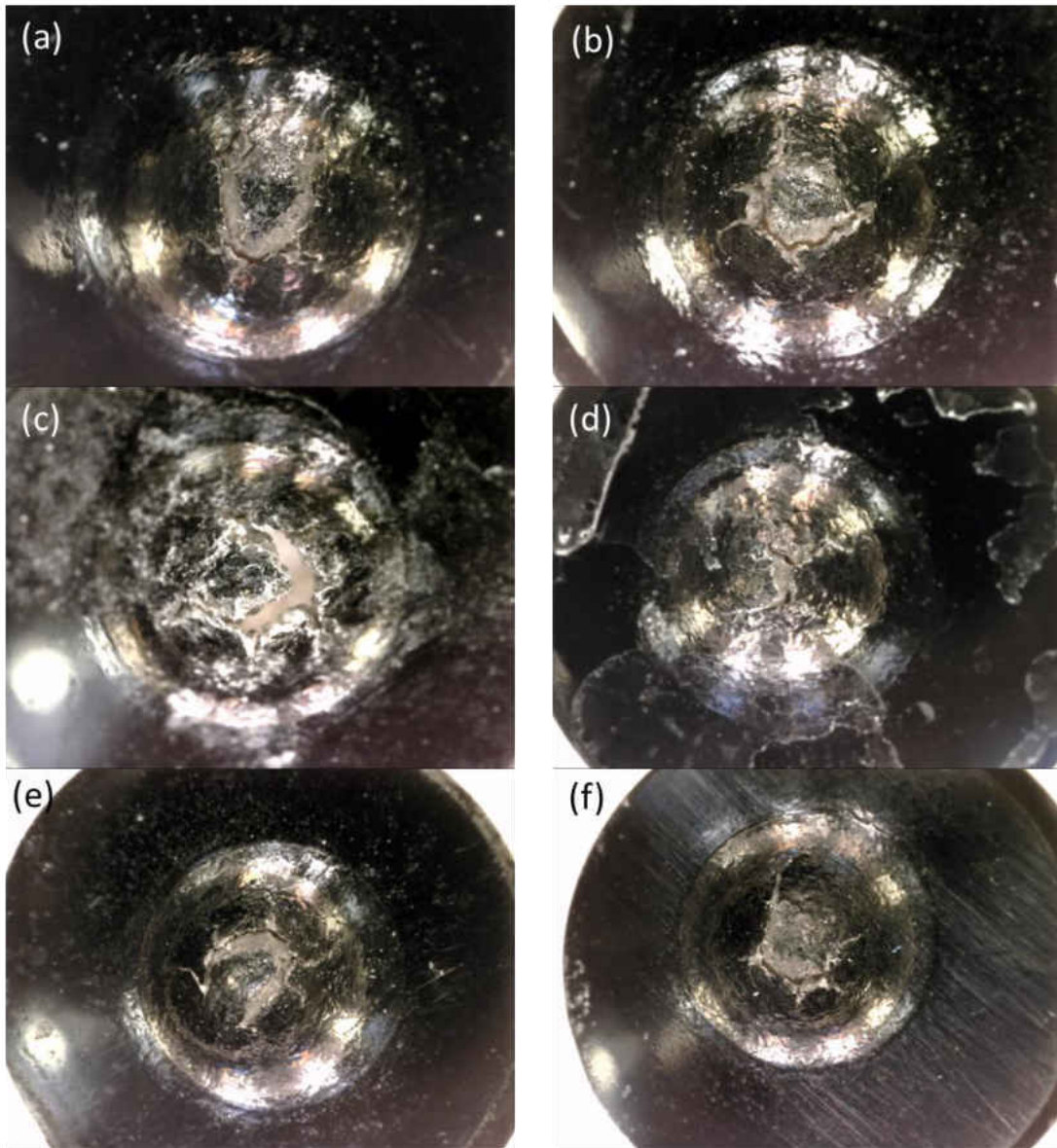


Figure 5.34 - Fracture surfaces of samples sourced from RX study samples for tests (a) T7 (RX1), (b) T6 (RX2), (c) T5 (RX3), (d) T4 (RX4), (e) T9 (RX7), and (f) T8 (RX8).

All of the longitudinal samples, (b), (d), and (f), have similarly shaped fractures, with a similarly sized and proportioned portion of the sample surface lifting away from the fracture. The transverse samples, on the other hand, show a minor evolution in the fracture surface. The

transverse samples in Figure 5.34 (a) and (e) have a separated portion that is thinner than the longitudinal counterparts, but very similar to each other. Comparing these to (c), however, reveals that the longer recrystallization cycle causes the fracture surface of the sample to resemble more closely that of the longitudinal samples, as the lifted portion is proportionately wider than those of the short duration (a) recrystallization and non-recrystallized (e) samples. Consequently, the samples shown in (c) and (d), which are the long duration recrystallization samples in transverse and longitudinal orientation, respectively, feature fracture patterns which bear close resemblance to one another. This denotes a reduction in anisotropy in the shape and distribution of the microstructure, causing the fracture behavior to evolve. This supports findings from monotonic SPT data on these samples, as the directional anisotropy between identically treated samples is reduced with increasing recrystallization cycle times.

For more homogeneous materials, such as the 304 stainless steel, some variation in fracture locations is present at elevated temperatures, likely due to increased plastic deformation (stretching) facilitated by the elevated temperature. A comparison of the fracture surfaces of monotonically loaded 304SS at room temperature and 300°C is shown in Figure 5.35. The side view of the high temperature sample, (b2), shows increased plasticity in comparison to the room temperature sample, (a2), in the form of an elongated, conically-shaped bulge, in contrast to the shorter, more spherical bulge of the room temperature sample. Due to increased plasticity and thinning on the sides of the bulge, the high temperature sample, (b), features a crack located circumferentially on the bulge, rather than traversing through the bottom like the room temperature sample, (a). The high temperature sample also shows other signs of increased damage in the texture of the material, in the form of small tears or ripples. For cyclic tests,



however, although the cyclic data of the single punch  $R=0$  tests for 304SS, trials F1 and F5, show variations in both cycle count and displacement level, morphologically the room temperature and 200°C samples appear to have deformed and fractured similarly.

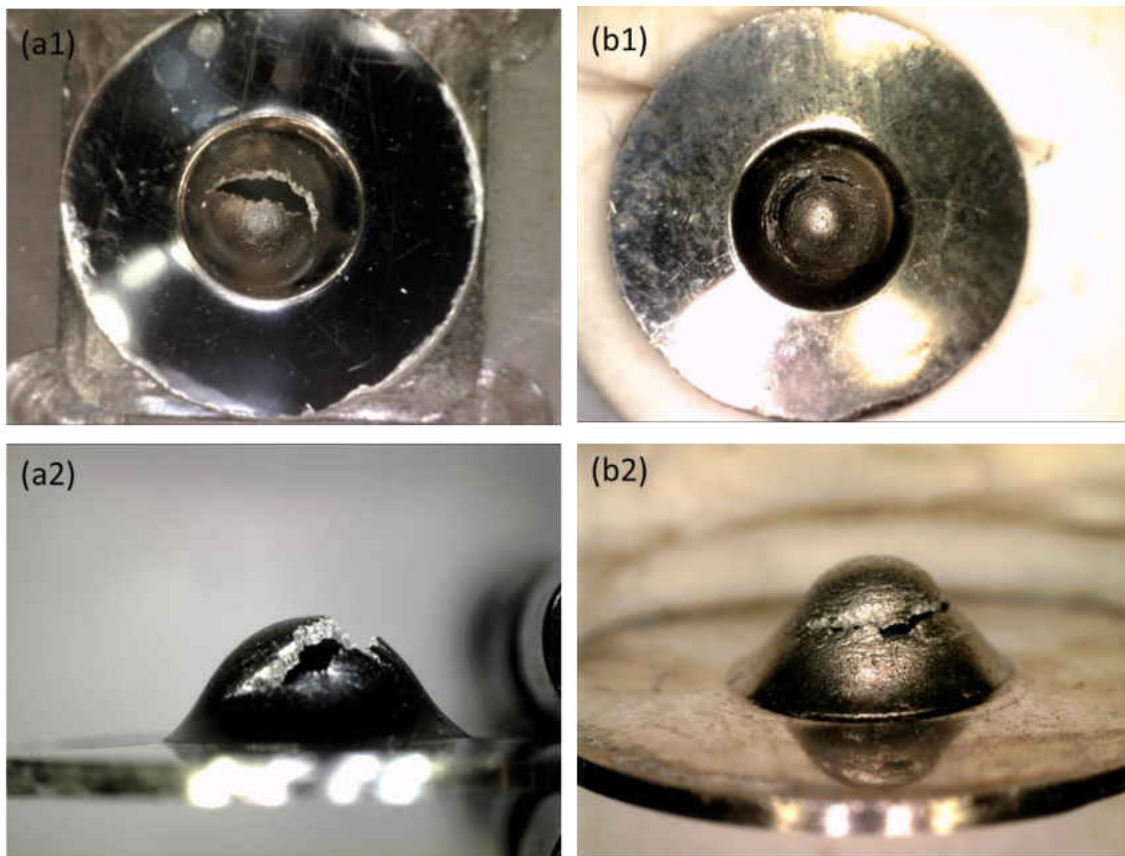


Figure 5.35 - Fracture surfaces of monotonically loaded 304SS at (a) RT and (b) 300°C.

The effects of fatigue test parameter variations can also be seen elsewhere in the fracture morphology of several comparative test trials for both conventional and SLM materials. For example, some variation can be seen when comparing the different load levels implemented for otherwise identical samples of 304SS tested with  $R=0$  at room temperature, as seen in Figure

5.36. Due to the extended duration of cycling sustained by the sample subjected to a lower load level of 1kN, there is increased deformation, which appears more uniform in appearance circumferentially than that of the 1.5kN sample, but also has increased levels of damage to the surface in the form of waves or ripples, due to increased thinning in the walls of the bulge. This is due to the delayed onset of fracture allowing for added plastic deformation of the 1kN sample.

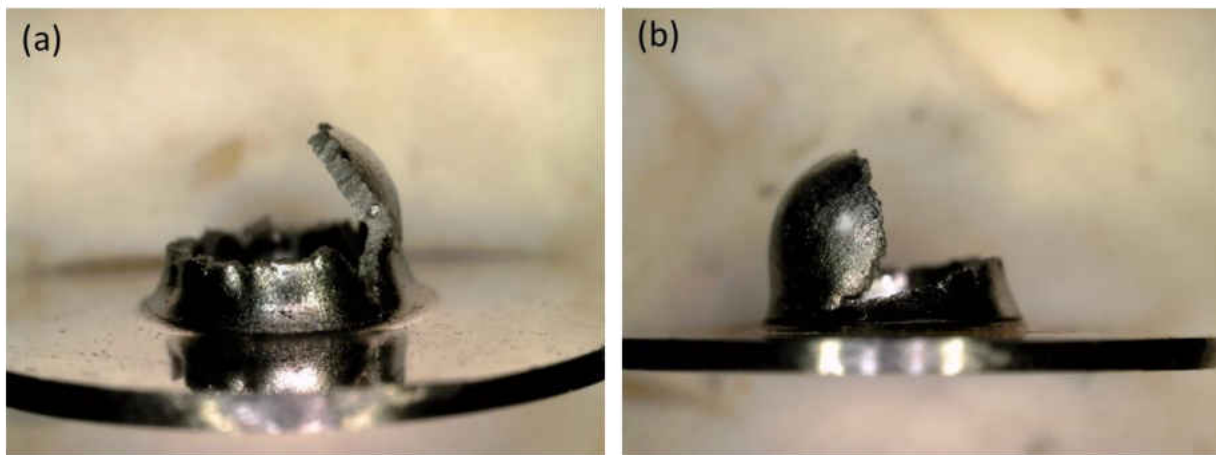


Figure 5.36 - Fracture morphology of 304SS tested at room temperature with cyclic loading of  $R=0$  to (a) 1kN and (b) 1.5kN.

Cyclic load level effects extend to the SLM materials as well. This can be observed by comparing the samples shown previously in Figure 5.30 to those in Figure 5.37, which compares the samples of the two fatigue tests of IN939V fully heat treated samples loaded to 0.5kN, F10 and F11, conducted with  $R=0$  at  $427^{\circ}\text{C}$ . The transverse sample cycled at the lower load level of 0.4kN, Figure 5.30 (b), shows a more distinct central crack than that subjected to the higher load of 0.5kN, Figure 5.37 (b), which is characterized by relatively straight cracks radiating from a central point relative to its lower-load counterpart. This is caused by an increase in intergranular

crack deflection facilitated by the lower load level. It is difficult to determine if this is the case for the vertical counterparts of these, as the higher load level sample in that pair, Figure 5.37 (a), was subjected to a longer duration test after crack initiation and underwent a significantly higher amount of damage, making it difficult to compare the two. Given the similarities of the samples shown in Figure 5.30, however, and the shape of the fracture surfaces on the remainder of the sample, it is expected that the two orientations would not differ much in this respect. All of these samples, regardless of the extent of damage, appear to have fractured radially.

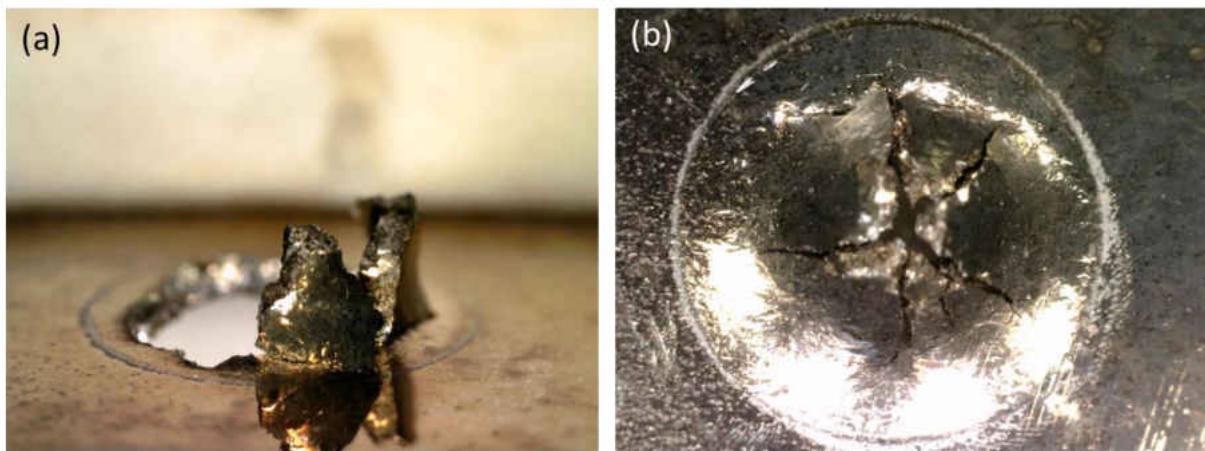


Figure 5.37 - Samples of fully heat treated IN939V tested with  $R=0$  to 0.5kN at 427°C in (a) longitudinal (F10) and (b) transverse (F11) orientations.

Additional cyclic parameter effects are present when considering the R ratio and control mode utilized, whether it was  $R=0$  (load control) or  $R=-1$  (load or displacement control). The type of loading implemented in a cyclic test affects the fracture behavior more dramatically than the load level. The fracture surfaces of F2, F3, and F4 are shown in Figure 5.38, in top (1), bottom (2), and side (3) views. This shows the difference between room temperature cyclically

loaded 304SS samples with (a)  $R=0$  load control (F2), (b)  $R=-1$  load control (F3), and (c)  $R=-1$  displacement control (F4). The  $R=0$  sample, which was tested with the single punch setup, shows a smooth bulge and uniform circumferential fracture similar to its monotonic counterpart, but with an elongated bulge, as the cyclic application to a set load leads to gradual stretching and slower fracture when compared to the monotonic test, allowing for increased plastic deformation. The  $R=-1$  load-controlled sample has a significantly smaller bulge, with increased cracking stemming from the main fracture. Despite this, the general shape of the deformity shows some similarities, as the bulge protrudes from the lower face, indicating that the main deformation is imparted by the upper punch, as the initial loading induces enough plastic deformation downwards that reverse loading by the lower punch does not fully reverse the deformation. The displacement-controlled  $R=-1$  samples, on the other hand, show only minimal protrusion of the surfaces, but with considerable damage and cracking surrounding the final fracture. The profile view of the fracture surface reveals only slight protrusion, indicating the direction in which the sample failed, despite fully reversed displacement, to be dictated by the initial loading direction. In these samples, plastic deformation is fully reversed due to the use of displacement control, which is analogous to strain control in conventional cyclic testing. There is evidence of increased surface damage to this sample as compared to its load-controlled counterpart, due to the repetitive application and reversal of plastic deformation causing increased impact from the punches, with the displacement-controlled sample showing signs of material flaking or being ground off from the sample.

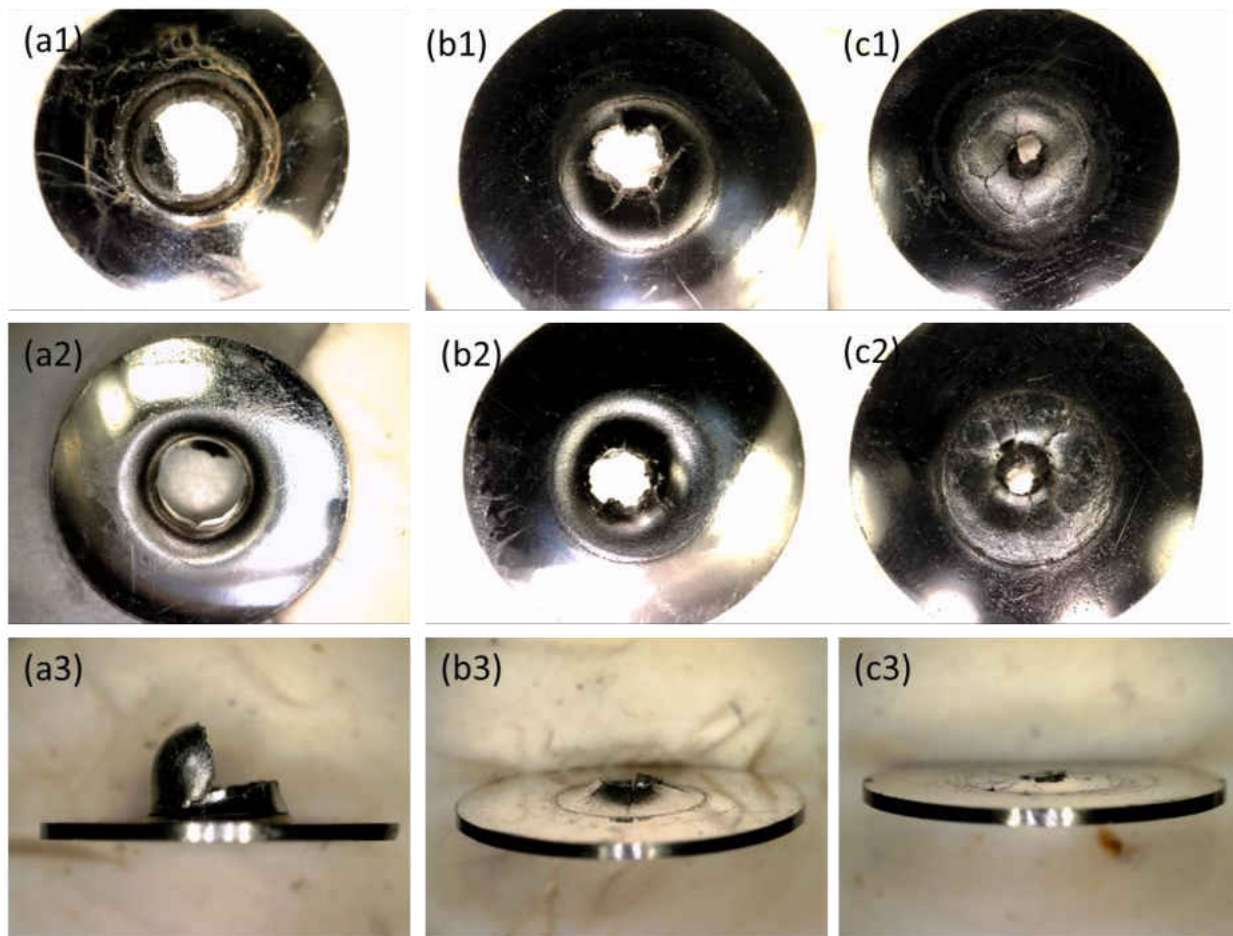


Figure 5.38 - Fracture morphology for cyclically loaded 304SS room temperature samples with control modes of (a) R=0 load control (F2), (b) R=-1 load control (F3), and (c) R=-1 displacement control (F4).

The application of an elevated temperature during reversed cyclic loading results in significantly higher levels of deformation when compared to those tests conducted at room temperature. This can be attributed to an increase in plastic deformation facilitated by the higher temperature setting. In Figure 5.39, the effects of increases temperature can be seen on the resultant fractures when 304SS samples are cycled at R=-1 under (a) load and (b) displacement control conditions otherwise identical to those shown in Figure 5.38 (b) and (c), respectively.

The load-controlled sample in Figure 5.39 (a) features a significantly larger bulge than the room temperature counterpart, as the initial application of load stretches the sample much farther than at room temperature, so that reversed load applications do not return the sample to its original shape. Correspondingly, the high temperature displacement controlled sample, Figure 5.39 (b) is also affected by the increased plasticity, so that resultant fracture morphology more closely resembles that of the room temperature load controlled sample Figure 5.38 (b) than (c), the displacement controlled counterpart. Additionally, Figure 5.39(c) shows the effects of implementing a hold time to cyclic conditions of R-1 with load control. This sample, CF1, was subjected to creep-fatigue conditions by adding a 15s hold time at a load of 0.5kN, but conditions were otherwise identical to those which the sample in (a) was subjected to. There does not appear to be any obvious significant morphological difference between these two samples at final fracture, though the data suggests a large reduction in cyclic life due to the hold time, which allows for increased displacement during each 0.5kN loading phase.



Figure 5.39 - Fracture of cyclically loaded 304SS samples at 200°C with control modes of (a) R=-1 load control, (b) R=-1 displacement control, and (c) R=-1 load control with 15s hold time.

As the data suggests, fracture behavior is dependent on manufacturing, processing, and testing conditions. A general comparison of the fracture morphology of conventionally produced 304SS samples to SLM manufactured IN939V samples reveals more brittle behavior for the SLM material, as fractures begin in a central point and tend to branch and deflect, while increased stretching and a continuous fracture typically characterize the 304 samples. For SLM materials, orientation effects can clearly be seen in as-manufactured samples for both monotonic and cyclic testing, and significantly less so for fully post-processed samples, though some differences are present under certain loading conditions. Additionally, the variation of the recrystallization cycle duration resulted in only slight differences in overall fracture morphology, suggesting that in terms of fracture behavior, the HIP and heat treatment cycles alone significantly reduce orientation effects. For both SLM and conventional materials under cyclic loading, final fracture morphology will be highly dependent on application type (single or dual punch) and the control parameters employed therein. Future work of high interest in this sense would involve in-situ monitoring of fracture formation and development of AM materials in the as-manufactured state, as well as inspection of final fracture morphology using 3D imaging technologies such as CT scanning.

## **CHAPTER 6: CORRELATION OF SMALL PUNCH AND CONVENTIONAL TEST RESULTS**

Results from the small punch test trials presented throughout Chapter 5 will be compared to conventional test results in this chapter to assess the suitability of SPT for characterizing SLM materials, as well as conventional ones. Assessment will be made on accuracy of material properties established via the use of the inverse method and through those established using correlation values and formulae presented in Chapter 2. Comparisons of percentage differences of sample and test variations, such as orientation and temperature, will be made between conventional and small punch test results.

### **6.1 Comparison of SPT and Conventional Test Result Trends**

It has been shown that material properties from conventional tests correlate linearly with equivalent properties determined via the small punch test. As such, variances in orientations should also vary linearly, and differences between them should be similar despite the test method. Percentage differences between testing and manufacturing conditions will thus be compared between tensile and SPT results to assess the accuracy of the SPT results.

#### **6.1.1 Conventional 304SS**

Tensile material property values for 304 stainless steel are readily available in literature, as the material is widely used for a variety of applications. The material property values of interest to this study are given in Table 6.1 at the various temperatures correlating to those of the small punch tests performed here. Percent different values calculated here represent the drop in the material property value of interest at each temperature as compared to room temperature



material specifications. These show a gradual reduction, though at different scales, of each property as temperature rises. These trends will be used to provide context for the data for the SPT tests conducted at those temperatures, using percent differences to quantify their likeness, and comment on the accuracy the SPT as pertaining sensitivity to temperature.

Table 6.1 – Material properties of 304 stainless steel at various temperatures [302, 303].

	<b>RT</b>	<b>200°C</b>	<b>315°C</b>
<b><i>E (Gpa)</i></b>	196	183	174.5
<b><i>% diff. E</i></b>	-	6.63	10.97
<b><i>σ<sub>y</sub> (MPa)</i></b>	297	160	145.5
<b><i>% diff. σ<sub>y</sub></i></b>	-	46.1	51.01
<b><i>σ<sub>uts</sub> (MPa)</i></b>	680	472	453.5
<b><i>% diff. σ<sub>ult</sub></i></b>	-	30.58	33.31

As noted in section 5.1.2, the SPT response of T12, the monotonic SPT trial conducted at 300°C is characterized by severe irregularities to the initial portion of the  $P$ - $\delta$  curve. Consequently, this affects the calculation of the equivalent material property values for which this portion of the response is utilized. As such, the SPT counterparts to trends shown in Table 6.1, found in

Table 5.3, show inconsistencies when comparing the 300°C values to room temperature values. Additional data was included there to facilitate this comparison, utilizing the initial loading cycle of trial F5, conducted at 200°C, though no ultimate strength value is given there due to the cyclic nature of the test. However, comparing the normalized max load difference between 300°C and room temperature SPT values, 32.98%, to that between the tensile values, 33.31%, shows a difference of under 1%. Of note, the values for the tensile properties are taken

as approximations at 315°C, so the real difference is likely somewhat larger, but logically would not be much higher. Contrastingly, the percentage change for the tensile yield strength between room temperature and 200°C is 46.13%, significantly higher than that of the SPT counterparts at only 12.42%. The difference between the elastic moduli, however, is much smaller; 13.34% for SPT and 6.63% for tension. While the difference here is notable, it could be explained by factors such as material post-processing which could affect microstructure and subsequently behavior at elevated temperatures, as tensile data was gathered from literature and not directly acquired from the same source material used for SPT samples. The large difference in yield strengths is cause for concern, however, and casts doubt on the method used to determine the SPT yield point.

A limited comparison of fully-reversed fatigue testing of conventional 304 stainless steel can be facilitated by comparing tests F6 and F7 to the results of [302], namely the results of trials K004 and K021. Trials K004 and K021 were conducted with fully-reversed cycling at 200°C with strain ranges of 1.0% and 0.7%, respectively. A comparison of these based on the strain yields a low/high ratio of 0.7. The SPT trails F6 and F7 were also conducted with reversible loading at 200°C, though with different control modes, F6 being load-controlled at a range of  $\pm 0.5\text{kN}$  and F7 being displacement-controlled at  $\pm 0.5\text{mm}$ . The load control test shows a displacement range of roughly 0.5mm for the majority of the duration of the curve, whereas the displacement control test has a range closer to  $\pm 0.4\text{mm}$  due to the inherent compliance errors between the load frame and the LVDT. Comparison of these yields a displacement ratio of 0.625, similar to that of the conventional fatigue results presented in [302], and this is used as a basis for a limited comparison of the methodologies. The stress histories of the conventional fatigue tests from [302] as well as those from F6 and F7 are shown in Figure 6.1 (a) and (b),

respectively. The conventional results show similar behavior in the early stages of the stress-life curves, but with a significant shortening of cycles for the higher strain range. The SPT results show similar trends, though to a more exaggerated extent. Notable from Figure 6.1 is the likeness of the displacement control results to the conventional curves, as the stress history develops in a similar fashion, though the cycle count is much lower, as the equivalent strain for the displacement used is likely magnitudes higher. There are, however, discrepancies in making the comparison, as F6 and F7 utilize different control modes. As such, the displacement control test, F7, experienced a strain history centered about zero, whereas the load control test, F6, always had a positive displacement. Additionally, due to the control type, F6 displays a more linear stress history than that of F7, as well as a sudden rupture as opposed to a gradual accumulation of damage as the material was increasingly displaced in order to satisfy the control condition. These discrepancies limit the ability to even compare the SPT trials to each other.

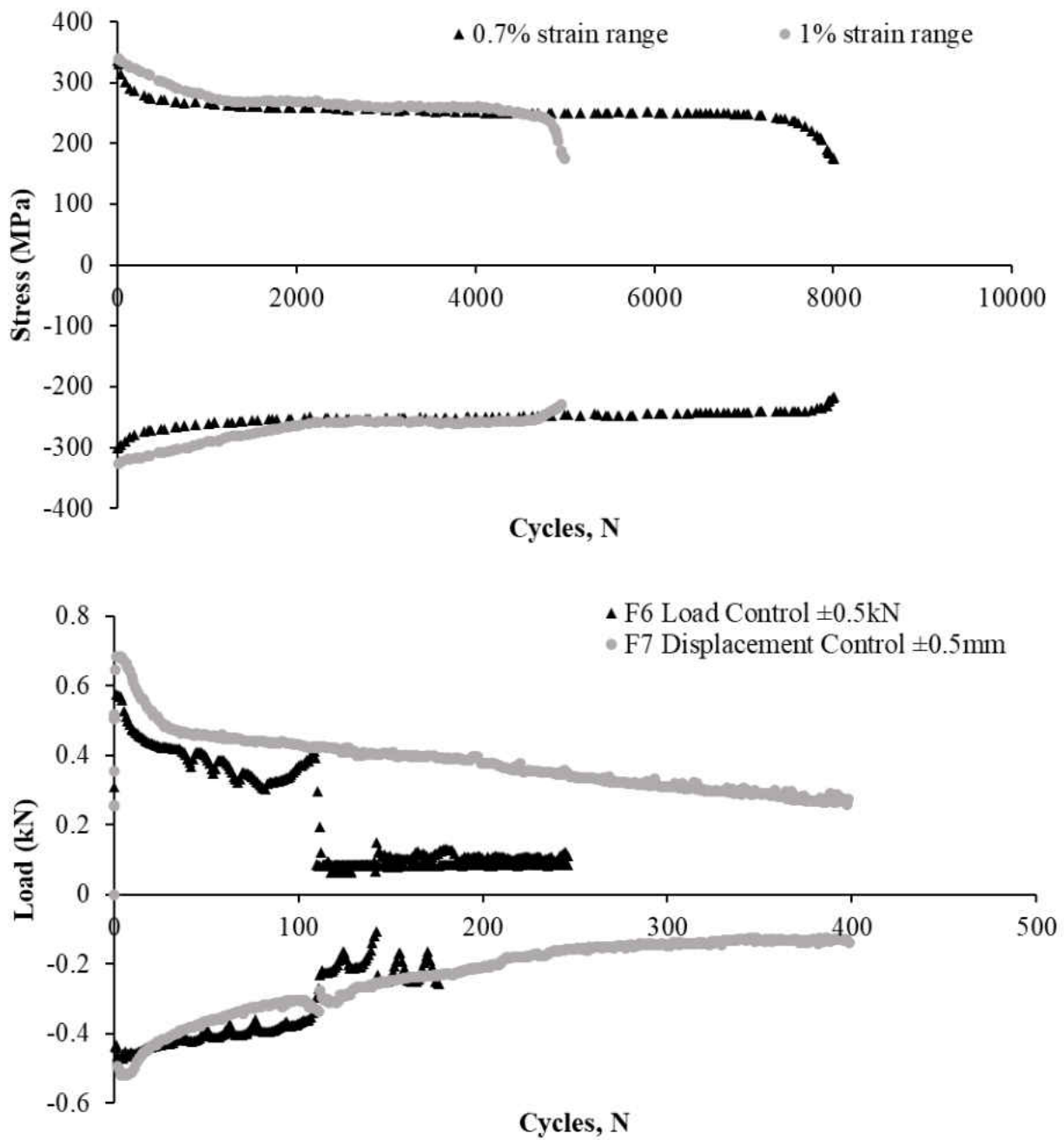


Figure 6.1 - Comparison of (a) conventional fatigue tests [302] with (b) dual-punch reverse-loading SPT cyclic tests (F6 and F7) of 304SS at 200°C.

### 6.1.2 SLM IN939V

Comparing the differences between the orientations for strength and modulus for IN939V found via SPT to those seen in the tensile recrystallization study outlined in section 3.2.1, it is evident that some discrepancies exist in the SPT data. A summary of the material property values from these tests, as well as an analysis of the anisotropy as it evolves with respect to recrystallization time are given in Table 6.2. Once again, the material property values have been normalized with respect to average cast values due to the proprietary nature of the material. The percentage differences between orientations in the tensile results show clear indications of reduced strengths with increasing recrystallization time in both orientations, though this is accompanied with a slight increase in anisotropy, which is exacerbated more in the ultimate strengths than in yield strengths. The values for Young's Modulus, however, show a clear reduction in anisotropy, achieved by a simultaneous reduction in the horizontal sample moduli and an increase in the vertically-produced sample moduli. These trends are reflected in the SPT results, for both the general changes in strength and in the change in level of anisotropy. This indicates good correlation between the tensile and SPT trials, though the inconsistencies in the SPT results suggest the need for replicates when using SPT to evaluate materials, as small changes in test results can easily affect material property calculations and thus the comparison of results such as those of interest to this study.

Table 6.2 – Material property values from tensile test results of the recrystallization study outlined in section 3.2.1.

	<b>RX1 (H,Base)</b>	<b>RX2 (V,Base)</b>	<b>RX3 (H,3X Base)</b>	<b>RX4 (V,3X Base)</b>	<b>RX7 (H,0)</b>	<b>RX8 (V,0)</b>
$\sigma_y$ (ksi/ksi)	1.130	1.049	1.123	1.034	1.261	1.201
% diff. yield		7.159		7.944		4.762
$\sigma_{uts}$ (ksi/ksi)	1.259	1.171	1.250	1.097	1.249	1.215
% diff. UTS		7.035		12.27		2.713
$E$ (ksi/ksi)	1.121	0.936	1.077	1.017	1.067	0.791
% diff. $E$		16.52		5.536		25.89

Further comparison of SPT data for selective laser melted IN939V is facilitated with results from conventional tests from the study on which the test matrices completed here were based. This included, among others, tension tests of fully heat-treated samples at varying temperatures. The percent differences between orientations (using transverse values as a basis for the error calculation) for select conventional tensile test results are given in Table 6.3, only those relevant to this study are shown. Although some scatter is present in the data, the conventional tensile test results generally show a decrease in strength differences with increasing temperature, though ductility values suffer, as do the differences between the orientations, with longitudinally-manufactured samples mostly conserving ductility through increasing temperatures up to 649°C. This suggests some residual anisotropy persists between layers despite full treatment, with increased brittleness in a transverse loading situation when compared to longitudinal loading. The relevant difference values for comparison to those presented in Table 6.3 were given in Table 5.4 for T2 and T3, which were conducted at room temperature, and T13 and T14, which were conducted at 427°C. These results indicate a slight advantage in the longitudinal direction over the transverse, though at a reduced scale in comparison to tensile results. A general reduction in strength is seen with increased temperature as well.

Table 6.3 – Directional differences of tensile tested SLM IN939V at room temperature and 427°C, using transverse values as a basis for calculation.

	RT	427°C
<i>% diff. <math>\sigma_y</math></i>	9.29	7.55
<i>% diff. <math>\sigma_{uts}</math></i>	6.71	4.35
<i>% diff. <math>E</math></i>	7.45	8.20

Several factors need to be considered when making comparisons between these tables, however. The first, as stated in the discussion of the values of Table 5.4 in section 5.1.2, is of the evident error present in the displacement results of T13, as they cause large directional differences, lead to calculation of unreasonably high stiffness, and indicate an increase in strength for heated tests over room temperature results. As such, a comparison of trends with increasing temperature is difficult to conduct. Additionally, the samples used for the SPT tests were sourced from the same donor material, varying cutting direction to acquire the different orientation, whereas those for conventional tests were manufactured in bars with the length aligned along the orientation of interest. As discussed previously, the shape of the donor source can affect material microstructure due to differences in heating gradients as the sample is being built. These factors could affect the overall comparison between these trials, especially when comparing anisotropy and a dominant build direction. This is seen when considering the level of difference between directions for SPT versus tensile. That is, the results for the SPT tests indicate a variation of only 2-3% between directions at room temperature, whereas those for the tensile tests range from 6-9%. In this case, the SPT samples were sourced from the same test block, but the tensile samples were manufactured in such a way as to limit necessary machining, either vertically or horizontally depending on the sample.

Due to the limited capabilities of the heating system in the current experimental setup, comparison of SPT fatigue results to conventional fatigue results is limited. Differences in loading and temperature are present between conventional and SPT data sets so direct comparison is not possible, though general trends can be discerned for both. With respect to IN939V results, conventional results will be discussed but cannot be shown, due to concerns of proprietary information. Conventional fatigue tests of IN939V were conducted at 649°C with  $R=0$ , using strain control, whereas those of the SPT tests were conducted at 427°C with  $R=0$  using load control. Once again, these test results may also be susceptible to differences in manufacturing due to the original sample geometry, as conventional samples were manufactured in the orientation they would be tested, while SPT samples for both orientations were sourced from the same block. In general, conventional results favor the transverse direction for these tests, though some variation to directional dominance can be seen with respect to temperature and strain range. Transverse samples also required higher stress ranges than the longitudinal samples for each of the displacement ranges tested. Of note, conventional results of  $R=-1$  tests favored the longitudinal direction over the transverse direction in terms of cycles to failure. In comparison, the SPT results seem to indicate opposite trends, as results favor the longitudinal direction in terms of life. Transverse samples are also shown to be more sensitive to load changes in the SPT tests, whereas the conventional results show that longitudinal samples are more sensitive to changes in strain range, though both show a significant decrease in life with increased loading range. As noted, several factors differ between the studies, including control type and temperature, yet the trends clearly indicate disagreement between the two methods for tests conducted with  $R=0$ .



### 6.1.3 DMLS GP1

Material properties for the EOS 17-4PH stainless steel equivalent, GP1, are available for comparison to SPT data from tensile and cyclic tests conducted on the samples which also served as the source for the SPT samples [304]. The tensile material properties are shown in Table 6.4, along with a calculation of the percentage difference between the two axes along which the transverse tension samples were built. Percentage differences are calculated with respect to the sample built along the y-axis. Of note, the values for Young's modulus from the tension tests are not given here, these were determined from the initial loading of cyclic tests. The data in Table 6.4 shows a directional dependence with respect to the orientation of the long axis of the sample on the build plate, with the y-axis sample showing at least an 11% increase over the x-axis sample in strength parameters. Tensile test responses show both an upper and lower yield point, which vary 16% and 14%, respectively, between the y- and x-axis samples, with a difference of 12% for the ultimate tensile strength and -3% for the Young's modulus, indicating a higher value for the x-axis sample. Comparatively, the SPT data shows differences of 12% for yield load, 2% for max load, and 19% for the Young's modulus. While the difference in SPT yield loads is close to the difference of the lower yield points of the tensile tests, the SPT data is incomplete (as the max load for frame was reached before load peaked), so the depiction of the max strength as compared to tensile tests is inaccurate, as the loading of the SPT samples exceeded the capacity of the load frame before the samples failed. In terms of correlation between SPT and tensile test results, then, data available is limited, though the yield strength differentials show promise. In the case of the moduli, however, while the SPT data conserves the trend of higher values for the sample produced along the y-axis, the data from [304] indicates a minimal advantage for the x-

axis sample. The source data, however, comes from the first cycle of fatigue tests within the work, rather than from the tensile tests, so rate-related differences could be possible. In terms of cyclic behavior, the SPT results continue to indicate an advantage in strength for the sample manufactured along the Y-axis over the sample manufactured along the X-axis. The conventional low cycle fatigue results presented in [304] seem to indicate similar behavior, though this advantage switches with stabilized cycle results; the duration of cycling in SPT is not long enough to indicate whether or not this would be the case.

Table 6.4 – Material properties of DMLS GP-1 [304].

	<b>x-axis</b>	<b>y-axis</b>	<b>% diff.</b>
$\sigma_{y\_upper}(MPa)$	597	698	14.5
$\sigma_{y\_lower}(MPa)$	534	638	16.3
$\sigma_{uts}(MPa)$	956	1086	11.97
$E(MPa)$	164571	159171	-3.393

#### 6.1.4 DMLS IN625 and IN718

The small punch test results of DMLS IN718 and IN625 produced results with trends inconsistent to those of traditionally manufactured materials, as stated in section 5.1.5. However, consideration for differences stemming from manufacturing and the adaptation of a material to additive methods must be given, as materials may sometimes be modified to some extent to allow manufacturability and the methodology affects material properties. As such, the material properties for each material in the as-manufactured condition as provided by the manufacturer when using the recommended processing parameters are given in Table 6.5. Of note, the IN718 data was provided with respect to manufacturing orientation, while the IN625 was not, and

presumably the maximums are provided. The SPT results in Table 5.7 give consistently higher values for the analogues of the material properties in Table 6.5 for IN625 as compared to IN718. However, the manufacturer-supplied data shows that the IN718 should have higher material property values than the IN625, similar to what is seen with conventional versions of these materials, though to a lesser extent. This indicates likely error in manufacturing of one or both of these materials, or large error in testing with the SPT, as the differences in the trends are quite distinct. Additional testing types and analyses of the source materials is required to determine the exact source of the error. As the IN625 and IN718 samples used for SPT were manufactured in opposing orientations (longitudinal vs. transverse, respectively), additional uncertainty exists when comparing resulting trends to those provided by the manufacturers, given that the data for IN25 is not provided with respect to orientation.

Table 6.5 – Material properties of AM IN625 and IN718 as reported by Stratasys and EOS, respectively [305, 306].

	<b>IN625 (unspecified)</b>	<b>IN718 (horizontal)</b>
$\sigma_{uts}$ (MPa)	1006.63	1060
$\sigma_y$ (MPa)	668.79	780
$E$ (GPa)	179.26	160

## **6.2 Correlation of Material Properties**

As was reviewed in section 2.3.3, linear relationships exist between small punch test data and tensile data for the same material. Equivalent values for mechanical properties are determined by normalizing corresponding inflection points in the force-displacement data. These linear relationships involve the use of a correlation constant to equate them, which is determined

by establishing the linear relationship by plotting tensile mechanical properties against their SPT counterparts. As shown previously, plotting various materials together yields correlation values which may be used to estimate material properties of a range of materials from their SPT results.

Plotting the various additively manufactured materials tested here against tensile mechanical properties reveals a relationship which is incompatible with those cited previously for various conventionally produced metals. The plots shown in Figure 6.2 give correlations for IN939V for the ultimate tensile strength,  $\sigma_{uts}$ , and its SPT equivalent  $P_{max}/\delta_{mt}$ , the yield strength,  $\sigma_y$ , and its equivalent  $P_y/t^2$ , and the Young's modulus,  $E$ , with  $k/t$ , the initial slope normalized by the sample thickness. Due to confidentiality concerns, these values are normalized with respect to typical properties exhibited by the cast equivalent. Of the three plots shown in Figure 6.2, only the correlation for Young's modulus shows a reasonable trend for the linear fit used, although the correlation plots for the yield and ultimate strengths have higher  $R^2$  values. The plots for  $\sigma_y$  and  $\sigma_{uts}$ , however, are skewed by the presence of outliers which affect the linear trendline, as they reduce the relative scatter of the data around it by increasing its length so much. This is not the case for the Young's modulus plot, however, as all of the results are clustered around the trendline to some extent.

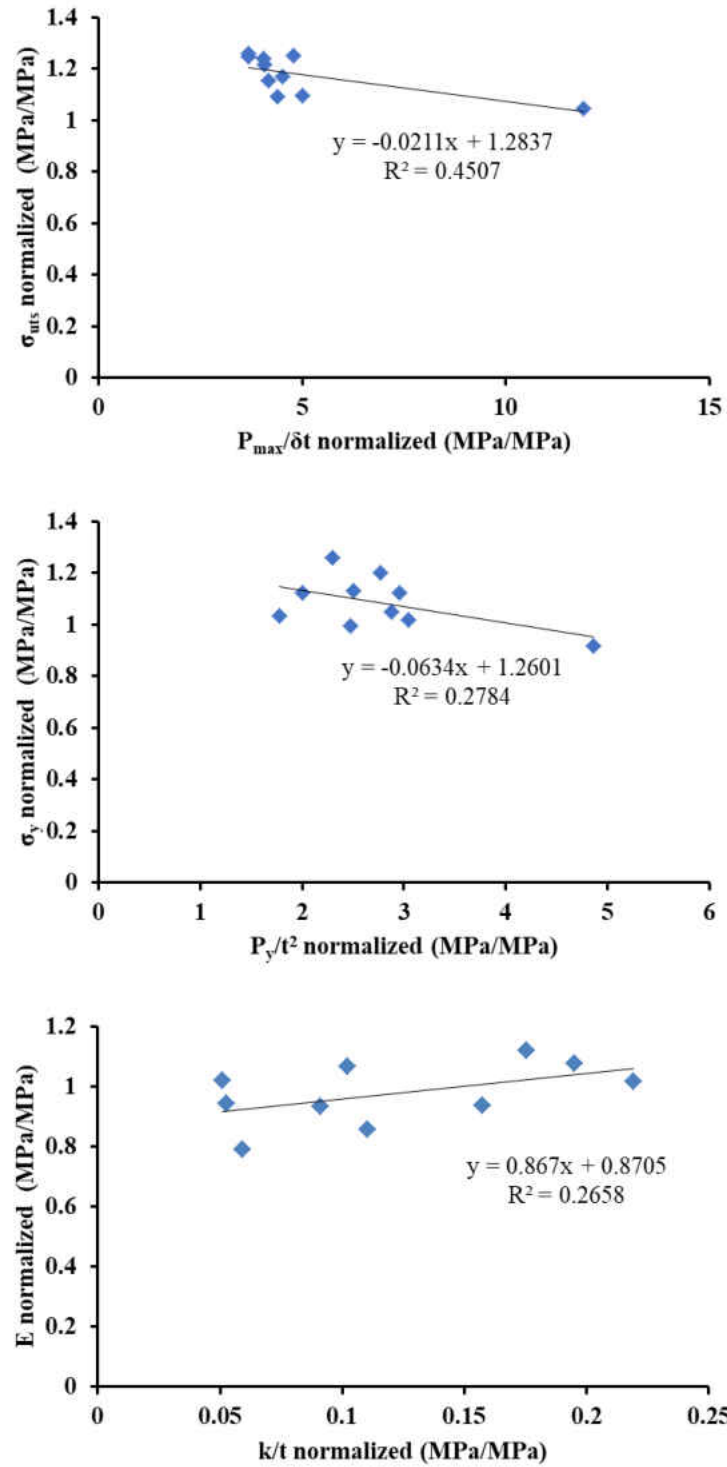


Figure 6.2 - Normalized correlation plots of material properties from tension tests with corresponding SPT inflection points.

Eliminating the outliers present in the data has a severe impact on the correlation plots for  $\sigma_y$  and  $\sigma_{uts}$ , though the extent of that impact varies between the two. For the correlation plot of  $\sigma_y$  with  $P_y/t^2$  one obvious outlier exists, that of T13 which appears far to the right of all other points. Considering the data without this point gives much closer grouping, but with vertical spread and lacking lateral distribution, the  $R^2$  of the linear fit is reduced to 0.0049 with a correlation constant of -0.0142 and an intercept value of 1.1395. For  $\sigma_{uts}$  the fit of the trendline, and therefore the ability of this linear model to describe the data, are improved considerably in terms of  $R^2$  when removing the outliers. If the data of T13, which is the lone point appearing on the far right of the plot, is not considered, then the adjusted model fits with an  $R^2$  of 0.3391, a decrease in fit from the original  $R^2$  value of 0.4507, though visually the trendline makes more sense after the adjustment. Excluding one additional point, that of T5 which utilized RX3 and whose results were indicated as atypical in section 5.1.3 due to being abnormally high, then the  $R^2$  value then increases to 0.7352. The outcome of these omissions is shown in Figure 6.3. Although there are general abnormalities in the trends of the SPT results normalized with respect to  $\delta$  and  $t$  for the tests using the RX trial samples, that of RX3 exhibits the highest level of inconsistency, and as such it has the greatest effect on the correlation plot. Further consideration of omissions can be made for the other high temperature test, T14, as it no longer fits within the testing bounds of the other data since T13 is omitted due to being erroneous. Doing so changes the  $R^2$  to 0.8654. Even considering these omissions, the model still shows scatter and a less than perfect fit but suggests that the use of the small punch test to evaluate changes in processing and testing conditions is feasible, as a linear relationship does exist. Characteristic of these correlation plots for all but

that of  $E$  is the negative slope, or correlation constant, and high intercept value for the linear fit, both of which differ from the relationships published widely in literature.

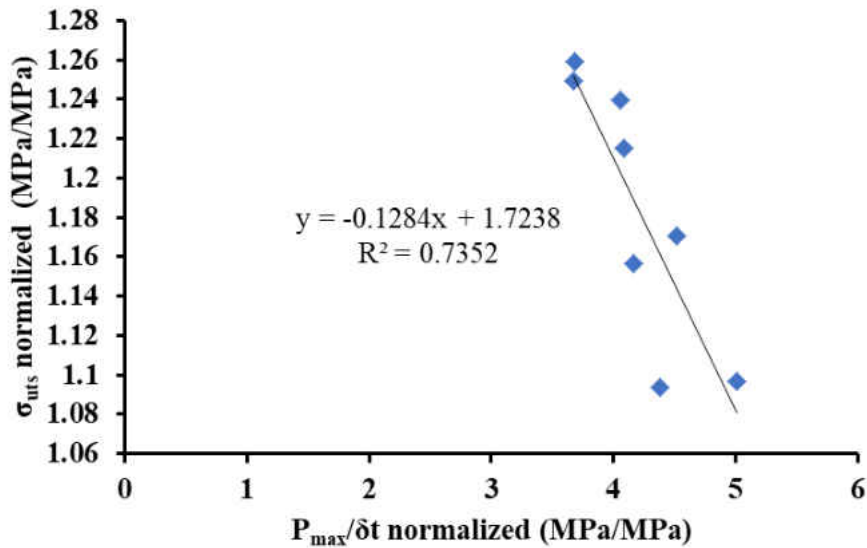


Figure 6.3 - Normalized correlation plot of  $\sigma_{uts}$  for IN939V data with outliers omitted.

The addition of the other materials tested to the normalized IN939V data has varying effects on the correlation plots. The results of combining the other materials with the IN939V data are shown in Figure 6.4. For the  $\sigma_{uts}$  plot this includes only the IN625 and IN718 data, as the strength of the GP1 samples exceeded the 2kN load limit of the test frame so  $P_{max}$  data is not available for these. For the  $\sigma_y$  and  $E$  plots this includes IN625, IN718, and GP1. Again, the data has been normalized with respect to IN939V cast data due to confidentiality concerns, and the results of T13 omitted. Introduction of the additional material data for the  $\sigma_{uts}$  correlation serves only to add significant scatter to the plot and diminishes the quality of the linear fit. For the  $\sigma_y$  correlation plot, however, the data shows independent linear trending and fits well within the bounds of the IN939V data, improving significantly upon the previous linear fit for the IN939V

data alone. For the Young's modulus, the additional material data fits within the lateral bounds of the IN939V data, but adds scatter along the vertical axis, diminishing the fit as perceived by the calculated  $R^2$  value due to a lack of trending within the limited additional AM data independently.



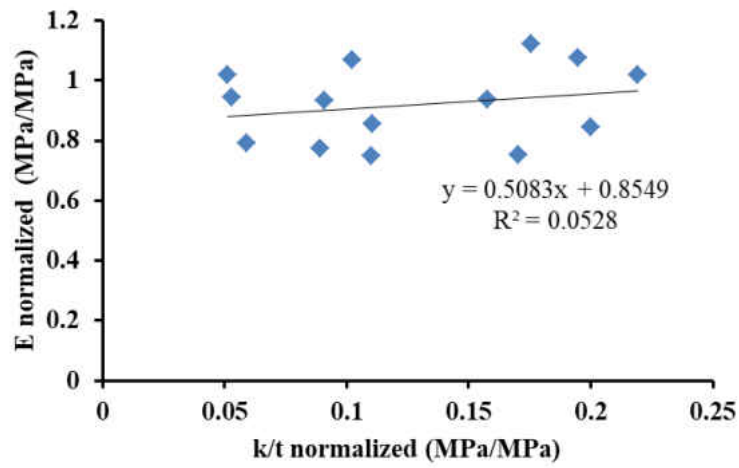
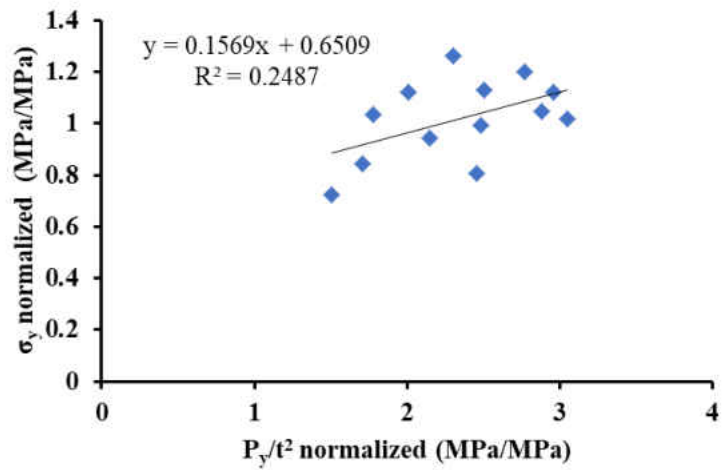
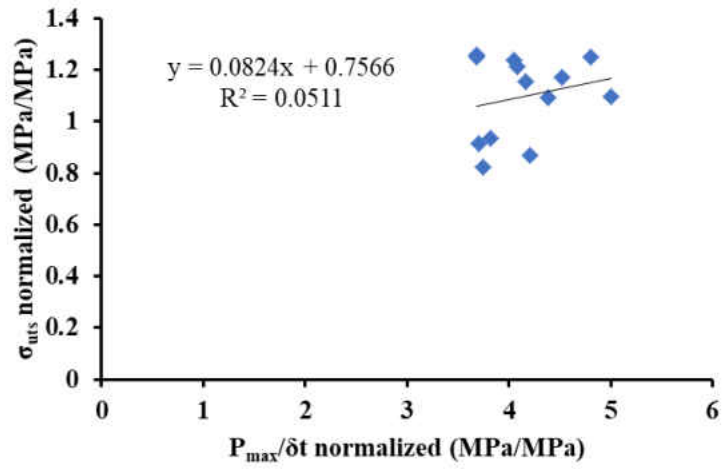


Figure 6.4 - Normalized correlation plots for assimilated data of all AM materials tested.

Regardless of the varying effects, however, the combined data serves to enforce the idea that the small punch test can be used to evaluate the evolution of AM materials due to processing parameters and post-processing techniques. Notable changes in the plots in Figure 6.4 as compared to those in Figure 6.3 include positive correlation constants for all of three relationships examined, trending closer to what is typically found in literature. This suggests that relationships can be established for estimating material properties for AM materials. Refinement of the linear models will require additional AM material data and refined testing procedures, however, given the outliers within the present study.

Within the wider context of literature, however, the data fits well, though enough data could not be gathered for a Young's modulus correlation plot. The plots in Figure 6.5 and Figure 6.6 account for an expanded array of materials from various sources, building on the relationship established in [12], and including the experimental data from this study. Several of the sources added are generalized via material class despite the inclusion of material variations, such as various grades of boiler steels (4), Al alloys (5), and iron-based powdered metals (6 varieties + HT versions). These present added variety which strengthens the validity of the correlation. The plots show the correlations of the  $\sigma_{uts}$  and  $\sigma_y$  as determined via tensile testing against the corresponding SPT values  $P_{max}/\delta_{mt}$  and the  $P_{y(t/10)}/t^2$ , respectively. Although the combined data add scatter which reduce the  $R^2$  values from those seen in [12], the data points fit well along the trend line, and the correlation values produced for the linear fit with a zero-value y-intercept are similar to those proposed by Garcia et al. as cited in section 2.3.3. Using a non-zero y-intercept for the yield strength correlation value increases the fit as described by the  $R^2$  value but only by a minor amount and changes the correlation factor by a more significant amount. The difference is

more pronounced for the ultimate tensile strength correlation, however, and as such a non-zero intercept is more appropriate for a large variety of materials. Some materials gathered from literature seem to present a special case in terms of behavior, such as MnMoNi55 in the yield plot or the H11 in the tensile strength plot; in the case of H11 the point is not included in the trendline due to the severe impact on fit. While the class of material matters, these plots and the resulting correlation are also sensitive to individual researchers' methodology, errors, the sensitivity and accuracy of their displacement measurements, and the stiffness of their testing systems, as shown in [307]. Note that no correlation plot is given here for the range of collected data. This is due to both the general lack of data given in literature to support this relationship, as well as the poor fit presented by the data found. Creating a correlation using only the limited data found in literature, the fit line is characterized by an  $R^2$  value of 0.431; adding the results of the various AM materials from this study reduces this to 0.266. The poor fit may again be an indication of the inadequacy of utilizing the  $k/t$  value to establish a correlation with the Young's modulus, and that an alternative method should be pursued, such as that suggested in [221].

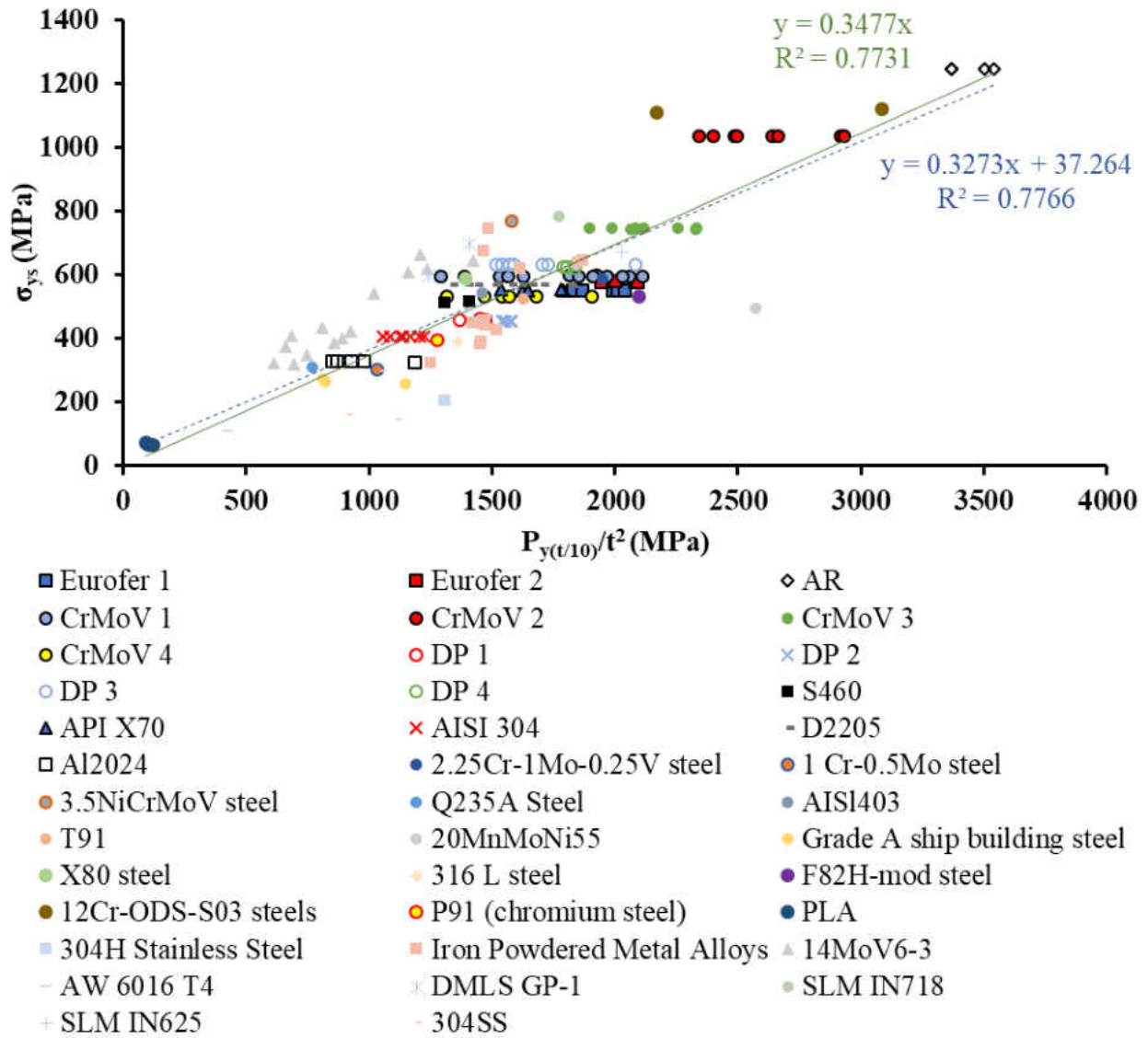


Figure 6.5 - Correlation of tensile and SPT yield data, compiled from experimental data and [12, 19, 24, 30, 207, 213, 215, 219, 220, 276, 277, 283, 302-304, 307-310].

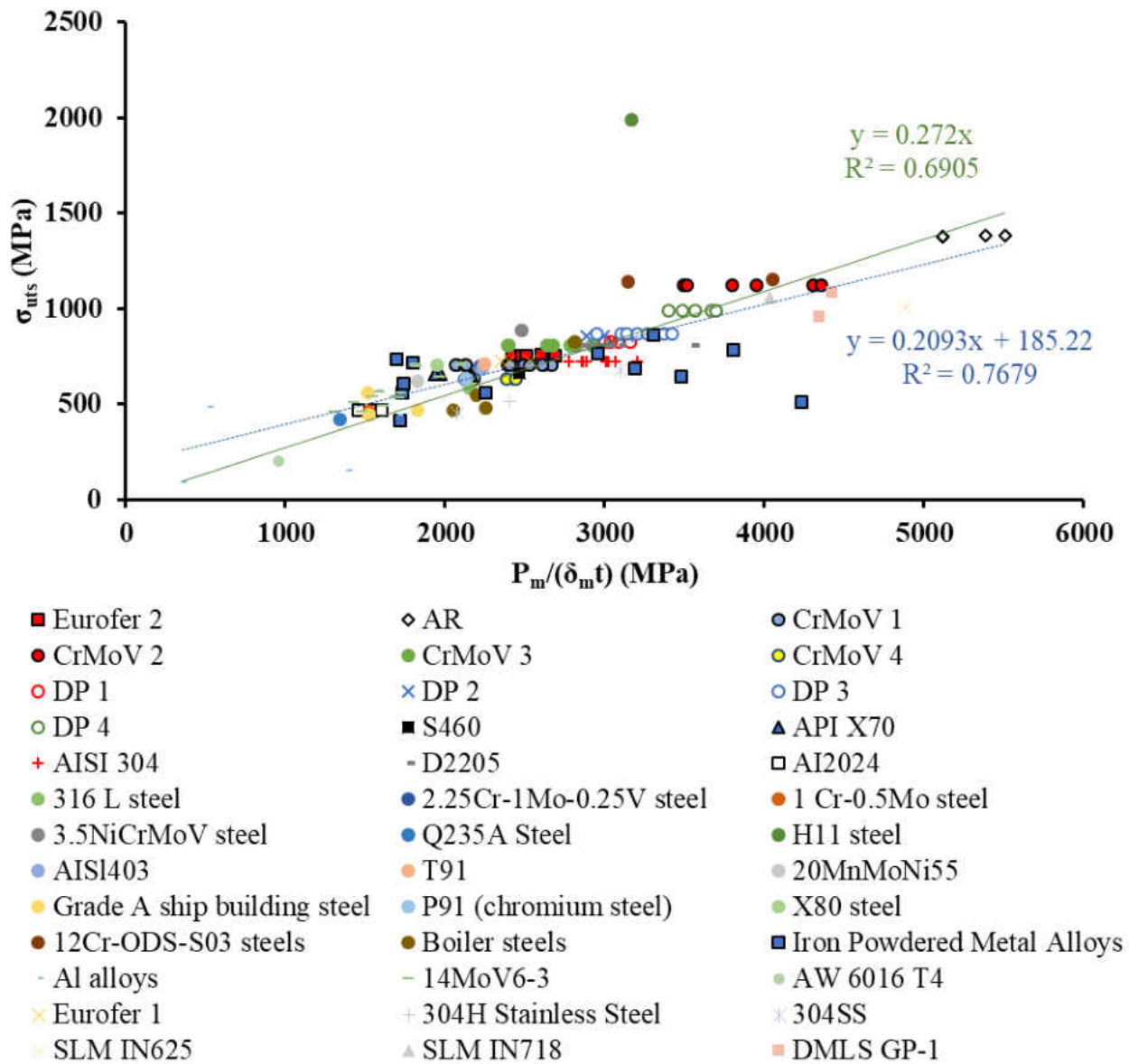


Figure 6.6 - Correlation of tensile and SPT tensile strength data, compiled from experimental data and [12, 19, 24, 30, 207, 213, 215, 219, 220, 276, 277, 283, 302-304, 307-311].

The added data for the tested AM materials are on the higher end of the data range and present a wide spectrum of results depending on treatment and testing temperature. Although not considered additive, the powdered metal alloys in [30] present a similar sensitivity and variance,

as shown in Figure 6.6, which skews the trendline. Excluding these can change the trendline  $R^2$  values to 0.7965 and 0.8471 with and without a zero-value y-intercept, respectively. A similar effect is seen when considering the IN939V data in the yield correlation, which changes the correlation relationships to

$$\sigma_{ys} = 0.3345 \frac{P_y}{t^2} + 35.94 \quad (R^2 = 0.7513) \quad (33)$$

$$\sigma_{ys} = 0.3539 \frac{P_y}{t^2} \quad (R^2 = 0.7485) \quad (34)$$

The effect is minor, however, on both the correlation constants and the fit value, indicating that the calculated constants should provide suitable estimates of the yield strength. Including the IN939V data in the  $\sigma_{uts}$  correlation produces an adverse effect, however, as the data falls closely around the existing fit line, and as such improves the fit, even including the scatter presented by the powdered metal alloy data. The all-inclusive relationships between  $\sigma_{uts}$  and  $P_{max}$  then become

$$\sigma_{uts} = 0.2243 \frac{P_{max}}{\delta_m t} + 153.3 \quad (R^2 = 0.8082) \quad (35)$$

$$\sigma_{uts} = 0.2727 \frac{P_{max}}{\delta_m t} \quad (R^2 = 0.7653) \quad (36)$$

These relationships can then be used to produce material property estimates, which can be compared to conventional test results. The added scatter and diminished  $R^2$  values are reflected in the values predicted using the non-zero y-intercept relationships, Equations 30 and 32, as well as in the high and varied errors as compared to published tensile material properties, as seen in Table 6.6. The yield strength errors in particular showcase a range of error indicating

both under- and over-estimation. These can be likely be linked to errors in the initial portion of the  $P$ - $\delta$  curve, which is utilized for determining  $P_y$ . The error range for  $\sigma_{uts}$  estimation is smaller and consistently over-estimates versus the actual value, particularly the higher temperature test. As such, though the fits of the correlation relationships indicate the ability to make reasonable estimates of material properties, the calculations indicate that these relationships are not wholly reliable for acquiring material properties. Therefore, they may be used to assess trends in data due to processing changes in order to establish best practices in terms of processing and testing, but not recommended as a substitution to conventional testing for determining material properties. Rather, these methods should be implemented to expedite and economize the process of refining process settings for production of AM materials, and the correlations established used to give numerical trends, with full-sized test coupons produced to tensile test standards used for final determination of material properties.

Table 6.6 – Error calculation for strength properties predicted using experimental results and correlation relationships established in this study.

	$P_{y(u/10)}/t^2$	$\sigma_{ys}$ pred.	$\sigma_{ys}$ actual	% error	$P_{max}/\delta_{mt}$	$\sigma_{uts}$ pred.	$\sigma_{uts}$ actual	% error
<b><i>T17 GP-1 X-axis</i></b>	1243.41	444.23	597	<b>25.59</b>	4347.5	1128.44	956	<b>-18.04</b>
<b><i>T18 GP-1 Y-axis</i></b>	1411.63	499.29	698	<b>28.47</b>	4427.69	1146.43	1086	<b>-5.56</b>
<b><i>T15 IN625</i></b>	2028.07	701.05	668.79	<b>-4.82</b>	4881.1	1248.13	1006.63	<b>-23.99</b>
<b><i>T16 IN718</i></b>	1773.20	617.63	780	<b>20.82</b>	4301.15	1118.05	1060	<b>-5.48</b>
<b><i>T1 304SS RT</i></b>	1050.00	380.93	297	<b>-28.26</b>	3100.33	848.705	680	<b>-24.81</b>
<b><i>T12 304SS 300°C</i></b>	1110.00	400.57	145.5	<b>-175.30</b>	2077.91	619.374	453.5	<b>-36.58</b>
<b><i>F5 304SS 200°C</i></b>	917.00	337.40	160	<b>-110.87</b>				

### **6.3 Summary**

Comparison of experimental small punch test data and equivalent conventionally-sourced data indicates good agreement between them. For monotonic SPT tests of SLM materials, trends are mostly preserved with respect to variations of orientation and processing conditions, as well as with changes in test conditions. The SPT results reflect the sensitivity of the methodology to track changes in material properties due to alterations to microstructure caused by process parameter variation. Though some negative correlations were seen in cyclic test comparisons, these tests should be considered to have primarily served as proof-of-concept runs for the apparatus design and the methodologies proposed. Further tests of this nature should be constructed with considerations for equivalent load and displacement levels using equations such as those for equivalent strain, considering the  $\pm 0.5\text{mm}$  displacement-controlled trial was effectively conducted at a 200% strain level with respect to sample thickness. The reversed-cycling results themselves, however, are a promising indicator for the novel design presented here, due to their likeness to traditional test results.

The strength of the match of these trends is not reflected in estimation of material properties. The plots correlating SPT and tensile properties generally have  $R^2$  values indicating an acceptable goodness-of-fit with a wide array of materials, including those produced via AM. However, there are still significant levels of scatter which produce high errors when using the linear relationships determined from these plots to estimate material properties from the experimental results. Likewise, the visual fits of the simulated responses produced by the optimization of numerical model to each test response were generally on the high side as indicated by the calculated  $R^2$  values and correspondingly low error.



The methodology presented here correlates well with conventional test results and is thus suitable for the purposes of analyzing SLM material evolution due to process and post-process parameter variation. This allows for the use of the SPT to economize the optimization of process parameters and post-processing routines. The determination of material properties, however, is best conducted via traditional testing techniques once best practices for manufacturing have been determined via SPT. Estimates may be acquired with the correlation relationships and the use of the inverse method as presented here, but these should serve as a basis for inspecting trends. Although the correlation plots seem to indicate usability for many materials and corroborates the findings in literature, the collection of these shows that the differences in test setups and procedures will produce enough scatter to make estimates unreliable. Formal standardization is needed to promote uniformity in order to remedy these issues and improve the accuracy and usability of these relationships.

## CHAPTER 7: CONCLUSIONS

The rapid evolution of additive manufacturing technologies has had a disruptive effect on the modern manufacturing landscape. The added complexity afforded by AM techniques continues to influence the design and implementation of these technologies into industries such as medical, automotive, aerospace, and energy. As these techniques are implemented, more materials are adapted for use with them, but due to the inherent characteristics of layer-wise manufactured materials, they must first be fully characterized, and their processing optimized to ensure the strength and safety requirements of the applications are met. To economize the time and cost involved in optimizing new materials for AM, the small punch test has been investigated in this study as a means to track morphological changes due to processing and post-processing parameter variations. As such, a framework has been created in this study by which the small punch test may be utilized to optimize processing parameters and post-processing operations for additively manufactured materials. This has been shown by studying the effects of varying post-processing conditions on the material properties of samples produced with selective laser melting in varying orientations and geometries. Additionally, efforts have been expended towards the advancement of acceptance of the SPT as a methodology for material characterization, expanding the capabilities and applicability of such.

A novel SPT device was developed and used to characterize conventionally produced 304 stainless steel as well as an assortment of additive manufactured materials in a variety of processing conditions. Several test types, conditions, and control modes were investigated to investigate the independent effects, and the variations and trends between tests were compared to equivalent conventional tests. Correlation plots of tensile material properties and corresponding

inflection points from  $P$ - $\delta$  data were created to find the relevant linear relationships between them. The practices developed here can thus be recommended for use in determining optimal process-parameter settings at a reduced cost in terms of time and material, with the conclusions of such a study then used to produce tensile samples for determining material properties. The simplicity and accessibility of the apparatus developed is ideal for such a purpose, allowing for testing to be conducted at a number of facilities, rather than requiring the complex testing mechanisms used for conventional testing of these high-strength materials. An overview of the accomplishments made within this investigation is provided:

- **A variety of test methodologies were implemented using the small punch test to evaluate material properties.** Small punch test methodologies were implemented in this study to examine the mechanical properties of materials including conventionally manufactured 304 stainless steel and various AM materials. The experimental device developed here is capable of reproducing small punch tests equivalent to several conventional tests. Test methods include those equivalent to conventional tests such as tensile, fatigue, and the introduction of creep-fatigue, all under various conditions and with materials at different stages of processing but utilizing the same simple sample design. A compact heating device allowed for testing at various temperatures, and results showed high sensitivity to these conditions, as is seen in conventional tests. Optical microscopy was utilized to correlate SPT results with changes in fracture morphology as they relate to differences in the processing state of the samples.

- **Developed experimental routines to investigate processing parameters involved in AM.** The experimental matrix executed in this study was designed to test the differences in processing and post-processing parameters of AM materials, including manufacturing orientation, the application of heat treatment, and differences in the heat treatments applied. The responses of the materials under these varied conditions were manifest in the  $P$ - $\delta$  responses of the monotonic loading tests, as well as in the  $P$ - $N$  and  $\delta$ - $N$  plots of the cyclic responses. Several variations of control were tested during the study to establish best practices for future endeavors, and in the hopes of advancing efforts to formally standardize the SPT. As has been shown, adaptation of this methodology has the potential to expedite the optimization of processing and post-processing routines for new AM materials, economizing the time and cost required to bring components made with these materials to market.
- **A novel adaptation for cyclic reversible loading was developed.** To emulate the effects of conventional fatigue testing more closely, a novel cyclic testing apparatus was developed. This removable adaptation allows for the application of fully-reversed loading routines, mimicking those utilized with conventional fatigue tests. Results show trends similar to responses seen with conventional fully-reversed fatigue tests, though on a reduced scale. Several loading and control types were explored, yielding a recommendation for best practice for continued work. Additionally, the effects of a hold time were explored, mimicking those conditions seen in creep-fatigue testing.

- **Relationships were established for correlating conventional and SPT material properties.** Working from the basis of correlation factors provided in literature, SPT and tensile tests results have been collected from several works and presented together to propose a refined set of factors. These factors are inclusive of a diverse set of materials, including those presented here. The results produced here fit well within the body of these collected works, though together they tend to present some additional scatter. The scatter in these plots can be largely attributed to differences in testing apparatuses and methodologies of different researchers, as variations in system stiffness have been shown to affect results. The goodness of fit shown in these plots indicates high promise for establishing universal correlation factors for different classes of materials which produce quality material property estimates and bodes well for efforts to standardize SPT practices.
- **A numerical model was developed to establish SPT sensitivity to variation of conditions and implemented for the inverse solution.** An axis-symmetric numerical representation of the apparatus used in this study developed in ANSYS and used for numerous purposes. First, a parametric study was conducted to confirm the ability of the SPT to track small changes to material properties as caused by variations in processing parameters. This model was then further developed and used to implement an inverse solution, whereby the properties of the model were altered to match the equivalent experimental response until an optimal solution was found with minimized error. The optimized solution can

then be used to estimate material properties and an equivalent tensile stress-strain curve.

## CHAPTER 8: RECOMMENDATIONS

A methodology has been established which can be used for the assessment of microstructural and mechanical property evolution of AM materials due to changes in processing parameters. In the course of the study, however, and in the results presented in Chapters 5 and 6, it has become evident that these methods can benefit from refinement and further study. Suggestions to address these issues are addressed here, along with ideas for refining and enhancing the quality of future studies. These recommendations will aid in focusing future studies utilizing the novel fatigue procedures developed here, optimizing novel AM materials, as well as in efforts to standardize SPT practices.

- **Establishment of test procedures for increased accuracy and sensitivity.** The occurrence of outliers and their negative effects on results due to procedural errors or otherwise has been shown. As the small punch test is lacking formal standardization, errors such as these are not surprising. This is especially true when considering the scale of the test, where small deviations in sample or measurement quality can translate into large errors. Improvements to general test practices include increased accuracy measurements for displacement, established heat-up and soak procedures to avoid initial deformation from thermal expansion, and general experimental design considerations. In part, this could be achieved by focusing studies using design of experiments techniques to emphasize variable effects on individual test modes, including multiple replicates to curb the influence of outliers and gauge the effects of possible interactions. As SLM materials have been shown vulnerable to defects, the use of multiple donors (or

locations with a donor) for each sample type should also be considered, to avoid the possibility that an entire donor component is in itself an outlier. Sample sectioning and polishing routines should be refined to achieve uniform thickness and finish to mitigate any such complications and prevent the occurrence of defects which could cause premature failure. Finally, as it has been shown that sample donor geometry can affect material properties, it is suggested that future studies utilize simple, identical donor geometries for evaluating the variables of interest and the effects of directionality.

- **Refine fatigue/cyclic testing procedures.** Several cyclic small punch experiments were developed and tested in this study, with loading direction and control modes variants affecting results. The results for these vary accordingly, with some tests more closely resembling the behavior of conventional fatigue tests. Refinements for cyclic SPT include control, such as in explicitly using displacement control for the dual punch setup, to resemble strain controlled conventional fatigue tests, while single punch tests should be load controlled. Regardless of which is used, however, lower load and displacement levels should be utilized to lengthen the test duration and examine more closely the deformation evolution. A suggestion is made to utilize relationships such as those presented in Chapter 2 for determining equivalent strain levels. An overall refinement in procedures should reduce errors, especially as there are concerns that initial thermal expansion of the sample causes undue deformation which affects results. The final objective of a concerted effort into refining the fatigue apparatus and



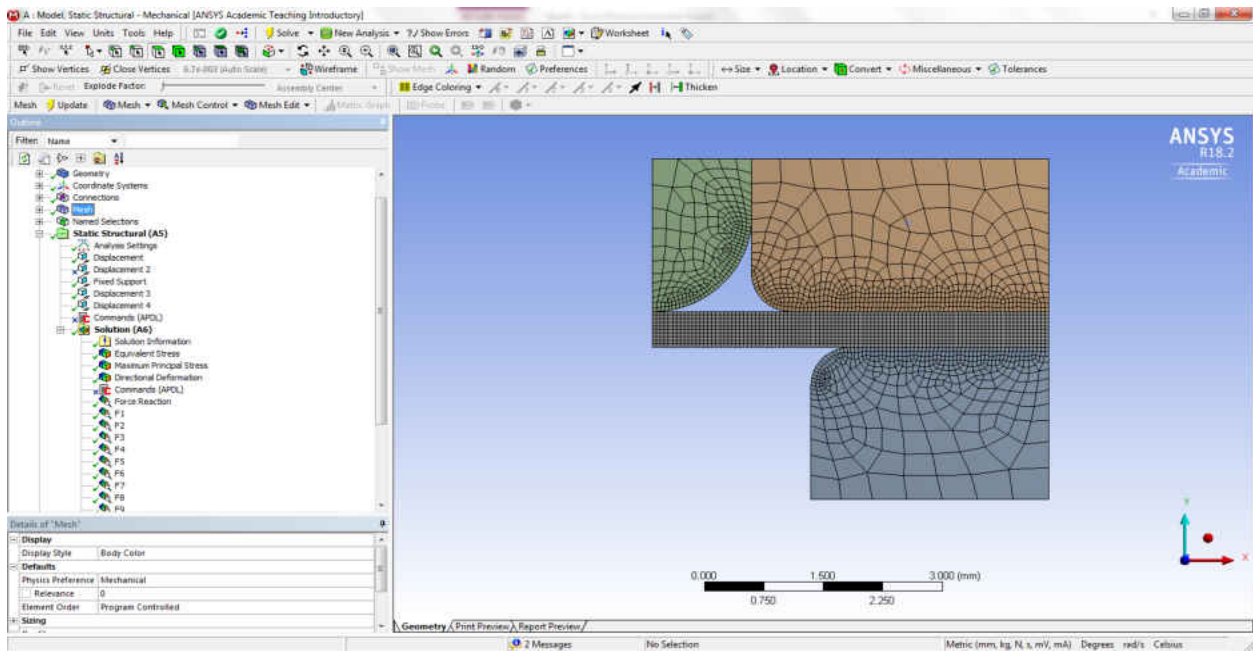
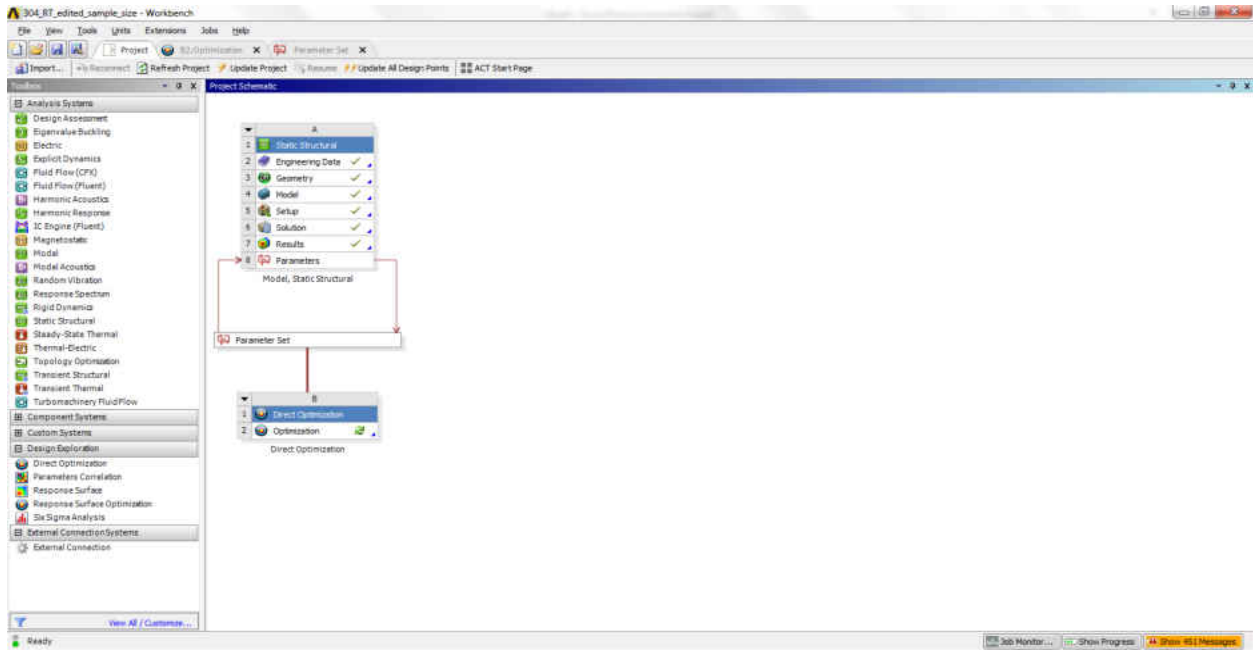
procedures would be to find an equivalency model relating conventional and cyclic SPT quantities, such as those which exist for tensile and creep testing.

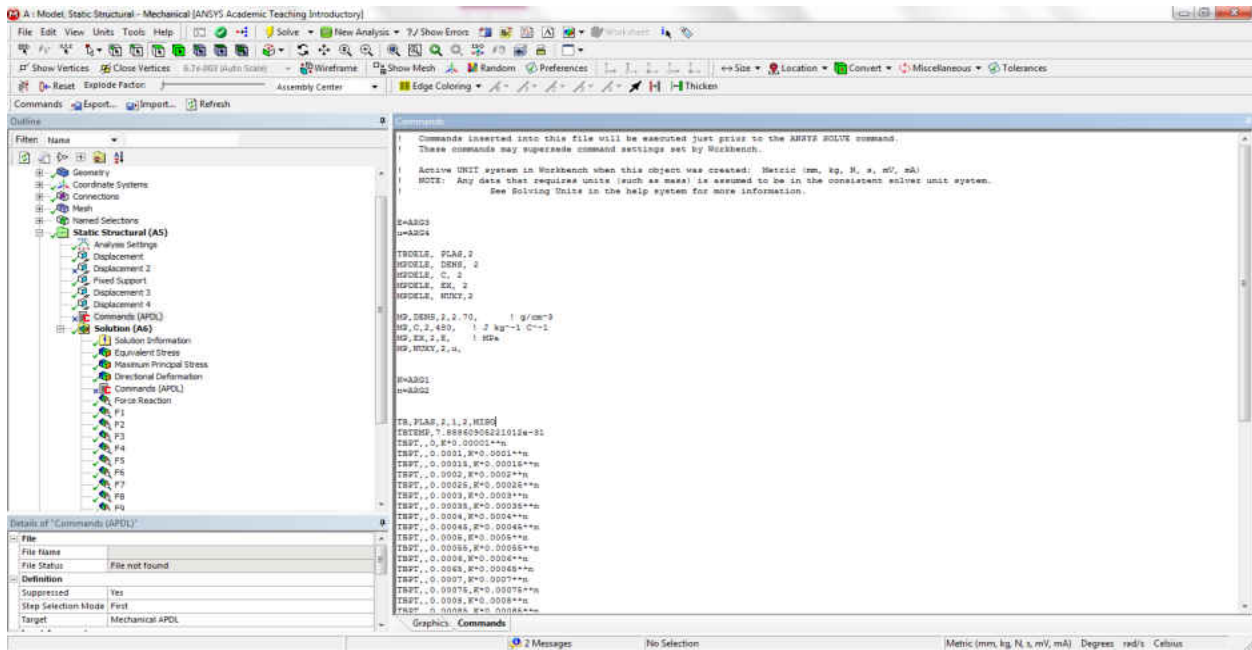
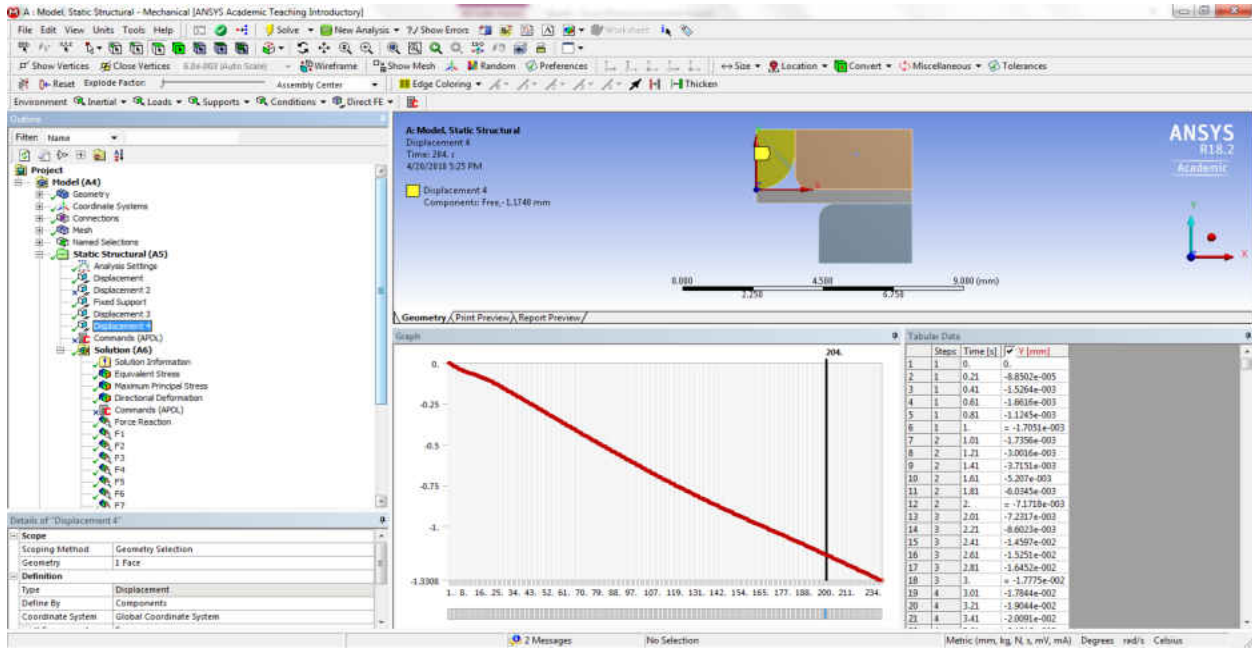
- **Reconfigure test setup to better accommodate dual punch configuration and heating apparatus.** Although the pipe furnace used in the experimental setup is compact in size, the overall design of the test apparatus does not afford much extra space for necessary heat shielding. The dual punch configuration was intentionally designed to eliminate slack in the system, minimizing extra space. However, due to the compactness of the design, heat from the furnace leaks onto the rest of the components and little room exists for adequate heat shielding to be installed, limiting the allowable temperature range. Redesign of core components for future tests should consider integration of high-temperature testing and environmental capabilities. These capabilities are essential to accurate replication of operating conditions for fatigue and creep testing for high temperature applications. Such could be achieved by inclusion of environmental chamber or a refined setup utilizing a direct heating source such as a microheater. Isolation of heat to eliminate thermal wear on sensitive components, as well as accurate monitoring of heat loads on samples should also be considered.
- **Improvement of FEA model performance and optimization routine.** Although the least squares optimization method utilized in this study produced simulated responses with a high approximation to experimental results, the material properties estimated with these were less accurate. The use of constants determined via the inverse method did not produce accurate representations of the

respective stress-strain curves. As such, a more accurate method of producing curve fits is required, such as the use of neural networks or advanced damage models for the latter portion of the simulated  $P$ - $\delta$  responses. Additional considerations could be made for the use of multi-directional models to accommodate for the directionally-dependent microstructures of AM materials, such as with representation of the experimental setup with a quarter-symmetric model.

## **APPENDIX A: ANSYS WORKBENCH MODEL**

The below screenshots are provided as a reference for building a model an optimization program such as that which was utilized in this study using ANSYS:





304\_RT\_edited\_sample\_size - Workbench

File Edit View Tools Units Extensions Jobs Help

Project R2 Optimization Parameter Set

Update All Design Points

Outline of All Parameters

ID	Parameter Name	Value	Unit
1			
2	Input Parameters		
3	Model, Static Structural (A1)		
4	P8 - Young's Modulus	1.94E+05	MPa
5	P25 - Commands (APDL) ARG1	1275	
6	P26 - Commands (APDL) ARG2	0.45	
7	P33 - XYPlane.R7	1.25	mm
8	P34 - XYPlane.H14	2	mm
9	P35 - XYPlane.R15	0.5	mm
10	P36 - XYPlane.V13	2	mm
11	P37 - XYPlane.V17	2	mm
12	P38 - XYPlane.R24	0.5	mm
13	P39 - XYPlane.PunchDiameter	1.25	mm
14	New input parameter	New name	New expression
15	Output Parameters		
16	Model, Static Structural (A1)		
17	P10 - Force Reaction 2 Y Axis	303.48	N
18	P11 - F1.2 Y Axis	186.06	N
19	P12 - F1.3 Y Axis	204.9	N
20	P14 - F4 Y Axis	274.43	N
21	P15 - F5 Y Axis	335.2	N
22	P16 - F6 Y Axis	405.52	N
23	P18 - Force Reaction 2 Y Axis	513.84	N
24	P19 - F10 Y Axis	579.66	N
25	P20 - F9 Y Axis	554.6	N
26	P22 - F7 Y Axis	473.44	N
27	P27 - Directional Deformation Maximum	1.3308	mm
28	P28 - Directional Deformation Minimum	-0.0038429	mm
29	P29 - F1.2 Y Axis	37.878	N
30	P30 - F1.3 Y Axis	39.426	N
31	P31 - F1.4 Y Axis	75.962	N
32	P32 - F1.5 Y Axis	88.369	N
33	P13 - Output Parameter	5.454E+06	kg <sup>1/2</sup> m <sup>-2</sup> s <sup>-4</sup>

Table of Design Points

Name	P8 - Young's Modulus	P25 - Commands (APDL) ARG1	P26 - Commands (APDL) ARG2	Units
1				
2				
3	DP 0 (Current)	1.94E+05	1275	0.45
4	DP 1	2.079E+05	390	1
5	DP 2	2.079E+05	1047	0.04
6	DP 3	2.2E+05	9000	0.33
7	DP 4	1.94E+05	8000	0.3
8	DP 5	1.94E+05	2331.7	0.33429
9	DP 10	1.94E+05	2331.7	0.36198
10	DP 11	1.94E+05	2777.4	0.4E285
11	DP 12	1.94E+05	2336.1	0.35858
12	DP 13	1.94E+05	2332.1	0.35918
13	DP 14	1.94E+05	2331.7	0.35914
14	DP 15	1.94E+05	2331.7	0.35813
15	DP 16	1.94E+05	2331.7	0.35813
16	DP 17	1.94E+05	2331.7	0.35913

Properties of Schematic:

Property	Value
1	
2	
3	Solution Process
4	Update Option
5	Design Point Inflation
6	Partial Update
7	Retain Partial Update
8	License Checkout
9	Retained Design Point
10	Design Point Report
11	Report Snapshot

304\_RT\_edited\_sample\_size - Workbench

File Edit View Tools Units Extensions Jobs Help

Project R2 Optimization Parameter Set

Update Clear Generated Data Refresh Approve Generated Data

Outline of Schematic R2: Optimization

ID	Property	Value	Unit
1	Optimization Study	Enabled	Marketing
2	Minimize P13	Goal, Minimize P13 (Default importance)	
3	Optimization Method		
4	NLPQL	The NLPQL method (Nonlinear Programming by Quadratic Lagrangian) is a gradient-based algorithm to provide a refined, local, optimization result. It supports a single output parameter objective, multiple constraints and is limited to continuous parameters. The starting point must be specified to determine the region of the design space to explore.	
5	Configuration	Approximate derivatives by Central difference and find 3 candidates in a maximum of 25 iterations.	
6	Status	Not Converged	

Properties of Outline: Optimization

Property	Value	Unit
1	Design Points	
2	Preserve Design Points After Ok Run	
3	Failed Design Points Management	
4	Number of Retries	2
5	Retry Delay	60
6	Optimization	
7	Method Name	NLPQL
8	Finite Difference Approximation	Central
9	Allowable Convergence (%)	1E-06
10	Maximum Number of Iterations	25
11	Maximum Number of Candidates	3
12	Optimization Status	
13	Converged	No
14	Number of Iterations	0
15	Number of Evaluations	0

## **APPENDIX B: REPRODUCTION PERMISSIONS**

## RE: 2017 turbo expo proceedings permission

Beth Darchi <DarchiB@asme.org>

Tue 3/27/2018 2:40 PM

To: Jonathan Torres <jonathantorres@knights.ucf.edu>;

Dear Prof. Torres,

It is our pleasure to grant you permission to use **all or any part** of the ASME paper "Characterization and Optimization of Selective Laser Melting Materials Through Small Punch Testing," by Jonathan Torres and Ali P. Gordon, Paper No. GT2017-64896, cited in your letter for inclusion in a dissertation entitled A FRAMEWORK FOR MINIATURIZED MECHANICAL CHARACTERIZATION OF TENSILE, CREEP, AND FATIGUE PROPERTIES OF SLM ALLOYS to be published by the University of Central Florida.

Permission is granted for the specific use as stated herein and does not permit further use of the materials without proper authorization. Proper attribution must be made to the author(s) of the materials. **Please note:** if any or all of the figures and/or Tables are of another source, permission should be granted from that outside source or include the reference of the original source. ASME does not grant permission for outside source material that may be referenced in the ASME works.

As is customary, we request that you ensure full acknowledgment of this material, the author(s), source and ASME as original publisher. Acknowledgment must be retained on all pages where figure is printed and distributed.

Many thanks for your interest in ASME publications.

Sincerely,

**Beth Darchi**  
Publishing Administrator  
ASME  
[2 Park Avenue](#)  
[New York, NY 10016-5990](#)  
[darchib@asme.org](mailto:darchib@asme.org)



## REFERENCES

- [1] T. T. Wohlers and W. Associates, *Wohlers Report 2014: 3D Printing and Additive Manufacturing State of the Industry Annual Worldwide Progress Report*. Wohlers Associates, 2014.
- [2] C. M. Cheah, C. K. Chua, C. W. Lee, C. Feng, and K. Totong, "Rapid prototyping and tooling techniques: a review of applications for rapid investment casting," *The International Journal of Advanced Manufacturing Technology*, vol. 25, no. 3, pp. 308-320, 2005.
- [3] J. A. Bernstein *et al.*, "Fabrication and Analysis of Porous Superalloys for Turbine Components Using Laser Additive Manufacturing," in *49th AIAA/ASME/SAE/ASEE Joint Propulsion Conference*(Joint Propulsion Conferences: American Institute of Aeronautics and Astronautics, 2013.
- [4] J. C. Snyder, C. K. Stimpson, K. A. Thole, and D. J. Mongillo, "Build Direction Effects on Microchannel Tolerance and Surface Roughness," *Journal of Mechanical Design*, vol. 137, no. 11, pp. 111411-111411-7, 2015.
- [5] S. Seyed Farid Seyed *et al.*, "A review on powder-based additive manufacturing for tissue engineering: selective laser sintering and inkjet 3D printing," *Science and Technology of Advanced Materials*, vol. 16, no. 3, p. 033502, 2015.
- [6] B. P. Conner *et al.*, "Making sense of 3-D printing: Creating a map of additive manufacturing products and services," *Additive Manufacturing*, vol. 1–4, pp. 64-76, 10// 2014.
- [7] C. International, "Additively manufactured fuel nozzle for GE LEAP jet engine.," ed: GE, 2015.
- [8] A. Debicari, J. Moor, B. Lagow, and S. Tewari, "Additive Manufacturing for Superalloys-Producibility and Cost Validation (Preprint)," DTIC Document2011.
- [9] R. Hurst, V. Bicego, and J. Foulds, *Small Punch Testing for Creep: Progress in Europe* (Proceedings of the ASME Pressure Vessels and Piping Division). New York, N.Y.: American Society of Mechanical Engineers, 2007.
- [10] R. Hurst and K. Matocha, "Where are we now with the European Code of Practice for Small Punch Testing," *Determination of Mechanical Properties of Materials by Small Punch and other Miniature Testing Techniques*. Ostrava, OCELOT sro, pp. 4-18, 2012.

- [11] S. Cicero, R. Lacalle, and F. Gutiérrez-Solana, "Application of Small Punch Techniques for the Determination of Gold Mechanical Properties," *Strain*, vol. 47, pp. e484-e492, 2011.
- [12] T. E. García, C. Rodríguez, F. J. Belzunce, and C. Suárez, "Estimation of the mechanical properties of metallic materials by means of the small punch test," *Journal of Alloys and Compounds*, vol. 582, pp. 708-717, 2014.
- [13] V. L. Giddings, S. M. Kurtz, C. W. Jewett, J. R. Foulds, and A. A. Edidin, "A small punch test technique for characterizing the elastic modulus and fracture behavior of PMMA bone cement used in total joint replacement," *Biomaterials*, vol. 22, no. 13, pp. 1875-1881, 7// 2001.
- [14] D. J. Jaekel, D. W. MacDonald, and S. M. Kurtz, "Characterization of PEEK biomaterials using the small punch test," *Journal of the Mechanical Behavior of Biomedical Materials*, vol. 4, no. 7, pp. 1275-1282, 10// 2011.
- [15] R. Prakash and S. Arunkumar, "Evaluation of Damage in Materials Due to Fatigue Cycling Through Static and Cyclic Small Punch Testing," in *Small Specimen Test Techniques: 6th Volume*: ASTM International, 2014.
- [16] X. Mao and H. Takahashi, "Development of a further-miniaturized specimen of 3 mm diameter for tem disk ( $\phi$  3 mm) small punch tests," *Journal of Nuclear Materials*, vol. 150, no. 1, pp. 42-52, 1987/09/01 1987.
- [17] P. Kumar, B. K. Dutta, J. Chattopadhyay, and R. S. Shriwastaw, "Numerical evaluation of J-R curve using small punch test data," *Theoretical and Applied Fracture Mechanics*, 2016.
- [18] Z. Zhou, Y. Zheng, X. Ling, R. Hu, and J. Zhou, "A study on influence factors of small punch creep test by experimental investigation and finite element analysis," *Materials Science and Engineering: A*, vol. 527, no. 10-11, pp. 2784-2789, 2010.
- [19] K. Milička and F. Dobeš, "Small punch testing of P91 steel," *International Journal of Pressure Vessels and Piping*, vol. 83, no. 9, pp. 625-634, 2006.
- [20] S. Davies, S. Jeffs, R. Lancaster, and G. Baxter, "High Temperature Deformation Mechanisms in a DLD Nickel Superalloy," *Materials*, vol. 10, no. 5, p. 457, 2017.
- [21] S. Dadbakhsh, L. Hao, and N. Sewell, "Effect of selective laser melting layout on the quality of stainless steel parts," *Rapid Prototyping Journal*, vol. 18, no. 3, pp. 241-249, 2012.

- [22] R. C. Hurst, R. J. Lancaster, S. P. Jeffs, and M. R. Bache, "The contribution of small punch testing towards the development of materials for aero-engine applications," *Theoretical and Applied Fracture Mechanics*, vol. 86, pp. 69-77, 2016.
- [23] R. J. Lancaster, R. Banik, R. C. Hurst, M. R. Bache, and G. Baxter, "Application of small punch test methods to advanced manufactured structures," in *3rd International Conference Small Scale Test Techniques*, Schloss Seggau Seggau, 2014, pp. 170-178.
- [24] E. Altstadt, M. Serrano, M. Houska, and A. García-Junceda, "Effect of anisotropic microstructure of a 12Cr-ODS steel on the fracture behaviour in the small punch test," *Materials Science and Engineering: A*, vol. 654, pp. 309-316, 1/27/ 2016.
- [25] C. Rodríguez, J. G. Cabezas, E. Cárdenas, F. Belzunce, and C. Betegón, "Mechanical properties characterization of heat-affected zone using the small punch test," *Welding Journal*, vol. 88, no. 9, pp. 188-192, 2009.
- [26] B. Gülçimen, A. Durmuş, S. Ülkü, R. C. Hurst, K. Turba, and P. Hähner, "Mechanical characterisation of a P91 weldment by means of small punch fracture testing," *International Journal of Pressure Vessels and Piping*, vol. 105-106, pp. 28-35, 2013.
- [27] L. Zhao, H. Jing, L. Xu, Y. Han, J. Xiu, and Y. Qiao, "Evaluating of creep property of distinct zones in P92 steel welded joint by small punch creep test," *Materials & Design*, vol. 47, pp. 677-686, 2013.
- [28] P. Wanjara and M. Jahazi, "Application of Shear Punch Testing to Study Microstructure-Property Relationships in Electron Beam Welded 17-4 PH Stainless Steel," *Canadian Metallurgical Quarterly*, vol. 48, no. 3, pp. 317-326, 2009/09/01 2009.
- [29] M. Fernández, C. Rodríguez, F. J. Belzunce, and T. E. García, "Use of small punch test to estimate the mechanical properties of powder metallurgy products employed in the automotive industry," *Powder Metallurgy*, vol. 58, no. 3, pp. 171-177, 2015/07/01 2015.
- [30] M. Fernández, C. Rodríguez, F. J. Belzunce, and T. E. García, "Use of small punch test to estimate the mechanical properties of sintered products and application to synchronizer hubs," *Metal Powder Report*, 2016.
- [31] G. Çam and M. Koçak, "Progress in joining of advanced materials Part 2: Joining of metal matrix composites and joining of other advanced materials," *Science and Technology of Welding and Joining*, vol. 3, no. 4, pp. 159-175, 1998.
- [32] M. J. Donachie and S. J. Donachie, *Superalloys: A Technical Guide, 2nd Edition*. Materials Park, OH: ASM International, 2002.

- [33] M. R. Jahangiri, S. M. A. Boutorabi, and H. Arabi, "Study on incipient melting in cast Ni base IN939 superalloy during solution annealing and its effect on hot workability," *Materials Science and Technology*, vol. 28, no. 12, pp. 1402-1413, 2012/12/01 2012.
- [34] B. B. Seth, "Superalloys - The Utility Gas Turbine Perspective," *Minerals, Metals and Materials Society/AIME, Superalloys 2000(USA)*, pp. 3-16, 2000.
- [35] R. Quigg, "New alloy developments in single crystal and DS alloys," *High Temperature Materials and Processes(UK)*, vol. 11, no. 1, pp. 247-254, 1993.
- [36] T. M. Pollock and S. Tin, "Nickel-based superalloys for advanced turbine engines: chemistry, microstructure and properties," *Journal of propulsion and power*, vol. 22, no. 2, pp. 361-374, 2006.
- [37] K. Harris and J. B. Wahl, "Developments in superalloy castability and new applications for advanced superalloys," *Materials Science and Technology*, vol. 25, no. 2, pp. 147-153, 2009.
- [38] I. A. Choudhury and M. A. El-Baradie, "Machinability of nickel-base super alloys: a general review," *Journal of Materials Processing Technology*, vol. 77, no. 1-3, pp. 278-284, 5/1/ 1998.
- [39] A. K. Jena and M. C. Chaturvedi, "The role of alloying elements in the design of nickel-base superalloys," *Journal of Materials Science*, journal article vol. 19, no. 10, pp. 3121-3139, 1984.
- [40] R. Bowman, "Superalloys: A primer and history," in *9th International Symposium on superalloys*, 2000.
- [41] D. Fournier and A. Pineau, "Low cycle fatigue behavior of inconel 718 at 298 K and 823 K," *Metallurgical Transactions A*, journal article vol. 8, no. 7, pp. 1095-1105, 1977.
- [42] R. C. Reed, *The Superalloys: Fundamentals and Applications*. Cambridge University Press, 2008.
- [43] Y. Murata, M. Morinaga, N. Yukawa, H. Ogawa, and M. Kato, "Solidification structures of Inconel 718 with microalloying elements," *Superalloys*, vol. 718, pp. 81-88, 1994.
- [44] J. J. Schirra, R. H. Caless, and R. W. Hatala, "The effect of Laves phase on the mechanical properties of wrought and cast+ HIP Inconel 718," *Superalloys 718, 625,706 and various derivatives*, pp. 375-388, 1991.
- [45] A. Russell and K. L. Lee, *Structure-property relations in nonferrous metals*. John Wiley & Sons, 2005.

- [46] S. Floreen, G. Fuschs, and W. Yang, "The metallurgy of alloy 625. Superalloys 718, 625 and Various Derivatives," *The Minerals Metals and Materials Society*, 1991.
- [47] Z. Pirowski, "Application of nickel superalloys on castings for conventional energy equipment items," *Teka Komisji Motoryzacji i Energetyki Rolnictwa*, vol. 11, 2011.
- [48] E. M. Lehockey, G. Palumbo, and P. Lin, "Improving the weldability and service performance of nickel-and iron-based superalloys by grain boundary engineering," *Metallurgical and Materials Transactions A*, journal article vol. 29, no. 12, pp. 3069-3079, 1998.
- [49] J. J. Schirra, "Effect of heat treatment variations on the hardness and mechanical properties of wrought Inconel 718," *Superalloys 718, 625, 706 and Various Derivatives*, pp. 431-438, 1997.
- [50] G. Sjoberg *et al.*, "Evaluation of the IN 939 alloy for large aircraft engine structures," in *Superalloys 2004* Warrendale, PA: TMS 2004, pp. 441-450.
- [51] M. A. González Albarrán *et al.*, "Effect of Preweld Heat Treatment on the Microstructure of Heat-Affected Zone (HAZ) and Weldability of Inconel 939 Superalloy," *Journal of Materials Engineering and Performance*, vol. 23, no. 4, pp. 1125-1130, 2014.
- [52] E. Hari Krishna, K. Prasad, V. Singh, and V. Kumar, "A comparative evaluation of low cycle fatigue behavior of conventional and modified INCONEL 718," *Transactions of the Indian Institute of Metals*, journal article vol. 63, no. 2, pp. 515-516, 2010.
- [53] Y. Desvallées, M. Bouzidi, F. Bois, and N. Beaudé, "Delta phase in Inconel 718: mechanical properties and forging process requirements," *Superalloys 718, 625, 706 and Various Derivatives*, pp. 281-291, 1994.
- [54] R. M. Kearsey, J. Tsang, S. Oppenheimer, and E. McDevitt, "Microstructural Effects on the Mechanical Properties of ATI 718Plus® Alloy," *Jom*, vol. 64, no. 2, pp. 241-251, 2012.
- [55] M. R. Jahangiri and M. Abedini, "Effect of long time service exposure on microstructure and mechanical properties of gas turbine vanes made of IN939 alloy," *Materials & Design*, vol. 64, pp. 588-600, 12// 2014.
- [56] M. R. Jahangiri, H. Arabi, and S. M. A. Boutorabi, "Comparison of microstructural stability of IN939 superalloy with two different manufacturing routes during long-time aging," *Transactions of Nonferrous Metals Society of China*, vol. 24, no. 6, pp. 1717-1729, 6// 2014.

- [57] J. Zhu *et al.*, "High-temperature-oxidation-induced ordered structure in Inconel 939 superalloy exposed to oxy-combustion environments," *Materials Science and Engineering: A*, vol. 566, pp. 134-142, 2013.
- [58] M. V. Nathal, R. A. Mackay, and R. G. Garlick, "Temperature dependence of  $\gamma$ - $\gamma'$  lattice mismatch in Nickel-base superalloys," *Materials Science and Engineering*, vol. 75, no. 1, pp. 195-205, 1985/11/01 1985.
- [59] P. K. Footner and B. P. Richards, "Long — term growth of superalloy  $\gamma'$  particles," *Journal of Materials Science*, journal article vol. 17, no. 7, pp. 2141-2153, 1982.
- [60] M. A. González, D. I. Martínez, A. Pérez, H. Guajardo, and A. Garza, "Microstructural response to heat affected zone cracking of prewelding heat-treated Inconel 939 superalloy," *Materials Characterization*, vol. 62, no. 12, pp. 1116-1123, 2011.
- [61] S. A. David, S. S. Babu, and J. M. Vitek, *Weldability and microstructure development in nickel-base superalloys* (Conference: 1997 conference on numerical analysis of weldability, Graz (Austria), 29 Sep - 1 Oct 1997; Other Information: PBD: 1997). ; Oak Ridge National Lab., TN (United States), 1997, p. Medium: ED; Size: 30 p.
- [62] M. B. Henderson, D. Arrell, R. Larsson, M. Heobel, and G. Marchant, "Nickel based superalloy welding practices for industrial gas turbine applications," *Science and Technology of Welding and Joining*, vol. 9, no. 1, pp. 13-21, 2004/02/01 2004.
- [63] O. A. Ojo and M. C. Chaturvedi, "On the role of liquated  $\gamma'$  precipitates in weld heat affected zone microfissuring of a nickel-based superalloy," *Materials Science and Engineering: A*, vol. 403, no. 1-2, pp. 77-86, 2005.
- [64] J. Wahl and K. Harris, "Advanced Ni base superalloys for small gas turbines," *Canadian Metallurgical Quarterly*, vol. 50, no. 3, pp. 207-214, 2011.
- [65] S. Shaw, "Response of IN-939 to process variations," *Superalloys 1980*, pp. 275-284, 1980.
- [66] J. J. Schirra, C. A. Borg, and R. W. Hatala, "Mechanical property and microstructural characterization of vacuum die cast superalloy materials," in *Superalloys 2004*, 2004: The Minerals, Metals, and Materials Society.
- [67] W. Hoffelner, "High-cycle fatigue-life of the cast nickel base-superalloys in 738 LC and IN 939," *Metallurgical Transactions A*, journal article vol. 13, no. 7, pp. 1245-1255, 1982.
- [68] S. R. Hegde, R. M. Kearsey, and J. C. Beddoes, "Designing homogenization—solution heat treatments for single crystal superalloys," *Materials Science and Engineering: A*, vol. 527, no. 21-22, pp. 5528-5538, 2010.

- [69] C. Y. Zhang, Y. P. Ren, and X. S. Chen, "The Development Situation of Selective Laser Melting Metal Powder Based on 3D Printing," *Applied Mechanics and Materials*, vol. 518, no. 1, p. 12, 02/06/Number 1/February 2014 2014.
- [70] B. Song *et al.*, "Differences in microstructure and properties between selective laser melting and traditional manufacturing for fabrication of metal parts: A review," *Frontiers of Mechanical Engineering*, vol. 10, no. 2, pp. 111-125, 2015.
- [71] J. P. Kruth, G. Levy, F. Klocke, and T. H. C. Childs, "Consolidation phenomena in laser and powder-bed based layered manufacturing," *CIRP Annals - Manufacturing Technology*, vol. 56, no. 2, pp. 730-759, 2007.
- [72] N. Hopkinson and P. Dicknes, "Analysis of rapid manufacturing—using layer manufacturing processes for production," *Proceedings of the Institution of Mechanical Engineers, Part C: Journal of Mechanical Engineering Science*, vol. 217, no. 1, pp. 31-39, 2003.
- [73] L. Rickenbacher, A. Spierings, and K. Wegener, "An integrated cost-model for selective laser melting (SLM)," *Rapid Prototyping Journal*, vol. 19, no. 3, pp. 208-214, 2013.
- [74] B. D. Gould *et al.*, "Performance and Limitations of 3D-Printed Bipolar Plates in Fuel Cells," *ECS Journal of Solid State Science and Technology*, vol. 4, no. 4, pp. P3063-P3068, January 1, 2015 2015.
- [75] B. Lyons, M. Batalov, P. Mohanty, and S. Das, "Rapid Prototyping of PEM Fuel Cell Bi-Polar Plates Using 3D Printing and Thermal Spray Deposition," in *Proc. SFF Symposium, Austin, TX, 2005*, pp. 446-457: Citeseer.
- [76] A. Meadowcroft, K. Gulia, and K. Kendall, "3D Printing and Prototyping Manifolds for Microtubular Solid Oxide Fuel Cells (mSOFCs)," *International Journal of Science and Research*, vol. 4, no. 11, pp. 709-712, 2015.
- [77] L. Huynh, J. Rotella, and M. D. Sangid, "Fatigue behavior of IN718 microtrusses produced via additive manufacturing," *Materials & Design*, vol. 105, pp. 278-289, 2016.
- [78] L. E. Murr *et al.*, "Microstructure and mechanical behavior of Ti-6Al-4V produced by rapid-layer manufacturing, for biomedical applications," *J Mech Behav Biomed Mater*, vol. 2, no. 1, pp. 20-32, Jan 2009.
- [79] B. Vandenbroucke and J. P. Kruth, "Selective laser melting of biocompatible metals for rapid manufacturing of medical parts," *Rapid Prototyping Journal*, vol. 13, no. 4, pp. 196-203, 2007.

- [80] J. P. Kruth, P. Mercelis, J. Van Vaerenbergh, L. Froyen, and M. Rombouts, "Binding mechanisms in selective laser sintering and selective laser melting," *Rapid Prototyping Journal*, vol. 11, no. 1, pp. 26-36, 2005/02 2005.
- [81] D. Zhang, W. Niu, X. Cao, and Z. Liu, "Effect of standard heat treatment on the microstructure and mechanical properties of selective laser melting manufactured Inconel 718 superalloy," *Materials Science and Engineering: A*, vol. 644, pp. 32-40, 2015.
- [82] F. Liu, X. Lin, G. Yang, M. Song, J. Chen, and W. Huang, "Microstructure and residual stress of laser rapid formed Inconel 718 nickel-base superalloy," *Optics & Laser Technology*, vol. 43, no. 1, pp. 208-213, 2011.
- [83] P. Mercelis and J. P. Kruth, "Residual stresses in selective laser sintering and selective laser melting," *Rapid Prototyping Journal*, vol. 12, no. 5, pp. 254-265, 2006.
- [84] P. Edwards and M. Ramulu, "Fatigue performance evaluation of selective laser melted Ti-6Al-4V," *Materials Science and Engineering: A*, vol. 598, pp. 327-337, 2014.
- [85] E. Chlebus, K. Gruber, B. Kuźnicka, J. Kurzac, and T. Kurzynowski, "Effect of heat treatment on the microstructure and mechanical properties of Inconel 718 processed by selective laser melting," *Materials Science and Engineering: A*, vol. 639, pp. 647-655, 2015.
- [86] L. E. Murr *et al.*, "Microstructural Architecture, Microstructures, and Mechanical Properties for a Nickel-Base Superalloy Fabricated by Electron Beam Melting," *Metallurgical and Materials Transactions A*, journal article vol. 42, no. 11, pp. 3491-3508, 2011.
- [87] L. Thijs, K. Kempen, J.-P. Kruth, and J. Van Humbeeck, "Fine-structured aluminium products with controllable texture by selective laser melting of pre-alloyed AlSi10Mg powder," *Acta Materialia*, vol. 61, no. 5, pp. 1809-1819, 3// 2013.
- [88] Q.-l. Zhang, J.-h. Yao, and J. Mazumder, "Laser Direct Metal Deposition Technology and Microstructure and Composition Segregation of Inconel 718 Superalloy," *Journal of Iron and Steel Research, International*, vol. 18, no. 4, pp. 73-78, 2011.
- [89] L. L. Parimi, R. G. A. D. Clark, and M. M. Attallah, "Microstructural and texture development in direct laser fabricated IN718," *Materials Characterization*, vol. 89, pp. 102-111, 2014.
- [90] F. Brenne *et al.*, "Microstructural design of Ni-base alloys for high-temperature applications: impact of heat treatment on microstructure and mechanical properties after selective laser melting," *Progress in Additive Manufacturing*, vol. 1, no. 3-4, pp. 141-151, 2016.



- [91] P. Lehto, H. Remes, T. Saukkonen, H. Hänninen, and J. Romanoff, "Influence of grain size distribution on the Hall–Petch relationship of welded structural steel," *Materials Science and Engineering: A*, vol. 592, pp. 28-39, 2014.
- [92] E. O. Hall, "The Deformation and Ageing of Mild Steel: III Discussion of Results," *Proceedings of the Physical Society. Section B*, vol. 64, no. 9, p. 747, 1951.
- [93] N. J. Petch, "The cleavage strength of polycrystals," *The Journal of the Iron and Steel Institute*, vol. 174, pp. 25-28, 1953 1953.
- [94] J. Coteló, H. Bearden, J. Torres, K. Smith, B. van Deurson, and A. P. Gordon, "Characterization of 3DP Polylactic Acid Under Monotonic and Cyclic Torsional Conditions," *Additive Manufacturing*, vol. In Review., 2016.
- [95] J. Torres, M. Cole, A. Owji, Z. DeMastry, and A. P. Gordon, "An Approach for Mechanical Property Optimization of Fused Deposition Modeling with Polylactic Acid via Design of Experiments.," *Rapid Prototyping Journal*, Print vol. In Press, Submitted July 2014 2016.
- [96] J. Torres, J. Coteló, J. Karl, and A. P. Gordon, "Mechanical Property Optimization of FDM PLA in Shear with Multiple Objectives," (in English), *JOM*, vol. 67, no. 5, pp. 1183-1193, 2015/05/01 2015.
- [97] T. L. Starr, T. J. Gornet, and J. S. Usher, "The effect of process conditions on mechanical properties of laser-sintered nylon," *Rapid Prototyping Journal*, vol. 17, no. 6, pp. 418-423, 2011/10/04 2011.
- [98] K. N. Amato *et al.*, "Microstructures and mechanical behavior of Inconel 718 fabricated by selective laser melting," *Acta Materialia*, vol. 60, no. 5, pp. 2229-2239, 2012.
- [99] L. Rickenbacher, T. Etter, S. Hovel, and K. Wegener, "High temperature material properties of IN738LC processed by selective laser melting (SLM) technology," *Rapid Prototyping Journal*, vol. 19, no. 4, pp. 282-290, 2013.
- [100] J. Witzel, T. Schopphoven, A. Gasser, and I. Kelbassa, "Development of a model for prediction of material properties of laser clad Inconel 718 as related to porosity in the bulk material," presented at the 30th International Congress on Applications of Lasers & Electro-Optics, Orlando, FL, 2011.
- [101] H. K. Rafi, T. L. Starr, and B. E. Stucker, "A comparison of the tensile, fatigue, and fracture behavior of Ti–6Al–4V and 15-5 PH stainless steel parts made by selective laser melting," *The International Journal of Advanced Manufacturing Technology*, vol. 69, no. 5-8, pp. 1299-1309, 2013.

- [102] H. Brodin, O. Andersson, and S. Johansson, "Mechanical Behaviour and Microstructure Correlation in a Selective Laser Melted Superalloy," in *ASME Turbo Expo 2013: Turbine Technical Conference and Exposition*, 2013, pp. V05AT21A009-V05AT21A009: American Society of Mechanical Engineers.
- [103] P. Kanagarajah, F. Brenne, T. Niendorf, and H. J. Maier, "Inconel 939 processed by selective laser melting: Effect of microstructure and temperature on the mechanical properties under static and cyclic loading," *Materials Science and Engineering: A*, vol. 588, pp. 188-195, 2013.
- [104] T. Trosch, J. Strößner, R. Völkl, and U. Glatzel, "Microstructure and mechanical properties of selective laser melted Inconel 718 compared to forging and casting," *Materials Letters*, vol. 164, pp. 428-431, 2016.
- [105] T. Vilaro, C. Colin, and J. D. Bartout, "As-Fabricated and Heat-Treated Microstructures of the Ti-6Al-4V Alloy Processed by Selective Laser Melting," *Metallurgical and Materials Transactions A*, vol. 42, no. 10, pp. 3190-3199, 2011.
- [106] K. G. Prashanth *et al.*, "Microstructure and mechanical properties of Al-12Si produced by selective laser melting: Effect of heat treatment," *Materials Science and Engineering: A*, vol. 590, pp. 153-160, 2014.
- [107] E. Yasa, K. Kempen, J.-P. Kruth, L. Thijs, and J. Van Humbeeck, "Microstructure and mechanical properties of maraging steel 300 after selective laser melting," in *Solid Freeform Fabrication Symposium Proceedings*, 2010, pp. 383-396.
- [108] J. Sun, Y. Yang, and D. Wang, "Parametric optimization of selective laser melting for forming Ti6Al4V samples by Taguchi method," *Optics & Laser Technology*, vol. 49, pp. 118-124, 2013.
- [109] T. Hua, C. Jing, L. Xin, Z. Fengying, and H. Weidong, "Research on molten pool temperature in the process of laser rapid forming," *Journal of Materials Processing Technology*, vol. 198, no. 1-3, pp. 454-462, 3/3/ 2008.
- [110] K. Abd-Elghany and D. L. Bourell, "Property evaluation of 304L stainless steel fabricated by selective laser melting," *Rapid Prototyping Journal*, vol. 18, no. 5, pp. 420-428, 2012/07/27 2012.
- [111] J. D. Williams and C. R. Deckard, "Advances in modeling the effects of selected parameters on the SLS process," *Rapid Prototyping Journal*, vol. 4, no. 2, pp. 90-100, 1998/06 1998.
- [112] G. Pyka, G. Kerckhofs, I. Papantoniou, M. Speirs, J. Schrooten, and M. Wevers, "Surface Roughness and Morphology Customization of Additive Manufactured Open Porous Ti6Al4V Structures," *Materials*, vol. 6, no. 10, pp. 4737-4757, 2013.

- [113] B. Song, S. Dong, H. Liao, and C. Coddet, "Process parameter selection for selective laser melting of Ti6Al4V based on temperature distribution simulation and experimental sintering," *The International Journal of Advanced Manufacturing Technology*, vol. 61, no. 9-12, pp. 967-974, 2011.
- [114] F. Wang, X. H. Wu, and D. Clark, "On direct laser deposited Hastelloy X: dimension, surface finish, microstructure and mechanical properties," *Materials Science and Technology*, vol. 27, no. 1, pp. 344-356, 2011/01/01 2011.
- [115] F. Wang, "Mechanical property study on rapid additive layer manufacture Hastelloy® X alloy by selective laser melting technology," *The International Journal of Advanced Manufacturing Technology*, vol. 58, no. 5-8, pp. 545-551, 2011.
- [116] A. B. Spierings, T. L. Starr, and K. Wegener, "Fatigue performance of additive manufactured metallic parts," *Rapid Prototyping Journal*, vol. 19, no. 2, pp. 88-94, 2013/03 2013.
- [117] L. Löber, C. Flache, R. Petters, U. Kühn, and J. Eckert, "Comparison of different post processing technologies for SLM generated 316l steel parts," *Rapid Prototyping Journal*, vol. 19, no. 3, pp. 173-179, 2013.
- [118] H. A. Stoffregen, K. Butterweck, and E. Abele, "Fatigue analysis in selective laser melting: review and investigation of thin-walled actuator housings," in *25th Solid Freeform Fabrication Symp.*, 2014.
- [119] J.-P. Kruth, M. Badrossamay, E. Yasa, J. Deckers, L. Thijs, and J. Van Humbeeck, "Part and material properties in selective laser melting of metals," in *Proceedings of the 16th International Symposium on Electromachining*, 2010.
- [120] L. Thijs, F. Verhaeghe, T. Craeghs, J. V. Humbeeck, and J.-P. Kruth, "A study of the microstructural evolution during selective laser melting of Ti-6Al-4V," *Acta Materialia*, vol. 58, no. 9, pp. 3303-3312, 2010.
- [121] M. Badrossamay and T. Childs, "Layer formation studies in selective laser melting of steel powders," in *Proc. SFF Symp., Austin, Texas, USA*, 2006, pp. 268-279.
- [122] H. Asgharzadeh and A. Simchi, "Effect of sintering atmosphere and carbon content on the densification and microstructure of laser-sintered M2 high-speed steel powder," *Materials Science and Engineering: A*, vol. 403, no. 1-2, pp. 290-298, 8/25/ 2005.
- [123] M. Rombouts, J. P. Kruth, L. Froyen, and P. Mercelis, "Fundamentals of Selective Laser Melting of alloyed steel powders," *CIRP Annals - Manufacturing Technology*, vol. 55, no. 1, pp. 187-192, 2006.

- [124] T. Niendorf, S. Leuders, A. Riemer, H. A. Richard, T. Tröster, and D. Schwarze, "Highly Anisotropic Steel Processed by Selective Laser Melting," *Metallurgical and Materials Transactions B*, journal article vol. 44, no. 4, pp. 794-796, 2013.
- [125] Y. Ning, J. Y. H. Fuh, Y. S. Wong, and H. T. Loh, "An intelligent parameter selection system for the direct metal laser sintering process," *International Journal of Production Research*, vol. 42, no. 1, pp. 183-199, 2004/01/01 2004.
- [126] J. P. Kruth, L. Froyen, J. Van Vaerenbergh, P. Mercelis, M. Rombouts, and B. Lauwers, "Selective laser melting of iron-based powder," *Journal of Materials Processing Technology*, vol. 149, no. 1-3, pp. 616-622, 6/10/ 2004.
- [127] A. K. Singh and R. Srinivasa Prakash, "DOE based three-dimensional finite element analysis for predicting density of a laser-sintered part," *Rapid Prototyping Journal*, vol. 16, no. 6, pp. 460-467, 2010/10/05 2010.
- [128] D. Gu and Y. Shen, "Effects of processing parameters on consolidation and microstructure of W-Cu components by DMLS," *Journal of Alloys and Compounds*, vol. 473, no. 1-2, pp. 107-115, 2009.
- [129] D. Gu and Y. Shen, "Processing conditions and microstructural features of porous 316L stainless steel components by DMLS," *Applied Surface Science*, vol. 255, no. 5, pp. 1880-1887, 2008.
- [130] K. A. Mumtaz, P. Erasenthiran, and N. Hopkinson, "High density selective laser melting of Waspaloy®," *Journal of Materials Processing Technology*, vol. 195, no. 1-3, pp. 77-87, 1/1/ 2008.
- [131] Q. Jia and D. Gu, "Selective laser melting additive manufacturing of Inconel 718 superalloy parts: Densification, microstructure and properties," *Journal of Alloys and Compounds*, vol. 585, pp. 713-721, 2014.
- [132] L. N. Carter, K. Essa, and M. M. Attallah, "Optimisation of selective laser melting for a high temperature Ni-superalloy," *Rapid Prototyping Journal*, vol. 21, no. 4, pp. 423-432, 2015.
- [133] L. N. Carter *et al.*, "Process optimisation of selective laser melting using energy density model for nickel based superalloys," *Materials Science and Technology*, pp. 1-5, 2016.
- [134] B. Song, S. Dong, Q. Liu, H. Liao, and C. Coddet, "Vacuum heat treatment of iron parts produced by selective laser melting: Microstructure, residual stress and tensile behavior," *Materials & Design (1980-2015)*, vol. 54, pp. 727-733, 2014.

- [135] B. Van Hooreweder, R. Boonen, D. Moens, J.-P. Kruth, and P. Sas, "On the Determination of Fatigue Properties of Ti6Al4V Produced by Selective Laser Melting," 2012.
- [136] Q. Jia and D. Gu, "Selective laser melting additive manufactured Inconel 718 superalloy parts: High-temperature oxidation property and its mechanisms," *Optics & Laser Technology*, vol. 62, pp. 161-171, 2014.
- [137] M. Averyanova, E. Cicala, P. Bertrand, and D. Grevey, "Optimization of selective laser melting technology using design of experiments method," in *Innovative Developments in Virtual and Physical Prototyping: Proceedings of the 5th International Conference on Advanced Research in Virtual and Rapid Prototyping, Leiria, Portugal, 28 September-1 October, 2011*, 2011, p. 459: CRC Press.
- [138] N. Klingbeil *et al.*, "Effects of process variables and size scale on solidification microstructure in laser-based solid freeform fabrication of Ti-6Al-4V," DTIC Document 2004.
- [139] G. Kasperovich, J. Haubrich, J. Gussone, and G. Requena, "Correlation between porosity and processing parameters in TiAl6V4 produced by selective laser melting," *Materials & Design*, vol. 105, pp. 160-170, 2016.
- [140] J. C. Nelson, S. Xue, J. W. Barlow, J. J. Beaman, H. L. Marcus, and D. L. Bourell, "Model of the selective laser sintering of bisphenol-A polycarbonate," *Industrial & Engineering Chemistry Research*, vol. 32, no. 10, pp. 2305-2317, 1993/10/01 1993.
- [141] U. Lakshminarayan, S. Ogrzydziak, and H. Marcus, "Selective laser sintering of ceramic materials," University of Texas at Austin, 1992.
- [142] P. L. Blackwell, "The mechanical and microstructural characteristics of laser-deposited IN718," *Journal of Materials Processing Technology*, vol. 170, no. 1-2, pp. 240-246, 2005.
- [143] I. Tabernerero, A. Lamikiz, S. Martínez, E. Ukar, and J. Figueras, "Evaluation of the mechanical properties of Inconel 718 components built by laser cladding," *International Journal of Machine Tools and Manufacture*, vol. 51, no. 6, pp. 465-470, 2011.
- [144] Y. Lu *et al.*, "Study on the microstructure, mechanical property and residual stress of SLM Inconel-718 alloy manufactured by differing island scanning strategy," *Optics & Laser Technology*, vol. 75, pp. 197-206, 2015/12/01/ 2015.
- [145] S. Catchpole-Smith, N. Aboulkhair, L. Parry, C. Tuck, I. A. Ashcroft, and A. Clare, "Fractal scan strategies for selective laser melting of 'unweldable' nickel superalloys," *Additive Manufacturing*, vol. 15, pp. 113-122, 2017/05/01/ 2017.

- [146] L. N. Carter, C. Martin, P. J. Withers, and M. M. Attallah, "The influence of the laser scan strategy on grain structure and cracking behaviour in SLM powder-bed fabricated nickel superalloy," *Journal of Alloys and Compounds*, vol. 615, pp. 338-347, 2014.
- [147] F. Liu *et al.*, "The effect of laser scanning path on microstructures and mechanical properties of laser solid formed nickel-base superalloy Inconel 718," *Journal of Alloys and Compounds*, vol. 509, no. 13, pp. 4505-4509, 2011.
- [148] A. B. Anwar and Q.-C. Pham, "Selective laser melting of AlSi10Mg: Effects of scan direction, part placement and inert gas flow velocity on tensile strength," *Journal of Materials Processing Technology*, vol. 240, pp. 388-396, 2017.
- [149] B. Zhang, L. Dembinski, and C. Coddet, "The study of the laser parameters and environment variables effect on mechanical properties of high compact parts elaborated by selective laser melting 316L powder," *Materials Science and Engineering: A*, vol. 584, pp. 21-31, 2013.
- [150] A. Vasinonta, J. Beuth, and M. Griffith, "Process maps for controlling residual stress and melt pool size in laser-based SFF processes," in *Solid freeform fabrication proceedings*, 2000, vol. 8, p. 206: Proc. 2000 Solid Freeform Fabrication Symposium, Austin.
- [151] E. Chlebus, B. Kuźnicka, T. Kurzynowski, and B. Dybała, "Microstructure and mechanical behaviour of Ti—6Al—7Nb alloy produced by selective laser melting," *Materials Characterization*, vol. 62, no. 5, pp. 488-495, 2011.
- [152] S. Leuders *et al.*, "On the mechanical behaviour of titanium alloy TiAl6V4 manufactured by selective laser melting: Fatigue resistance and crack growth performance," *International Journal of Fatigue*, vol. 48, pp. 300-307, 2013.
- [153] I. Yadroitsev, P. Krakhmalev, and I. Yadroitsava, "Selective laser melting of Ti6Al4V alloy for biomedical applications: Temperature monitoring and microstructural evolution," *Journal of Alloys and Compounds*, vol. 583, pp. 404-409, 1/15/ 2014.
- [154] T. Etter, K. Kunze, F. Geiger, and H. Meidani, "Reduction in mechanical anisotropy through high temperature heat treatment of Hastelloy X processed by Selective Laser Melting (SLM)," *IOP Conference Series: Materials Science and Engineering*, vol. 82, no. 1, p. 012097, 2015.
- [155] C.-N. Wei, H.-Y. Bor, and L. Chang, "Effect of hot isostatic pressing on microstructure and mechanical properties of CM-681LC nickel-base superalloy using microcast," *Materials transactions*, vol. 49, no. 1, pp. 193-201, 2008.
- [156] S. Tammam-Williams, P. J. Withers, I. Todd, and P. B. Prangnell, "The Effectiveness of Hot Isostatic Pressing for Closing Porosity in Titanium Parts Manufactured by Selective

- Electron Beam Melting," *Metallurgical and Materials Transactions A*, journal article vol. 47, no. 5, pp. 1939-1946, 2016.
- [157] W. Tillmann, C. Schaak, J. Nellesen, M. Schaper, M. E. Aydinöz, and K. P. Hoyer, "Hot isostatic pressing of IN718 components manufactured by selective laser melting," *Additive Manufacturing*, vol. 13, pp. 93-102, 2017/01/01/ 2017.
- [158] P. Kobryn and S. Semiatin, "Mechanical properties of laser-deposited Ti-6Al-4V," in *Solid Freeform Fabrication Proceedings*, 2001, pp. 6-8: Austin.
- [159] Z. Wang, K. Guan, M. Gao, X. Li, X. Chen, and X. Zeng, "The microstructure and mechanical properties of deposited-IN718 by selective laser melting," *Journal of Alloys and Compounds*, vol. 513, pp. 518-523, 2012.
- [160] M. Thöne, S. Leuders, A. Riemer, T. Tröster, and H. Richard, "Influence of heat-treatment on selective laser melting products—eg Ti6Al4V," in *Solid freeform fabrication symposium SFF, Austin Texas*, 2012.
- [161] A. Riemer, S. Leuders, M. Thöne, H. A. Richard, T. Tröster, and T. Niendorf, "On the fatigue crack growth behavior in 316L stainless steel manufactured by selective laser melting," *Engineering Fracture Mechanics*, vol. 120, pp. 15-25, 2014.
- [162] S. Kumar, "Microstructure and wear of SLM materials," in *Solid Freeform Fabrication Symposium*, 2008, pp. 128-142.
- [163] P. Lipinski, A. Barbas, and A. S. Bonnet, "Fatigue behavior of thin-walled grade 2 titanium samples processed by selective laser melting. Application to life prediction of porous titanium implants," *J Mech Behav Biomed Mater*, vol. 28, pp. 274-90, Dec 2013.
- [164] Q. L. Huang, X. J. Liu, X. Yang, R. R. Zhang, Z. J. Shen, and Q. L. Feng, "Specific heat treatment of selective laser melted Ti-6Al-4V for biomedical applications," *Frontiers of Materials Science*, vol. 9, no. 4, pp. 373-381, Dec 2015.
- [165] M. Ma, Z. Wang, and X. Zeng, "Effect of energy input on microstructural evolution of direct laser fabricated IN718 alloy," *Materials Characterization*, vol. 106, pp. 420-427, 8// 2015.
- [166] H. Qi, M. Azer, and A. Ritter, "Studies of Standard Heat Treatment Effects on Microstructure and Mechanical Properties of Laser Net Shape Manufactured INCONEL 718," *Metallurgical and Materials Transactions A*, journal article vol. 40, no. 10, pp. 2410-2422, 2009.
- [167] A.-C. Yeh, K.-W. Lu, C.-M. Kuo, H.-Y. Bor, and C.-N. Wei, "Effect of serrated grain boundaries on the creep property of Inconel 718 superalloy," *Materials Science and Engineering: A*, vol. 530, pp. 525-529, 2011.

- [168] A. A. Popovich, V. S. Sufiiarov, I. A. Polozov, and E. V. Borisov, "Microstructure and Mechanical Properties of Inconel 718 Produced by SLM and Subsequent Heat Treatment," *Key Engineering Materials*, vol. 651-653, pp. 665-670, 2015.
- [169] T. Vilaro, C. Colin, J. D. Bartout, L. Nazé, and M. Sennour, "Microstructural and mechanical approaches of the selective laser melting process applied to a nickel-base superalloy," *Materials Science and Engineering: A*, vol. 534, pp. 446-451, 2012.
- [170] X. P. Li *et al.*, "A selective laser melting and solution heat treatment refined Al–12Si alloy with a controllable ultrafine eutectic microstructure and 25% tensile ductility," *Acta Materialia*, vol. 95, pp. 74-82, 8/15/ 2015.
- [171] Z. Hu, H. Zhu, H. Zhang, and X. Zeng, "Experimental investigation on selective laser melting of 17-4PH stainless steel," *Optics & Laser Technology*, vol. 87, pp. 17-25, 1// 2017.
- [172] E. Brandl, U. Heckenberger, V. Holzinger, and D. Buchbinder, "Additive manufactured AlSi10Mg samples using Selective Laser Melting (SLM): Microstructure, high cycle fatigue, and fracture behavior," *Materials & Design*, vol. 34, pp. 159-169, 2012.
- [173] M. P. Manahan, A. S. Argon, and O. K. Harling, "The development of a miniaturized disk bend test for the determination of postirradiation mechanical properties," *Journal of Nuclear Materials*, vol. 104, pp. 1545-1550, 1981/01/01 1981.
- [174] M. Manahan, A. Browning, A. Argon, and O. Harling, "Miniaturized disk bend test technique development and application," in *The Use of Small-Scale Specimens for Testing Irradiated Material*: ASTM International, 1986.
- [175] W. R. Corwin and G. E. Lucas, *The Use of Small-scale Specimens for Testing Irradiated Material: A Symposium Sponsored by ASTM Committee E-10 on Nuclear Technology and Applications, Albuquerque, NM, 23 Sept. 1983* (no. 888). ASTM International, 1986.
- [176] M. Eto *et al.*, "Development of a miniaturized bulge test (small punch test) for post-irradiation mechanical property evaluation," in *Small specimen test techniques applied to nuclear reactor vessel thermal annealing and plant life extension*: ASTM International, 1993.
- [177] T. Linse, M. Kuna, J. Schuhknecht, and H. Viehrig, "Application of the small-punch test to irradiated reactor vessel steels in the brittle-ductile transition region," in *Small Specimen Test Techniques: 5th Volume*: ASTM International, 2009.
- [178] G. E. Lucas, "Review of small specimen test techniques for irradiation testing," *Metallurgical Transactions A*, journal article vol. 21, no. 5, pp. 1105-1119, 1990.



- [179] E. M. Rabenberg *et al.*, "Mechanical behavior of AISI 304SS determined by miniature test methods after neutron irradiation to 28dpa," *Journal of Nuclear Materials*, vol. 448, no. 1-3, pp. 315-324, 2014.
- [180] M. Suzuki *et al.*, "Evaluation of toughness degradation by small punch (SP) tests for neutron-irradiated 214Cr-1Mo steel," *Journal of Nuclear Materials*, vol. 179, pp. 441-444, 1991/03/01 1991.
- [181] T. Ishii *et al.*, "Development of a small specimen test machine to evaluate irradiation embrittlement of fusion reactor materials," *Journal of Nuclear Materials*, vol. 283–287, Part 2, pp. 1023-1027, 12// 2000.
- [182] I. Klevtsov, A. Dedov, and A. Molodtsov, "Using of Small Punch Test for Determination of Tensile Properties for Power Plant Steels," presented at the 6th International DAAAM Baltic Conference, Tallinn, Estonia, 2008.
- [183] I. Klevtsov, A. Dedov, and A. Molodtsov, "Measurement of the tensile and yield strength of boiler steels by small punch and tensile test methods," *Estonian Journal of Engineering*, vol. 15, no. 2, pp. 99-107, 2009.
- [184] M. Coleman, H. Alshehri, R. Banik, W. Harrison, and S. Biroasca, "Deformation mechanisms of IN713C nickel based superalloy during Small Punch Testing," *Materials Science and Engineering: A*, vol. 650, pp. 422-431, 2016.
- [185] *ASTM E8-04, Standard Test Methods for Tension Testing of Metallic Materials*, 2004.
- [186] J. S. Ha and E. Fleury, "Small punch tests to estimate the mechanical properties of steels for steam power plant: II. Fracture toughness," *International Journal of Pressure Vessels and Piping*, vol. 75, no. 9, pp. 707-713, 8// 1998.
- [187] M. Suzuki, M. Eto, Y. Nishiyama, K. Fukaya, and T. Isozaki, "Estimation of toughness degradation by microhardness and small punch tests," in *Small specimen test techniques applied to nuclear reactor vessel thermal annealing and plant life extension*: ASTM International, 1993.
- [188] J.-M. Baik, J. Kameda, and O. Buck, "Development of small punch tests for ductile-brittle transition temperature measurement of temper embrittled Ni-Cr steels," in *The use of small-scale specimens for testing irradiated material*: ASTM International, 1986.
- [189] M. Bruchhausen *et al.*, "Recent developments in small punch testing: Tensile properties and DBTT," *Theoretical and Applied Fracture Mechanics*, vol. 86, Part A, pp. 2-10, 12// 2016.

- [190] A. Hayashi and T. Iwamoto, "An Experimental Evaluation of Energy Absorption of TRIP Steel by Small Punch Test," in *Key Engineering Materials*, 2017, vol. 725, pp. 60-65: Trans Tech Publ.
- [191] A. Husain, R. Sharma, and D. K. Sehgal, "Small Punch and Indentation Tests for Structural Health Monitoring," *Procedia Engineering*, vol. 173, pp. 710-717, 2017/01/01 2017.
- [192] *ASTM F2977, Standard Test Method for Small Punch Testing of Polymeric Biomaterials Used in Surgical Implants*, 2013.
- [193] K. k. m. m. c. Matocha and R. r. c. h. p. n. Hurst, "Small Punch Testing - The Transition from a Code of Practice to a European Testing Standard," *Key Engineering Materials*, Article vol. 734, pp. 3-22, 04/14/ 2017.
- [194] *CEN CWA 15627: Small Punch Test Method for Metallic Materials*, 2006.
- [195] K. Matocha, "Small-Punch Testing for Tensile and Fracture Behavior: Experiences and Way Forward," in *Small Specimen Test Techniques: 6th Volume*: ASTM International, 2015.
- [196] J. M. Alegre, I. I. Cuesta, and H. L. Barbachano, "Determination of the fracture properties of metallic materials using pre-cracked small punch tests," *Fatigue & Fracture of Engineering Materials & Structures*, vol. 38, no. 1, pp. 104-112, 2015.
- [197] D. Andrés, M. Lorenzo, R. Lacalle, J. A. Álvarez, and J. M. Alegre, "Application of the Small Punch Creep test to predict times to rupture on magnesium alloys," *Theoretical and Applied Fracture Mechanics*, vol. 86, pp. 45-50, 2016.
- [198] R. Lacalle, J. A. Álvarez, and F. Gutiérrez-Solana, "Analysis of key factors for the interpretation of small punch test results\*," *Fatigue & Fracture of Engineering Materials & Structures*, vol. 31, no. 10, pp. 841-849, 2008.
- [199] V. Karthik, P. Visweswaran, A. Vijayraghavan, K. V. Kasiviswanathan, and B. Raj, "Tensile–shear correlations obtained from shear punch test technique using a modified experimental approach," *Journal of Nuclear Materials*, vol. 393, no. 3, pp. 425-432, 2009.
- [200] R. Kopriva, M. Brumovsky, M. Kytka, M. Lasan, J. Siegl, and K. Matocha, "Application of Miniature Small Punch Test Specimen in Determination of Tensile Properties," in *Small Specimen Test Techniques: 6th Volume*: ASTM International, 2015.
- [201] S. P. Jeffs and R. J. Lancaster, "Elevated temperature creep deformation of a single crystal superalloy through the small punch creep method," *Materials Science and Engineering: A*, vol. 626, pp. 330-337, 2/25/ 2015.

- [202] J. R. Foulds, P. J. Woytowitz, T. K. Parnell, and C. W. Jewett, "Fracture toughness by small punch testing," *Journal of testing and evaluation*, vol. 23, no. 1, pp. 3-10, 1995.
- [203] A. Janča, J. Siegl, and P. Haušild, "Small punch test evaluation methods for material characterisation," *Journal of Nuclear Materials*, vol. 481, pp. 201-213, 12// 2016.
- [204] C. Rodríguez, I. I. Cuesta, M. L. Maspoch, and F. J. Belzunce, "Application of the miniature small punch test for the mechanical characterization of polymer materials," *Theoretical and Applied Fracture Mechanics*, vol. 86, Part A, pp. 78-83, 12// 2016.
- [205] I. Simonovski, S. Holmström, and M. Bruchhausen, "Small punch tensile testing of curved specimens: Finite element analysis and experiment," *International Journal of Mechanical Sciences*, vol. 120, pp. 204-213, 1// 2017.
- [206] I. I. Cuesta, J. M. Alegre, and M. Lorenzo, "Influence of strain state in mechanical behaviour of aluminium alloys using the Small Punch Test," *Materials & Design*, vol. 54, pp. 291-294, 2// 2014.
- [207] I. I. Cuesta, J. M. Alegre, and M. Lorenzo, "Influence of strain state in mechanical behaviour of aluminium alloys using the Small Punch Test," *Materials & Design (1980-2015)*, vol. 54, pp. 291-294, 2014.
- [208] J. Isselin and T. Shoji, "Yield Strength Evaluation by Small-Punch Test," 2009.
- [209] M. Eskner and R. Sandström, "Mechanical Property Evaluation Using the Small Punch Test," *Journal of Testing and Evaluation*, vol. 32, no. 4, pp. 282-289, 2004.
- [210] R. Lacalle, J. García, J. Álvarez, and F. Gutiérrez-Solana, "Obtención mediante el ensayo small punch de las propiedades de tracción de materiales metálicos," in *Anales de Mecánica de la Fractura*, 2009, vol. 26, pp. 501-506.
- [211] M. A. Contreras, C. Rodríguez, F. J. Belzunce, and C. BetegÓN, "Use of the small punch test to determine the ductile-to-brittle transition temperature of structural steels," *Fatigue & Fracture of Engineering Materials & Structures*, vol. 31, no. 9, pp. 727-737, 2008.
- [212] M. C. Kim, J. B. Lee, M. W. Kim, and B. S. Lee, "Empirical Correlation between Parameters from Small Punch and Tensile Curves of Mn-Mo-Ni Low Alloy Steels by Using Test and FE Analysis," in *Key Engineering Materials*, 2007, vol. 353, pp. 420-423: Trans Tech Publ.
- [213] I. I. Cuesta, C. Rodríguez, T. E. García, and J. M. Alegre, "Effect of confinement level on mechanical behaviour using the small punch test," *Engineering Failure Analysis*, vol. 58, Part 1, pp. 206-211, 12// 2015.

- [214] P. M. Bravo Díez, M. Preciado Calzada, D. Cárdenas Gonzalo, and J. Calaf Chica, "Change of mechanical properties of AM60B alloy with heat treatments and its correlation with small punch tests," *Theoretical and Applied Fracture Mechanics*, vol. 86, Part A, pp. 101-108, 12// 2016.
- [215] P. Kumar, B. K. Dutta, J. Chattopadhyay, and R. S. Shrivastaw, "Numerical evaluation of J-R curve using small punch test data," *Theoretical and Applied Fracture Mechanics*, vol. 86, pp. 292-300, 2016.
- [216] F. Auricchio and R. L. Taylor, "A generalized elastoplastic plate theory and its algorithmic implementation," *International Journal for Numerical Methods in Engineering*, vol. 37, no. 15, pp. 2583-2608, 1994.
- [217] I. I. Cuesta, C. Rodríguez, F. J. Belzunce, and J. M. Alegre, "Analysis of different techniques for obtaining pre-cracked/notched small punch test specimens," *Engineering Failure Analysis*, vol. 18, no. 8, pp. 2282-2287, 12// 2011.
- [218] S. S. Bhavikatti, *Theory of plates and shells. [electronic resource]*. New Delhi : New Age International, 2012., 2012.
- [219] C. Rodríguez, D. Arencón, J. Belzunce, and M. L. Maspoch, "Small punch test on the analysis of fracture behaviour of PLA-nanocomposite films," *Polymer Testing*, vol. 33, pp. 21-29, 2014.
- [220] E. Fleury and J. S. Ha, "Small punch tests to estimate the mechanical properties of steels for steam power plant: I. Mechanical strength," *International Journal of Pressure Vessels and Piping*, vol. 75, no. 9, pp. 699-706, 8// 1998.
- [221] J. C. Chica, P. M. Bravo Díez, and M. Preciado Calzada, "Improved correlation for elastic modulus prediction of metallic materials in the Small Punch Test," *International Journal of Mechanical Sciences*, vol. 134, pp. 112-122, 2017/12/01/ 2017.
- [222] C. Rodríguez, M. Fernández, J. Cabezas, T. E. García, and F. J. Belzunce, "The use of the small punch test to solve practical engineering problems," *Theoretical and Applied Fracture Mechanics*, 2016.
- [223] B. Lindqvist, "Influence of microstructure and porosity on fatigue properties of sintered steels," *Met. Powder Rep.*, vol. 44, no. 6, pp. 443-448, 1989.
- [224] U. Engström, C. Larsson, and R. Frykholm, "Cost effective materials for heat treated gear applications," *EURO PM2011, Barcelona*, 2011.
- [225] J. Parker and J. James, "Disc-Bend Creep Deformation Behaviour of 0. 5 Cr 0. 5 Mo 0. 25 V Low Alloy Steel," *Creep and fracture of engineering materials and structures*, pp. 651-660, 1993.

- [226] F. Dobeš and K. Milička, "Comparison of conventional and small punch creep tests of mechanically alloyed Al–C–O alloys," *Materials Characterization*, vol. 59, no. 7, pp. 961-964, 2008.
- [227] F. Dobeš and K. Milička, "On the Monkman–Grant relation for small punch test data," *Materials Science and Engineering: A*, vol. 336, no. 1–2, pp. 245-248, 10/25/ 2002.
- [228] F. Hou, H. Xu, Y. Wang, and L. Zhang, "Determination of creep property of 1.25Cr0.5Mo pearlitic steels by small punch test," *Engineering Failure Analysis*, vol. 28, pp. 215-221, 2013.
- [229] D. Andrés, P. Dymáček, R. Lacalle, and J. A. Álvarez, "Influence of different factors on the Small Punch Creep test," presented at the 4th International Small Sample Test Technique, Shanghai, 2016.
- [230] T. Nakata, S. Komazaki, Y. Kohno, and H. Tanigawa, "Effects of Geometry and Dimension of Specimen and Rig on Small Punch Creep Property," *Experimental Mechanics*, journal article vol. 57, no. 3, pp. 487-494, 2017.
- [231] T. H. Hyde, W. Sun, and J. A. Williams, "Requirements for and use of miniature test specimens to provide mechanical and creep properties of materials: a review," *International Materials Reviews*, vol. 52, no. 4, pp. 213-255, 2007/07/01 2007.
- [232] J. Chakrabarty, "A theory of stretch forming over hemispherical punch heads," *International Journal of Mechanical Sciences*, vol. 12, no. 4, pp. 315-325, 1970.
- [233] M. Bruchhausen, K. Turba, F. de Haan, P. Hähner, T. Austin, and Y. de Carlan, "Characterization of a 14Cr ODS steel by means of small punch and uniaxial testing with regard to creep and fatigue at elevated temperatures," *Journal of Nuclear Materials*, vol. 444, no. 1-3, pp. 283-291, 2014.
- [234] X. Ling, Y. Zheng, Y. You, and Y. Chen, "Creep damage in small punch creep specimens of Type 304 stainless steel," *International Journal of Pressure Vessels and Piping*, vol. 84, no. 5, pp. 304-309, 2007.
- [235] F. Dobeš and P. Dymáček, "Estimation of Anisotropy of Creep Properties in Al and Mg Alloys by Means of Small Punch Test," in *Key Engineering Materials*, 2017, vol. 734, pp. 137-143: Trans Tech Publ.
- [236] C. Wen, T. Xu, and K. Guan, "Correlation Factor Study of Small Punch Creep Test and Its Life Prediction," *Materials*, vol. 9, no. 10, p. 796, 2016.
- [237] S. Holmström, P. Auerkari, R. Hurst, and D. Blagoeva, "Using small punch test data to determine creep strain and strength reduction properties for heat affected zones," *Materials Science and Technology*, vol. 30, no. 1, pp. 63-66, 2013.

- [238] E. Budzacoska *et al.*, "Predicting the J integral fracture toughness of Al 6061 using the small punch test," *Fatigue & Fracture of Engineering Materials & Structures*, vol. 30, no. 9, pp. 796-807, 2007.
- [239] X. Mao, H. Takahashi, and T. Kodaira, "Supersmall punch test to estimate fracture toughness J<sub>Ic</sub> and its application to radiation embrittlement of 2.25Cr-1Mo steel," *Materials Science and Engineering: A*, vol. 150, no. 2, pp. 231-236, 1992/02/29 1992.
- [240] K. Guan, L. Hua, Q. Wang, X. Zou, and M. Song, "Assessment of toughness in long term service CrMo low alloy steel by fracture toughness and small punch test," *Nuclear Engineering and Design*, vol. 241, no. 5, pp. 1407-1413, 5// 2011.
- [241] M. Suzuki, M. Eto, Y. Nishiyama, K. Fukaya, M. Saito, and T. Misawa, "Small specimen test techniques for the evaluation of toughness degradation," *Journal of Nuclear Materials*, vol. 191, pp. 1023-1027, 1992/09/01 1992.
- [242] W. K. Lee, D. R. Metzger, A. Donner, and O. E. Lepik, "The use of a small punch test procedure to determine mechanical properties," in *Small Specimen Test Techniques*: ASTM International, 1998.
- [243] W. Geary and J. T. Dutton, "The Prediction of Fracture Toughness Properties from 3MM Diameter Punch Discs," in *Small Specimen Test Techniques*: ASTM International, 1998.
- [244] X. Mao, M. Saito, and H. Takahashi, "Small punch test to predict ductile fracture toughness J<sub>IC</sub> and brittle fracture toughness K<sub>IC</sub>," *Scripta Metallurgica et Materialia*, vol. 25, no. 11, pp. 2481-2485, 1991/11/01 1991.
- [245] P. Kumar, J. Chattopadhyay, and B. K. Dutta, "On the correlation between minimum thickness and central deflection during small punch test," *Journal of Nuclear Materials*, vol. 475, pp. 37-45, 7// 2016.
- [246] Y. Joo, T. Hashida, H. Takahashi, and K. Shimomura, "The Use of Small Punch (Bulge) Tests to Estimate Fracture Stress in the Lower Shelf Regime," *Journal of Testing and Evaluation*, vol. 20, no. 5, pp. 336-342, 1992.
- [247] M. Afzal Khan, M. M. Nazeer, A. Naeem, and A. G. Atkins, "Computer modeling of elasto-plastic fracture mechanics of ball indentation in ductile aluminium sheet," in *Euro-Mat 95 Conference, Symposium D*, Padova, Italy, 1995, pp. 491-494.
- [248] J.-B. Ju, J.-i. Jang, and D. Kwon, "Evaluation of fracture toughness by small-punch testing techniques using sharp notched specimens," *International Journal of Pressure Vessels and Piping*, vol. 80, no. 4, pp. 221-228, 2003.

- [249] K. Tanaka, T. Amita, T. Satou, K. Koba, J. Kusumoto, and A. Kanaya, "Evaluation on high temperature fracture toughness of CrMoV cast steel by small punch testing," *International Journal of Pressure Vessels and Piping*, vol. 86, no. 9, pp. 643-648, 2009.
- [250] R. Lacalle, J. A. Álvarez, and F. Gutiérrez-Solana, "Use of small punch notched specimens in the determination of fracture toughness," in *ASME 2008 Pressure Vessels and Piping Conference*, 2008, pp. 1363-1369: American Society of Mechanical Engineers.
- [251] K. Turba, B. Gülçimen, Y. Z. Li, D. Blagoeva, P. Hähner, and R. C. Hurst, "Introduction of a new notched specimen geometry to determine fracture properties by small punch testing," *Engineering Fracture Mechanics*, vol. 78, no. 16, pp. 2826-2833, 2011.
- [252] I. I. Cuesta and J. M. Alegre, "Determination of the fracture toughness by applying a structural integrity approach to pre-cracked Small Punch Test specimens," *Engineering Fracture Mechanics*, vol. 78, no. 2, pp. 289-300, 1// 2011.
- [253] *ASTM E399-12e3, Standard Test Method for Linear-Elastic Plane-Strain Fracture Toughness  $K_{Ic}$  of Metallic Materials*, 2012.
- [254] *ESIS P2-92, Procedure for Determining the Fracture Behaviour of Materials*, 1992.
- [255] E. Martínez-Pañeda, I. I. Cuesta, I. Peñuelas, A. Díaz, and J. M. Alegre, "Damage modeling in Small Punch Test specimens," *Theoretical and Applied Fracture Mechanics*, vol. 86, pp. 51-60, 2016.
- [256] T. Misawa, S. Nagata, N. Aoki, J. Ishizaka, and Y. Hamaguchi, "Fracture toughness evaluation of fusion reactor structural steels at low temperatures by small punch tests," *Journal of Nuclear Materials*, vol. 169, pp. 225-232, 1989/12/02 1989.
- [257] M. Abendroth and S. Soltysiak, "Assessment of Material Properties by Means of the Small Punch Test," in *Recent Trends in Fracture and Damage Mechanics*, G. Hütter and L. Zybelle, Eds.: Springer International Publishing, 2016, pp. 127-157.
- [258] J. H. Bulloch, "A study concerning material fracture toughness and some small punch test data for low alloy steels," *Engineering Failure Analysis*, vol. 11, no. 4, pp. 635-653, 2004.
- [259] M. Jayakumar and G. E. Lucas, "The determination of flow distribution by analysis of indentation geometry," *Journal of Nuclear Materials*, vol. 122, no. 1, pp. 840-844, 1984/05/02 1984.
- [260] G. Lucas, G. Odette, and J. Sheckherd, "Shear punch and microhardness tests for strength and ductility measurements," in *The Use of Small-Scale Specimens for Testing Irradiated Material*: ASTM International, 1986.

- [261] R. K. Guduru, K. A. Darling, R. Kishore, R. O. Scattergood, C. C. Koch, and K. L. Murty, "Evaluation of mechanical properties using shear-punch testing," *Materials Science and Engineering: A*, vol. 395, no. 1-2, pp. 307-314, 2005.
- [262] M. B. Toloczko, M. L. Hamilton, and G. E. Lucas, "Ductility correlations between shear punch and uniaxial tensile test data," *Journal of Nuclear Materials*, vol. 283-287, Part 2, pp. 987-991, 12// 2000.
- [263] M. B. Toloczko, R. J. Kurtz, A. Hasegawa, and K. Abe, "Shear punch tests performed using a new low compliance test fixture," *Journal of Nuclear Materials*, vol. 307-311, Part 2, pp. 1619-1623, 12// 2002.
- [264] M. L. Hamilton, M. B. Toloczko, and G. E. Lucas, *Recent progress in shear punch testing* (Conference: International symposium on miniaturized specimens for testing of irradiated materials, Julich (Germany), 22-23 Sep 1994; Other Information: PBD: Sep 1994). ; Pacific Northwest Lab., Richland, WA (United States), 1994, p. Medium: P; Size: 13 p.
- [265] M. B. Toloczko, K. Abe, M. L. Hamilton, F. A. Garner, and R. J. Kurtz, "The effect of test machine compliance on the measured shear punch yield stress as predicted using finite element analysis," *Materials Transactions, JIM*, vol. 41, no. 10, pp. 1356-1359, 2000.
- [266] R. K. Guduru, K. A. Darling, R. O. Scattergood, C. C. Koch, and K. L. Murty, "Mechanical properties of electrodeposited nanocrystalline copper using tensile and shear punch tests," *Journal of Materials Science*, vol. 42, no. 14, pp. 5581-5588, 2007.
- [267] R. K. Guduru, R. O. Scattergood, C. C. Koch, K. L. Murty, and A. V. Nagasekhar, "Finite element analysis of a shear punch test," *Metallurgical and Materials Transactions A*, journal article vol. 37, no. 5, pp. 1477-1483, 2006.
- [268] J. A. H. Ramaekers and J. A. G. Kals, "Strain, stresses and forces in blanking," Technische Hogeschool Eindhoven, Eindhoven 1986 1986, Available: <http://repository.tue.nl/436187>.
- [269] V. Karthik *et al.*, "Tensile properties of modified 9Cr-1Mo steel by shear punch testing and correlation with microstructures," *International Journal of Pressure Vessels and Piping*, vol. 88, no. 10, pp. 375-383, 2011.
- [270] V. Karthik *et al.*, "Characterization of mechanical properties and microstructure of highly irradiated SS 316," *Journal of Nuclear Materials*, vol. 439, no. 1-3, pp. 224-231, 8// 2013.



- [271] M. Madia, S. Foletti, G. Torsello, and A. Cammi, "On the applicability of the small punch test to the characterization of the 1CrMoV aged steel: Mechanical testing and numerical analysis," *Engineering Failure Analysis*, vol. 34, pp. 189-203, 2013.
- [272] P. Egan, M. P. Whelan, F. Lakestani, and M. J. Connelly, "Small punch test: An approach to solve the inverse problem by deformation shape and finite element optimization," *Computational Materials Science*, vol. 40, no. 1, pp. 33-39, 2007.
- [273] T. Linse, M. Kuna, J. Schuhknecht, and H. W. Viehrig, "Usage of the small-punch-test for the characterisation of reactor vessel steels in the brittle–ductile transition region," *Engineering Fracture Mechanics*, vol. 75, no. 11, pp. 3520-3533, 2008.
- [274] S. Yang, Y. Cao, X. Ling, and Y. Qian, "Assessment of mechanical properties of Incoloy800H by means of small punch test and inverse analysis," *Journal of Alloys and Compounds*, vol. 695, pp. 2499-2505, 2/25/ 2017.
- [275] Y. Z. Li, P. Stevens, J. F. Geng, D. F. Ma, and L. Xu, "Determination of Creep Properties from Small Punch Test with Reverse Algorithm," in *Key Engineering Materials*, 2017, vol. 734, pp. 212-236: Trans Tech Publ.
- [276] A. Husain, D. K. Sehgal, and R. K. Pandey, "An inverse finite element procedure for the determination of constitutive tensile behavior of materials using miniature specimen," *Computational Materials Science*, vol. 31, no. 1-2, pp. 84-92, 2004.
- [277] E. N. Campitelli, P. Spätig, R. Bonadé, W. Hoffelner, and M. Victoria, "Assessment of the constitutive properties from small ball punch test: experiment and modeling," *Journal of Nuclear Materials*, vol. 335, no. 3, pp. 366-378, 2004.
- [278] S. Jónás, S. Szávai, P. Rózsahegyi, and R. Beleznai, "Determination of Material Properties Using Small Punch Test."
- [279] G. Chen, P. C. Zhai, and A.-J. Shao, "Appraisalment of creep properties of 12Cr1MoV steel by Small Punch creep test method," in *Materials Science Forum*, 2005, vol. 492, pp. 545-550: Trans Tech Publ.
- [280] J. R. Foulds, M. Wu, S. Srivastav, and C. W. Jewett, "Fracture and tensile properties of ASTM cross-comparison exercise A 533B steel by small punch testing," in *Small Specimen Test Techniques*: ASTM International, 1998.
- [281] I. I. Cuesta, J. M. Alegre, and R. Lacalle, "Determination of the Gurson–Tvergaard damage model parameters for simulating small punch tests," *Fatigue & Fracture of Engineering Materials & Structures*, vol. 33, no. 11, pp. 703-713, 2010.

- [282] B. K. Dutta, S. Guin, M. K. Sahu, and M. K. Samal, "A phenomenological form of the  $q_2$  parameter in the Gurson model," *International Journal of Pressure Vessels and Piping*, vol. 85, no. 4, pp. 199-210, 4// 2008.
- [283] K. Guan, T. Xu, X. Zhang, and Z. Wang, "Effect of microdefects on load-deflection of small punch test by experimental investigation and finite element analysis," *International Journal of Pressure Vessels and Piping*, vol. 110, pp. 14-16, 2013.
- [284] J. Hůlka, P. Kubík, and J. Petruška, "Sensitivity Analysis of Small Punch Test," *Engineering Mechanics*, p. 128, 2012.
- [285] P. Kumar, B. K. Dutta, and J. Chattopadhyay, "Implementation of Theory of Plasticity for Parametric Study on the Relation Between Thickness Change and Central Deflection and Fracture Point Location During Small Punch Test," *Procedia Engineering*, vol. 173, pp. 1101-1107, 2017/01/01 2017.
- [286] S. Goyal, V. Karthik, K. V. Kasiviswanathan, M. Valsan, K. B. S. Rao, and B. Raj, "Finite element analysis of shear punch testing and experimental validation," *Materials & Design*, vol. 31, no. 5, pp. 2546-2552, 5// 2010.
- [287] G. E. Lucas, G. R. Odette, M. Sokolov, P. Spätig, T. Yamamoto, and P. Jung, "Recent progress in small specimen test technology," *Journal of Nuclear Materials*, vol. 307–311, Part 2, pp. 1600-1608, 12// 2002.
- [288] T. Hirose, H. Sakasegawa, A. Kohyama, Y. Katoh, and H. Tanigawa, "Effect of specimen size on fatigue properties of reduced activation ferritic/martensitic steels," *Journal of Nuclear Materials*, vol. 283–287, Part 2, pp. 1018-1022, 12// 2000.
- [289] M. Li and J. F. Stubbins, "Subsize Specimens for Fatigue Crack Growth Rate Testing Metallic Materials," *ASTM SPECIAL TECHNICAL PUBLICATION*, vol. 1418, pp. 321-338, 2002.
- [290] M. L. Villarraga, A. Edidin, M. Herr, and S. M. Kurtz, "Multiaxial fatigue behavior of oxidized and unoxidized UHMWPE during cyclic small punch testing at body temperature," *Highly crosslinked and thermally treated ultra-high molecular weight polyethylene for joint replacements*, vol. ASTM STP, vol. 1445, 2004.
- [291] M. S. Corporation, "MTS Criterion Electromechanical Systems Model 42," ed, 2015.
- [292] J. Torres and A. P. Gordon, "Characterization and Optimization of Selective Laser Melting Materials Through Small Punch Testing," in *ASME Turbo Expo 2017: Turbomachinery Technical Conference and Exposition* Charlotte, NC, 2017, vol. 6, no. 50916, p. V006T24A017, Volume 6: Ceramics; Controls, Diagnostics and Instrumentation; Education; Manufacturing Materials and Metallurgy: American Society of Mechanical Engineers.

- [293] I. Peñuelas, I. I. Cuesta, C. Betegón, C. Rodriguez, and F. J. Belzunce, "Inverse determination of the elastoplastic and damage parameters on small punch tests," *Fatigue & Fracture of Engineering Materials & Structures*, vol. 32, no. 11, pp. 872-885, 2009.
- [294] A. International, *Atlas of Stress-strain Curves*. Metals Park, Ohio: ASM International, 2002.
- [295] R. F. Benck, R. E. Franz, and D. A. DiBerardo, "Quasi-Static Stress-Strain Curves, S-7 Tool Steel," DTIC Document1980.
- [296] T. B. Gibbons and R. Stickler, "IN939: Metallurgy, Properties and Performance," in *High Temperature Alloys for Gas Turbines 1982*, R. Brunetaud, D. Coutsouradis, T. B. Gibbons, Y. Lindblom, D. B. Meadowcroft, and R. Stickler, Eds.: Springer Netherlands, 1982, pp. 369-393.
- [297] The International Nickel Company, "Properties of Some Metals and Alloys," ed: Nickel Institute, 2002.
- [298] H. Eiselstein and D. Tillack, "The invention and definition of alloy 625," *Superalloys*, vol. 718, no. 625, pp. 1-14, 1991.
- [299] L. C. Pardini, F. Levy Neto, and B. McEnaney, "Modelling of mechanical properties of CRFC composites under flexure loading," *Journal of the Brazilian Society of Mechanical Sciences*, vol. 22, pp. 203-216, 2000.
- [300] A. Azzam and W. Li, "An experimental investigation on the three-point bending behavior of composite laminate," in *IOP Conference Series: Materials Science and Engineering*, 2014, vol. 62, no. 1, p. 012016: IOP Publishing.
- [301] M. S. Moreno, A. R. Gutierrez, and J. M. Vicente, "Flexural testing on carbon fibre laminates taking into account their different behaviour under tension and compression," in *IOP Conference Series: Materials Science and Engineering*, 2016, vol. 139, no. 1, p. 012047: IOP Publishing.
- [302] J. Karl, "Thermomechanical Fatigue Life Prediction of Notched 304 Stainless Steel," Ph.D. Mechanical Engineering, Mechanical and Aerospace Engineering, University of Central Florida, 2013.
- [303] S. Keller, "Creep-Fatigue Crack Initiation and Propagation of a Notched Stainless Steel," Ph.D. Mechanical Engineering, Mechanical and Aerospace Engineering, University of Central Florida, 2013.
- [304] S. F. Siddiqui, N. O’Nora, A. A. Fasoro, and A. P. Gordon, "Modeling the Influence of Build Orientation on the Monotonic and Cyclic Response of Additively Manufactured Stainless Steel GP1/17-4PH," in *ASME 2017 International Mechanical Engineering*

*Congress & Exposition*, Tampa, Florida, USA, 2017: American Society of Mechanical Engineers.

- [305] EOS, "Material data sheet EOS NickelAlloy IN718," E. O. S. GmbH, Ed., ed, 2014.
- [306] Stratasys, "Inconel 625 Direct Metal Laser Sintering Material Specifications," I. Stratasys Direct, Ed., ed, 2015.
- [307] K. Matocha, L. Kander, M. Filip, O. Dorazil, K. Guan, and Y. Xu, "The Effect of Stiffness of the Loading System on Determination of Tensile Characteristics from the Results of Small Punch Tests," *Acta Metallurgica Slovaca*, vol. 20, no. 4, 2014.
- [308] I. I. Cuesta, J. M. Alegre, and R. Lacalle, "Determination of the Gurson-Tvergaard damage model parameters for simulating small punch tests," *Fatigue & Fracture of Engineering Materials & Structures*, pp. no-no, 2010.
- [309] D. Sunjaya, T. Wei, R. Harrison, and W. Y. Yeung, "Finite Element Modelling of Small Punch Test on 304H Stainless Steel," *Key Engineering Materials*, vol. 345-346, pp. 1165-1168, 2007.
- [310] S. S. Yang, X. Ling, Y. Qian, and R. B. Ma, "Yield Strength Analysis by Small Punch Test Using Inverse Finite Element Method," *Procedia Engineering*, vol. 130, pp. 1039-1045, 2015/01/01/ 2015.
- [311] M. Sanders, F. Di Bella, and H. Liang, "Mechanical Behavior of Aluminum Alloys During Small Punch Test," 2011.